Prediction of mass transfer performances in trickle-bed reactors equipped with innovative catalyst shapes

Hanane Bouras

THÈSE de DOCTORAT DE L'UNIVERSITÉ DE LYON

Opérée au sein de :

l'Université Claude Bernard Lyon 1

Ecole Doctorale 206
Chimie, Procédés, Environnement

Spécialité de doctorat : Procédés

Soutenue publiquement le 28/01/2021, par :

Hanane Bouras

Etude expérimentale et numérique des transferts de matière externes dans différents réacteurs catalytiques triphasiques en régime ruisselant

---

Devant le jury composé de :

Mme VINKOVIC, Ivana Professeure, Université Claude Bernard Lyon 1	**Présidente**
Mme JULCOUR, Carine Directrice de Recherches, CNRS	**Rapporteure**
M. LI, Huai Zhi Professeur, Université de Lorraine	**Rapporteur**
Mme CHARTON, Sophie Directrice de Recherches, CEA	**Examinatrice**
M. HAROUN, Yacine Ingénieur de Recherches, IFPEN	**Examinateur**
M. FONGARLAND, Pascal Professeur, Université Claude Bernard Lyon 1	**Directeur de thèse**
M. AUGIER, Frédéric Ingénieur de Recherches, IFPEN	**Invité**
M. PHILIPPE, Régis Chargé de Recherches, CNRS	**Invité**

Université Claude Bernard – LYON 1

Administrateur provisoire de l'Université	M. Frédéric FLEURY
Président du Conseil Académique	M. Hamda BEN HADID
Vice-Président du Conseil d'Administration	M. Didier REVEL
Vice-Président du Conseil des Etudes et de la Vie Universitaire	M. Philippe CHEVALLIER
Vice-Président de la Commission de Recherche	M. Jean-François MORNEX
Directeur Général des Services	M. Pierre ROLLAND

COMPOSANTES SANTE

Département de Formation et Centre de Recherche en Biologie Humaine	Directrice : Mme Anne-Marie SCHOTT
Faculté d'Odontologie	Doyenne : Mme Dominique SEUX
Faculté de Médecine et Maïeutique Lyon Sud - Charles Mérieux	Doyenne : Mme Carole BURILLON
Faculté de Médecine Lyon-Est	Doyen : M. Gilles RODE
Institut des Sciences et Techniques de la Réadaptation (ISTR)	Directeur : M. Xavier PERROT
Institut des Sciences Pharmaceutiques et Biologiques (ISBP)	Directrice : Mme Christine VINCIGUERRA

COMPOSANTES & DEPARTEMENTS DE SCIENCES & TECHNOLOGIE

Département Génie Electrique et des Procédés (GEP)	Directrice : Mme Rosaria FERRIGNO
Département Informatique	Directeur : M. Behzad SHARIAT
Département Mécanique	Directeur M. Marc BUFFAT
Ecole Supérieure de Chimie, Physique, Electronique (CPE Lyon)	Directeur : Gérard PIGNAULT
Institut de Science Financière et d'Assurances (ISFA)	Directeur : M. Nicolas LEBOISNE
Institut National du Professorat et de l'Education	Administrateur Provisoire : M. Pierre CHAREYRON
Institut Universitaire de Technologie de Lyon 1	Directeur : M. Christophe VITON
Observatoire de Lyon	Directrice : Mme Isabelle DANIEL
Polytechnique Lyon	Directeur : Emmanuel PERRIN
UFR Biosciences	Administratrice provisoire : Mme Kathrin GIESELER
UFR des Sciences et Techniques des Activités Physiques et Sportives (STAPS)	Directeur : M. Yannick VANPOULLE
UFR Faculté des Sciences	Directeur : M. Bruno ANDRIOLETTI

To my loving parents
To my inspiring husband
To my adoring family

Acknowledgements

First of all, I would like to thank Pierre Porot and Philippe Maurel for giving me the opportunity to carry out this research work within Process Design and Modeling Division of IFP Energies Nouvelles. Thank you for welcoming me in your team.

I am also thankful to my reviewers Ms. Carine Julcour and Pr. Huai Zhi Li for their precious time spent reviewing this dissertation. Many thanks to Ms. Sophie Charton and Pr. Ivana Vinkovic who accepted to be part of the jury to evaluate this research project. A great work of appreciation to all thesis committee members for your goodwill and all your insightful comments to help improve this work.

I would like to express my sincere gratitude to Pascal Fongarland, thesis director, for his guidance and trust throughout the last three years. Your vision of the project and scientific support contributed deeply to the success of this work. To Frédéric Augier, thesis co-director, your profound expertise and knowledge have been of a great help to overcome encountered technical challenges and contributed to the positive outcome of this work, and for that thank you. To Yacine Haroun, thesis supervisor, thank you for your constant help, availability and precious support which helped push the limits of this work. To Régis Philippe, thesis supervisor, thank you for your positive thinking, endless trust and fine listening which were key to pursuing this PhD thesis. It was a pleasure learning from your deep scientific knowledge. Finally, I would like to thank Manel Fourati for her availability and supervision during the first years of this research work. To all of you, the time and effort you dedicated to this research work are appreciated more than I can express. In you I have found mentors, it was a pleasure to learn from you and you will continue to inspire me to find passion in my work and life.

My work would have been unfinished if it was not for the LGPC members who helped me develop experimental skills and build a solid backbone. Thank you Frédéric Bornette and

Fabrice Campoli for your priceless help with the design and initiation of the experimental setup. My appreciation goes to Boris Guicheret for his essential multi-skilled lab assistance. Thank you Valérie Meille and Stéphanie Pallier for your invaluable support with catalyst preparation and coating. Thank you Laurent Vanoye for your fundamental support with GC analysis. To Marie-Line Zanota, thank you for your time spent helping me with image analysis even on short notice. To all LGPC members I would like to address special thanks for your time, priceless lab assistance, kindness and heart-warming welcome among you.

Next I would like to thank Francisco Fortunato Bodziony for his willingness to learn, dedication and determination which lead to high quality numerical results. Also, I would like to express my gratitude to all IFPEN engineers with whom I had the chance to interact, thank you for your hospitality, your patience and your CFD technical insights.

I will not forget the office's atmosphere emmiting good working vibes each and every day, this was only possible thanks to Phuong, Giulia, Olivier, Stefan, Maxime, Gabriel, Vincenzo, Iana, Ana Rita, Andrea and Thi Thu. Thank you for all the coffee breaks and friday croissants tradition shared together.

For my PhD companions, IFPEN and LGPC colleagues, thanks to you I have appreciated this worth-living experience. A special thanks to Laureline and Elsy, my colleagues who turned out to be my closest friends, thank you for turning this wonderful professional work to a passionate long term friendship that supported me throughout this experience.

Finally, I would be forever grateful to my parents Rkia and Hassan for giving me the opportunity to pursue my dreams, for their tremendous trust and constant believe in me. To my family, thank you for your understanding and encouragements. To my husband Nawfal, thank you for always being there for me. To my friends, thank you for standing by me during these long three years.

Contents

List of Figures

List of Tables

Nomenclature

Greek Symbols

α_i	Volume fraction of phase i	$-$
β	Liquid film thickness proposed by [147]	m
β_L	Liquid saturation	$-$
δ_c	Mass transfer boundary layer thickness	m
δ_{cata}	Catalyst layer thickness	m
δ_A	Arithmetic mean liquid film thickness	m
δ_H	Harmonic mean liquid film thickness	m
δ_L	Liquid film thickness	m
δ_{geo}	Geometric liquid film thickness given by $\delta_{geo} = V_{liq}/A_{LS}$	m
ε_L	Total liquid holdup	$-$
$\varepsilon_{L,d}$	Dynamic liquid holdup	$-$
$\varepsilon_{L,s}$	Static liquid holdup	$-$
η_S	Efficiency factor	$-$
Γ	Solubility flux proposed by [126]	$mol/m^2.s$
ε_G	Gas holdup	$-$
κ	Numerical interface curvature	$-$
λ	Flow parameter proposed by [35]	$-$
μ_i	Dynamic viscosity of phase i	$Pa.s$
φ	Level-Set function	$-$
Φ_c	Chemical absorption flux	mol/s
Φ_k	Two-phase parameter proposed by [117] for phase k	$-$
Φ_P	Physical absorption flux	mol/s
ε_B	Bed porosity	$-$

Ψ	Flow parameter proposed by [35]	–
ψ	Sphericity factor proposed by [30]	–
ρ_{cata}	Catalyst density	g/cm^3
ρ_i	Density of phase i	kg/m^3
ρ_m	Mixture density given by $\rho_m = \alpha_L \rho_L + (1-\alpha_L)\rho_G$	kg/m^3
σ	Standard deviation	–
σ_c	Critical surface tension	N/m
σ_i	Surface tension of phase i	N/m
θ	Contact angle	$\circ$
χ	$\sqrt{\Delta P_L/\Delta P_G}$ proposed by [117]	Pa/m
X_{AMS}	α-methylstyrene conversion	%

Subscripts

G	Gas
L	Liquid
S	Solid

Other Symbols

a_c	Reaction rate expression	$mol/g_{Pd}.s$
A_{cata}	External catalyst area	m^2
a_{GL}	Gas-liquid interfacial area	m^{-1}
A_i	Gas chromatography peak area of component i	pA
a_{LS}	Liquid-solid interfacial area	m^{-1}
A_p	Catalyst particle area	m^2
a_S	Specific solid area given by $a_S = A_{cata} \cdot (1-\varepsilon_B)$	m^2
Ca	Capillary number $Ca = \mu V/\sigma_L$	–
$C_{n-dodecane}$	Internal standard (n-dodecane) concentration	mol/l
$C^*_{H_2}$	Thermodynamic equilibrium concentration of hydrogen	mol/m^3
C_{H_2}	Hydrogen concentration	mol/m^3
C_i	Solute concentration in phase i	mol/m^3
C^i_{AMS}	Initial α-methylstyrene concentration	mol/l
C^i_k	i-th species concentration in phase k	mol/m^3

$\overline{C_{S,H_2}}$	Average hydrogen surface concentration	mol/m^3
d_e	Particle equivalent diameter $d_e = \frac{6V_P}{A_P}$	m
D_e	Effective hydrogen diffusivity	m^2/s
d_e^*	Corrected particle equivalent diameter $d_e^* = \psi d_e$	s
D_h	Harmonic mixture diffusion coefficient proposed by [126]	m^2/s
d_h	Hydraulic diameter	m
D_i	Diffusion coefficient in phase i	m^2/s
D_m	Molecular diffusion coefficient	m^2/s
D_{m,H_2}	Hydrogen molecular diffusion coefficient	m^2/s
d_P	Particle diameter	m
ΔP_G	gas flow single phase pressure drop	Pa/m
ΔP_L	liquid flow single phase pressure drop	Pa/m
ΔP_{LG}	two-phase pressure drop	Pa/m
E	Acceleration factor	–
f	Wetting efficiency	–
Fr_i	Froude number of phase i $Fr_i = V_{S,i}^2/(g \cdot d_P)$	–
Ga_i	Galileo number of phase i $Ga_i = (d_P^3 g \rho_i^2)/\mu_i^2$	–
G	gas superficial flow rate	$kg/m^2.s$
Ha	Hatta number	–
He	Henry's constant	–
K	Liquid-phase reaction rate constant	s^{-1}
k	Reaction rate constant $8.33 \cdot 10^{-3}$	$mol^{1-n}.m^{3n}/g_{Pd}.s$
k_i	Gas chromatography correlation coefficient for component i	–
k_{GL}	Gas-liquid mass transfer coefficient	m/s
$k_{GL}.a_{GL}$	Gas-liquid mass transfer coefficient	s^{-1}
k_{LS}	Liquid-solid mass transfer coefficient	m/s
K_{ov}	Overall gas-liquid-solid mass transfer coefficient	m/s
$K_{ov,FM}$	Film model overall gas-liquid-solid mass transfer coefficient	m/s
$K_{ov,FM}^*$	Modified film model overall gas-liquid-solid mass transfer coefficient	m/s

K_R	Overall gas-liquid-solid mass transfer coefficient determined using resistances-in-series model	m/s
L	Liquid superficial flow rate	$kg/m^2.s$
m_{cata}	Catalyst mass	g
Mo_L	Liquid Morton number $Mo_L = (g\mu_L^4)/(\rho_L\sigma_L^3)$	–
m_{Pd}	Palladium mass	g
n	Reaction rate order for hydrogen 0.73	–
P	Operating pressure	Pa
Φ_n	Thiele modulus	–
Q_i	flow rate of phase i	ml/min
r_{app}	Apparent reaction rate	$mol/g.s$
Re_L^*	Modified Reynolds number given by $Re_L^* = \frac{V_{S,L}d_e^*\rho_L}{\mu_L(1-\varepsilon_B)}$	–
Re_i	Reynolds number of phase i $Re_i = (V_{S,i}d_P\rho_i)/\mu_G$	–
S	Shape factor	–
Sc_L	Schmidt number $Sc_L = \mu_L/(\rho_L D_m)$	–
Sh	Sherwood number $Sh = K_{ov}\delta_{geo}/D_m$	–
Sh_{GLS}	Gas-liquid-solid Sherwood number	–
S_m	Source term of the concentration transport equation	$kg.mol/(m^6)$
S_p	External surface of a particle	m^2
T	Operating temperature	$^\circ$ *or* K
u_i	Velocity of phase i	m/s
U_I	Interface velocity proposed by [147]	m/s
V_{liq}	Liquid volume	m^3
V_p	Catalyst particle volume	m^3
V_r	Slip velocity	m/s
$V_{S,i}$	Superficial velocity of phase i	m/s
We_i	Weber number of phase i $We_i = (\rho_i V_{S,i}^2 d_P)/\sigma_L$	–
w_{Pd}	Palladium mass fraction	%
Z	Independent variable proposed by [194]	–

Acronyms / Abbreviations

ABS Acrylonitrile Butadiene Styrene

AMS α-methylstyrene

ANN Artificial Neural Network

BPL Bullet Physics Library

CAD Computer-Aided Design

CFD Computational Fluid Dynamics

CICSAM Compressive Interface Capturing Scheme For Arbitrary Meshes

CLSVOF Coupled Level-Set and Volume-Of-Fluid

CSF Continuum Surface Force

CSS Continuum Surface Stress

CT Computed Tomography

CWAO Catalytic Wet Air Oxidation

DEM Discrete Element Method

FFMR Falling Film Micro-structured Reactor

FID Flame Ionization Detector

GC Gas Chromatogaphy

GLS Gas-Liquid-Solid

GRG Generalised Reduced Gradient

HDN Hydro-denitrogenation

HDS Hydro-desulfurization

HDT Hydrotreatment

HPC High Performance Computing

HRIC High Resolution Interface Capturing

LS Level-Set

MCH Methylcyclohexane

MRI Magnetic Resonance Imaging

NNA Neural Network Approach

PNM Pore Network Model

REV Representative Elementary Volume

RTD Residence Time Distribution

SSE Sum of Squared Errors

TBR Trickle-Bed Reactor

TOC Total Organic Carbon

VOF Volume-Of-Fluid

Chapter 1

Introduction

Multiphase systems are key elements of several industrial processes and have been at the cutting edge of technology development in the chemical industry. The importance of multiphase reactors is highlighted by their wide variety of application fields, including waste water treatment, pharmaceuticals, petrochemical and petroleum industries. Multiphase reactors are defined as containers where several phases are contacted (gas, liquid or solid) resulting in a change in the chemical composition of one or more phases. They are classified into two main categories: two-phase systems (gas-liquid, gas-solid or liquid-solid), and three-phase systems (gas-liquid-solid).

The advent of multiphase reactors dates back to the mid twentieth century, where the chemical industry has shifted from commodity and bulk chemicals to high added-value products. This shift was triggered in the petroleum industry, with the production of specialised products with well defined functions and properties such as high-octane gasoline. Consequently, more and more industrial fields started working on resource wastage reduction, by replacing the less selective processes used earlier with highly selective alternatives. This is achieved using a catalyst to enhance a given reaction rate by lowering its activation energy.

Catalytic processes represent more than 90% of the chemical production processes. Depending on the physical nature of the catalyst, catalysis is either heterogeneous (solid catalyst) or homogeneous (soluble catalyst), our interest in this work is focused on heterogeneous catalytic multiphase reactors, and more specifically Gas-Liquid-Solid reactors (GLS).

Gas-Liquid-Solid reactors are the most spread catalytic multiphase unit processes, they are used when a simultaneous contacting is required between gas, liquid and solid phases. Usually, the reactant is contained in the gas phase, and the heterogeneous catalysis reaction occurs at the surface or within the catalyst particles. Some examples of reactions carried out in GLS

reactors include hydrogenation, alkylation, hydro-treatment, hydro-conversion, Fischer-Tropsch synthesis, and so forth.
The design of GLS reactors relies on the solid catalyst features, the catalyst is either in the form of a suspension when the particle size is small, or loaded and fixed when the particle size is large. GLS reactors can thus be subdivided into two main classes: (i) suspended bed reactors (slurry, agitated tanks and fluidized beds) and (ii) fixed bed reactors. The first class being out of scope, it will not be detailed in the present work. Instead, we will focus on the second class, i.e fixed bed reactors.

Extensively studied in the literature, fixed-bed reactors consist of an assembly of solid particles, randomly loaded and firmly fixed within a column, they have been addressed in many detailed reviews among which [Charpentier et al., 1969, Charpentier and Favier, 1975, Sie, 1991, Al-Dahhan and Dudukovic, 1991, Sie, 1996, Larachi et al., 1998, Sie and Krishna, 1998, Attou et al., 1999, Larachi et al., 2002]. Apart from the solid particles' size, the fixed-bed reactor selection is mainly based on phases' flow direction. Thus, the three available technologies are downward co-current flow, upward co-current flow and counter-current flow. Choosing one or another fixed-bed reactor technology is very much dependent on the: (i) flow pattern, (ii) reaction rate, (iii) mass transfer, (iv) heat transfer and (v) operating conditions.
Each technology has its advantages and drawbacks. The counter-current configuration is rarely used as it is usually source of overloading and flooding issues. Nevertheless, this flow configuration remains interesting in catalytic distillation, since it allows for in-situ separation or selective removal of catalyst inhibitor by-products. When high liquid holdups are required or not detrimental to overall performance (liquid-phase side reaction or too low mass transfer resistances), an interesting configuration can be the co-current upflow. Due to the more conductive continuous liquid phase, the latter configuration offers indeed an advantageous overall heat transfer performance. However, possible drawbacks may rise from this contacting mode, such as the risk of facing large pressure drops and mechanical stress on catalyst particles.

Also known as Trickle-bed reactors, co-current downflow fixed-bed reactors are the most widely used gas-liquid-solid contactors, owing to their relatively easy conception and operability. They are the best technology for many industrial processes to perform hydrogenation, hydration, hydrogenolysis, oxidations, waste-water treatment, etc. The gas and liquid flow co-currently downward through the catalyst particle bed, offering a better mechanical stability of the catalyst. When compared to suspended bed GLS reactors, trickle-bed reactors have a low liquid/solid volume ratio and operate almost in plug flow, allowing to achieve the highest conversion levels [Goto and Smith, 1975, Hofmann, 1978, Shah, 1979]. However, mass transfer limitations are

usually encountered in trickle-bed reactors. Besides, flow conditions may cause partial catalyst wetting, possibly leading to hot spot formation when exothermic reactions are considered. The fluid/solid interfacial area in these reactors is low because of the large particle size. In the present work, our focus lies on trickle-bed reactors for their presence in several crude oil refining steps.

Despite the vast collection of works studying the various phenomena involved in trickle-bed reactors [Satterfield, 1975, Hofmann, 1977, Gianetto et al., 1978, M. and Smith, 1983, Gianetto and Silveston, 1986, Gianetto and Specchia, 1992], much remains to be understood about their fundamental complex multiphase behaviour. Because they operate at high pressure and temperature, industrial trickle-bed reactors are usually opaque, thus little can be directly measured based on observations or imaging. They are considered as a black box, and are designed using reactor models based on hydrodynamic and mass transfer behaviours hypothesis. At the contrary, cold reactor mock-ups can operate at low pressure and temperature conditions, but the phases' properties as well as the gas solubility are different than industrial conditions, making it difficult to achieve high accuracy estimations of the key parameters (namely pressure drop, catalyst wetting, mass transfer coefficients, etc.).

The majority of published works focused on hydrodynamic characterisation in trickle-bed reactors using either invasive or non-invasive methods. This lead to the development of empirical correlations regarding the key hydrodynamic parameters (namely liquid saturation, pressure drop and wetting efficiency). The same does not apply on mass transfer, as only few works focused on investigating the transfer phenomena ($k_{GL}.a_{GL}$,k_{LS},a_{GL},a_{LS}, etc.), and suggested correlations which show disparities and are unreliable. Furthermore, to the best of our knowledge, attention is yet to be attributed to the particle shape and polydispersity effects on mass transfer. This is perhaps due to the difficulty to investigate these effects with current experimental techniques.

In spite of the numerous experimental correlations available in the literature, a deeper knowledge of the hydrodynamic and transfer phenomena occurring in these unit processes is necessary, and would have a positive impact on their design and optimisation. Furthermore, it appears important to improve thermodynamic and physical consistency of external gas-liquid and liquid-solid mass transfers, as well as their coupling to heterogeneous catalysis. This, however, is not possible to achieve experimentally because of the measurements' complexity in industrial operating conditions.

In the effort to provide fundamental quantitative information on trickle-bed reactors, Computational Fluid Dynamics simulations are increasingly used to investigate thoroughly the

various complex flow phenomena. CFD allows a precise description of the system using partial differential equations for momentum and transport equations. There are two main numerical methods used to predict multiphase flow within TBRs: (i) Euler-Euler method and (ii) Volume-Of-Fluid method. The first method considers the three phases as being an interpenetrating continuum, meaning that the solid geometry is not needed for the calculation, instead, a closure law is used to account for the fluid/solid interaction. The second method, i.e Volume-Of-Fluid, tracks explicitly the gas/liquid and liquid/solid interfaces, and solves the two-phase flow through the actual solid loading.
In order to reach a high resolution, the Volume-Of-Fluid method requires very fine mesh cells, especially close to the gas/liquid and liquid/solid interfaces. The mesh quality has a direct impact on mesh size which, in turn, increases the calculation time. Consequently, up until now, this method has been employed on small numerical domains with only few particles. With the development of High Performance Computing (HPC) clusters, the predictions of more substantial numerical domains containing hundreds of catalyst particles is possible using the Volume-Of-Fluid method.

The present work aims to study the complex coupling of multiphase hydrodynamics and mass transfer. Therefore, a CFD numerical model, capable of coupling the two-phase flow and concentration transport with a heterogeneous catalysis reaction, is developed. After being applied on representative volumes of trickle-bed reactors, local hydrodynamic parameters (pressure drop, wetting, liquid retention,...) and mass transfer coefficients ($k_{GL}.a_{GL}$,$k_{LS}.a_{LS}$,...) are the principal outcome of the developed numerical model. Accordingly, a profound investigation of trickle-bed reactors becomes possible in order to expand our knowledge on wetting efficiency and mass transfer coefficients performance. Through the present work, we wish to answer some fundamental interrogations on: (i) whether the VOF approach could predict accurately the trickling flow, (ii) whether CFD can help develop hydrodynamic and mass transfer correlations and (iii) the way hydrodynamics and catalyst shape impact mass transfer.

Chapter 2

State of the art

2.1 Characteristics of Trickle-Bed Reactors

Trickle-bed reactors are Gas-Liquid-Solid contactors employed for many decades to manufacture high added-value products. Depending on the application process, one or more catalyst fixed loadings can be contained is these reactors as shown in figure 2.1.

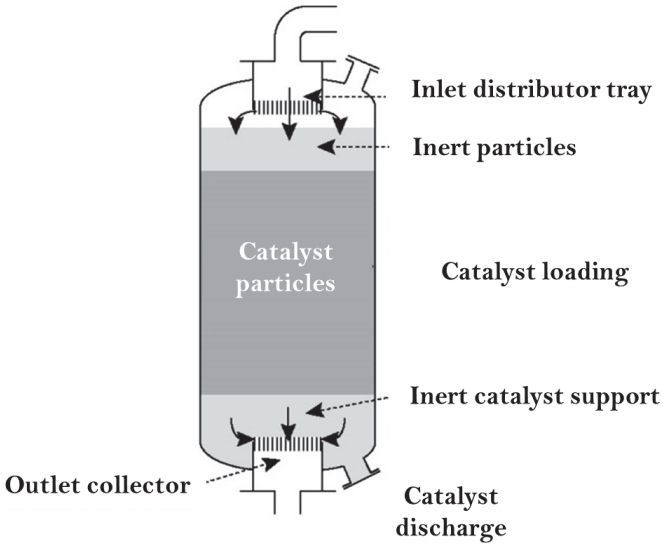

Figure 2.1 Typical industrial trickle-bed reactor schematics

At the top of the reactor, the gas and liquid effluents are distributed over the first solid loading. Parallel to the fluids' flow through the reactor, the reagents travel through the phases to react at the surface of the catalyst particles. Effluents exit the reactor at the bottom with a new chemical composition of the phases. Heat transfer performance is known to be poor in

trickle-bed reactors. Thus, in order to avoid hot-spot apparition in the loading, the catalyst bed is usually subdivided into a series of fixed beds, and temperature control is ensured by cold gas quenches.

Trickle-bed reactors owe their popularity to the unique advantages they offer for large volume processing in the chemical and petroleum industries. The increasingly severe specifications around petroleum-derived products nowadays contribute to their ever-more popularity, thus, through hydro-desulfurization (HDS) and hydro-denitrogenation (HDN) reactions, trickle-bed reactors contribute significantly to the production of low sulphur and nitrogen content fuels. Not only they are used in refineries, but they also carry out successfully a wide spectrum of reactions in other application fields as shown in table 2.1.

Table 2.1 Examples of chemical reactions carried out in trickle-bed reactors

Reaction type	Process	Reference
Petroleum processing	Atmospheric and vacuum residus desulfurization	[Meyers, 1996]
	Hydrocracking for production of high quality middle-distillate fuels	[Meyers, 1996]
	Production of lubricating oils	[Meyers, 1996]
Hydrogenation reactions	Selective hydrogenation of butadiene to butene	[Charpentier, 1976, Shah, 1979]
	hydrogenation of vinylacetylene to butadiene	[Charpentier, 1976, Shah, 1979]
	hydrogenation of glucose to sorbitol	[Germain et al., 1979]
Oxidation reactions	wet air oxidation of acetic acid	[Levec and Smith, 1976]
	Oxidation of ethanol	[Goto and Mabuchi, 1984]
	Oxidation of SO_2	[Hartman and Coughlin, 1971, Mata and Smith, 1981, Haure et al., 1990, Kiared and Zoulalian, 1992]
F-T synthesis	Fischer-Tropsch reaction	[Nishizawa et al., 2014]

With the development of new applications such as bio-fuels, the demand for deeper understanding of TBR phenomena has never been bigger. To uncover the high potential of TBRs for current and future applications, it is essential to fully grasp fundamental phenomena to reach the best performances.

2.1.1 Flow regimes

Simultaneous two-phase flow through a particle bed demonstrates several interfacial area structures, each structure corresponds to a specific flow regime. The assessment of momentum and transfer phenomena (such as velocity, pressure drop, mass transfer, etc.) requires a clear flow regime distinction. Various parameters are responsible for promoting one flow regime or another, such as loading density, fluid flow rates, fluids' physico-chemical properties and so forth [Attou and Boyer, 1999]. The four main flow regimes identified in trickle-bed reactors shown in figure 2.2 are :

— Trickle flow observed at low gas and liquid flow rates
— Pulse flow observed at moderate gas and liquid flow rates
— Spray flow observed at high gas flow rate and low liquid flow rate
— Bubble flow observed at high gas and liquid flow rates

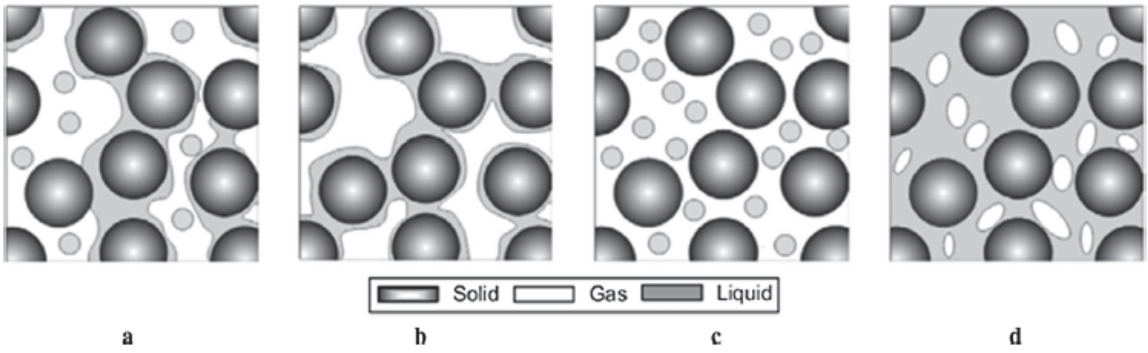

Figure 2.2 Schematic representation of flow regimes in trickle-bed reactors: (a) trickle flow, (b) pulse flow, (c) spray flow and (d) bubbly flow

In trickle flow regime, the gas and liquid flow respectively as continuous and semi-continuous phases. According to Ng and Chu [1987], liquid kinetic energy at very low flow rate conditions is not high enough to overpower interfacial forces at the liquid-solid interface, leading to partial wetting of the catalyst particles, this regime is called partial wetting trickle flow (typically for $V_{S,L} \leq 1 cm/s$). On the other hand, the wetting shifts from partial to total for high enough liquid flow rates, where the liquid phase fully covers the loading's surface.

The transition from trickle flow to pulse flow can be observed visually as both fluid phases flow semi-continuously. In the pulse flow regime, the liquid bridges the gaps between the particles and accumulates to form liquid plugs. Gas phase pockets appear between the different liquid plugs, and hold liquid films at the catalyst surface. This leads to observable gas and liquid rich slugs flowing alternatively through the particle loading. Consequently, fluctuations are noticeable in liquid holdup and pressure drop.
The difference between gas and liquid flow rates in spray regime promotes the shear forces applied on the gas/liquid interface, leading to the dispersion of liquid droplets in the continuous gas phase. Sometimes, this regime is hard to distinguish from trickle regime as both gas phase flows are similar. By contrast, the turbulent energy is sufficient enough to breakup the gas into bubbles. Therefore, in the bubble flow regime, the gas phase is dispersed in the liquid continuous phase. This high interaction regime induces reactor's instability.

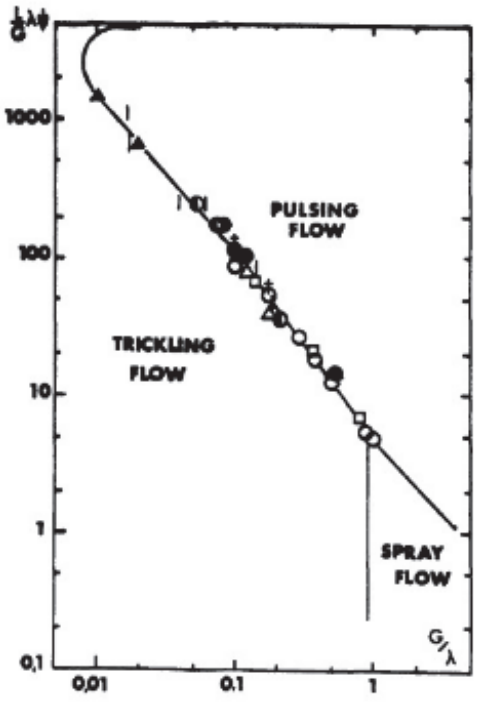

Figure 2.3 Trickle-bed reactor flow map proposed by Charpentier and Favier [1975] where $\lambda = \left(\frac{\rho_G}{\rho_{air}}\frac{\rho_L}{\rho_{water}}\right)^{0.5}$ and $\Psi = \frac{\sigma_{water}}{\sigma_L}\left(\frac{\mu_L}{\mu_{water}}\left(\frac{\rho_{water}}{\rho_L}\right)^2\right)^{0.33}$

Although the trickling regime allows for high stability operations, the high wetting efficiencies along with high mass transfer rates encountered in the pulse regime makes it more suitable

for mass transfer limited reactions. Therefore, a great majority of industrial trickle-bed reactors are operated in the boundary region separating trickling flow from pulsing flow.

Flow regime is of high importance when designing trickle-bed reactors, it impacts significantly critical parameters such as pressure drop, liquid holdup and mass transfer coefficients. For this reason, a vast corpus of works focused on mapping transitions from one regime to another, and on identifying the relevant hydrodynamic descriptors. Several authors proposed correlations and flow maps to facilitate flow regime identification, among whom Charpentier and Favier [1975] who proposed the flow map presented in figure 2.3. However, the use of these charts is not recommended during the design phase since no universal flow map was achieved. The flow map presented in figure 2.3 is based on coordinates previously introduced by Baker [1954], given by:

$$\frac{L}{G}\lambda\Psi \quad and \quad \frac{G}{\lambda} \tag{2.1}$$

Where L and G are respectively the gas and liquid superficial flow rates. λ and Ψ are flow parameters given by:

$$\lambda = \left(\frac{\rho_G}{\rho_{air}}\frac{\rho_L}{\rho_{water}}\right)^{0.5} \quad and \quad \Psi = \frac{\sigma_{water}}{\sigma_L}\left(\frac{\mu_L}{\mu_{water}}\left(\frac{\rho_{water}}{\rho_L}\right)^2\right)^{0.33} \tag{2.2}$$

Where G and L subscripts refer to gas and liquid, ρ_i, μ_i and σ_i are respectively density, viscosity and surface tension of phase i. Computing these parameters' values enable to estimate the flow regime region covered by the investigated gas and liquid flow rates and properties.

2.1.2 Pressure drop

Pressure drop is a fundamental design parameter in trickle-bed reactors since it affects the inter-phase mass transfer coefficients, wetting efficiency and heat transfer performance. Depending on the reactor's geometric features (column diameter, particle size and shape), operating conditions (flow rates and flow regime) and fluids' physico-chemical properties, pressure drop throughout the reactor changes.

Two-phase pressure drop is considerably affected by particle bed characteristics. Indeed, dense loadings with low void fraction values tend to increase pressure drop throughout the reactor. Likewise, reducing the particle's size results in an increase of pressure drop due to the higher tortuosity of gas-liquid flow [Tukac and Hanika, 1992]. The same does not apply on the

reactor's geometry, as pressure drop is less sensitive to column's diameter when compared to the particle size [Gunjal et al., 2005].

According to Sato et al. [1973], pressure drop does not exhibit abrupt changes at the transition boundaries from one flow regime to another. However, pressure drop behaves differently depending on the flow regime. Hysteresis behaviour is observed in the trickle flow regime due to the wetting [Gunjal et al., 2005], and pressure drop increases faster when compared to pulse and bubble flow regimes [Rao et al., 1983, Sai and Varma, 1987]. Based on the aforementioned observations, correlations should be developed separately in each regime.

As for physico-chemical properties of the two-phase system, pressure drop increases with both liquid viscosity and surface tension. This is mainly due to the increase of shear forces at the gas-liquid and liquid-solid interfaces [Morsi et al., 1982, Sai and Varma, 1987].

The importance of pressure drop led to the development of numerous correlations in the literature, based on experiments mostly carried out at atmospheric pressure conditions. Available models can be classified into three categories, as explained hereinafter.

Correlations based on Lockhart-Martinelli

The two-phase pressure drop investigations in trickle-bed reactors started with the work of [Lockhart and Martinelli, 1949], who developed a pressure drop correlation for two-phase flow through horizontal tubes. Thus, two-phase pressure drop ΔP_{LG} is correlated to the following dimensionless numbers:

$$\chi^2 = \Delta P_L / \Delta P_G \tag{2.3}$$

$$\Phi_G^2 = \Delta P_{LG} / \Delta P_G \tag{2.4}$$

$$\Phi_L^2 = \Delta P_{LG} / \Delta P_L \tag{2.5}$$

ΔP_L and ΔP_G correspond to the single phase pressure drops obtained when only gas or liquid flow through the open tube.

This model was the foundation to many other experimental works. Some examples include correlations proposed by [Larkins et al., 1961], [Sato et al., 1973], [Midoux et al., 1976], [Rao et al., 1983], [Tosun, 1984] and [Ratman et al., 1993]. Estimating two-phase pressure drops requires the assessment of ΔP_L and ΔP_G at the same operating conditions. Given the difficulty to maintain identical operating conditions to multiphase flow, single-phase pressure drops are usually estimated using Ergun law given in equation (2.6) [Ergun, 1952].

$$\frac{\Delta P}{z} = \frac{150(1-\varepsilon_B)^2}{\varepsilon_B^3}\frac{u\mu}{d_p^2} + \frac{1.75(1-\varepsilon_B)}{\varepsilon_B^3}\frac{u^2\rho}{d_p} \tag{2.6}$$

Correlations based on bed characteristics and operating conditions

To overcome this challenge, several correlations were proposed based on known operating conditions, such as fluids' flow rates and properties, as well as loading characteristics. Turpin and Huntington [1967] suggested an independent variable Z expressed in terms of Reynolds numbers as $Z = Re_G^{1.167}/Re_L^{0.767}$, and used the two-phase friction factor (equation (2.7)) to correlate the two-phase pressure drop ΔP_{LG}.

$$f_{LG} = \frac{\Delta P_{LG} d_e}{2\rho_G u_G^2} \tag{2.7}$$

Where d_e is the particle's equivalent diameter given by:

$$d_e = \frac{2d_p\varepsilon_B}{3(1-\varepsilon_B)} \tag{2.8}$$

The independent variable Z has been employed and discussed by many other authors. In order to account for the new physico-chemical properties, Specchia and Baldi [1977] introduced a correction factor Ψ to the independent variable proposed by Turpin and Huntington [1967]. On the other hand, Rao et al. [1983] used a similar expression for the independent variable Z. Whilst Sai and Varma [1987] suggested modifying the expression of Z by setting both exponents to 1. In their expressions, these correlations share some common points such as using the void fraction to the power of 3 to account for bed porosity effect on pressure drop.

Phenomenological correlations

Due to the empiric nature of the aforementioned correlations, a different approach was presented by Holub et al. [1992]. The authors modelled the complex void space geometry of the loading by an annular flow in a slit in order to develop a phenomenological correlation valid in low interaction regime (see table 2.2). This model exhibited better agreement between estimated and experimental pressure drops at atmospheric operating pressure. Since the correlation parameters can be determined from single phase flow through the loading (i.e E_1 and E_2), this model is more convenient than the previously presented correlations.

Over the last three decades, more and more emphasis has been placed on developing correlations at high operating pressure conditions. Hasseni et al. [1987] were the first to investigate the effect of operating pressure on two-phase pressure drop in trickle-bed reactors, providing basis for other authors to conduct studies at high pressures such as [Wammes et al., 1991a,b],

[Larachi et al., 1991c, 1994] and [Al-Dahhan and Dudukovic, 1994]. Within the scope of these works, the model developed at atmospheric pressure by Holub et al. [1992] has been extended by Al-Dahhan and Dudukovic [1994] to account for high operating pressures, and a good agreement was reached with experimental data collected at high pressure conditions. The model has been later on modified by Al-Dahhan et al. [1998] to add gas-liquid interaction and account for high gas flow rate effect.

Recently, based on a model first developed by [Attou et al., 1999], Boyer et al. [2007] proposed a mechanistic model which accounts for liquid film flow tortuosity in TBRs. This new correlation predicts accurately pressure drop for a variety of two-phase systems, on a wide operating conditions range. Considering co-current, isothermal and steady state flow of newtonian fluids, the correlation is developed based on mass and momentum equations for gas and liquid phases as the following:

$$\begin{cases} \frac{d((1-\varepsilon_G)\rho_L u_L)}{dz} = 0 \\ \frac{d(\varepsilon_G \rho_G u_G)}{dz} = 0 \\ \frac{d((1-\varepsilon_G)\rho_L u_L^2)}{dz} = -(1-\varepsilon_G)\frac{dP}{dz} + (1-\varepsilon_G)\rho_L g + F_{LG} - F_{LS} = 0 \\ \frac{d(\varepsilon_G \rho_G u_G^2)}{dz} = -\varepsilon_G \frac{dP}{dz} + \varepsilon_G \rho_G g - F_{LG} = 0 \end{cases} \tag{2.9}$$

Where subscripts (G,L,S) refer respectively to gas, liquid and solid. u_i and ρ_i are respectively i-th phase velocity and density, ε_G is the gas holdup and g is the gravitational acceleration. F_{LG} and F_{LS} are respectively the gas-liquid and liquid-solid interfacial forces.

The main difference between models of Boyer et al. [2007] and Attou et al. [1999] lies in interfacial forces. Indeed, Attou et al. [1999] includes an additional interfacial force F_I in the gas phase momentum equation. Whereas, Boyer et al. [2007] integrated F_I in gas-liquid and liquid-solid interaction terms (F_{GL} and F_{LS}). Based on a mechanistic approach, the authors provided closure laws to model the interfacial forces as the following:

$$F_{LS} = (1-\varepsilon_G)\left(A_{LS}\mu_L V_{S,L} + B_{LS}\rho_L V_{S,L}^2\right)(1-\varepsilon_G)^n + \varepsilon_G\left(A_{GL}\mu_G V_{S,G} + B_{GL}\rho_G V_{S,G}^2\right) \tag{2.10}$$

$$F_{LG} = \varepsilon_G\left(A_{GL}\mu_G(V_r + V_{S,G} - + B_{GL}\rho_G(V_r^2 + V_{S,G}^2)\right) \tag{2.11}$$

Where $V_{S,G}$ and $V_{S,L}$ are respectively gas and liquid superficial velocities, whereas the slip velocity V_r, A_{LS}, A_{GL}, B_{LS} and B_{GL} are given by:

$$V_r = V_{S,G} - \left(\frac{\varepsilon_G}{1-\varepsilon_G} V_{S,L} \right) \tag{2.12}$$

$$A_{LS} = 150 \frac{(1-\varepsilon_B)^2}{(1-\varepsilon_G)^3 \varepsilon_B^3 d_P^2} \tag{2.13}$$

$$B_{LS} = 1.75 \frac{(1-\varepsilon_B)}{(1-\varepsilon_G)^3 \varepsilon_B^3 d_P} \tag{2.14}$$

$$A_{GL} = 150 \frac{(1-\varepsilon_G \varepsilon_B)^2}{\varepsilon_G^3 \varepsilon_B^3 d_P^2} \left(\frac{1-\varepsilon_B}{1-\varepsilon_G \varepsilon_B} \right)^{2/3} \tag{2.15}$$

$$B_{GL} = 1.75 \frac{(1-\varepsilon_G \varepsilon_B)}{\varepsilon_G^3 \varepsilon_B^3 d_P} \left(\frac{1-\varepsilon_B}{1-\varepsilon_G \varepsilon_B} \right)^{1/3} \tag{2.16}$$

With ε_B the bed porosity and d_P the particle diameter. These expressions are obtained from modified Ergun equations in single gas or liquid flows. A tortuosity term ($(1-\varepsilon_G)^n$) is included in equation (2.10) to account for liquid film curvature change from single-phase to two-phase flow conditions.

Combining equations (2.9 to 2.16), two-phase pressure drop and gas holdup are determined from the following equations:

$$\begin{cases} F_{LS} = -\frac{dP}{dz} + g\left[(1-\varepsilon_G)\rho_L + \varepsilon_G \rho_G\right] \\ F_{LG} = -\varepsilon_G \frac{dP}{dz} + \varepsilon_G \rho_G g \end{cases} \tag{2.17}$$

According to Boyer et al. [2007], this model predicts pressure drop and liquid saturation with $\pm 20\%$ maximum deviation.

When dealing with non-spherical particles, such as extrudates, Trahan et al. [2014] recommend accounting for particle shape effect on pressure drop through a sphericity factor. First introduced by Brown [1950], the sphericity factor is defined as the following:

$$\psi = \frac{A_{Sphere,P}}{A_P} = \frac{\pi^{1/3}(6V_P)^{2/3}}{A_P} \tag{2.18}$$

Where $A_{Sphere,P}$ is the area of a sphere having the same volume as the considered particle, A_P and V_P are respectively particle's area and volume. For spherical particles, the sphericity factor is obviously unity. Nevertheless, equivalent diameter of non-spherical particles requires correction through the sphericity factor ψ, given as follows:

$$d_e^* = \psi \cdot d_e \tag{2.19}$$

With d_e^* the corrected equivalent diameter and d_e the particle's equivalent diameter.

Equivalent diameter is an important parameter since it describes hydraulic behaviour within catalytic reactors. Therefore, it is commonly characterised experimentally through pressure drop measurements. It should be noted that experiments are conducted thoroughly for each new particle shape. Given the complexity and long duration of experimental characterisation, it is important to explore alternative means. In this vein, Computational Fluid Dynamics (CFD) could be employed to characterise easily and promptly equivalent diameters of new particle shapes, as well as to assess reactor's performance using innovative particle shapes.

Table 2.2 Examples of two-phase pressure drop correlations at atmospheric pressure conditions

Reference	Correlation		Approach
[Larkins et al., 1961]	$log\left(\frac{\Delta P_{LG}}{\Delta P_G+\Delta P_L}\right)=\frac{0.416}{0.666+log(\chi)^2}$	for $0.05<\chi<30$	Empirical
[Sato et al., 1973]	$log\left(\frac{\Delta P_{LG}}{\Delta P_G+\Delta P_L}\right)=\frac{0.70}{1+log(\chi/1.2)^2}$	for $0.1<\chi<20$	Empirical
[Midoux et al., 1976]	$\Phi_L=1+\chi^{-1}+1.14\cdot\chi^{-0.54}$		Empirical
[Turpin and Huntington, 1967]	$log\,(f_{LG})=7.96-1.33\cdot lnZ+0.0021\cdot(lnZ)^2+0.0078\cdot(lnZ)^3$		Empirical
[Holub et al., 1992]	$\Psi_L=\frac{\Delta P_{LG}}{\rho_L g\overline{Z}}+1=\left(\frac{\varepsilon_B}{\varepsilon_L}\right)^3\left[\left(\frac{E_1 Re_L}{(1-\varepsilon_B)Ga_L}+\frac{E_2 Re_L^2}{(1-\varepsilon_B)^2 Ga_L}\right)\right]$ $\Psi_G=\frac{\Delta P_{LG}}{\rho_G g\overline{Z}}+1=\left(\frac{\varepsilon_B}{\varepsilon_B-\varepsilon_L}\right)^3\left[\left(\frac{E_1 Re_G}{(1-\varepsilon_B)Ga_G}+\frac{E_2 Re_G^2}{(1-\varepsilon_B)^2 Ga_G}\right)\right]$ $\Psi_L=1-\frac{\rho_G}{\rho_L}(\Psi_G-1)$		Phenomenological

2.1.3 Liquid holdup

Liquid holdup is an important TBR design parameter for its impact on pressure drop, mean liquid residence time, mean liquid film thickness surrounding catalyst particles, heat and mass transfer coefficients, and so forth. The liquid holdup is whether defined with respect to the reactor volume, in which case it is named total liquid holdup ε_L, or defined per unit void volume and called liquid saturation β_L.

In a particle loading, the liquid holdup consists of two components: (i) dynamic holdup $\varepsilon_{L,d}$ and (ii) static holdup $\varepsilon_{L,s}$. The former represents the constantly renewed liquid volume inside the loading, and the latter quantifies the remaining liquid after complete draining. The total liquid holdup within the reactor is defined as $\varepsilon_{L,d} + \varepsilon_{L,s}$.

As liquid holdup affects reactants' conversion through liquid residence time, it is important to carry a thorough study on its evolution with bed characteristics, operating conditions and physico-chemical properties of the two-phase system.

The particle size as well as the reactor's diameter influence liquid holdup. Gunjal et al. [2005] reported that liquid holdup increases with decreasing particle size because of the high specific area. Furthermore, higher liquid holdup values are achieved for small column diameters. This is mainly due to low gas-liquid interactions within the loading. However, wall effects become negligible in large diameter columns, making the liquid holdup no longer sensitive to the reactor's geometry.

Many of the numerous literature studies on liquid holdup in TBRs reported significant liquid flow rate and viscosity effects. The dynamic liquid holdup increases inherently with liquid flow rate, and decreases with gas flow rate. Besides, at constant gas and liquid flow rates, an increase in shear stress and liquid-solid interaction is observed, inducing high liquid holdup and residence times. The same is achieved when surface tension increases.

Since liquid holdup is essential for TBR design, several works provided experimental correlations to estimate this parameter. They can be classified in two main categories: (i) correlations developed based on [Lockhart and Martinelli, 1949] dimensionless numbers (eq. (2.3)-(2.5)) and (ii) correlations to bed characteristics and fluids' properties.

Correlations based on [Lockhart and Martinelli, 1949] dimensionless parameters

Within the first category, liquid holdup is correlated to dimensionless parameters suggested by Lockhart and Martinelli [1949]. Several authors based their models on these parameters,

among which are Larkins et al. [1961], Hochman and Effron [1969], Charpentier and Favier [1975] etc. As mentioned in section 2.1.2, this group of correlations requires the knowledge of single phase pressure drops, which are challenging to measure in similar conditions as in two-phase flow. Instead, Ergun equation can be employed assuming similar constants for gas and liquid single-phase flows. Furthermore, some of the available correlations do not account explicitly for bed and geometry characteristics, hence the development of the second correlations group.

Correlations to bed characteristics and fluids' properties

In the second category, liquid holdup is correlated to flow rates, two-phase system properties and particle loading features. Several literature contributions are available, among which are Turpin and Huntington [1967], Larachi et al. [1991c], Burghardt et al. [1995]. The vast majority of existing correlations was developed under ambient temperature and atmospheric pressure conditions. However, these operating conditions are far from real industrial conditions, leading to high deviations in liquid holdup estimations. In addition, a thorough literature review shows that gas superficial velocity effect on liquid holdup is yet to be explored and included in empirical models. In order to propose a general correlation, Benkrid et al. [1997] developed a model based on 1542 experimental data points collected from the following investigations [Charpentier and Favier, 1975, Morsi, 1979, Purwasasmita, 1985, Sosa, 1981, Larachi et al., 1991c,a,b, Rode et al., 1994]. The authors highlighted important standard deviations obtained when using literature correlations under the same conditions.

In a different approach, Larachi et al. [2004] developed a correlation using Artificial Neural Network (ANN) computing and dimensional analysis. More than 1100 measurement data points available in literature were used to assess correlations accuracy. The database covers a wide ride range of operating conditions, bed and liquid properties. The authors proposed a correlation able to predict total liquid saturation at $\pm 21.3\%$.

More recently, Boyer et al. [2007] proposed a mechanistic model to estimate liquid saturation. Based on mass and momentum transport equations, as well as gas-liquid and liquid-solid interaction closure laws, the authors suggested a predictive model for both two-phase pressure drop and liquid saturation. For more details on this model, the reader is referred to section 2.1.2.

2.1.4 Catalyst wetting efficiency

Wetting efficiency is a crucial feature in trickle-bed reactors as it determines the extent of catalyst utilization. Catalyst wetting is observed at two different scales: (i) external wetting at the particle scale and (ii) internal wetting at the pore scale. The former is the fraction of external catalyst surface covered by a liquid film, and the latter is the fraction of pores' surface covered by liquid. Three possible wetting configurations might occur: (i) complete wetting where catalyst particles are surrounded and soaked with liquid, (ii) partial wetting where liquid surrounds only a fraction of the solid particle or (iii) incomplete wetting where the solid particle is completely dry.

In trickle-bed reactors, complete internal wetting is usually assumed due to strong capillarity effects [Colombo et al., 1976]. Thus, research works focused on external wetting efficiency, henceforward referred to as wetting efficiency. Along with flow regime, pressure drop and liquid holdup, wetting efficiency influences the reactors overall performance. Depending on the limiting reagents nature, the reaction rate is either impacted in a positive or negative manner. For gas-phase limited reactions, partial wetting conditions promote reagent's conversion due to direct access to the catalyst's surface. In contrast, liquid-phase limited reactions are enhanced by external catalyst wetting extent.

With the intent of characterising wetting efficiency effect on reaction rate, Bondi [1971] studied hydrodesulfurization in a pilot-plant reactor. Assuming negligible mass transfer resistances, the author concluded that partial wetting leads to lower reaction rate constants when compared to total wetting conditions. This effect has been reported by Montagna et al. [1977] and van Klinken and van Dongen [1980] respectively for hydrotreatment and hydrodenitrogenation reactions. The opposite effect was noted for gas-phase limited reactions. Sedriks and Kenney [1973] studied crotonaldehyde hydrogenation using a palladium supported catalyst. The authors reported higher reaction rate constants for a dry bed in comparison to a pre-wetted bed. Similarly, Satterfield and Ozel [1973] reported a negative effect on benzene hydrogenation reaction rate when liquid flow rate increases.

To account for catalyst wetting effect on reaction rate, Ishigaki and Goto [1999] decomposed reaction rate into two contributions: (i) wetted catalyst reaction rate and (ii) dry catalyst reaction rate. The authors suggested an apparent reaction rate model depending on wetting efficiency expressed as follows:

$$r_{app} = f \cdot r(C_L) + (1 - f) \cdot r(C_L^S) \tag{2.20}$$

where C_L and C_L^S are the reagent's concentration respectively in the liquid phase and at the dry catalyst surface.
In the same vein, Bazer-Bachi et al. [2011] proposed simple rules to include partial wetting in fixed bed reactor models. Reactor performance was simulated under partial wetting conditions considering various kinetics, mass and heat transfer limitations. The authors accounted for partial wetting influence through definition of apparent physical properties, such as diffusion coefficient or Thiele modulus.

The wetting efficiency is defined by the ratio of wetted surface to total catalyst surface. Several experimental investigations were performed to quantify this parameter. The two main categories of measurement techniques are (i) non-invasive methods and (ii) invasive methods. The most common non-invasive measurement technique is dye adsorption, it has been used by many authors to determine wetting efficiencies in fixed bed reactors [Colombo et al., 1976, Burghardt et al., 1990, Al-Dahhan and Dudukovic, 1995, van Houwelingen et al., 2006, Baussaron et al., 2007a,b, Julcour-Lebigue et al., 2009]. The technique consists of injecting a dye tracer along with the liquid phase into a TBR, the wetted surface is then pigmented and measured to obtain wetting efficiency. Other direct measurement methods can be used such as Magnetic Resonance Imaging (MRI), Computed Tomography (CT) and photographic technique [Sederman et al., 2001, Sederman and Gladden, 2001, Mantle et al., 2001, Gladden and Sederman, 2002, Gladden et al., 2003]. Even though they are effective, direct approaches are usually applied in lab-scale reactors, operating at ambient pressure and temperature conditions. This means that an offset might be observed between reactor performances at laboratory and industrial conditions.
Regarding indirect methods, the dynamic tracer technique is the most widely used in literature [Colombo et al., 1976, Schwartz et al., 1976, Sicardi et al., 1980, Burghardt et al., 1995, Al-Dahhan and Dudukovic, 1995]. Similarly to dye adsorption, this method consists of injecting one or multiple adsorbable tracers with the liquid phase. The tracers' concentrations are monitored at the reactor's outlet in order to identify their Residence Time Distribution (RTD). Unlike the direct techniques, this approach is applicable under industrial pressure and temperature operating conditions. However, a reactor model is necessary to extract the wetting efficiency. The other indirect methods reported in the literature are the hydrodynamic technique as well as chemical and mass transfer measurements [Ruecker and Agkerman, 1987, Llano et al., 1997, Pironti et al., 1999, Kundu et al., 2003].

Wetting efficiency is inherently and strongly governed by liquid flow rate, but concurrently affected by bed characteristics and operating conditions. At the reactor scale, poorly designed

liquid distributors induce non-uniform liquid distributions within the reactor, leading to low wetting efficiency values. At the particle scale, Baussaron et al. [2007a] reported that low particle diameters promote high wetting efficiencies. This behaviour is attributed to important interactions at the liquid-solid interface. Nevertheless, small particles enhance wetting at the expense of pressure drop.

Several wetting efficiency correlations were proposed in literature. Shulman et al. [1955] were the pioneers of wetting efficiency modelling. The authors performed experiments in a pyrex column containing naphtalene Raschig rings and Berl saddles. Air-water system at ambient temperature and pressure conditions trickle through the loading. A mass transfer measurement technique was used to determine catalyst wetting efficiency. The developed correlations are presented in table 2.3.

Later on, Onda et al. [1967] carried a thorough investigation grounded on their own experimental data as well as available data in literature. The experiments were performed using three different particle shapes, namely spheres, Raschig rings and Berl saddles. The wetting efficiencies are measured in ambient pressure and temperature conditions, and a correlation is proposed based on (Re_L,Fr_L,We_L) dimensionless numbers (cf table 2.3). The correlation predicts wetting efficiency values within $\pm$20%.

In an effort to develop a more general correlation, a statistical approach was adopted by Puranik and Vogelpohl [1974]. This work was motivated by the considerable discrepancies noted between available correlations at the time. The authors proposed a correlation based on experimental data of [Mayo et al., 1935, Grimley, 1945, Fujita and Sacuma, 1954, Hikita and Kataoka, 1956, Shulman et al., 1955, Onda et al., 1967] obtained using different invasive and non-invasive measurement techniques. The maximum standard deviation is 12.5%, and all the predictions are within $\pm$20% error envelope.

Since the above mentioned works proposed correlations considering large non-porous particles, Mills and Dudukovic [1981] performed experiments using porous alumina beads in an attempt to approach realistic configurations. The authors used the dynamic tracer method to evaluate external contacting efficiency of porous particles. Because of the lack of information on critical surface tension σ_C, the model of Onda et al. [1967] could not be used even though it includes all the relevant dimensionless groups (i.e Re_L,Fr_L,We_L). However, the exponential formulation proposed by Onda et al. [1967] was retained by Mills and Dudukovic [1981] as it allows for proper asymptotic behaviour description. The most general correlation was grounded on experimental data as well as [Herskowitz et al., 1979] chemical reaction data.

So far, the wetting efficiency investigations were carried out at atmospheric pressure and ambient temperature conditions. Hence, the work of Ring and Missen [1991] focused on accurately quantifying wetting efficiency in high pressure and temperature conditions, using the dynamic tracer technique. The experiments were performed in a stainless steel column at P=10MPa, and temperatures varied between 330°C, 350°C and 370°C. The authors correlated the wetting efficiency to the linear superficial velocity as can be seen in equation (2.21).

$$f = 1 - exp\left(-118 \cdot V_{S,L}^{0.634}\right) \tag{2.21}$$

Contrarily to other factors, only few studies investigated the gas velocity effect on wetting efficiency. Two opposite effects are suspected to occur when gas velocity increases: (i) liquid holdup decreases and so is the wetting efficiency and (ii) the gas-liquid shear force increases leading to higher wetting efficiencies. Among these few studies, Burghardt et al. [1995] proposed a wetting efficiency model including the gas velocity effect. The experiments were carried out in a glass column containing porous alumina particles, at atmospheric pressure and ambient temperature conditions. The authors reported a negative gas velocity effect on wetted catalyst surface extent. As can be seen from table 2.3, a gas Reynolds number was used to account for the gas effect on wetting efficiency.

Later on, along the same line as Ring and Missen [1991], high pressure investigations were performed by Al-Dahhan and Dudukovic [1995]. The authors studied wetting of porous extrudates within a stainless steel column, at pressure conditions up to 4.93MPa. Even though the developed correlation depends on two-phase pressure drop, sometimes complex to determine, the predictions reach a 3.7% mean relative error and are globally bounded at $\pm 10\%$

These correlations and others are reported in table 2.3. Although many correlations have been developed to estimate wetting efficiencies, many of them give dispersed results when used at the same system conditions. For a trickle-bed reactor operated at atmospheric pressure and $Re_G = 86.3$, Ranade et al. [2011] concluded that some correlations give similar results [El-Hisnawi et al., 1982, Mills and Dudukovic, 1981, Ring and Missen, 1991] while others give much lower wetting efficiency predictions [Burghardt et al., 1990, 1995, Al-Dahhan and Dudukovic, 1995] (cf. figure 2.4).

Recently, Julcour-Lebigue et al. [2009] focused on developing a new general correlation accounting for poorly studied effects such as liquid viscosity, bed porosity, particle diameter and wall effects. The authors performed experiments at atmospheric pressure, ambient temperature and no gas flow. The dye adsorption technique was used to mark the wetted catalyst areas, and

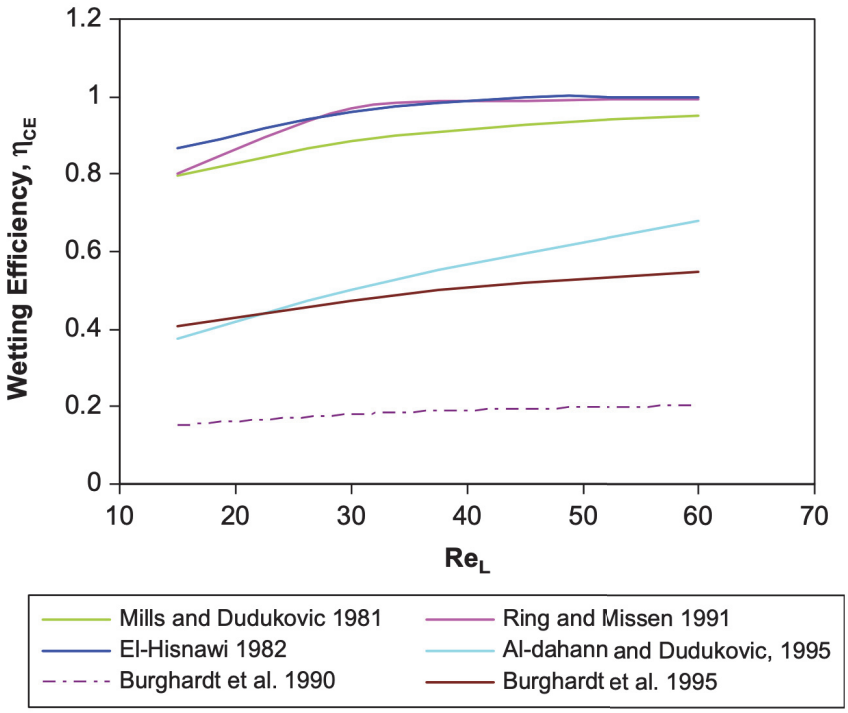

Figure 2.4 Wetting efficiency (η_{CE}) predicted using various correlations [Ranade et al., 2011]

wetting efficiencies were obtained from processing cross section images using MatLab. The proposed correlation is reported in table 2.3. The Froude and Morton dimensionless groups were found to be descriptive of wetting efficiency behaviour, and $\pm 5\%$ wetting efficiency predictions are obtained.

This analysis of literature contributions on wetting efficiency uncovered few grey areas. First of all, accuracy of measured wetting efficiency values depends on employed experimental techniques. Even though direct methods are more powerful, their application is limited to ambient temperature and atmospheric pressure conditions. Contrarily, indirect techniques, which allow for high temperature and pressure investigations, are less accurate since they rely on reactor modelling. Moreover, despite wettability differences, solid wetting is usually investigated using non-porous rather than porous catalyst particles. This impacts wetting efficiency since liquid-solid interactions are modified. Furthermore, given the opposite conclusions established in literature, gas superficial velocity effect on wetting efficiency is yet to be determined.

Table 2.3 Examples of wetting efficiency correlations at atmospheric pressure conditions

Reference	Correlation	Experimental conditions
[Shulman et al., 1955]	for Berl saddles: $f = 0.35 \cdot \left(\frac{\dot{m}_L}{\dot{m}_G}\right)^{0.20}$ for Raschig rings: $f = 0.24 \cdot \left(\frac{\dot{m}_L}{\dot{m}_G}\right)^{0.25}$	Air/water Temperature: 20°C to 23°C Column diameter: $D = 254mm$ Raschig rings, Berl saddles
[Onda et al., 1967]	$f = 1 - exp\left(-1.45 \cdot (Re_L)^{0.1} \cdot (Fr_L)^{-0.05} \cdot (We_L)^{0.2} \cdot \left(\frac{\sigma_C}{\sigma_L}\right)^{0.75}\right)$ for $0.04 < Re_L < 500$, $2.5 \cdot 10^{-9} < Fr_L < 1.8 \cdot 10^{-2}$ $1.2 \cdot 10^{-8} < We_L < 0.27$ and $0.3 < \sigma_C/\sigma_L < 2.0$	Liquids: water, ethanol, glycerol Temperature: 20°C Column diameter: $D = 120mm$ Ceramic and glass spheres, ceramic Raschig rings, ceramic Berl saddles
[Puranik and Vogelpohl, 1974]	$f = 1.045 \cdot (Re_L)^{0.041} \cdot (We_L)^{0.133} \cdot (\sigma_C/\sigma_L)^{-0.182}$ for $0.5 < Re_L < 850$, $7.7 \cdot 10^{-7} < Fr_L < 4.7 \cdot 10^{-3}$ $21 \cdot 10^{-7} < We_L < 12 \cdot 10^{-3}$ and $0.3 < \sigma_C/\sigma_L < 1.05$	Experimental works of : [Mayo et al., 1935, Grimley, 1945, Fujita and Sacuma, 1954, Hikita and Kataoka, 1956, Shulman et al., 1955, Onda et al., 1967]
[Mills and Dudukovic, 1981]	$f = 1 - exp\left(-1.35 \cdot Re_L^{0.333} \cdot Fr_L^{0.235} \cdot We_L^{-0.170} \left(\frac{a_S d_P}{\varepsilon_B^2}\right)^{-0.0425}\right)$	Helium/hexane at ambient temperature

Table 2.3 – Examples of wetting efficiency correlations at atmospheric pressure conditions [Continued from previous page]

Reference	Correlation	Experimental conditions
	$f = tanh\left(0.664 \cdot Re_L^{0.333} \cdot Fr_L^{0.195} \cdot We_L^{-0.171} \left(\frac{a_S d_P}{\varepsilon_B^2}\right)^{-0.0615}\right)$	Column diameter: $D = 13.5mm$ porous alumina beads
[Herskowitz, 1981]	$f = 1.301 + 0.0739 \cdot ln(V_{S,L})$ for $2 \cdot 10^{-4} < V_{S,L} < 1 \cdot 10^{-2}$	experimental data of Herskowitz et al. [1979]
[Burghardt et al., 1995]	$f = 3.38 \cdot Re_L^{0.222} \cdot Re_G^{-0.083} \left(Ga_L^*\right)^{-0.516}$	Nitrogen/n-hexane at ambient temperature Column diameter: $D = 32mm$ porous alumina spheres, crushed pellets
[Gonzalez-Mendizabal et al., 1998]	$f = 1 - exp\left(-4.265 \cdot 10^{-2} (Re_L)^{0.745} (Re_G)^{0.079}\right)$ for $6.71 < Re_L < 117.90, \quad 32.00 < Re_G < 204.19$	Air/water at ambient temperature Column diameter: $D = 67mm$ Cylindrical particles
[Julcour-Lebigue et al., 2009]	$f = 1 - exp\left(-1.986 \cdot Fr_L^{0.139} \cdot Mo_L^{0.0195} \cdot \varepsilon_B^{-1.55}\right)$	Liquids: heptane, gasoil, heptane+gasoil, water, ethanol Temperature: 25°C Column diameter: $D = 57mm$ porous alumina: spheres, cylinders and trilobes

2.1.5 Gas-Liquid-Solid mass transfer

For the heterogeneous catalytic reaction to occur, the involved reagents need to reach the catalyst's active sites. However, as trickle-bed reactors usually operate at the trickle flow regime, the phases interactions are low leading to low interfacial mass transfer rates. Consequently, for fast intrinsic kinetics, reaction rate is often limited by interfacial mass transfer.
For instance, a gas-phase reagent (A) and a liquid-phase reagent (B) undergo the following heterogeneous catalytic reaction:

$$\nu_A A_{gas} + \nu_B B_{liquid} \rightarrow \nu_C C_{liquid} \tag{2.22}$$

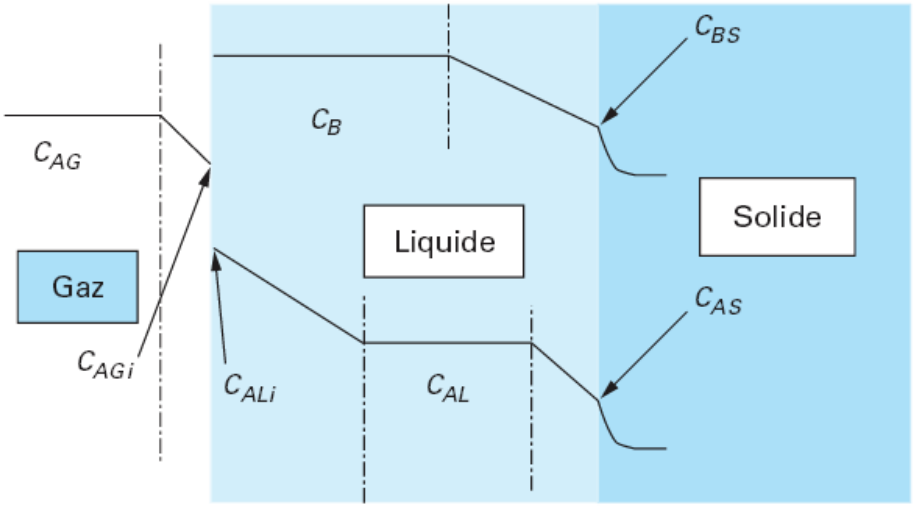

Figure 2.5 Interfacial gradients likely to appear in Trickle-Bed Reactors [Rode and Charpentier, 2011]

In the low interaction regime, the reagents as well as the product go through different steps for the reaction to happen:

— Transfer of A_{gas} to the gas-liquid interface
— Transfer of A_{gas} through the gas-liquid interface towards the liquid bulk
— Transfer of A_{gas} and B_{liquid} to the catalyst external surface
— Intraparticle diffusion of A_{gas} and B_{liquid} into the catalyst's pores
— Physical adsorption of A_{gas} and B_{liquid} on catalyst's active sites
— Chemical reaction described in equation (2.22)
— C_{liquid} desorption

— Intraparticle diffusion of C_{liquid}

— Transfer of C_{liquid} from the catalyst's surface to the liquid

The different mass transfer steps involved in the above detailed process may present limitations to the reactor's performance. Therefore, it is crucial to investigate mass transfer behaviour in order to ensure that the reactor is operated in the kinetic regime. The following sections are focused on the three relevant types of mass transfer rates in TBRs: (i) gas-liquid, (ii) liquid-solid and (iii) gas-solid mass transfer rates.

Gas-liquid mass transfer

In theory, mass transfer at the gas-liquid interface disguises two different transfer components: (i) gas-side mass transfer and (ii) liquid-side mass transfer. The former refers to reagent's migration from the gas' bulk to the gas-liquid interface, and the latter from the gas-liquid interface to the liquid bulk. In reality, the gas-side mass transfer rate is usually neglected as the vast majority of gases used are in pure states. Also, gas-side mass transfer is not limiting for low gas-phase reagent solubilities. Henceforward, the gas-liquid mass transfer will refer implicitly to the liquid-side component.

Several research works focused on experimental characterisation of gas-liquid mass transfer in trickle-bed reactors. Chemically enhanced absorption of a gas-component into a liquid phase is the most widely used experimental technique. The gas-component reacts irreversibly with a liquid component, and absorption flux is obtained according to the penetration theory. Afterwards, gas-liquid interfacial area a_{GL} and mass transfer coefficient $k_{GL}a_{GL}$ are accessed.

Midoux et al. [1984] measured the gas-liquid interfacial area by investigating the carbamation reaction of cyclohexylamine, monoethanolamine and diethanolamine in several solvents (toluene, ethanol and glycol). At constant liquid flow rate, the authors noted an increase in interfacial area with gas flow rate. Conversely, an increase in interfacial area with liquid flow rate and viscosity was established for constant gas flow rate. Moreover, interfacial area is found to be greater for foaming systems than non-foaming systems. Similar conclusions on gas and liquid flow rate effects were later on confirmed by Goto and Smith [1975], Lara-Marquez et al. [1992, 1993],Wild et al. [1992] and Larachi et al. [1991-1994].

Furthermore, particle shape effect on gas-liquid mass transfer was investigated by Larachi et al. [1998] using the diethanolamine carbamation reaction. Interfacial area measurements were performed on spheres (glass and alumina) and extrudates (activated carbon and propylene). When compared to spherical particles, the authors stated that extrudates allow for higher gas-liquid interfacial areas. Larachi et al. [1998] compared porous to non-porous particles, and showed that interfacial area values are higher with porous particles.

Critically important, particle diameter impacts significantly gas-liquid mass transfer. Indeed, the two-phase pressure drop increases with decreasing particle diameter, leading to higher phase interaction within the particle loading. In these conditions, Larachi et al. [2003] found that smaller-sized particles induce higher gas-liquid interfacial area values, thus increasing the mass transfer coefficient $k_{GL}a_{GL}$. Lara-Marquez et al. [1992] observed a greater particle size effect on gas-liquid mass transfer for high liquid flow rates.

Gas-liquid mass transfer is also dependent on operating conditions and gas/liquid properties such as viscosity, density, surface tension and so forth. Many authors established a positive influence of liquid viscosity on gas-liquid mass transfer rates due to higher inter-phase interactions [Morsi et al., 1982, Midoux et al., 1984, Larachi et al., 2003]. However, mass transfer rates are not susceptible to change with gas phase viscosity and liquid phase density.
Furthermore, Larachi et al. [1998] reported an increase in gas-liquid mass transfer rates with operating pressure. The authors observed that gas-phase density increases with operating pressure leading to higher gas-liquid interactions. The gas phase forms small bubbles within the liquid phase, thus improving gas-liquid interfacial area a_{GL}. In addition, Al-Dahhan and Dudukovic [1994] found that liquid distribution is enhanced at high operating pressure values, hence increasing wetting efficiency and gas-liquid interfacial area.

In order to estimate the gas-liquid interfacial area a_{GL} and mass transfer coefficient $k_{GL}a_{GL}$, several authors suggested correlations for trickle-bed reactors. Some of these correlations are listed in table 2.4.
In an effort to provide an order of magnitude for k_{GL}, Hirose et al. [1974] investigated gas-liquid mass transfer through two different processes. $k_{GL}a_{GL}$ was measured based on oxygen desorption from saturated water to nitrogen, while gas-liquid interfacial area a_{GL} was measured through chemical absorption of CO_2 in aqueous sodium hydroxide. The experiments were conducted at atmospheric pressure conditions using a glass beads loading. In order to account for their impact on gas-liquid mass transfer, the authors correlated $k_{GL}a_{GL}$ and a_{GL} to the gas and liquid superficial velocities, as well as particle diameter. Mass transfer coefficient k_{GL} values were found to have an order of magnitude around 10^{-4} m/s.
Later on, Charpentier [1976] modelled both $k_{GL}a_{GL}$ and a_{GL} based on previously published experimental works of [Gianetto et al., 1973, Ufford and Perona, 1973, Hirose et al., 1974, Shende and Sharma, 1974, Goto and Smith, 1975]. The authors proposed correlations based on the two-phase pressure drop ΔP_{LG} and liquid dissipation energy E_L (cf. table 2.4).
In order to investigate flow regime transition boundaries, Fukushima and Kusaka [1977] proposed gas-liquid interfacial area correlations for all flow regimes. The authors performed

experiments at atmospheric pressure conditions, using fixed beds of ceramic Raschig rings and spheres. The chemical absorption technique was used to measure a_{GL}. Fukushima and Kusaka [1977] proposed four different correlations for the spray, trickle, pulse and dispersed bubbly flow regions. Equating two of these four correlations allows to develop a correlation for transition boundaries between flow regimes.

The above correlations have been restricted to aqueous systems, justifying the research work of Morsi et al. [1980] who investigated the difference between interfacial area values using aqueous and organics liquids. Later on, Morsi [1989] developed $k_{GL}a_{GL}$ and a_{GL} correlations for organic liquids. Experiments were performed at atmospheric pressure conditions using spherical catalyst particles (Co/Mo/Al_2O_3). The authors compared their results to the correlations of Satterfield [1975] and Charpentier [1976], which were developed using highly ionic aqueous solutions. This comparison pointed out high discrepancies, mainly due to liquid properties. In addition, $k_{GL}a_{GL}$ values were about four times higher for organic systems rather than aqueous systems.

Recently, in a different attempt to model mass transfer in TBRs, Iliuta et al. [1999] applied the Neural Network Approach (NNA) to develop more general correlations. Later on, about 4000 experimental mass transfer data points were used by Larachi et al. [2003] to propose general correlations for $k_{GL}a_{GL}$ and a_{GL} through NNA. When employed within their validity ranges, Wild et al. [1992] and Turek and Lange [1981] models allowed a good agreement between experimental and estimated parameters. Nevertheless, Larachi et al. [2003] correlations showed a substantial error reduction when compared to experimental values.

Table 2.4 Some literature a_{GL} and $k_{GL}a_{GL}$ correlations

Reference	Correlation
[Hirose et al., 1974]	$a_{GL} = 175 \cdot d_P^{-0.8} \cdot V_{S,G}^{0.6} \cdot V_{S,L}^{0.5}$
	$k_{GL}a_{GL} = 1.0 \cdot d_P^{-0.5} \cdot V_{S,G}^{0.8} \cdot V_{S,L}^{0.8}$
[Charpentier, 1976]	$a_{GL} = 0.05 \cdot a_S \cdot \left(\Delta P_{LG} \frac{\varepsilon_B}{a_S}\right)^{0.5}$
	$k_{GL}a_{GL} = 0.0011 \cdot E_L \cdot (D_A / 2.4 \cdot 10^{-9})$
[Fukushima and Kusaka, 1977]	$a_{GL} = 3.9 \cdot 10^{-3} \frac{1-\beta_L}{d_P} \cdot Re_L^{0.4} \left(\frac{d_P}{d_c}\right) \varphi^{-0.1}$
[Morsi, 1989]	$a_{GL} = 0.66 \left(\Delta P_{LG} + \varepsilon_B g[\beta_L \rho_L + (1-\beta_L)\rho_G]\right)^{0.65}$

Table 2.4 – Some literature a_{GL} and $k_{GL}a_{GL}$ correlations [Continued from previous page]

Reference	Correlation
	$k_{GL}a_{GL} = D_A^{0.5} \cdot 14 \cdot 10^{-3} \left(\Delta P_{LG} + \varepsilon_B g[\beta_L \rho_L + (1-\beta_L)\rho_G]\right)^{1.46}$
[Midoux et al., 1984]	$a_{GL} = 1.47 \cdot 10^5 \cdot \varepsilon_B \left(\frac{\varepsilon_B^2 \xi_{LG}}{a_S\left(\frac{\dot{m_L}}{\rho_L} + \frac{\dot{m_G}}{\rho_G}\right)}\right)^{0.65}$ $k_{GL}a_{GL} = 7.22 \cdot 10^7 \cdot \varepsilon_B \sqrt{D_A} \left(\frac{\varepsilon_B^2 \xi_{LG}}{a_S\left(\frac{\dot{m_L}}{\rho_L} + \frac{\dot{m_G}}{\rho_G}\right)}\right)^{1.23}$
[Ratnam and Varma, 1991]	$a_{GL} = 17.0 \cdot V_{S,L}^{0.30} \cdot \varepsilon_B^{-1.20} \cdot d_e^{-0.50}$
[Ratnam et al., 1994]	$a_{GL} = 375 \cdot Mo_L^{0.05} \cdot \varepsilon_B^{1.40} \cdot \left[\Delta P_{LG} \frac{V_{S,L}}{\varepsilon_B}\right]^{0.40}$
[Larachi et al., 1998]	$a_{GL} = a^\circ \frac{f}{f^\circ} \left[1 + \kappa \left(\frac{\mu_G}{\mu_L}\right)^{1/6} \frac{Ca}{\varepsilon_B} \left(1 + 2.5\left(1 - \frac{\beta_L}{\beta_L^\circ}\right)\right)\left(\frac{1}{\beta_l} - \frac{1}{\beta_L^\circ}\right)\right]$ $k_{GL}a_{GL} = a^\circ \frac{f}{f^\circ} \left[k_{GL}^\circ + \frac{\kappa^2 D}{3\varepsilon_B^3} \left(\frac{\mu_G}{\mu_L}\right)^{1/3} \left(a^\circ \frac{f}{f^\circ}\right) \frac{Ca^2}{\beta_L \beta_L^\circ} \left(\frac{1}{\beta_L} - \frac{1}{\beta_L^\circ}\right) \left(1 + 2.5\left(1 - \frac{\beta_L}{\beta_L^\circ}\right)\right)^2\right]$

Many other gas-liquid mass transfer correlations are available in literature, more detailed reviews are provided by Saroha and Nigam [1996], Larachi et al. [1998, 2003]. To sum up, most of available correlations show high discrepancies when used in different reactor operation settings [Larachi et al., 2003]. This is mainly due to the limited experimental operating conditions range (namely gas and liquid flow rates, two-phase system properties and so forth). Moreover, most of previously reported mass transfer studies were limited to aqueous reacting and non-reacting systems, at atmospheric pressure and ambient temperature conditions. Therefore, estimating mass transfer in a TBR under industrial operating conditions would undoubtedly be biased, since they involve organic liquids flow (such as hydrocarbons) under high pressure and temperature conditions.

Liquid-solid mass transfer

Given its importance in trickle-bed reactors, liquid-solid mass transfer has been experimentally studied by many authors, such as [Specchia et al., 1978, Chou et al., 1979, Kawase

and Ulbrecht, 1981, Latifi et al., 1988, Lakota and Levec, 1990]. However, it has not been studied as much as gas-liquid mass transfer. Three main liquid-solid mass transfer measurement categories are commonly encountered: (i) chemical methods where a heterogeneous catalysis liquid-phase reaction occurs, (ii) physical methods where no chemical reaction is required and (iii) electrochemical methods where a mass transfer limited electrochemical reaction is employed.

The influence of operating conditions, gas-liquid flow rates and TBR features on liquid-solid mass transfer was discussed in literature. First, liquid-solid mass transfer rate increases with liquid flow rate, while gas flow rate effect is debatable. Specchia et al. [1978], Lakota and Levec [1990] and Highfill and Al-Dahhan [2001] reported increasing liquid-solid mass transfer rates with gas flow rate, meanwhile Goto and Smith [1975] and Nigam et al. [2002] reported invariant mass transfer rates with respect to gas flow rate.

Regarding operating conditions effect, more specifically operating pressure, Highfill and Al-Dahhan [2001] reported an increase of 50% in mass transfer coefficient k_{LS} when pressure increases from 22 to 36 bar. When operating pressure exceeds a certain value, the authors noticed that liquid-solid mass transfer increases more significantly. However, experimental data was insufficient to define this critical pressure value.

According to Goto and Smith [1975], liquid-solid mass transfer rate is not affected by particle size. Intriguingly, Hirose et al. [1976], Satterfield et al. [1978] and Larachi et al. [2003] reported increasing liquid-solid mass transfer rate with decreasing particle diameter. The opposite trend has been reported by Specchia et al. [1978] and Rao and Drinkenburg [1985]. Given the previous trends, the particle diameter effect is obviously complex and requires a better understanding of local hydrodynamic and transfer phenomena.

Generally, in trickle-flow regime, the liquid-solid mass transfer is heavily dependent on solid wetting extent. As explained previously in section 2.1.4, the odds of encountering partial wetting are high in trickle flow regime, impacting both reaction and liquid-solid mass transfer. Therefore, the majority of liquid-solid mass transfer correlations include consistently solid wetting efficiency to account for the real liquid-solid interfacial area. In literature, liquid-solid mass transfer models correlate the product of the Schmidt and Sherwood dimensionless numbers to the gas and liquid Reynolds numbers. The general formulation is given in equation (2.23).

$$Sh \cdot Sc_L^{-1/3} \cdot f = a \cdot Re_L^b \cdot Re_G^c$$
$$Sh = \frac{k_{LS} d_P}{D_m} \quad \text{and} \quad Sc_L = \frac{\mu_L}{\rho_L D_m} \tag{2.23}$$

Where a,b and c are fitting constants. The main liquid-solid mass transfer correlations are reported in table 2.5, the reader is referred to [Naderifar, 1995] and [Larachi et al., 2003] for more detailed literature reviews.

Table 2.5 Some literature liquid-solid mass transfer correlations

Reference	Correlation
[Goto et al., 1975]	$Sh \cdot f \cdot Sc_L^{-1/3} = 1.31 \cdot Re_L^{0.564}$ for $0.2 < Re_L < 20$
[Specchia et al., 1978]	for $V_{S,G} = 0$: $Sh \cdot f \cdot Sc_L^{-1/3} = 2.79 \cdot Re'^{\,0.70}_L$ for $V_{S,G} \neq 0$: $ln\left(f \cdot Sh \cdot Sc_L^{-1/3}\right) = 1.84 + 0.311 \cdot ln\left(We \cdot 10^3\right) - \frac{6.33}{ln\left(We \cdot 10^3\right)^2}$ where $Re'_L = \frac{\rho_L \cdot V_{S,L}}{\mu_L \cdot a}$ and $We = \frac{\rho_L V_{S,L}^2 d_P}{\varepsilon_L^2 \gamma_L}$
[Satterfield et al., 1978]	$Sh \cdot f \cdot Sc_L^{-1/3} = 0.815 \cdot Re_L^{0.822}$ for $< Re_L < 60$
[Rao and Drinkenburg, 1985]	$Sh \cdot f \cdot Sc_L^{-1/3} = 0.24 \cdot \left(\frac{Re_L^*}{\varepsilon_{L,d}}\right)^{0.75}$ where $Re_L^* = \frac{\dot{m}_L \cdot d_P}{\varepsilon_L \cdot \mu_L}$
[Lakota and Levec, 1990]	$Sh^* \cdot Sc_L^{-1/3} = 0.487 \cdot Re_L^{*\,0.425}$ for $15 < Re_L^* < 600$, $Re_L^* = \frac{Re_L \cdot \varepsilon_B}{\varepsilon_{L,d}}$ and $Sh^* = \frac{Sh \cdot \varepsilon_B}{1-\varepsilon_B}$
[Latifi et al., 1997]	$Sh \cdot f \cdot Sc_L^{-1/3} = 1.70 \cdot Re_L^{0.62}$ for $5 < Re_L < 100$
[Zaki et al., 2004]	$Sh \cdot \varepsilon_B \cdot Sc_L^{-1/3} = 0.688 \cdot Re_L^{0.548}$ for $25 < Re_L < 600$
[Baussaron, 2007]	$Sh \cdot f \cdot Sc_L^{-1/3} = 8.58 \cdot 10^{-4} \cdot \left(\frac{Re_L}{\varepsilon_{L,d}}\right)^{1.91}$

In an effort to present a general correlation, Seguin et al. [1996] reviewed mass transfer in fixed beds and reported that mass transfer can be modelled following the same formulation reported in equation (2.23). Depending on the liquid Reynolds number value, the authors proposed ranges for each of the constants a and b (c=0). On the other hand, Larachi et al.

[2003] used the Neural Network Approach to develop a model based on nearly 900 data points extracted from literature. In trickle-flow regime, the authors noted a good agreement between experimental and estimated mass transfer rates using literature correlations, when they are employed within their validity range. Otherwise, high discrepancies were encountered.

2.2 Multiphase reactors: modelling approaches

Fixed-bed reactors modeling approaches are divided into two categories: (i) global approaches and (ii) local approaches [Froment and Bischoff, 1979]. Trickle-bed reactors involve complex phenomena, several of which occur at different characteristic scales starting from pore (nm) to reactor scale (m). Depending on empiricism and scale, one of these categories would be employed.

2.2.1 Global approaches

This category is based on model development at the reactor scale. These approaches are referred to as "Global" since they consider that the reactor is equivalent to a uniform continuous medium. The reactor is then considered as a "black box", where local interactions and smaller-scale phenomena are not accounted for explicitly. These approaches predict reactor's performance based only on known parameters such as flow rates, operating conditions, reaction rate, bed porosity, particle diameter and so forth. Global approaches are widely used in chemical engineering to model complex phenomena which are difficult to evaluate at the local scale. The main required outputs are:

— Flow regimes
— Pressure drop
— Liquid holdup
— Wetting efficiency
— Interfacial mass transfers

Owing to there less costly developments, global models are commonly employed to design trickle-bed reactors. Several experimental works proposed correlations for the above listed parameters, they have been presented earlier in sections (2.1.1 to 2.1.5). A large number of these correlations cannot be used beyond their validity domains. The main reason is that variations in operating parameters (flow rates, bed characteristics, etc.) might have an influence on gas-liquid-solid interactions at the microscopic scale. However, the influence

of microscopic phenomena on macroscopic performance is difficult to evaluate. Therefore, a rigorous mathematical description at the reactor's scale is for the time being unfeasible. The development of more rigorous reactor models requires a better understanding and integration of small-scale phenomena.

2.2.2 Local approaches

In opposition to global approaches, this category accounts for local features to simulate two-phase flow through reactors. Depending on the modeling objective, three different scales are identified: (i) macroscopic modeling at the reactor scale, (ii) mesoscopic modeling at the loading scale and (iii) microscopic modeling at the particle/pore scale. The macroscopic and mesoscopic approaches are based on Representative Elementary Volume (REV) concept, referring to a sufficient particle number contained in a volume. The objective is to achieve an average representation of variables.

Macroscopic modeling represents the reactor as a continuous medium including spatially variable properties. Euler-Euler method is the most widely used macroscopic approach to simulate fixed bed reactors. In this numerical method, the involved phases are mathematically considered as interpenetrating continua. The Euler-Euler method is based on space and time averaging of macroscopic variables (such as velocity), as well as the use of closure laws to model the unknown small-scale quantities. Providing constitutive relations to close the system is the key to achieve representative simulations.
The Euler-Euler method is based on the resolution of averaged mass and momentum conservation equations, for each phase involved in the multiphase flow. The governing equations for a gas-liquid flow are given by equation (2.24) [Boyer et al., 2007, Lappalainen et al., 2009a,b, Fourati et al., 2013].

$$\begin{cases} \frac{\partial}{\partial t}\left(\alpha_k \rho_k\right) + \vec{\nabla}\cdot\left(\alpha_k \rho_k \vec{u}_k\right) = 0, \qquad k = [G;L] \\ \frac{\partial}{\partial t}\left(\alpha_G \rho_G \vec{u}_G \vec{u}_G\right) = -\alpha_G \vec{\nabla} p + \vec{\nabla}\cdot\left(\alpha_G \bar{\bar{\tau}}_G\right) + \alpha_G \rho_G \vec{g} - \vec{F}_{GS} + \vec{F}_{i,L} + \vec{F}_{D,G} \\ \frac{\partial}{\partial t}\left(\alpha_L \rho_L \vec{u}_L \vec{u}_L\right) = -\alpha_L \vec{\nabla} p + \vec{\nabla}\cdot\left(\alpha_L \bar{\bar{\tau}}_L\right) + \alpha_L \rho_L \vec{g} - \vec{F}_{LS} + \vec{F}_{i,G} + \vec{F}_{D,L} \end{cases} \tag{2.24}$$

The different forces involved in the momentum equations require closure models. Boyer et al. [2007] suggested closure models for both friction forces between fluid phases and the solid phase ($\vec{F}_{GS}$ and $\vec{F}_{LS}$) and gas-liquid interface friction forces ($\vec{F}_{iL}$ and $\vec{F}_{iG}$). Dispersion

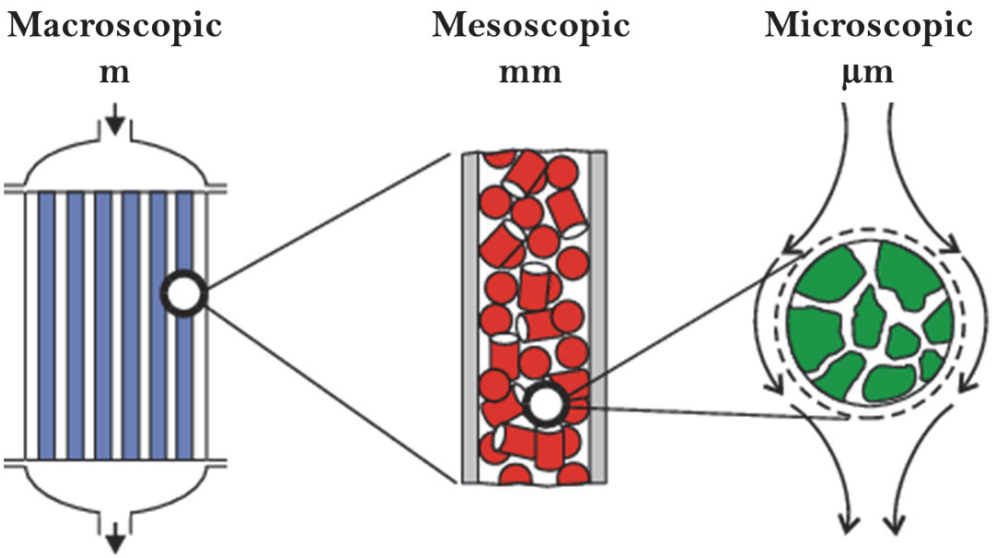

Figure 2.6 Local approaches modeling scales (from left to right) macroscopic, mesoscopic and microscopic

forces ($\vec{F}_{D,G}$ and $\vec{F}_{D,L}$) include capillary as well as mechanical effects to the numerical model. Several closure laws can be found in literature for mechanical dispersion [Baldi and Specchia, 1976, Lappalainen et al., 2009a,b, Fourati et al., 2013] and capillary pressure [Grosser et al., 1988, Attou and Ferschneider, 2000, Wilhite et al., 2005].
In their investigation, Solomenko et al. [2015] simulated liquid spreading within trickle-bed reactors using the Euler-Euler approach. The authors used closure laws mentioned above, they have modelled fluid/solid friction forces and fluid/fluid friction forces using models of Boyer et al. [2007], mechanical forces suggested by Lappalainen et al. [2009a] and capillary pressure contribution of Attou and Ferschneider [2000]. The results show a good qualitative description of experimental liquid saturation β_L observed in trickle-bed reactors. Later on, the Euler-Euler model of Solomenko et al. [2015] was employed by Augier et al. [2017] to investigate maldistribution effect on TBR reactive performance. Regarding hydrodynamic behaviour, a very satisfactory agreement was found between experimental and numerical liquid saturations (cf. figure 2.7). The authors reported a significant loss of reactive performance in comparison to homogeneous plug flow reactor.

Numerical predictions using Euler-Euler method are highly dependent on the closure laws [Boyer et al., 2005]. Eventually, macroscopic modeling improvement can be achieved using mesoscopic modeling. More constitutive closure laws can be developed and introduced to macroscopic modeling.

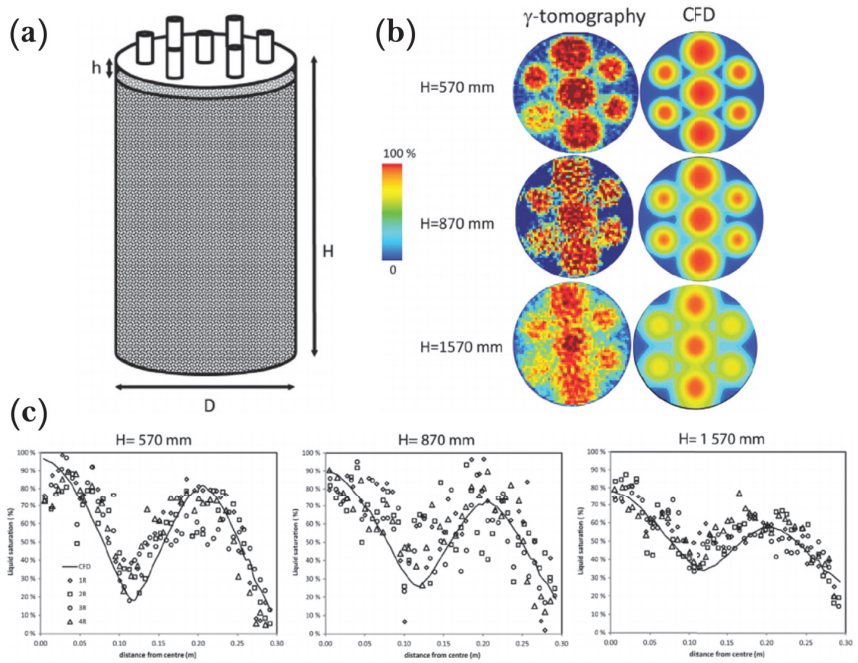

Figure 2.7 (a) experimental set-up, (b) qualitative comparison between experimental (γ-tomography) and CFD saturation profiles and (c) quantitative comparison between experimental and simulated liquid saturation values (Taken from [Augier et al., 2017])

Mesoscopic modeling on the other hand is used for two-phase flow predictions through a high finite number of particles. Direct numerical simulation considering a loading with hundreds of particles requires high computing power. Hence the advent of simplified models called "Pore Network". The latter assumes that the void volume within the reactor can be represented by a network of sites (pores) interconnected through bonds. The first step in Pore Network modeling is creating the topological skeleton from the void volume geometry. In recent developments, 3D images obtained by non-destructive X-ray micro-tomography were used to extract the necessary information for topological skeleton construction [Coenen et al., 2004, Dong and Blunt, 2009]. In general, each pore has attributes such as volume fractions in multiphase flows. The next step is to develop simplified behaviour laws capable of imitating simplified hydrodynamics for each component of the skeleton (pore or bond).
In the specific case of trickle-bed reactors, Pore Network models are used to investigate pressure drop and phase distribution within the reactors. It should be noted that behaviour laws are necessary to account for (i) fluid/fluid and fluid/solid interactions, (ii) gravitational and inertial forces, (iii) bed wettability and so forth. The complexity of latter phenomena restrains Pore Network modeling use to qualitative rather than quantitative predictions in TBRs.

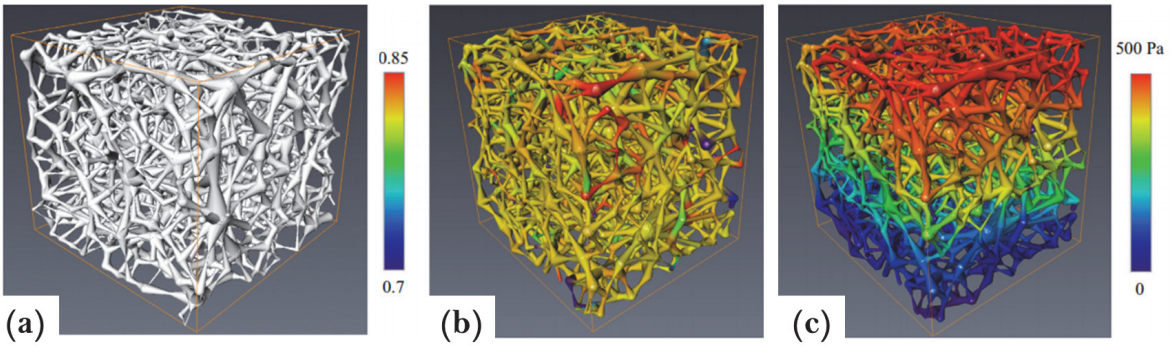

Figure 2.8 (a) Representation of the pore network used by Larachi et al. [2014] and Hannaoui et al. [2015], (b) Liquid throat saturation contours and (c) two-phase pressure drop in the network (Taken from [Hannaoui et al., 2015])

Larachi et al. [2014] used Pore Network modelling to simulate single-phase flow within a fixed bed reactor. The spheres loading was imaged using X-ray computed micro-tomography, the images were next converted into a 3D unstructured pore network (cf. figure 2.8-a). The authors noted remarkably good quantitative predictions of macroscopic frictional loss gradient. Later on, Hannaoui et al. [2015] used the pore network of Larachi et al. [2014] to analyse two-phase pressure drop within the TBR. The authors reported a good agreement between Pore Network Model and Attou and Boyer [1999] in terms of two-phase pressure drop. However, comparison of liquid saturation values between Pore Network Model and Attou and Boyer [1999], Larachi et al. [1991c] and Holub et al. [1992] revealed overestimated numerical predictions. The two-phase pressure drop and liquid saturation distributions are represented in figure 2.8-b,c.

Finally, **Microscopic modeling** is suitable to run predictive simulations on a few number of particles. At the microscopic scale, the numerical domain is small enough allowing for interface resolved direct numerical simulations. There are two fundamental approaches to simulate immiscible two-phase flow: (i) Lagrangian and (ii) Eulerian simulations. The former requires a flexible mesh moving as the fluid/fluid and fluid/solid interfaces deform, while the latter is based on a fixed mesh.

Lagrangian and Eulerian approaches have both advantages and drawbacks, selecting one approach is very much dependent on the problem's complexity and desired outcome. While being very accurate in interface tracking, simulating the breakage/coalescence of an interface is challenging with Lagrangian methods. In addition, interface distortion issues are commonly encountered for complex simulations due to the flexibility of the mesh. On the other hand, Eulerian approaches use an implicit representation of the interface through a volume fraction

scalar, making it easier to handle interface breakage/coalescence. However, mesh resolution is the key to predictive simulations as numerical diffusion at the interface might occur for coarse meshes, leading to mass conservation issues. Given the complexity of two-phase flow in trickle-bed reactors, the Euler-Lagrange approach use is scarce in literature due to its limited application scope.

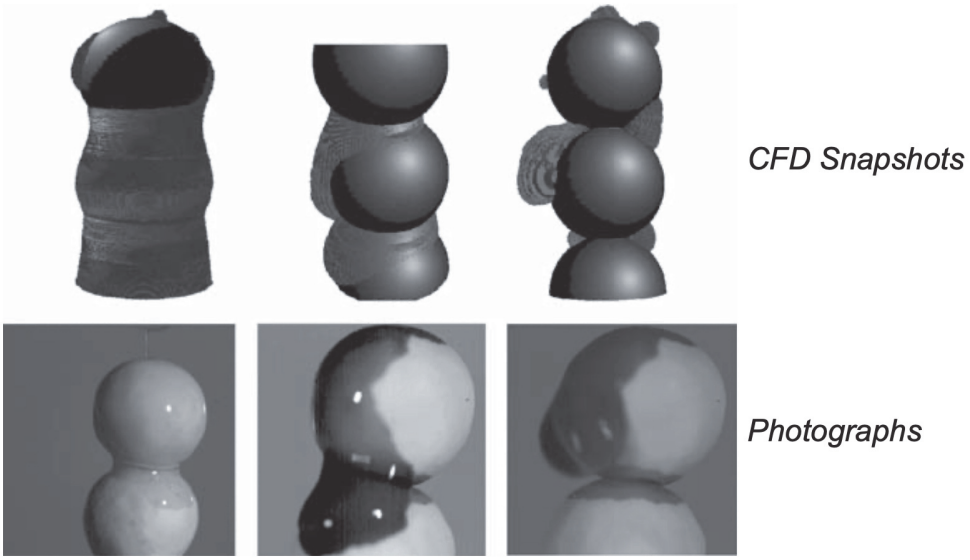

Figure 2.9 Qualitative comparison between experimental and predicted flow regimes (Taken from [Augier et al., 2010])

Trickle-bed reactors involve several hydrodynamic phenomena, they operate at four different flow regimes where fluid/fluid and fluid/solid interfaces' topology might change. Therefore, the Eulerian methods are the most commonly used to simulate hydrodynamic performance of these reactors. In this context, Volume-Of-Fluid (VOF) is the most spread Eulerian simulation method used for TBR predictions, its mathematical formulation is explained in details in section 2.4.1.

Augier et al. [2010] investigated wetting and catalyst efficiencies within trickle-bed reactors using VOF method. The numerical domain consisted of three spherical particles, around which gas and liquid flow cocurrently downward. The authors found a good qualitative agreement of flow regimes between CFD and experiments (cf. figure 2.9). In addition, a satisfactory quantitative agreement was found between experimental and predicted wetting efficiency values. Through these validations, the authors highlighted the relevance of VOF method in knowledge improvement of local phenomena.

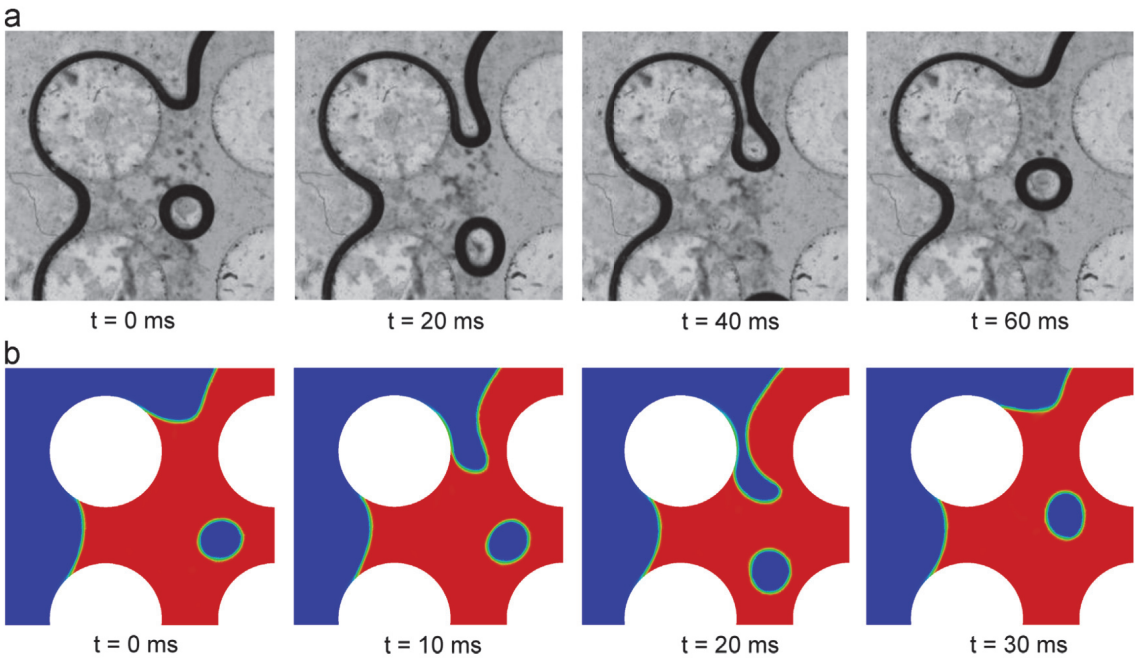

Figure 2.10 Comparison of (a) experimental and (b) simulated observation of a pich-off mechanism leading to the formation of a bubble. In numerical simulations snapshots, the red and blue colours represent respectively liquid and gas (Taken from [Horgue et al., 2013])

Finally, Horgue et al. [2013] conducted an experimental and numerical study to characterise the spreading of a liquid jet across in-line arrays of cylinders. In order to reduce computation time, the authors reduced the numerical domain to a 2D cross section of the experimental setup. As one can see from figure 2.10, VOF method provided good qualitative prediction of liquid spreading within the numerical domain. The authors reported that it is possible to simulate flow phenomenology observed experimentally using a 2D numerical domain, with some differences in time scales (fig. 2.10) caused by the simplified numerical domain.

2.3 CFD applied to Trickle-Bed Reactors

As explained earlier, trickle-bed reactors have been extensively characterised by means of empiric correlations through global modeling, namely for flow regime, two-phase pressure drop, liquid holdup, catalyst wetting efficiency and mass transfer. Although global models do not account for microscopic phenomena effect, they are simple and easy to build.

In the two past decades, with the development of computational resources, local modeling approaches are increasingly employed to improve TBR characterisation. This is achieved using

Computational Fluid Dynamics (CFD) to describe transport and transfer phenomena within trickle-bed reactors.
Several authors conducted numerical studies to investigate multiphase flow through trickle-bed reactors. A thorough analysis of literature reveals two predominantly encountered Eulerian-based multiphase modelling approaches: (i) Euler-Euler model for macroscopic simulations and (ii) Volume-Of-Fluid (VOF) model for microscopic simulations.

2.3.1 Macroscopic simulations

Due to its low computation cost, the Eulerian framework is commonly used to perform macroscopic investigations of trickle-bed reactors. Jiang et al. [2002a] developed an Eulerian k-fluid CFD model to simulate macroscale multiphase flow in packed beds. The model accounts for bed structure through a porosity distribution, and employs closure laws for fluid/fluid and fluid/solid interactions of Attou et al. [1999] and Holub et al. [1992] respectively. The authors reported in [Jiang et al., 2002b] a reasonable agreement between CFD results and the model of Saez and Carbonell [1985] regarding total liquid saturation β_L and two-phase pressure drop ΔP_{LG}.
Later on, Gunjal et al. [2005] suggested an Euler-Euler CFD model to predict measured hydrodynamic parameters in a trickle-bed reactor. The numerical model was first validated against experimental data of Specchia and Baldi [1977], Rao et al. [1983] and Szady and Sundaresan [1991]. Afterwards, the experimental reactor was reduced to a 2D-axisymmetric numerical domain, on which the CFD model was applied. The authors reported that experimental two-phase pressure drop and liquid holdup were well predicted by the numerical model.

In an effort to perform simulations in high-pressure conditions, Atta et al. [2007a,b] proposed an Euler-Euler CFD model based on relative permeability concept to characterise hydrodynamics in trickle-bed reactors. The authors first validated the CFD model under cold-flow conditions against experimental data of Specchia and Baldi [1977], Rao et al. [1983] and Szady and Sundaresan [1991]. Then, in their later work, Atta et al. [2010] compared the model's predictions with high-pressure experimental data of Al-Dahhan and Dudukovic [1994]. The authors reported a good agreement between CFD and experimental results regarding two-phase pressure drop and liquid holdup.
In the same context, [Lopes and Quinta-Ferreira, 2010b] performed hydrodynamic CFD simulations in a high-pressure trickle-bed reactor. An Eulerian k-fluid model was used to predict two-phase flow through a 3D representation of the particle bed. The authors validated

the numerical model using literature experimental data [Fukano and Ousaka, 1985, Burghardt et al., 2004, Giakoumakis et al., 2005]. The authors reported realistic predictions in pulse-flow regime regarding liquid holdup, pulse velocities and pulse frequencies, and their variation with gas and liquid superficial velocities. A very good agreement was reached between experimental data and CFD predictions in both trickle and pulse flow regimes.
Similarly, Beni and Khosravi-Nikou [2015] applied a CFD model to investigate TBR hydrodynamic performance at low and high pressure conditions. The numerical method consists of a two-phase Eulerian model based on the porous media concept. CFD simulations of two-phase flow through a 3D quarter of the particle bed were performed, and numerical predictions were compared to experimental results of Al-Naimi et al. [2011]. Beni and Khosravi-Nikou [2015] reported a realistic representation of two-phase pressure drop and dynamic liquid holdup variations with liquid superficial velocities, as well as very close predicted and experimental values.

So far, the Eulerian framework was used for pressure drop and liquid holdup predictions. Further advance has been made by a few authors, who coupled hydrodynamics to reaction performance within trickle-bed reactors. Lopes et al. [2007] and Lopes and Quinta-Ferreira [2007] proposed a CFD model coupling hydrodynamics to catalytic wet air oxidation (CWAO) of vanillic and phenolic acids respectively. The numerical model consists of an Euler-Euler two-fluid model coupled to species concentration transport (reaction) and energy equations. Predicted hydrodynamic performance of the reactor was confronted to available experimental data to validate the CFD model, before predicting the reactive performance. The authors reported a significant impact of bed temperature on total organic carbon (TOC) concentration, and negligible pressure impact.

For more details on Euler-Euler simulations of trickle-bed reactors, the reader is referred to the thorough review of Wang et al. [2013].

2.3.2 Microscopic simulations

Unlike Euler-Euler macroscopic simulations, only few authors investigated TBR performance using the Volume-Of-Fluid approach. The latter requires fine-enough mesh resolutions, leading generally to high computation costs. Therefore, the numerical domains are usually reduced to investigate small local scale phenomena.
In an attempt to improve understanding of wetting in trickle-bed reactors, Gunjal et al. [2003] investigated liquid drop over flat and spherical surfaces. The authors used the Volume-Of-

Fluid approach to solve the two-phase flow, including surface tension and wall adhesion effects. The CFD micro-scale droplet motion was qualitatively compared to experimental high speed imaging snapshots. The authors reported that CFD succeeded in capturing key features observed in experiments. The predicted droplet spread and recoiling velocities were closer to experimental values when a 3D numerical domain was employed.

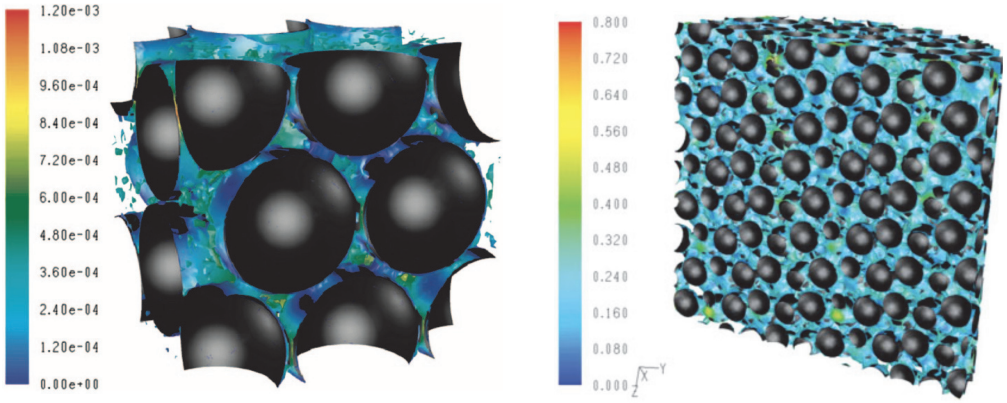

(a) 14 non-overlapping spheres (b) 200 non-overlapping spheres

Figure 2.11 (a) Instantaneous snapshot of liquid holdup isosurface ($\varepsilon_L = 0.15$) coloured by liquid velocity magnitude (m/s) (Taken from [Lopes and Quinta-Ferreira, 2009a])and (b) Semi-cylindrical slice of the catalytic bed coloured by liquid volume fraction (Taken from [Lopes and Quinta-Ferreira, 2009b])

In order to provide a realistic description of flow behaviour with trickle-bed reactors, Lopes and Quinta-Ferreira [2009a] conducted CFD simulations using a numerical domain extracted from a sphere loading. The numerical model consists of VOF approach including both surface tension and wall adhesion effects. The original particle loading is generated with non-overlapping spheres to prevent numerical difficulties, then a small volume of 14 spheres is extracted to be used in VOF simulations (cf. figure 2.11a). The CFD model was thoroughly validated against published two-phase pressure drop and liquid holdup experimental data. The authors reported a good agreement with experimental data for low gas flow rates. In their later work [Lopes and Quinta-Ferreira, 2009b], the authors simulated two-phase flow through the original particle loading -containing 200 non-overlapping spheres- using the developed CFD model (cf. figure 2.11b). The predicted liquid holdup and two-phase pressure drop were compared to experimental results of Nemec and Levec [2005], and a good agreement was reported by the authors.

In order to analyse reactive performance of trickle-bed reactors, Lopes and Quinta-Ferreira [2010a] coupled hydrodynamics to species transport to simulate catalytic wet air oxidation

(CWAO) of phenolic acids. The simulations were performed on the 200 non-overlapping spheres loading, where two-phase flow was solved using both Euler-Euler and VOF methods. The CFD model's accuracy for multiphase flow predictions was already validated in above-mentioned previous works. In the present work, numerical simulations aimed to understand temperature effect on total organic carbon (TOC) distribution within the loading. The authors reported that TOC removal and temperature elevation were both over-predicted by the VOF model. In addition, the Euler-Euler model was found to provide better predictions than the VOF model, probably because of a coarse meshing resolution.

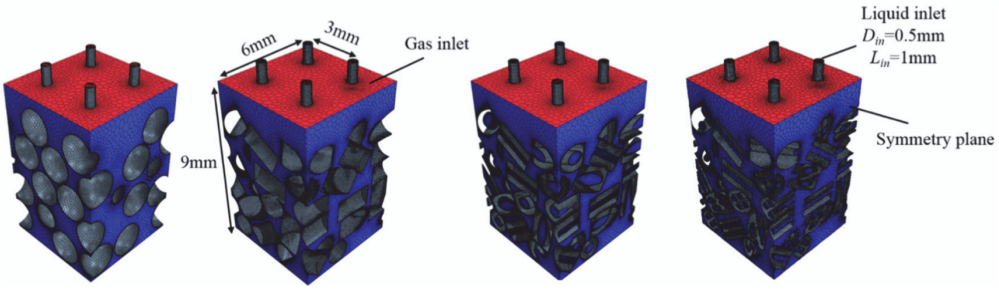

(a)

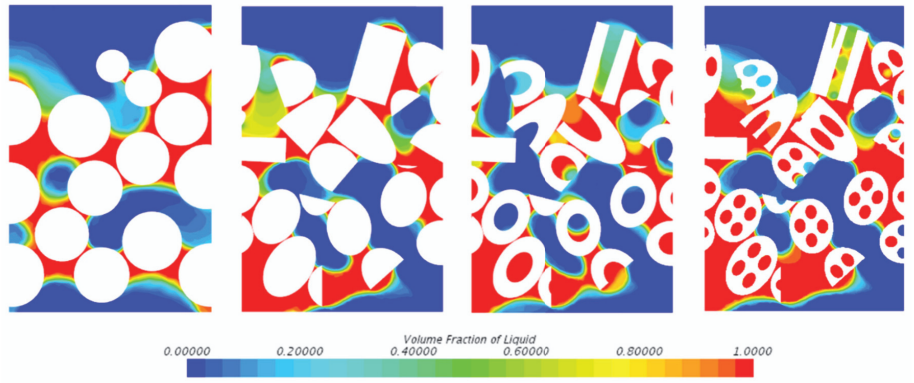

(b)

Figure 2.12 (a) Illustration of four simulated packing meshes using (from left to right) spheres, cylinders, single-hole cylinders and 4-hole cylinders and (b) Liquid distributions inside the four packing structures for $V_{S,G} = 0.245 m/s$ and $V_{S,L} = 8 \cdot 10^{-3} m/s$ (Taken from [Deng et al., 2020])

More recently, Deng et al. [2020] investigated the effect of particle shape on hydrodynamic performance in trickle-bed reactors using the VOF approach. The CFD model was applied on four different particle loadings containing spheres, cylinders, single-hole cylinders and 4-hole cylinders. The particle beds were generated using Discrete Element Method (DEM) to ensure random packing nature, then small volumes of (3x6x9)mm^3 were extracted to perform

simulations (figure 2.12a). The authors reported that the highest liquid holdup and wetting efficiency values were obtained for the 4-hole cylinders, while spherical and cylindrical particles achieve similar liquid holdups (figure 2.12b). The effect of liquid viscosity and density was studied as well, and the authors found increasing liquid holdup and wetting efficiencies for high liquid viscosity and low density values.

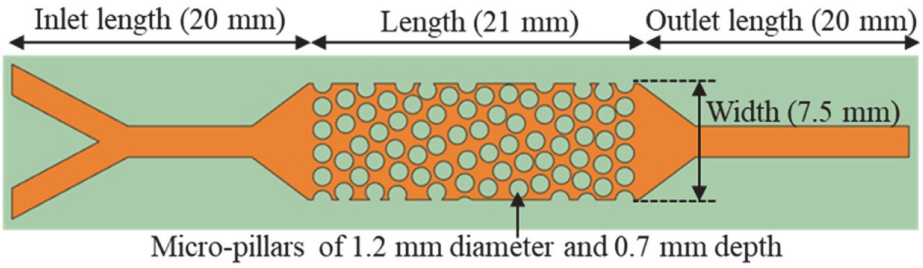

(a)

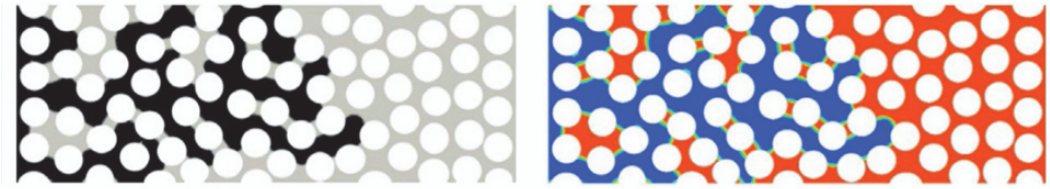

(b)

Figure 2.13 (a) A schematic of the micro-model (fluid domain is shown in orange and solid domain in green) and (b) example of comparison between experimental (left) and simulated (right) oil-water flow distribution ($Ca = 1.52 \cdot 10^{-4}$) (Taken from [Ambekar et al., 2021])

Finally, Ambekar et al. [2021] conducted an experimental and numerical study of two-phase flow within a pseudo-3D micro-model (figure 2.13a). This work aims to improve understanding of pore-scale phenomena such as water-flooding and interfacial tension effects on pore-scale two-phase flow dynamics. The two-phase flow was predicted using VOF approach, and qualitatively compared to experimental snapshots obtained by high-speeding imaging (figure 2.13b). The authors found a good agreement between predictions and experiments regarding dynamic liquid saturation and liquid distribution.

To sum up, although Euler-Euler method is the most widely used CFD model to predict two-phase flow in trickle-bed reactors, the Volume-Of-Fluid approach allows for a more accurate prediction of local small-scale phenomena. Simulations involving random particle loadings require the description of capillarity effects, namely surface tension and wall adhesion, which are easily included in the Volume-Of-Fluid method. These are not the only reasons why Volume-Of-Fluid method is more suitable for our investigation. Therefore, the latter approach

will be detailed in the next section 2.4.1. Regardless of numerical techniques, it is important to point out that the vast majority of TBR CFD simulations were conducted in isothermal conditions. Despite the relevance of including heat transfer to TBR simulations, this axis would not be developed in the present work.

2.4 Numerical models

In the last two decades, thanks to the increase of computing resources, microscopic scale Computational Fluid Dynamics (CFD) has been increasingly employed to improve understanding of local phenomena and mechanisms. Therefore, a broad range of numerical methods emerged to fulfil the requirements of two-phase flow modeling. Mirjalili et al. [2017] provided a classification for two-phase flows through a binary tree as can be seen in figure 2.14.

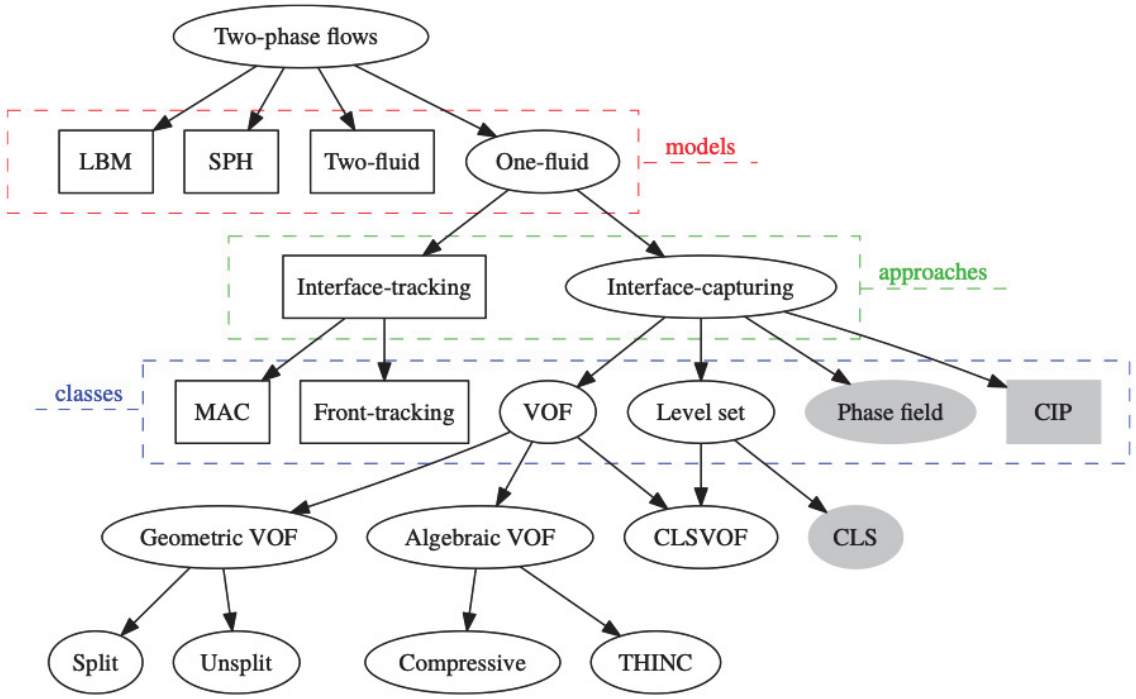

Figure 2.14 Classification of numerical methods for two-phase flows. The numerical methods covered in the present work are marked by white background ellipses. Figure taken from [Mirjalili et al., 2017]

The one-fluid model splits into two categories: (i) interface-tracking and (ii) interface-capturing approaches. In the former approaches, the fluid/fluid interface is explicitly represented by connected points, they are limited to simple two-phase problems due to mass conservation

issues. Interface-tracking methods being out of scope, they will not be detailed in the present work. Instead, we will focus on interface-capturing approaches.

Also called volume tracking methods, interface-capturing approaches usually represent the involved fluids using a volume fraction indicator function. Although reconstruction algorithms are required to locate the fluid/fluid interface, volume tracking approaches are mass-conservative and model effectively breakage/coalescence of the interface. Among these approaches, Level-Set and Volume-Of-Fluid methods are highly efficient in free-surface two-phase flow simulations.

The Level-Set method for capturing moving interfaces was first introduced by Osher and Sethian [1988]. In this method, the interface location is given by the zero iso-surface of an implicit function φ, obtained from the resolution of interface movement convection-diffusion equation. By setting the Level-Set function φ to be zero on the interface, positive on one side and negative on the other, both fluids are precisely identified by the sharp interface capturing feature. Therefore, high accuracy is achieved for interface curvature and normal vector computations. However, the method is knowingly exposed to mass conservation issues. At each time step, Level-Set method can generate small volume or mass loss in under-resolved regions, which accumulate to a significant mass balance issue.

On the other hand, the Volume-Of-Fluid method relies on a scalar function between zero and unity -generally volume fraction- to distinguish multiphase flow phases. This method models immiscible two-phase flow through the resolutions of one set of momentum equations and a volume fraction transport equation. Unlike the Level-Set method, VOF method is mass conservative. The principal drawbacks of VOF method are: (i) the requirement of accurate algorithms to reconstruct the fluid/fluid interface and (ii) the rise of spurious fluxes and velocity near the interface. The latter is due to inaccurate interface curvature computation, necessary for surface tension modeling.

In an effort to combine advantages of both Level-Set and VOF methods, Bourlioux [1995] introduced a novel numerical approach called Coupled Level-Set and Volume-Of-Fluid (CLSVOF). In this method, the interface tracking is provided by Level-Set method using the smooth Level-Set function to compute interface normal and curvature, while mass conservation is ensured by the Volume-Of-Fluid method through interface reconstruction. Therefore, the CLSVOF overcomes Level-Set and Volume-Of-Fluid drawbacks by combining their advantages.

2.4.1 Volume-Of-Fluid approach: governing equations

The present study aims to predict trickle-bed reactors performance. Therefore, considering unsteady, laminar, isothermal, Newtonian and incompressible two-phase flow, the governing equations two-phase flow predictions are presented in this section.

the two-phase flow is resolved through the continuity (eq. (2.25)), momentum (eq. (2.26)) and volume fraction transport (eq. (2.27)) equations :

$$\frac{\partial \rho_m}{\partial t} + \nabla \cdot (\rho_m \vec{u}) = 0 \tag{2.25}$$

$$\frac{\partial}{\partial t}(\rho_m \vec{u}) + \nabla \cdot (\rho_m \vec{u}\vec{u}) = \nabla \cdot \left[\mu_m \left(\nabla \vec{u} + \nabla \vec{u}^T\right)\right] - \nabla p + \rho_m \vec{g} + \vec{F} \tag{2.26}$$

Where ρ_m, μ_m p, $\vec{u}$ and $\vec{g}$ are respectively density, viscosity, pressure, velocity and gravity. $\vec{F}$ includes forces other than gravity, such as the surface tension force. The VOF method resolves a single momentum equation (eq. (2.26)), meaning that velocity and pressure fields are common to both phases.

The volume fraction equation, first introduced by Hirt and Nichols [1981], is given by:

$$\frac{1}{\rho_q}\left[\frac{\partial(\rho_q \alpha_q)}{\partial t} + \nabla \cdot (\rho_q \alpha_q \vec{u}) = S_{\alpha_q} + \sum_{p=1}^{n} (\dot{m}_{pq} - \dot{m}_{qp})\right] \tag{2.27}$$

Where $\dot{m}_{ij}$ accounts for mass transfer from phase i to phase j through evaporation or condensation, and S_{α_q} is a source term set to zero by default. ρ_q and α_q are the secondary phase density and volume fraction. The latter represents the fraction of a cell volume occupied by the secondary phase. On a discrete mesh, α_q is unity for cells occupied exclusively by the secondary phase, α_q is zero for cells containing exclusively the primary phase. The interface is indicated by α_q values between zero and unity as shown in figure 2.15.
For two-phase systems, equation (2.27) is solved only for the secondary phase q. The primary phase volume fraction α_p is computed from the following constraint:

$$\alpha_p + \alpha_q = 1 \tag{2.28}$$

Given that phases are distinguished through volume fractions α_k in the Volume-Of-Fluid approach, the mixture properties ρ_m and μ_m appearing in transport equations (eq. (2.25) & (2.26)) are defined as volume fraction averaged sums. Considering a gas-liquid fluid system, the mixture density is given by :

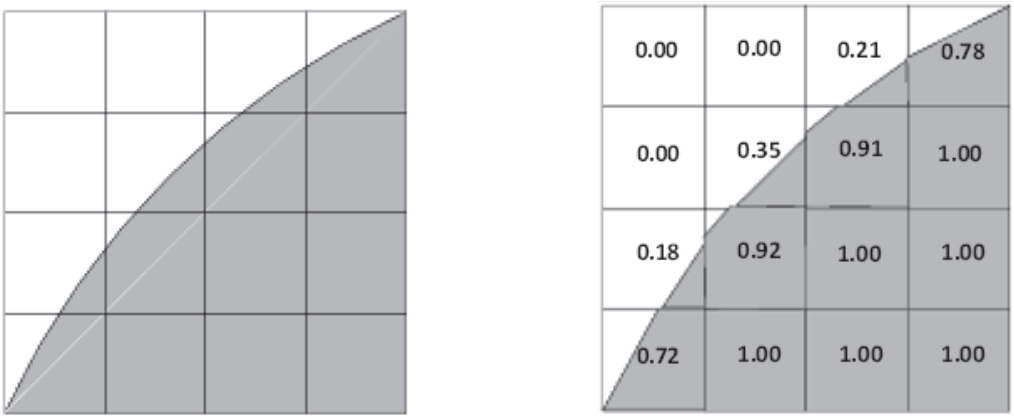

(a) (b)

Figure 2.15 Volume fraction representation on a discrete mesh (a) actual interface shape and (b) linear reconstruction of the interface

$$\rho_m = \alpha_L \rho_L + \alpha_G \rho_G \tag{2.29}$$

The same applies on other properties such as viscosity μ_m.

The Volume-Of-Fluid approach prediction quality is constrained by mesh resolution. As one can see from figure 2.15, the interface thickness is undoubtedly linked to cell-size. Coarse meshes result in significant numerical diffusion, leading to high interface thickness values. Besides, accurate computation of interface normal and curvature are necessary for a proper description of the surface tension force. This is achieved by selecting the appropriate differencing scheme (interface reconstruction and advection) among (i) algebraic schemes or (ii) geometric schemes.

VOF differencing schemes

A proper discretization of the convective term for volume fraction transport (eq. (2.27)) is essential for prediction accuracy. The conventional discretization schemes, such as upwind or central differencing schemes, are known to introduce numerical diffusion at the interface. To overcome this challenge, several techniques suitable for interface-capturing emerged.
VOF differencing schemes are essential to ensure a constant interface width and avoid numerical diffusion of the step interface. The commercial software ANSYS Fluent provides both geometric and algebraic schemes for VOF interface advection.

Geometric schemes

This category is based on an explicit geometric reconstruction of the interface. Therefore, a good approximation of the shape of the interface is achieved, and a proper estimation of fluxes between mesh cells. When a mesh cell is completely filled with one phase or another, ANSYS Fluent uses the conventional interpolation schemes to determine face fluxes. However, for mesh cells near the interface between two phases, one of the following schemes is used to handle interface resolution:

— Donor-Acceptor was first introduced by Hirt and Nichols [1981]. Considering a simple structured mesh, this differencing scheme identifies one cell as "donor" and its neighbour as "acceptor" (figure 2.16). The cell-to-cell flux is computed from the fluid amount sent by the donor cell to the acceptor cell. In order to ensure volume fraction boundedness, the transferred fluid volume is limited by the minimum of two values: (i) the filled volume in the donor cell or (ii) the free volume in the acceptor cell. This method is rarely used since several numerical problems are likely to arise.

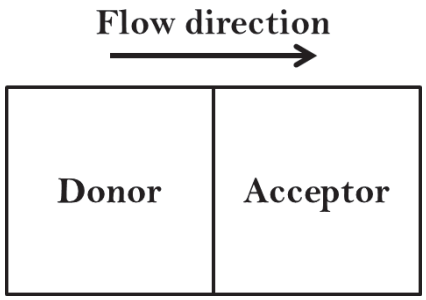

Figure 2.16 Schematic representation of "Donor-Acceptor" scheme

— Geo-Reconstruct is grounded on a Piecewise-Linear Interface Construction (PLIC) method. The latter assumes that the interface between two phases can be approximated by a linear slope line or plane in 2D and 3D simulations respectively. This scheme is considered to be the most accurate since it provides a good approximation of interface shape. However, a substantial amount of numerical operation is required in each time step -interface reconstruction then advection-, resulting in high computational times.

Figure 2.17 compares interface shapes achieved using "Donor-Acceptor" (fig. 2.17a) and Geo-Reconstruct (fig. 2.17b) schemes. As can be noted, the former scheme provides a step-shaped interface, while the Geo-Reconstruct scheme provides an interface resolution is similar to the actual interface shape (fig. 2.17c).

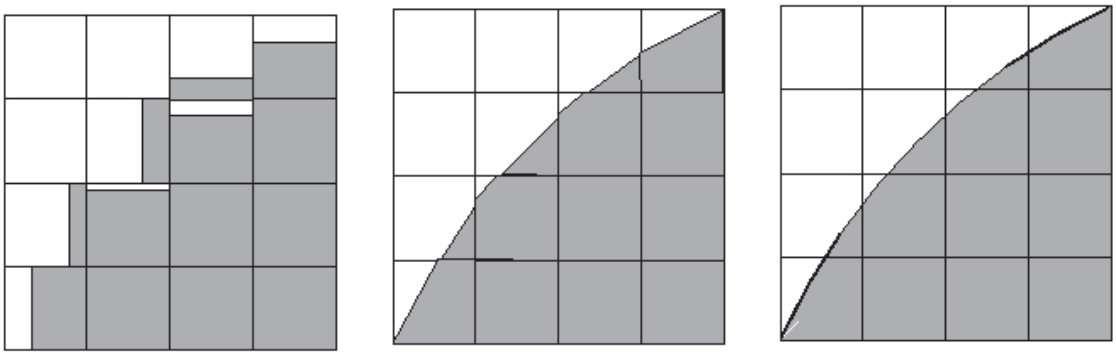

(a) (b) (c)

Figure 2.17 Volume-Of-Fluid interface shape: (a) "Donor-Acceptor" scheme, (b) Geo-Reconstruct scheme and (c) actual interface shape

Algebraic schemes

Unlike geometric schemes, the interface is not represented explicitly in algebraic methods. They are considered more efficient, suitable for all mesh topologies and easier to implement. In addition, since interface reconstruction is not required, these methods benefit from a low computational cost. ANSYS Fluent provides two high order schemes:

— Compressive Interface Capturing Scheme for Arbitrary Meshes (CICSAM) scheme was proposed by Ubbink [1997]. This differencing scheme is suitable for high viscosity ratios (μ_L/μ_G) two-phase flows. Even though the interface is not physically reconstructed, CICSAM provides an interface resolution almost as sharp as the Geo-Reconstruct scheme.

— Modified High Resolution Interface Capturing (HRIC) scheme proposed by Muzaferija et al. [1998]. Shortly, this method blends two conventional discretization schemes (upwind and downwind) to enhance its accuracy. In comparison to second order schemes, the modified HRIC scheme provides improved accuracy for VOF calculations. In addition, the method is less computationally expensive than Geo-Reconstruct scheme.

Jabbari et al. [2014] conducted a numerical study to compare interface-capturing schemes, namely Geo-Reconstruct, modified HRIC and CICSAM. The simulations were performed on the commercial code ANSYS Fluent. The authors reported that CICSAM provides the best balance between accuracy and computation effort, while Geo-Reconstruct was found to have the highest computational time.

Surface tension modeling

Free surface gas-liquid flow is characterised by inter-molecular forces between molecules, especially within the liquid phase. As a result, the molecules within the bulk of the phase are pulled equally in every direction by neighbouring liquid molecules, while molecules at the gas/liquid interface are attracted inward to the liquid bulk. This process results in internal pressure and forces the gas-liquid interface to contract to the minimum surface area possible. This mechanical phenomenon is called surface tension.

The significance of surface tension effects on two-phase flow is determined based on Reynolds, Capillary and Weber dimensionless numbers. Surface tension force is negligible if:

— $Re << 1$ and $Ca >> 1$

— $Re >> 1$ and $We >> 1$

Given Capillary and Weber numbers values in trickle-bed reactors, surface tension force cannot be neglected and should be accounted for in the simulations.

The surface tension force is represented by $\vec{F}$ in momentum conservation equation (2.26). Brackbill et al. [1992] introduced one of the earliest surface tension models called the Continuum Surface Force (CSF). The latter assumes that surface tension force is a continuous volume force. This model has been employed extensively in literature for interfacial flows, particularly in the Volume-Of-Fluid and Level-Set interface-capturing techniques.

Several other research works presented surface tension models, the reader is referred to [Vachaparambil and Einarsrud, 2019] for more details. Most recently, an alternative model to CSF was suggested by Lafaurie et al. [1994] known as Continuum Surface Stress (CSS). The latter includes surface tension effect through a stress tensor rather than an interfacial force. In the event surface tension is variable, the CSS model is more suitable to describe two-phase flow than CSF.

Due to the imbalance of pressure gradient and surface tension force, parasitic currents appear at the fluid/fluid interface, leading to spurious fluxes and velocities at the interface. Both CSF and CSS surface tension models are likely to cause these unphysical currents.

In the present work, the CSF model is used to account for surface tension force given by:

$$\vec{F} = \sigma \kappa \cdot \vec{\nabla} \alpha_q \tag{2.30}$$

Where σ is the surface tension and κ is the interface curvature. The latter is defined as the divergence of the unit normal vector n as the following:

$$\kappa = -\nabla \cdot \vec{n} = -\nabla \cdot \left(\frac{\vec{\nabla}\alpha_q}{\|\vec{\nabla}\alpha_q\|} \right) \tag{2.31}$$

Mesh resolution is important to accurately compute the interface curvature. The finer the mesh is, the less diffuse the interface is. Therefore, volume fraction gradient computation becomes more precise leading to spurious fluxes reduction.

2.4.2 Mass transfer simulation approaches

In trickle-bed reactors, detailed knowledge of hydrodynamic parameters such as pressure drop, liquid holdup and wetting efficiency is of fundamental importance. However, for an efficient reactor design, a detailed knowledge of interfacial mass transfer plays a major role.
As explained before, several experimental works arrived at correlations to describe both gas-liquid and liquid-solid mass transfer. However, these correlations show important discrepancies when applied on different two-phase systems. With the development of numerical simulation, several authors showed interest to local simulation of mass transfer in different industrial applications, such as spay towers or bubble columns.
To simulate species transfer in two-phase systems using VOF, two mass transfer simulation approaches emerge from literature: (i) two-field approach and (ii) single field approach. These approaches are detailed below.

Two-field species transport model

This approach solves concentration fields separately in each phase. That is to say, the gas-component concentration is solved within the gas phase, while being set to zero within the liquid phase, and vice versa. This method was suggested by Bothe and Fleckenstein [2013] to simulate mass transfer across deformable fluid interfaces.

This method is provided by ANSYS Fluent as multiphase species transport, the concentration convection-diffusion equation is given by:

$$\frac{\partial \alpha_k \rho_k C_k^i}{\partial t} + \nabla \cdot \left(\alpha_k \rho_k \vec{u}_k C_k^i - \alpha_k \rho_k D_{m,i} \nabla C_k^i \right) = S_k^i \tag{2.32}$$

Where subscript k stands for the k-th phase, and superscript i stands for i-th species. C_k^i and S_k^i are respectively concentration and source terms of species i in phase k. α_k, ρ_k, $\vec{u}_k$ are respectively volume fraction, density and velocity of phase k. $D_{m,i}$ is the molecular diffusion coefficient of species i.

To account for interfacial mass transfer, both phases equations (2.32) need to be coupled. This is achieved through the definition of mass transfer source terms S_k^i depending on interfacial mass transfer coefficients. Therefore, this approach cannot be employed in this work since the aim of the present work is to post-process gas-liquid and liquid-solid mass transfer coefficients.

One-field species transport model

Proposed by Haroun et al. [2010], the one-field approach solves the transport of one shared concentration field throughout the numerical domain. This approach has then been generalised by Marschall et al. [2012] to account for interface curvature effect. The fundamental concept of this approach is the advent of an additional concentration flux to account for thermodynamic equilibrium at the gas-liquid interface. The concentration transport equation is given by:

$$\frac{\partial \rho_m C}{\partial t} + \nabla \cdot (\rho_m \vec{u} C - \rho_m D_m \nabla C + \Gamma) = S_m \tag{2.33}$$

Where C is the shared concentration field, ρ_m, $\vec{u}$ and D_m are respectively the density, velocity and diffusion coefficient of the mixture defined as volume fraction averaged sums (cf. equation (2.29))

The term Γ presented in equation (2.33) is the novel concentration flux ensuring thermodynamic equilibrium at the interface through Henry's law. The three main expressions for this flux are reported in table 2.6, the reader is referred to their respective papers for more details on their mathematical development.

The formulations developed by Haroun et al. [2010], Marschall et al. [2012], Deising et al. [2016] allow for rigorous modelling of concentration jump at the interface. However, introducing these fluxes in ANSYS Fluent revealed to be challenging. Indeed, numerical solver modifications within ANSYS Fluent are actually impossible since it is a "black-box" software, for which solver code lines are not accessible. Consequently, the present work enforces the thermodynamic equilibrium concentration within the gas phase. This is based on two assumptions: (i) flowing gas is pure and (ii) gas-side mass transfer is negligible. Therefore, the thermodynamic equilibrium concentration is a boundary conditions to the following equation:

$$\frac{\partial \rho_m C}{\partial t} + \nabla \cdot (\rho_m \vec{u} C - \rho_m D_m \nabla C) = S_m \tag{2.34}$$

In our knowledge, local scale investigation using CFD simulations of interfacial mass transfers within trickle-bed reactors has not yet been achieved. The present work will make use of the

Table 2.6 Solubility flux expressions

Reference	Flux expression Γ
[Haroun et al., 2010]	$\Gamma = \rho_m D_h \frac{(1-He)\nabla\alpha_L}{\alpha_L + He\cdot(1-\alpha_L)} \cdot C$
[Marschall et al., 2012]	$\Gamma = \rho_m (D_L - D_G)\alpha_L \left(\frac{1}{\alpha_L + He(1-\alpha_L)} - 1 \right) \nabla C$
[Deising et al., 2016]	$\Gamma = \rho_m \Bigg[D_h \frac{(1-He)\nabla\alpha_L}{\alpha_L + He(1-\alpha_L)} C - (1-\gamma_f)(D_L - D_G)\alpha_L \left(\frac{1}{\alpha_L + He(1-\alpha_L)} - 1 \right) \nabla C - (1-\gamma_f) \frac{C}{\alpha_L + He(1-\alpha_L)} \left(He \frac{D_L - D_G}{\alpha_L + He(1-\alpha_L)} - (D_L - HeD_G) \right) \nabla\alpha_L \Bigg]$ where $\gamma_f = \vec{n}_{face} \cdot \vec{n}_{interface}$

single-field approach to couple hydrodynamics to mass transfer and heterogeneous catalysis within TBRs.

2.4.3 Heterogeneous reaction modeling

In order to account for a heterogeneous catalytic reaction at the liquid/solid interface, two conceptually different approaches can be used: (i) Reactive source term or (ii) reactive flux. The former is based on defining S_m is equation (2.34) for the heterogeneous catalytic reaction, and the latter accounts for the reaction through a surface flux boundary condition at the solid surface.

In the present work, the numerical domain consists of the void volume and does not include the solid catalyst volume. Therefore, concentration transport cannot be solved within the solid catalyst. However, source terms are volumetric fields in ANSYS Fluent, they are applied within cell volumes. The reactive source term is defined per unit volume catalyst, this approach would require either:

— Solid catalyst volume meshing, resolution of concentration transfer and applying the source term within the solid catalyst volume
— Or applying the source term in the first mesh cell near the solid surface

The major drawback of the reactive source approach is computational cost. The first requirement aforementioned clearly increases mesh size. On the other hand, in order to avoid undermining the concentration profile resolution within the liquid film, the second requirement necessitates very fine mesh cells near the solid surface. Moreover, reaction rates encountered in chemical engineering are usually non-linear, leading to a non-linear source term expression. Due to numerical stability issues, ANSYS Fluent recommends source term linearization which is frequently challenging.

As an alternative, the reactive flux is defined per unit catalyst surface. Therefore, catalyst volume meshing is not required to include the heterogeneous catalysis reaction. Given the reaction rate expression, reactive flux is expressed as the following:

$$Flux = -\frac{\rho_m \cdot r(C)}{S_{cata}} \tag{2.35}$$

Where $r(C)$ is the reaction rate expression and S_{cata} is the catalyst external surface area. The flux expressed in equation (2.35) is a supplementary boundary condition for concentration transport at the solid surface. As opposed to the first approach, the reactive flux approach does not compromise numerical stability, therefore flux linearization is not required. In the present work, the reactive flux approach is used to include heterogeneous catalysis reaction effect on mass transfer in trickle-bed reactors.

2.5 Conclusion

For nearly a century, deep understanding of hydrodynamics and mass transfer in gas-liquid-solid contactors has been the core element of several research works. As a result, an abundant database of experiments, models and correlations emerged for a variety of flow configurations and characteristics. Nevertheless, a substantial part of research works is based on experimentally fitted models, hardly applicable beyond validity domains. Same holds true for analytical models as they are developed for ideal problems, and grounded on simplifying assumptions. This has been demonstrated throughout the current chapter.

Regarding correlation development, whether it concerns hydrodynamic or mass transfer parameters, the experimental results are obtained using two main methods: (i) invasive and (ii)

non-invasive techniques. Both present advantages and limitations. The non-invasive techniques are commonly applied on aqueous systems, using non-porous particles, at low temperature and pressure conditions. Apart from allowing low measurement errors, the operating conditions and two-fluid systems are inconsistent with industrial conditions. On the other hand, even though non-invasive techniques are employed in industrial operating conditions, their accuracy is very much dependent on the reactor model used to post-process parameters of interest. Regardless of the experimental technique, this chapter emphasised on the contingent discrepancies obtained when estimating parameters through correlations.

With the increasing application of Computational Fluid Dynamics in the chemical engineering field, the local investigation of hydrodynamics and mass transfer using interface-tracking techniques (VOF) should be possible. This would allow to identify local mechanisms influencing hydrodynamics and mass transfer. For the time being, these techniques have been mainly employed to predict hydrodynamics, while very few studies investigated reactive mass transfer. Several numerical models have been presented, the numerical model used in the current work consists of Volume-Of-Fluid approach coupled to the one-field concentration transport (eq. (2.34)).

Therefore, the main objective of this work is to improve understanding of local mass transfer mechanisms using Computational Fluid Dynamics. Predictions are obtained through coupling of hydrodynamics and reactive mass transfer in complex and realistic two-phase flow configurations. To do so, numerical problems with increasing complexity and novelty are addressed, starting from a 2D vertical falling liquid film to trickle-bed reactors. Since TBRs usually operate in trickle-flow regime, this investigation focuses only on continuous liquid film flows in the presence of a gas-phase.

Within this context, in chapter 3, Computational Fluid Dynamics (CFD) are applied on a bi-dimensional vertical falling liquid film considering both hydrodynamics and mass transfer. Following development of the numerical model, predicted results are compared to analytical solutions for validation purposes.

Chapter 4 addresses gas-liquid-solid mass transfer in two configurations: (i) Falling Film Micro-structured Reactor (FFMR) and (ii) spherical particles string reactor. The former was experimentally investigated by Tourvieille et al. [2013] in gas-liquid-solid reactive mass transfer conditions. Apart from model validation, this case is studied to improve understanding of gas-liquid-solid mass transfer in heterogeneous catalysis conditions. In an effort to study flow-path tortuosity influence on overall mass transfer, developed CFD model is applied on a spherical particles string reactor.

In chapter 5, simultaneous experimental and numerical investigations are conducted on a 3D-printed milli-reactor. The specificity of this milli-reactor lies in its tortuous flow domain. Gas-liquid-solid mass transfer is measured and compared to CFD predictions in partial wetting conditions. Finally, chapter 6 is dedicated to trickle-bed reactors, more specifically to particle shape effect on hydrodynamics and mass transfer. The first part investigates hydrodynamic behaviour withing spheres, trilobes and quadrilobes loading. An expansion of wetting efficiency correlation proposed by Julcour-Lebigue et al. [2009] is conducted to include gas superficial velocity and particle shape effects. The second part focuses on particle shape influence on reactive gas-liquid-solid mass transfer.

Chapter 3

Numerical resolution of coupled hydrodynamics and reactive mass transfer

3.1 Introduction

Falling film contactors are an integral part of several industrial applications dealing with heat and mass transfer. Film condensation, gas-liquid contacting, gas absorption or solid dissolution are some examples of these applications. As a particular case of two-phase flow, falling film flow is driven by gravity and surface tension forces. They are characterised by small liquid film thicknesses and large interfacial areas, making them the major interest of extensive literature studies.

Broadly, three flow regimes can be distinguished in film flow: (i) laminar, (ii) wavy laminar and (iii) turbulent flows. Given its relatively simple analytical description, more concrete hydrodynamic and mass transfer expressions have been obtained for laminar flow, specifically for liquid film thickness, velocity profile and mass transfer coefficients. Therefore, a 2D laminar film flow is predicted using CFD and confronted to the analytical solutions available in literature. The main objectives are: (i) to evaluate the numerical model's accuracy through hydrodynamics and mass transfer predictions and (ii) to review the validity of resistances-in-series and film models.

First, hydrogen-water film flow is simulated and compared to the analytical solution of Nusselt [1916]. Then, hydrogen physical absorption into water is computed in order to quantify gas-liquid interfacial mass transfer. The results are compared to the analytical solution of Higbie [1935] in terms of gas-liquid mass transfer coefficient. Afterwards, hydrogen absorption accelerated by a liquid-phase reaction is studied. The predicted acceleration factors E are

validated against analytical expressions of Danckwerts [1970]. Following the validation step, the numerical model is employed to perform fully predictive simulations of: (i) solid dissolution into the liquid film and (ii) gas-liquid-solid mass transfer in the presence of a heterogeneous catalytic reaction.

3.2 Theoretical background

3.2.1 Gas-liquid mass transfer

Gas absorption is predicted through numerical resolution of equation (2.34). In steady state, the aforementioned equation is expressed as the following:

$$\nabla \cdot (\rho_m \vec{u} C - \rho_m D_m \nabla C) = S_m \tag{3.1}$$

The right hand-side is used in chemical absorption simulations and describes liquid-phase reaction ($S_m = -\rho_m \cdot K \cdot C$). Considering a control volume (dV) within the numerical domain, the diffusive flux between inlet (i) and outlet (o) is given by:

$$\|D_m \nabla C\| \cdot a_{GL} \cdot V_{liq} = \int_{A_i}^{A_o} \vec{u} \cdot \vec{n} \cdot C \, dA + K \cdot \int_0^{V_{liq}} C \, dV \tag{3.2}$$

Where A_i and A_o are the inlet and outlet areas of the control volume, K is the reaction rate constant and V_{liq} is the liquid volume within the control volume. Consequently, gas-liquid mass transfer coefficients are obtained through flux continuity as the following:

$$k_{GL} \cdot a_{GL} \cdot V_{liq} \cdot \left(\overline{C_R} - \overline{C_S}\right) = \|D_m \nabla C\| \cdot a_{GL} \cdot V_{liq} = \int_{A_i}^{A_o} \vec{u} \cdot \vec{n} \cdot C \, dA + K \cdot \int_0^{V_{liq}} C \, dV \tag{3.3}$$

Where k_{GL} is the gas-liquid mass transfer coefficient, a_{GL} is the specific gas-liquid interfacial area, $\overline{C_R}$ and $\overline{C_S}$ are the gas-liquid interface and solid surface average concentrations. This generalised equation is applicable to both physical and chemical absorptions, simply by respectively setting S_m to zero or reactive source term. Subsequently, the gas-liquid mass transfer coefficient is given by:

$$k_{GL} = \frac{\int_{A_i}^{A_o} \vec{u} \cdot \vec{n} \cdot C \, dA + K \cdot \int_0^{V_{liq}} C \, dV}{a_{GL} \cdot V_{liq} \cdot \left(\overline{C_R} - \overline{C_S}\right)} \tag{3.4}$$

In order to observe local variations of mass transfer coefficient, the numerical domain is subdivided into several control volumes at the post-processing step. The mass transfer coefficients are then determined in each control volume using equation (3.4).

Chemical absorption

Chemical gas absorption occurs when the solute undergoes an irreversible reaction within the solvent. In order to simulate chemical absorption, the solute consumption is included through a source term in equation (2.34). Considering a first order reaction rate, the source term is expressed as the following:

$$S_m = -\rho_m \cdot K \cdot C_{H_2} \tag{3.5}$$

Where K is the reaction rate constant and C_{H_2} is hydrogen's concentration in the liquid film. In the event simultaneous transfer and reaction occur, the gas absorption flux expression is modified to account for mass transfer acceleration. Gas-liquid interfacial transfer rate is then given by:

$$\Phi_C = E \cdot k_{GL} \cdot a_{GL} \cdot V_{liq} \cdot (C^*_{H_2} - C_{S,H_2}) \tag{3.6}$$

Where E refers to the acceleration factor expressed as the following:

$$E = \frac{\Phi_C}{\Phi_P} \tag{3.7}$$

Φ_C is the chemical absorption flux (equation (3.6)), and Φ_P is the physical absorption flux (equation (3.20)). The acceleration factor is essentially linked to the Hatta dimensionless number (Ha). The latter compares the reaction rate within the liquid film to the gas-liquid diffusion rate. For a first order reaction rate, the Hatta number is given by:

$$Ha = \sqrt{\frac{K \cdot D_m}{k_{GL}}} \tag{3.8}$$

Broadly, small Hatta number values indicate that hydrogen consumption is negligible within the liquid film. On the other hand, when the solute is entirely consumed by the reaction within the liquid film, Hatta number values increase. The correlation between E and Ha has been extensively studied, the reader is referred to Danckwerts [1970] for an exhaustive listing of literature models. The authors proposed as well an analytical model for the enhancement factor E given by:

$$E = \sqrt{1 + Ha^2} \tag{3.9}$$

The above presented model is used in the present work to validate the numerical predictions in terms of acceleration factor E.

3.2.2 Liquid-solid mass transfer

Following the same procedure as described in section 3.2.1, the liquid-solid averaged mass transfer coefficient is given by:

$$k_{LS} = \frac{\int_{A_i}^{A_o} \vec{u} \cdot \vec{n} \cdot C \, dA}{a_{LS} \cdot V_{liq} \cdot \left(\overline{C_S} - \overline{C_R}\right)} \tag{3.10}$$

Where k_{LS} is the liquid-solid mass transfer coefficient, a_{LS} is the specific liquid-solid interfacial area, $\overline{C_S}$ and $\overline{C_R}$ are the averaged concentrations respectively at the solid surface and gas-liquid interface. In order to observe local mass transfer coefficient variations, the numerical domain is subdivided into several control volumes at the post-processing step. The liquid-solid mass transfer coefficients are then determined in each control volume using equation (3.10).

3.2.3 Gas-liquid-solid mass transfer

Heterogeneous catalytic reaction implementation

In this work, the heterogeneous catalytic reaction is accounted for by a surface reaction modulated with a surface effectiveness factor η_S to take into account possible internal diffusion limitation. The following flux condition at the surface of the catalyst is derived.

$$Flux = -\rho_m \cdot \frac{\eta_S \rho_{cata} w_{Pd} V_{cata} a_c}{A_{S,cata}} \tag{3.11}$$

Where a_c is the intrinsic reaction rate, w_{Pd} is the Pd mass fraction in the catalyst, V_{cata} and ρ_{cata} are respectively the catalyst volume and density, and η_S is the surface efficiency factor which is estimated classically through the Thiele modulus Φ_n. Since the flux condition (eq. (3.11)) is applied at the catalyst's external surface, the concentration within the catalyst pores is not accessible. Smaller scale simulations are required to access such information. The α-methylstyrene catalytic hydrogenation reaction was considered with a Pd/Al_2O_3 catalyst. Due to its very fast intrinsic kinetics, this reaction is very often operated in full external mass

transfer regime and is a good candidate to probe chemically overall external mass transfer efficiency of different GLS reactor configurations [Meille et al., 2002, Meille and de Bellefon, 2004] . The reaction rate simplifies to an nth order reaction in the selected experimental conditions:

$$r = k \cdot C_{H_2}^n \tag{3.12}$$

Where n=0.73 and k is the reaction rate constant [Tourvieille et al., 2013]. Even though the flux condition is applied on the surface of the catalyst, the diffusion throughout the catalyst volume is accounted for by the efficiency factor, which is defined as the following for an nth order catalytic reaction and is estimated at each mesh cell:

$$\eta_S = \frac{1}{\Phi_n} = \left(\frac{\delta_{cata}^2 (n+1) \rho_{cata} w_{Pd} k C_{H_2}^{n-1}}{2 D_e} \right)^{-0.5} \tag{3.13}$$

Where δ_{cata} is the catalyst thickness, k is the reaction rate constant and D_e is the effective diffusivity. This latter parameter is estimated as $D_{m,H_2}/4$ since the tortuosity ranges from 2 to 3, and the internal porosity is nearly 0.6 [Tourvieille et al., 2013] and there is no Knudsen diffusion term. Since the reaction rate and flux condition depend on the hydrogen concentration, only one concentration convection-diffusion equation is solved for H_2 concentration. The overall mass transfer coefficient can be post-processed after the chemical species concentration computation, the total hydrogen consumption flux is used to calculate the global mass transfer coefficient $K_{ov} \cdot a_{GL}$ and the α-methylstyrene conversion X_{AMS} as follows directly linked to the 1:1 stoechiometry between the 2 reactants:

$$K_{ov} \cdot a_{GL} = \frac{Hydrogen\ consumption\ flux}{V_{liq}(C_{H_2}^* - \overline{C_{S,H_2}})} \tag{3.14}$$

$$X_{AMS} = \frac{Hydrogen\ consumption\ flux}{Q_L C_{AMS}^i} \tag{3.15}$$

a_{GL} is the gas-liquid interfacial area, V_{liq} is the liquid volume inside the reactor, C_{AMS}^i is the α-methylstyrene concentration fixed to 1 mol/l at the inlet, Q_L is the liquid volumetric flow rate. The gas-liquid interfacial area a_{GL} has been chosen arbitrarily. $C_{H_2}^*$ is the thermodynamic equilibrium concentration of H_2 in the liquid phase (mol/m^3) given by the following expression [Herskowitz et al., 1978] :

$$C^*_{H_2} = 1.3(0.0145.T(K) - 1.6985)P(bar) \tag{3.16}$$

Where T and P are the operating temperature and pressure. $\overline{C_{S,H_2}}$ used in equation (3.14) is the mean hydrogen concentration at the catalyst's surface.

Resistances-in-series modelling

Gas-Liquid-Solid reactor models usually use the resistances-in-series model to estimate the overall mass transfer coefficient, termed $K_R \cdot a_{GL}$ to distinguish it from $K_{ov} \cdot a_{GL}$ presented in equation (3.14), considering that the overall external mass transfer inside such reactors is governed by two drivers in series, gas-liquid and liquid-solid mass transfer resistances. First, a gaseous component diffuses from the gas bulk to the liquid film through the gas-liquid interface, the solute concentration stabilises inside the liquid volume and reaches a liquid bulk concentration, then it is consumed by the heterogeneous reaction at the catalyst surface. The overall mass transfer coefficient K_R is determined using the resistances-in-series model, defined as follows:

$$\frac{1}{K_R a_{GL}} = \frac{1}{k_{GL} a_{GL}} + \frac{1}{k_{LS} a_{LS}} \tag{3.17}$$

This model is developed assuming the presence of a liquid bulk inside the liquid film. The gas phase consists of pure H_2, and as the hydrogen is poorly soluble in the liquid phase, the gas-liquid mass transfer coefficient represents the liquid-side mass transfer. The mass transfer coefficients k_{GL} and k_{LS} are determined respectively from simulations of:

— Physical gas absorption into the liquid through the gas/liquid interface

— Physical solid dissolution into the liquid through the liquid/solid interface

3.3 Numerical set-up

In order to simulate 2D laminar gas-liquid flow along a vertical solid surface, the numerical domain reported in figure 3.1 is considered. Gas and liquid enter the domain separately from the top, and flow co-currently downward under gravity effect throughout the numerical domain. In case of gas absorption, the chemical species present in the gas phase migrate to the liquid phase.

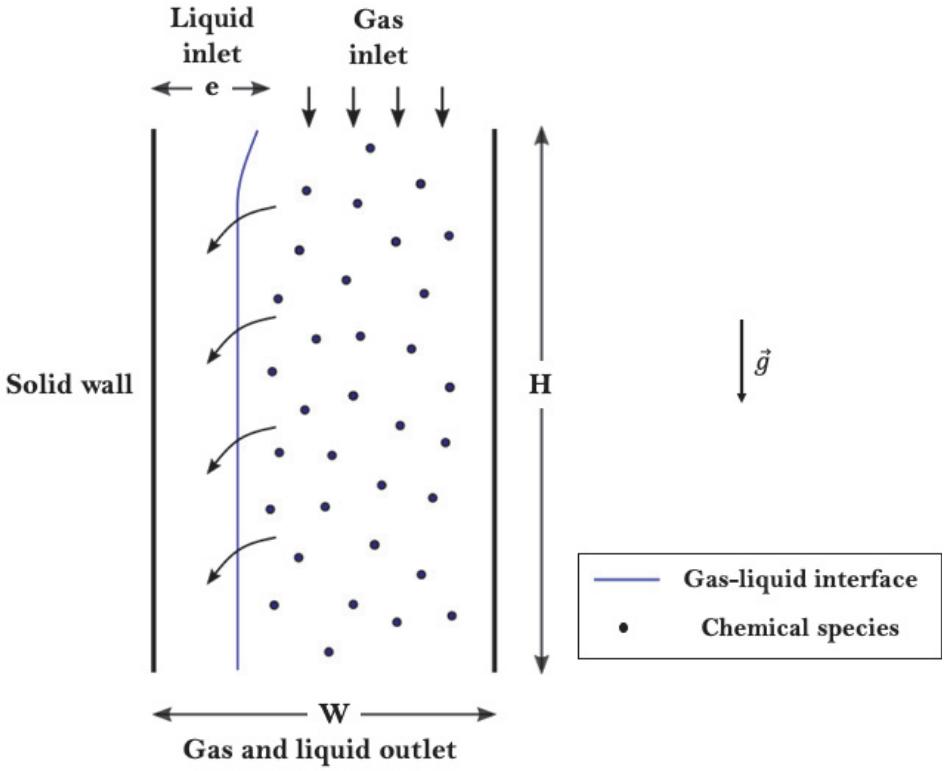

Figure 3.1 Schematic representation of the numerical domain

Table 3.1 Numerical domain dimensions, physico-chemical properties and two-phase flow Reynolds numbers

e [mm]	W [mm]	H [mm]	Re_L	Re_G	$\rho_L[kg/m^3]$	$\rho_G[kg/m^3]$	$\mu_L[Pa.s]$	$\mu_G[Pa.s]$
0.20	1.00	250.00	3.98	2.74	998	0.083	$1.003 \cdot 10^{-03}$	$8.5 \cdot 10^{-06}$

The domain's dimensions are given in table 3.1, where **H** is the height, **W** is the width and **e** is the liquid inlet size. These dimensions are thoroughly fixed to guarantee fully developed flow and concentration profiles. At the initial state, the numerical domain is filled with gas.

Regarding boundary conditions, the gas and liquid enter the domain at fixed velocity values, corresponding to Reynolds numbers reported in table 3.1. A no-slip boundary condition is implemented in both the western and eastern boundaries. In order to account for solid wettability, a constant 20° contact angle is enforced at the solid wall surface (western boundary). Finally, gas and liquid exit the domain at the southern boundary where gauge pressure -defined as $p - p_{atmospheric}$- is set to zero.

Table 3.2 Boundary conditions for mass transfer resolution

Case	Domain boundary				
	Gas inlet	liquid inlet	East	West	South
Gas absorption into the liquid film	$C = C^*$	$C = 0$	$C = C^*$	zero flux	zero flux
Solid dissolution into the liquid film	zero flux	$C = 0$	zero flux	$C = C^*$	zero flux
Gas-liquid-solid mass transfer in the presence of heterogeneous catalytic reaction	$C = C^*$	$C = 0$	$C = C^*$	Flux given by equation (2.35)	zero flux

As for mass transfer, the boundary conditions are reported in table 3.2 in accordance with investigated problems. In all instances, the solute concentration within the liquid phase is null at the inlet. The concentration C^* corresponds to the thermodynamic equilibrium concentration. As explained in section 2.4.2, assuming pure gas-phase composition and negligible gas-side mass transfer coefficient, C^* is enforced within the gas phase to include interfacial thermodynamic equilibrium in simulations.

3.4 Film flow hydrodynamics

The laminar falling liquid film flow was first investigated in the pioneering work of Nusselt [1916]. The authors proposed an analytical description of the velocity profile within the liquid film, given by the following expression:

$$U(y) = -\frac{U_I}{\beta^2} y(y - 2\beta) \tag{3.18}$$

U(y) is the liquid film velocity profile, β and U_I are respectively the liquid film thickness and interface velocity given by the following expressions:

$$\beta = \left(\frac{3\nu_L^2 Re_L}{g}\right)^{1/3}; \qquad U_I = \frac{\rho_L g \beta^2}{2\mu_L} \tag{3.19}$$

Where ν_L and μ_L are respectively the kinematic and dynamic viscosities, ρ_L is the liquid density and g is the gravitational acceleration. Figure 3.2a compares numerical predictions to the analytical solution of Nusselt [1916], regarding velocity profile evolution in the perpendicular direction to flow. Due to high mesh density, only 30% of CFD data points are reported in the figure to allow better visualisation. The analytical velocity profile (eq. (3.18)) is well predicted by CFD within the liquid film, reaching a maximum value at the gas-liquid interface. For further illustration, the predicted two-phase velocity profile is reported in figure 3.2b.

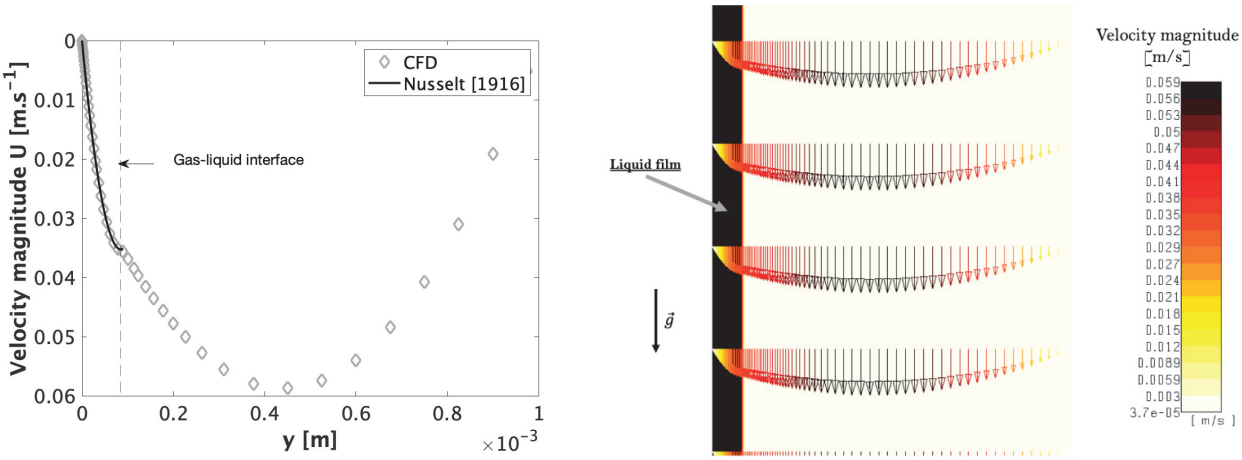

(a) (b)

Figure 3.2 (a) Velocity profile perpendicular to flow direction, comparison between numerical results and analytical solution of Nusselt [1916], (b) velocity vectors in the fully developed flow regime

Additional validation is reported in table 3.3, where numerical liquid film thickness and interface velocity are compared to equation (3.19). A good agreement is found between numerical and analytical solutions, since very low relative deviations are reached.

Table 3.3 Numerical and analytical interface velocity and liquid film thickness values

	Analytical solution	Numerical solution	Relative deviation
Interface velocity U_I [cm/s]	3.53	3.54	0.28%
Liquid film thickness β [μm]	85.03	84.62	0.48%

3.5 Gas absorption into laminar falling liquid film

In an effort to further establish the numerical model, this section focuses on gas absorption into the laminar falling liquid film for gas-liquid mass transfer analysis and validation. In gas absorption, chemical species migrate by diffusion across the interface from gas to liquid. Commonly, the chemical species and liquid phase are respectively referred to as solute and solvent. Depending on whether there is a simultaneous liquid-phase reaction following interfacial mass transfer, gas absorption is qualified to be either physical or chemical.

In physical gas absorption, the solute does not react within the liquid phase. Whereas, chemical gas absorption occurs when the solute undergoes an irreversible chemical transformation within the liquid phase. Both aforementioned absorption processes are considered to validate the numerical model, their simulations are presented herein.

In order to predict gas absorption into the liquid film, simulations are grounded on the following assumptions: (i) the gas is pure and (ii) the liquid is non-volatile. The former implies that only one chemical species is involved in the mass transfer process, while the latter supports the absence of mass transfer from liquid to gas. For model validation, the numerical results are compared to analytical solutions, the latter are presented hereinafter.

3.5.1 Physical gas absorption

Gas-liquid mass transfer is commonly driven by a difference in concentrations between the involved phases. The mass transfer flux is then given by:

$$\Phi_P = k_{GL} \cdot a_{GL} \cdot V_{liq} \cdot (C^*_{H_2} - C_{S,H_2}) \tag{3.20}$$

Where k_{GL} is the gas-liquid mass transfer coefficient, $C^*_{H_2}$ and C_{S,H_2} are respectively the thermodynamic equilibrium and solid surface concentrations of hydrogen.

Several theories have been proposed in literature to describe mass transfer by physical absorption, foremost among which is the Higbie penetration theory. In the latter theory, bulk liquid elements are brought to the gas-liquid interface by eddies, where they come into contact with the gas phase for a short definite period of time (t^*), after which the surface element is mixed with the liquid bulk again. As a result, Higbie [1935] proposed an analytical solution for gas-liquid mass transfer coefficient given by the following equation:

$$k_{GL}(x) = \sqrt{\frac{D_m U_I}{\pi x}} \tag{3.21}$$

Where D_m is the molecular diffusion coefficient of the solute, U_I the interface velocity and x the local distance with respect to the inlet. The mass transfer coefficient reported in equation (3.21) is a local parameter defined at each mesh cell of the interface. In order to determine the mean mass transfer coefficient over a specified interface length L, the integral average is used as follows:

$$k_{GL,M} = \frac{1}{L}\int_0^L k_{GL}(x)dx \tag{3.22}$$

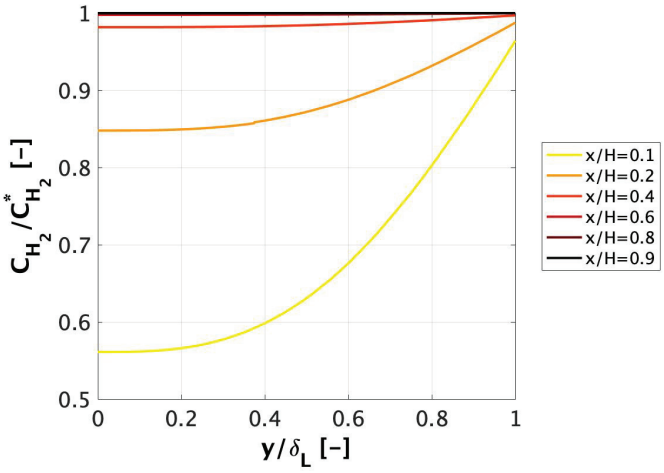

Figure 3.3 Predicted hydrogen concentration profiles within the liquid film for physical gas absorption at several horizontal locations x. The solid wall is located at y=0 and gas-liquid interface at $y = \delta_L$

Hydrogen concentration transport is solved numerically using the boundary conditions described in table 3.2 for gas absorption. Since the liquid is pure at the inlet, the solute concentration is fixed to zero. Given that the gas phase is pure, solute concentration is enforced to the thermodynamic equilibrium concentration $C^*_{H_2}$ within the gas phase. Subsequently, while flowing throughout the domain, the liquid phase comes into contact with the gas phase, allowing for solute interfacial transport by molecular diffusion.

Predicted hydrogen concentration profiles within the liquid film are shown in figure 3.3. As one can see, the liquid is increasingly enriched with hydrogen as the film travels throughout the domain. In addition, liquid saturation with hydrogen is reached for x/H>0.4. However, it is important to note that gas-liquid mass transfer occurs in absence of a bulk concentration. This is mainly due to low liquid film thickness, preventing concentration from reaching a constant value in the core of the liquid film.

Regarding interfacial mass transfer, figure 3.4 represents a comparison between averaged analytical and predicted gas-liquid mass transfer coefficients. Due to the high concentration gradient at the domain's inlet boundary, small deviations of k_{GL} are noticed for low x values. Indeed, the gas and liquid enter the domain respectively at maximum ($C^*_{H_2}$) and minimum (0) concentrations, leading to a high concentration gradient between both phases. Although the latter is handled by the numerical model, a certain establishment length is needed to stabilise concentration profile. This directly impacts k_{GL} since concentration gradient is the driving force of interfacial mass transfer.

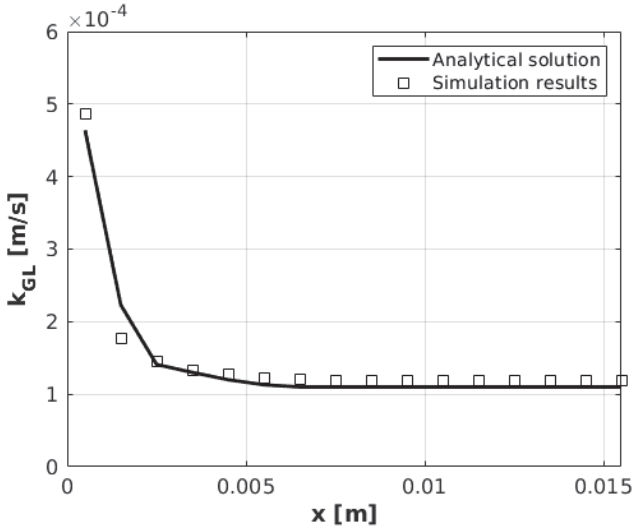

Figure 3.4 Mean gas-liquid mass transfer coefficient evolution, comparison between CFD predictions and analytical solution of Higbie [1935]

Due to the absence of bulk, the gas-liquid mass transfer coefficient is defined based on the maximum concentration difference, namely between the gas-liquid ($C^*_{H_2}$) and liquid-solid (C_{S,H_2}) interfaces. Following the establishment length, the gas-liquid mass transfer coefficient stabilises and reaches a constant value. Figure 3.4 shows that a good agreement is found between predicted and analytical k_{GL} values.

3.5.2 Chemical gas absorption

Chemical gas absorption is simulated using the corresponding boundary conditions presented in table 3.2. When compared to physical absorption, the particularity of this case is the addition of the source term given by equation (3.5). While the liquid flows over the vertical

plane, gas diffusion through the interface competes with the liquid-phase reaction, as both phenomena happen simultaneously.

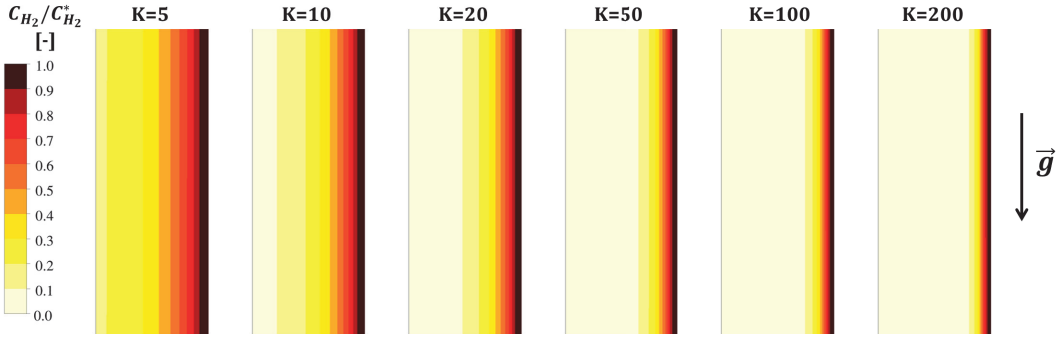

Figure 3.5 Predicted hydrogen's concentration within the liquid film for several reaction rate constants K

According to the numerical predictions, hydrogen's consumption within the liquid film increases with the reaction rate constant K, as shown in figure 3.5. Therefore, the gas-liquid mass transfer boundary layer becomes thinner, and the solute is consumed closer to the interface. In addition, the required establishment length for hydrogen's concentration profile is reduced for high reaction rate constants K, as shown in figure 3.6.

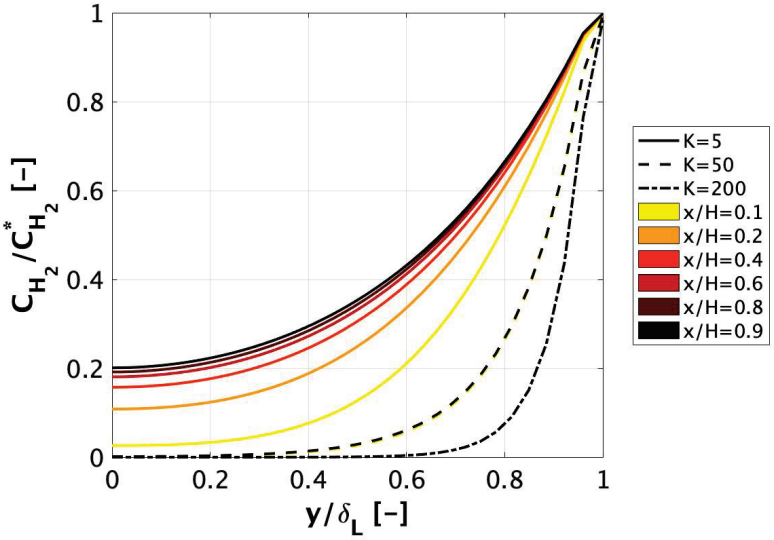

Figure 3.6 Predicted hydrogen's concentration profile for $K = 5s^{-1}$, $K = 50s^{-1}$ and $K = 200s^{-1}$ at different horizontal locations x of the numerical domain

For $K = 5s^{-1}$, gas diffusion is more significant than reaction consumption, since hydrogen concentration profile is consistent with pure diffusion previously shown in figure 3.3. As the

reaction rate constant K increases, the concentration profiles at different horizontal locations overlap, meaning that stabilisation is promptly reached. Based on the obtained concentration distributions, the average chemical absorption mass transfer coefficients are computed. As a result, it is possible to compute the average acceleration factors E, defined as the ratio between averaged chemical and physical absorption fluxes.

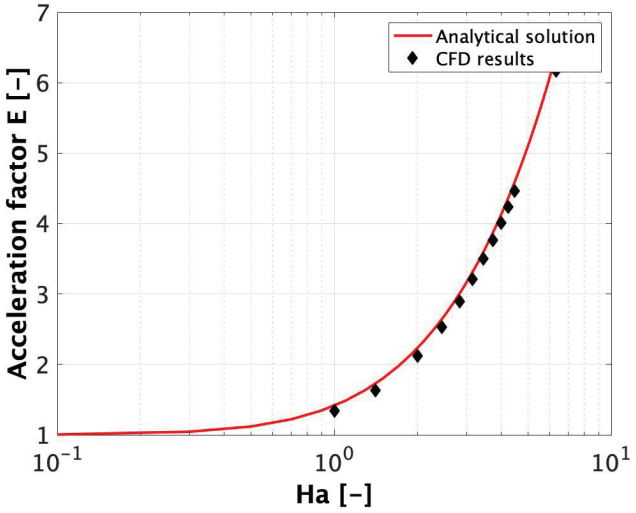

Figure 3.7 Evolution of the predicted mean acceleration factor E with mean Hatta dimensionless number. Comparison to the analytical solution of Danckwerts [1970]

A good agreement is reached between predicted and analytical acceleration factors, as shown in figure 3.7. Indeed, the predicted mean acceleration factors follow the same evolution specified by the model of Danckwerts [1970], for the considered Hatta numbers.

3.6 Solid dissolution

In previous sections, the numerical model proved to accurately predict gas-liquid mass transfer. In this context, following the most common experimental characterisation technique of liquid-solid mass transfer, solid dissolution into the liquid film is simulated. The objective is to predict the liquid-solid mass transfer coefficient in the absence of gas-absorption.

To do so, the concentration transport equation (2.34) is solved for hydrogen contained in the solid wall boundary, using the boundary conditions reported in table 3.2. The hydrogen concentration is null at the liquid inlet and within the gas phase. Therefore, as a result of the concentration gradient, hydrogen dissolves from to solid into the liquid phase by diffusion.

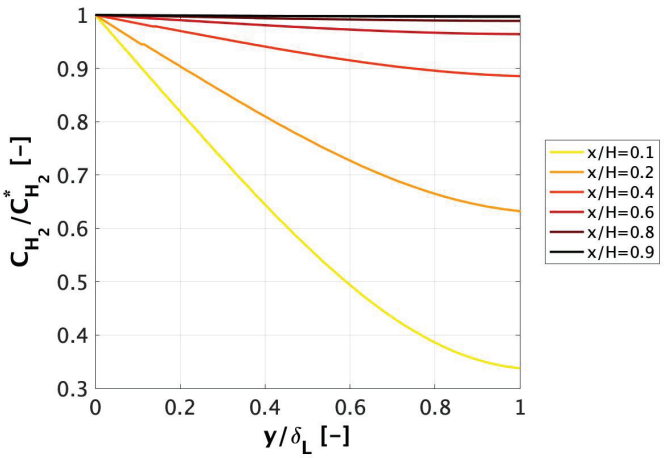

Figure 3.8 Solute concentration profile within the liquid film for solid dissolution at several horizontal locations x

Similarly to physical gas absorption, the liquid is increasingly enriched with hydrogen throughout the numerical domain, as shown in figure 3.8. In addition, absence of bulk concentration is observed for solid dissolution as well. Nonetheless, liquid film saturation is achieved later in this case as opposed to gas absorption. Indeed, total liquid film saturation is reached for x/H>0.4 in physical gas absorption against x/H>0.8 in solid dissolution.
This is reflected on the liquid-solid mass transfer, since a higher distance is required to achieve stabilisation as shown in figure 3.9. Furthermore, it is important to note that liquid-solid mass transfer coefficient is significantly lower than physical gas-liquid mass transfer coefficient. This is attributed to the contribution of convection in view of the velocity profile within the liquid film. Indeed, the no-slip condition near the solid wall is reflected by a null velocity, whereas maximum liquid velocity is reached at the gas-liquid interface as proven previously (section 3.4).

3.7 Gas-liquid-solid mass transfer

In an effort to approach industrial configurations, the numerical model is employed to predict gas-liquid-solid mass transfer in the falling liquid film. In this case, the gas solute migrates to the liquid film, before undergoing a heterogeneous catalytic reaction at the solid catalyst surface. As explained in chapter 2, the gas-liquid and liquid-solid mass transfer coefficients are commonly determined separately. Subsequently, the resistances-in-series model is employed to compute gas-liquid-solid mass transfer. Therefore, the main goal of this section

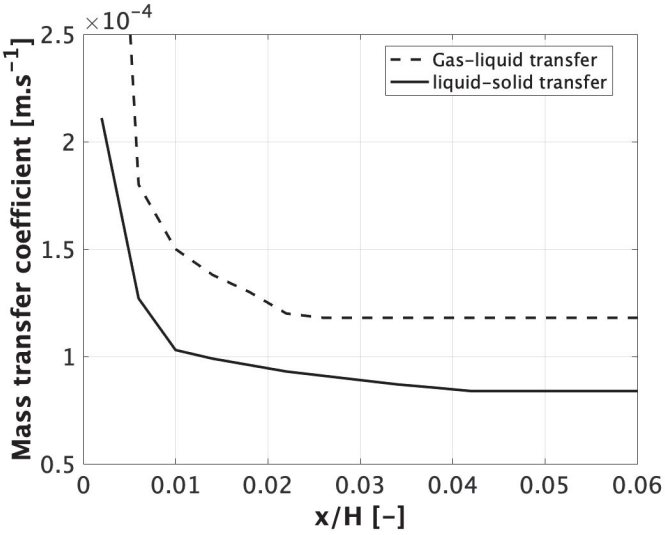

Figure 3.9 Comparison of predicted gas-liquid and liquid-solid mass transfer coefficients throughout the numerical domain

is to compare the predicted gas-liquid-solid mass transfer coefficient K_{ov} to K_R provided by the resistances-in-series (eq. (3.17)).

Hydrogen transport in three-phase mass transfer conditions is simulated using the corresponding boundary conditions (cf. table 3.2). The heterogeneous catalytic reaction is enforced through a flux condition at the catalyst's surface, as discussed in section 2.4.3. The fully developed hydrogen concentration profile is represented in figure 3.10 within the liquid film.

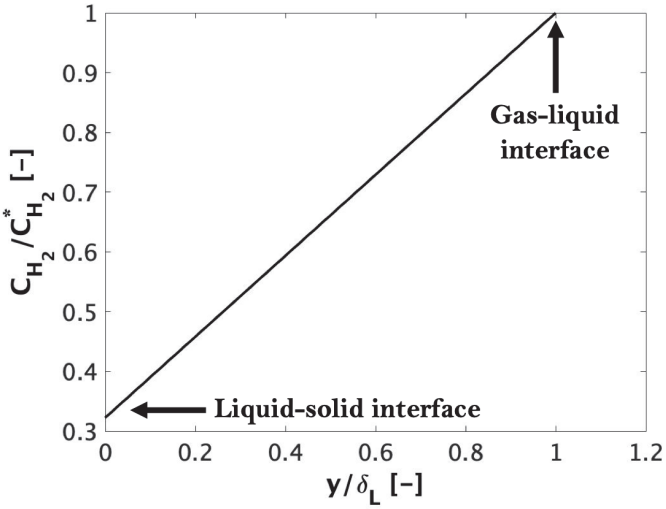

Figure 3.10 Predicted hydrogen concentration profile in the liquid film for gas-liquid-solid mass transfer in the presence of a heterogeneous catalytic reaction

Once again, the mass transfer occurs in absence of liquid bulk, since the obtained concentration profile is linear between the solid wall and gas-liquid interface. In addition, due to specific kinetics -nearly first order in solute and zeroth order in substrate- and gas conditions (pure and isobaric hydrogen flow), this concentration profile remains the same all along the domain's length.

The overall gas-liquid-solid mass transfer coefficient is computed from the following expression:

$$K_{ov} = \frac{\Phi_R}{a_{ov} V_{liq} (C^*_{H_2} - \overline{C_{S,H_2}})} \tag{3.23}$$

Where Φ_R is the hydrogen consumption flux resulting from the heterogeneous catalytic reaction, V_{liq} is the liquid volume, K_{ov} is the overall mass transfer coefficient and a_{ov} is the overall interfacial area. In the ideal case of film flow, gas-liquid and liquid-solid interfacial areas are fairly equal. Therefore, a_{ov} is chosen to be the gas-liquid interfacial area.

On one hand, the predicted overall mass transfer coefficient in the presence of heterogeneous catalytic reaction is of $K_{ov} = 5.99 \cdot 10^{-5} m.s^{-1}$. On the other hand, the resistances-in-series model is used to determine the overall mass transfer coefficient K_R, based on both $k_{GL}a_{GL}$ and $k_{LS}a_{LS}$ previously determined respectively for physical gas absorption and solid dissolution. The resistances-in-series model provides a gas-liquid-solid mass transfer coefficient of $K_R = 7.95 \cdot 10^{-5} m.s^{-1}$. The results exhibit a 27% deviation, since the resistances-in-series model overestimates the overall mass transfer coefficient. Actually, low liquid film thickness and laminar flow result in the absence of a bulk concentration in the liquid film, leading to deviations between predictions and resistances-in-series model.

Furthermore, an analytical solution is developed for this case study, in order to compare the obtained K_{ov} to its analytical value $K_{ov,A}$. In steady state conditions, assuming negligible convection, gas-liquid-solid mass transfer is described by the following system of equations:

$$\begin{cases} D_{m,H_2} \frac{d^2 C_{H_2}}{dy^2} = 0 \\ D_{m,H_2} \nabla C_{H_2}\big|_{y=0} = \Phi_R / A_{S,cata} \qquad at\ y = 0\ (catalyst\ surface) \\ C_{H_2}(y = \delta_L) = C^*_{H_2} \qquad at\ y = \delta_L\ (gas - liquid\ interface) \end{cases} \tag{3.24}$$

The corresponding analytical concentration profile derived from eq. (3.24) is given by:

$$C_{H_2}(y) = \frac{\Phi_R}{A_{S,cata} \cdot D_{m,H_2}} (y - \delta_L) + C^*_{H_2} \tag{3.25}$$

Therefore, grounded on the analytical hydrogen concentration profile aforementioned, the analytical overall gas-liquid-solid mass transfer coefficient $K_{ov,A}$ is computed from the following expression:

$$K_{ov,A} = \frac{D_{m,H_2} \frac{dC_{H_2}}{dy} A_{S,cata}}{a_{ov} V_{liq} (C^*_{H_2} - C_{S,H_2})} = \frac{\Phi_R}{a_{ov} V_{liq} (C^*_{H_2} - C_{S,H_2})} \tag{3.26}$$

Both analytical and predicted overall mass transfer coefficients are equal, namely $K_{ov,A}$ and K_{ov}. This result indicates that in this configuration, the vertical convective downflow does not impact horizontal concentration transport, since it is mainly ensured by diffusion.

Further analysis of multiphase mass transfer is carried out through film model analysis. the latter model suggests an expression for the overall mass transfer coefficient, based on the concentration boundary layer thickness. The film model mass transfer coefficient is given by:

$$K_{ov,m} = \frac{D_{m,H_2}}{\delta_c} \tag{3.27}$$

Where D_{m,H_2} is the hydrogen's molecular diffusion coefficient and δ_c is the concentration boundary layer thickness. In the present case, considering that δ_c is equal to the actual film thickness, a good agreement is obtained between predicted and film model overall mass transfer coefficients. The relative deviation is equal to 1.3% as reported in table 3.4, implying that the diffusion layer thickness (δ_c) is nearly equal to the hydrodynamic liquid film thickness (δ_h).

Table 3.4 Post-processing data of film model applied to vertical falling liquid film at different pressure conditions

Pressure [bar]	$C^*_{H_2}[mol/m^3]$	$K_{ov}a_{ov}[s^{-1}]$	$\delta_h[\mu m]$	$\delta_c[\mu m]$	Relative deviation [%]
1	3.10	0.692	84.62	85.77	1.37%
3	9.40	0.693	84.62	85.77	1.37%
5	16.40	0.692	84.62	85.77	1.50%

3.8 Conclusion

In this chapter, a numerical model has been developed in order to improve the understanding of a reactive falling liquid film over a semi-infinite plane. This model coupled a robust

hydrodynamic VOF description with consistent representations of gas-liquid and gas-liquid-solid mass transfers.

First, the two-phase flow hydrodynamic behaviour was validated against analytical solutions. In developed flow conditions, an excellent agreement is achieved between predictions and Nusselt's model [Nusselt, 1916], namely for liquid film velocity profile, interface velocity and liquid film thickness.

Afterwards, the model's accuracy was assessed for different mass transfers. Physical gas absorption is first simulated and compared to the solution of Higbie [1935]. Besides the good agreement between CFD and the model, it is found that gas-liquid mass transfer occurs in absence of a bulk concentration. This is mainly due to the low liquid film thickness within the reactor. Next, a liquid phase chemical species consumption is implemented to the numerical model, the aim is to simulate gas absorption in chemical conditions. While increasing the reaction rate constant, the mass transfer boundary layer is found to approach more and more the gas-liquid interface. The predicted acceleration factors were compared to the solution of Danckwerts [1970], which highlighted the accuracy of the model's predictions.

Following these validations, the numerical model was employed to predict liquid-solid mass transfer. Since interface velocity is significantly higher than near-wall velocity, liquid-solid mass transfer coefficient was lower than gas-liquid mass transfer coefficient. These two coefficients were then used to check the validity of resistances-in-series model. Finally, gas-liquid-solid mass transfer was simulated in the presence of α-methylstyrene hydrogenation to cumene. The overall mass transfer coefficient predictions were in good agreement with a developed analytical solution. In addition, the gas-liquid-solid mass transfer was well described by the film model, since a pure radial diffusion regime was reached at steady state. However, the resistances-in-series model was not suitable to describe mass transfer for this case, since it overestimates the mass transfer coefficient by 27%.

To sum up, hydrodynamic and mass transfer predictions were validated against several analytical solutions. Subsequently, the model provides accurate predictions and will be further assessed on more complex geometries in the following chapters.

Chapter 4

Numerical simulation of a Falling Film Micro-structured Reactor and a string reactor

4.1 Introduction

Gas-liquid-solid reactors are essential to a variety of industrial processes. To cover their wide application spectrum, several gas-liquid-solid reactor technologies have been developed in the last decades. The coupling between hydrodynamics and mass transfer is more complex for some reactors than for others, mainly because of geometrical features. Therefore, the aim of this chapter is to investigate the effect of catalyst's geometry on reactor's performances.

Previously validated against analytical solutions for a 2D falling liquid film (cf. chapter 3), the numerical model has been applied to simulate a 3D Falling Film Micro-structured Reactor (FFMR). The latter was employed by Tourvieille et al. [2013] and Tourvieille [2014], who conducted an experimental investigation of hydrodynamics and gas-liquid-solid mass transfer. Rather than flat catalyst surface, the liquid flows over semi-elliptical micro-channels within the FFMR. The authors used confocal microscropy to describe liquid flow qualitatively. In addition, gas-liquid-solid mass transfer was characterised in the presence of a heterogeneous catalytic reaction, i.e α-methylstyrene hydrogenation to cumene. These experimental results are used to evaluate the ability of CFD to predict hydrodynamic and mass transfer parameters in a realistic more complex set-up.

Afterwards, to go towards more complex geometries encountered in fixed bed reactors, the numerical model is employed to predict two-phase flow over a 3D spherical particles string. A similar geometry was employed by Augier et al. [2010]. The authors investigated experimentally and numerically two-phase flow over a stacking of three spherical particles. Compared to the FFMR, a tortuous flow-path is obtained for sequenced spherical particles. Even though this geometry is an ideal fixed bed reactor, tortuosity effect on gas-liquid interface and gas-liquid-solid mass transfer is studied.

In the present chapter, predictions of 3D Falling Film Micro-structured Reactors (FFMRs) are first presented. The results are compared to experimental results of Tourvieille [2014], in terms of liquid film thickness distribution and overall mass transfer coefficients. Afterwards, predictive simulations of a 3D falling film over a string of spherical particles are conducted. Numerical results are analysed to highlight the effect of geometry and tortuosity on gas-liquid-solid mass transfer.

4.2 3D simulation of a Falling Film Micro-structured Reactor (FFMR)

4.2.1 Numerical domain

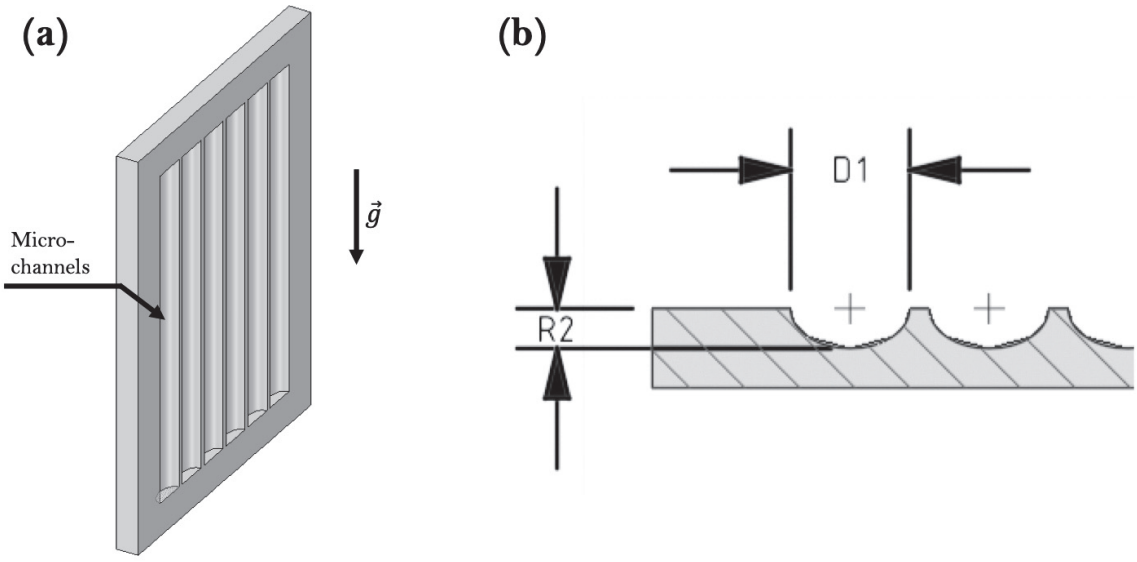

Figure 4.1 (a) Reactive plate and (b) micro-channels geometrical characteristics

In an effort to reproduce similar flow conditions, the numerical domain is built based on the work of Tourvieille et al. [2013] and Tourvieille [2014]. The experimental Falling Film Micro-structured Reactor (FFMR) consists of a reactive plate containing N similar semi-elliptical micro-channels, as shown in figure 4.1. In order to ensure an even inlet distribution, liquid is injected through a uniformly perforated pipe.
In their experimental work, Tourvieille [2014] tested two micro-channels dimensions D1xR2, as reported in table 4.1. As one can see, micro-channels aspect ratios are particularly high, reaching nearly 375 for the 600x200μm^2 channel. In addition, given the channels' total number, considering the entire FFMR would result in high computation times. Therefore, the numerical domain should be reduced.

Table 4.1 Falling Film Micro-structured Reactor dimensions [Tourvieille, 2014]

Reactor dimensions		
Reactor size (length x width x depth)	32.0cm x15.6cm x4.0cm	
Gas chamber height [mm]	4.5	
Uncoated channel dimensions		
Length [cm]	22.6	
Width (D1) [μm]	600	1200
Depth (R2) [μm]	200	400
Number of channels [-]	100	50

Assuming (i) even liquid inlet distribution and (ii) symmetrical flow within channels, the numerical domain is reduced to half a channel as shown in figure 4.2. It is worth noting that two-phase flow in high aspect ratio channels might exhibit instabilities, particularly at the gas-liquid interface. Therefore, channel's length is maintained to provide a realistic representation of two-phase flow.

Meshing was conducted within Pointwise since it provides desired freedom to properly mesh the geometry. It is important to note that near-wall mesh cells closely follow the semi-elliptical shape. As will be demonstrated later in this chapter, this is an important requirement to properly describe reactive flux at the catalyst's surface. Even though mesh is generated considering uncoated channels, the coated channel geometry is obtained simply through linear down-scaling.

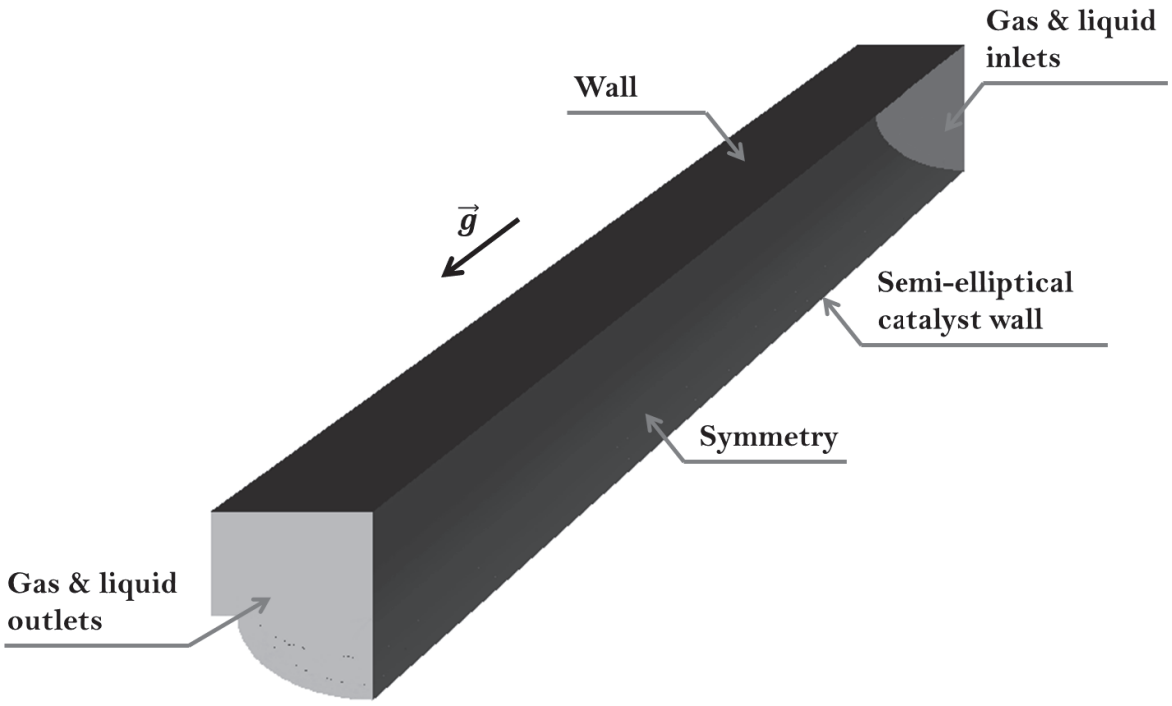

Figure 4.2 Boundary conditions employed to simulate the FFMR. The channel's length is 22.6cm.

4.2.2 Numerical set-up and boundary conditions

In order to simulate hydrodynamic and mass transfer performance in FFMRs, boundary conditions shown in figure 4.2 are considered. Assuming an even inlet liquid distribution, liquid flow rate is determined from the ratio of overall liquid flow rate to the number of channels. Since gas and liquid flow co-currently downward through the reactor, their corresponding inlet velocities are specified at the top of the domain. Near-wall flow is described through a no-slip boundary condition. In addition, capillarity effects are accounted for through a static contact angle. The latter parameter was not characterised experimentally, hence different contact angle values were tested in the model. To account for geometry reduction, symmetry-type boundary conditions are applied at the lateral walls. Moreover, since the gas chamber was reduced as well, a wall boundary condition with zero relative velocity was specified. Finally, a regular pressure outlet condition is applied at the exit.

Regarding mass transfer, hydrogen concentration is specified at the liquid and gas inlets respectively to 0 and $C^*_{H_2}$. The reagent's concentration is fixed within the gas-phase, and is equal to $C^*_{H_2}$. To account for heterogeneous catalytic reaction, the reactive flux condition is applied to the semi-elliptical catalyst wall. Finally, concentration flux is equal to zero elsewhere.

In order to avoid compatibility issues between the liquid phase and solid material of the FFMR, the hydrodynamic experiments were performed using ethanol instead of MCH+AMS/ hydrogen. For consistency purposes, hydrodynamic simulations are performed using ethanol, and reactive mass transfer simulations are carried out with MCH+AMS/hydrogen. Two-phase systems properties are reported in table 4.2.

Table 4.2 Physical properties of the two-phase systems

	Composition	Operating Pressure [bar]	Density ρ $[kg.m^{-3}]$	Viscosity μ $[kg/m.s]$	Surface tension σ_L [mN/m]
Gas phase	Pure hydrogen	1	0.086	$8.60 \cdot 10^{-6}$	-
		3	0.26	$8.61 \cdot 10^{-6}$	-
		5	0.43	$8.61 \cdot 10^{-6}$	-
Liquid phase	Ethanol	1, 3 and 5	789	$1.04 \cdot 10^{-3}$	21.8
	Methylcyclohexane and α-methylstyrene (MCH+AMS)		770	$1.00 \cdot 10^{-3}$	22

4.2.3 Hydrodynamic predictions

Tourvieille [2014] investigated two-phase flow throughout the FFMR for ethanol over uncoated channels. In order to visualise film flow, a fluorescent dye is mixed with liquid phase. Afterwards, liquid film profiles are observed at 8cm from liquid inlet through confocal microscopy. CFD simulations are conducted in experimental conditions, that is to say flow rates, liquid properties and channel geometry.

To be fully representative of the experimental work, and because starting procedure plays a significant role on wetting, the channel is initially overflowed with liquid at inlet liquid velocity. Regarding contact angle, it is found that liquid film profiles are well represented with contact angle values lower than 40°. Therefore, the simulations were conducted using a contact angle of 20°.

Liquid flow over a flat plane can take several forms. At large liquid flow rates, a continuous liquid sheet is formed on the solid surface, which might breakup at certain locations. Falling film micro-reactors are known for preventing film breakup, they facilitate the stability of the

liquid film and the corresponding gas-liquid interface and gas-liquid-solid 3-phase contact lines. Due to the combination of capillary forces and small channel widths, liquid is pulled up along the sides of the channels and covers up a significant portion of the channel width. The most desirable flow configuration is when the liquid flows in a meniscus shape as shown in figure 4.3, that is to say for small Weber numbers, as the interface shape is governed by the interfacial energy.

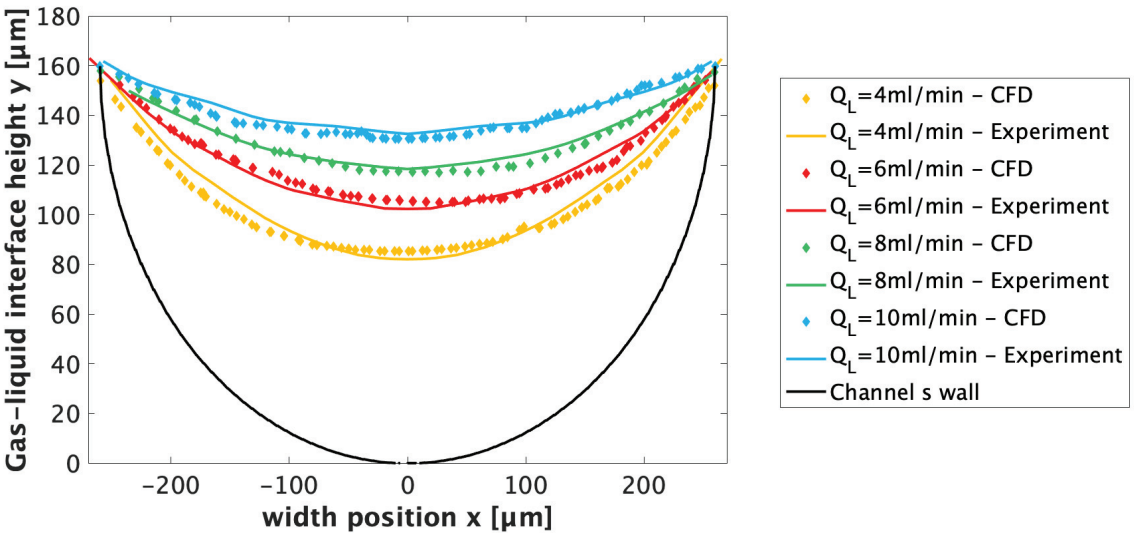

Figure 4.3 Comparison between numerical and experimental liquid film profiles for ethanol flow in a 600x200μm² channel, the liquid flow rate ranges from 4ml/min to 10ml/min. the simulations are performed in isothermal (T=283K) and isobaric (P=1bar) conditions

Downward co-current two-phase flows were simulated, and converged liquid film profiles were compared to the corresponding experimental results, as shown in figure 4.4. shows this comparison for different inlet liquid flow rates. The numerical results are in good agreement with the experimental values indicating a very good prediction of the hydrodynamics by the CFD simulations. The gas-liquid interface curves upwards moving from the channel's centre to the three-phase contact lines (always located at the edges of the channel due to the starting wetting procedure), and the interface is not disrupted across the numerical domain. The more the liquid flow rate increases, the flatter the interface becomes. Such behaviour was found in many experimental studies [Tourvieille et al., 2013, Yeong et al., 2006]. Besides, the liquid film is contained inside the channel regardless of tested liquid inlet flow rates in the investigated flow rate range. The results shown in figure 4.3 were obtained with a contact angle value of 20°.

Logically, as shown in figure 4.4, the corresponding specific gas-liquid area values are in good agreement with the experimental results, with a relative deviation to the experimental results only up to 10% at the lowest liquid flow rate. The variation of the specific gas-liquid area illustrates well the effect of liquid flow rate, as this latter increases, the interface flattens, the mean liquid thickness increases too leading to the decrease of the specific area.

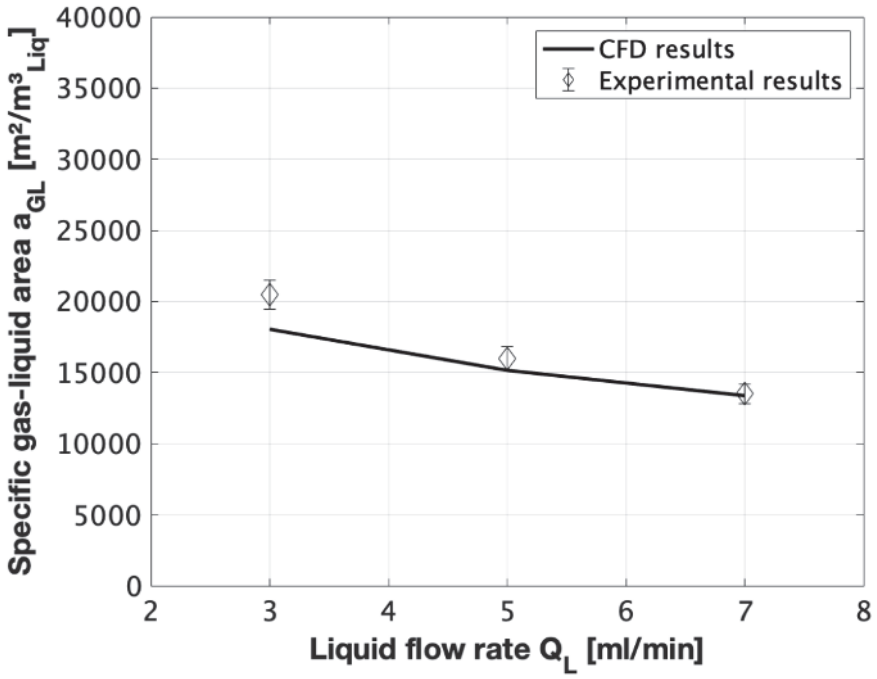

Figure 4.4 Specific gas-liquid area comparison for ethanol/H_2 flow at Q_L between 3ml/min and 7ml/min in a 600x200μm² channel, the simulations are performed in isothermal and isobaric conditions (T=283K, P=1bar). Numerical results are compared to experimental data of [Tourvieille, 2014]. Error bars represent $\pm$5%

4.2.4 Mass transfer analysis

In this section, the two-phase flow of hydrogen and methylcyclohexane/α-methylstyrene mixture is investigated, and two channel dimensions were simulated for further validation. The coated channels characteristics are summarised in table 4.3.

As one can see from figure 4.5, H_2 diffuses from the gas phase to the liquid phase, and is consumed by the heterogeneous catalytic reaction at the solid wall. Due to the liquid film thickness variation inside the channel, the liquid is saturated with H_2 near the three phase contact line as the liquid film thickness is lower at this location. Whereas, at the channel's

Table 4.3 Coated plate characteristics used by [Tourvieille et al., 2013] for 600x200μm^2 channels and [Tourvieille, 2014] for 1200x400μm^2 channels

Channel cross section dimensions [μm^2]	600x200	1200x400
Channel number per plate	100	50
Catalyst density $\rho_{cata}[g.m^{-3}]$	690278	737231
Palladium mass fraction w_{Pd} [%]	4.42	4.5
Palladium mass m_{Pd} per plate [mg]	22	49
Catalyst layer volume $V_{cata}[cm^3]$	0.72	1.46
Catalyst layer thickness δ_{cata} [μm]	40	80

centre, the liquid film thickness reached its maximum value leading to a lower H_2 concentration at the catalyst surface. In addition, the mass transfer fully developed regime is reached at 5mm from the channel's inlet, thus the concentration profile is the same at different plane cuts of the channel as shown in figure 4.5.

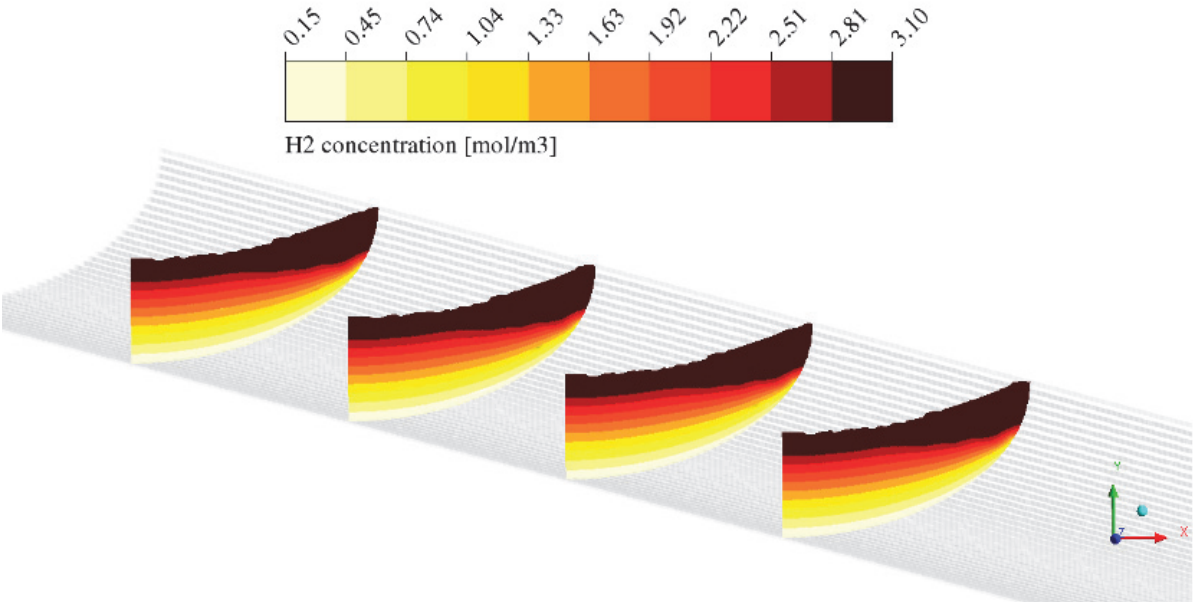

Figure 4.5 concentration profiles in the liquid film for the hydrogenation of α-methylstyrene to cumene in a 600x200μm² at $Q_L = 7ml/min$, T=283K and P=5bar. The outlet plane is located at z=0mm, the concentration profiles are shown from left to right at z=5mm, z=10mm, z=15mm and z=20mm.

Experimental liquid volumes were estimated using a developed correlation in [Tourvieille et al., 2013], which can explain the 20% difference between numerical and experimental liquid volumes reported in table 4.4.

Table 4.4 Summary of experimental and numerical values at P=5bar for the α-methylstyrene hydrogenation to cumene in a 600x200μm² channel

	Liquid flow rate Q_L [ml/min]	H_2 surface concentration $[mol/m^3]$	Liquid volume in the reactor $[m^3]$	H_2 consumption flux [mol/s]	α-methylstyrene conversion X_{AMS} [%]	$K_{ov}a_{GL}$ $[s^{-1}]$
Experimental values	3	4.30	$5.60\ 10^{-7}$	$3.46\ 10^{-5}$	70%	5.10
	5	4.80	$6.80\ 10^{-7}$	$3.79\ 10^{-5}$	47%	4.80
	7	4.30	$7.80\ 10^{-7}$	$3.40\ 10^{-5}$	30%	3.60
Numerical values	3	4.97	$8.24\ 10^{-7}$	$4.06\ 10^{-5}$	81%	4.31
	5	4.55	$9.70\ 10^{-7}$	$3.71\ 10^{-5}$	45%	3.23
	7	4.11	$1.08\ 10^{-7}$	$3.37\ 10^{-5}$	29%	2.54

As one can see from table 4.4, the experimental and CFD predicted H_2 consumption fluxes are in the same orders of magnitude and follow the same evolution with liquid flow rate. The relative deviation between CFD and experimental results are 17%, 2% and 0.8% at liquid flow rates of 3ml/min, 5ml/min and 7ml/min respectively. The same findings apply on the α-methylstrene conversions. However, the overall mass transfer coefficients $K_{ov}a_{GL}$ show significant deviations between experimental values and numerical values, this is mainly due to experimental liquid volumes estimations. According to Tourvieille et al. [2013], evaporation was noticed at low pressure in the experiment and a significant liquid volume was found at the gas outlet. Thus, the effective liquid volume inside the reactor in reaction conditions was lower than the one predicted through the correlation and the overall mass transfer coefficients were overestimated. However, evaporation was negligible at 5 bar, which means that data measured at 5 bar are the most reliable ones, especially concerning the H_2 consumption flux [Tourvieille et al., 2013].

The deviation in $K_{ov}a_{GL}$ even for the best experiment remains large because of an important difference in the liquid volume determination as already mentioned. For the experimental results, it is approached through a correlation and for this work it is precisely simulated using

the hydrodynamic model. That's why in the following, comparisons with experimental data will be carried out on the H_2 consumption flux (which is equivalent to a comparison in $K_{ov}a_{GL}V_{liq}$).

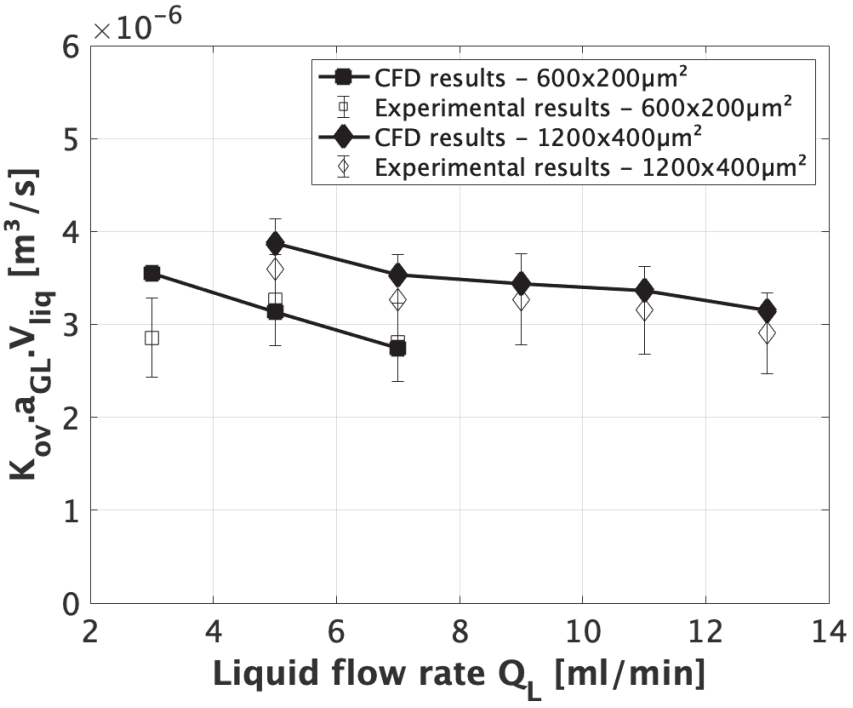

Figure 4.6 Comparison between experimental data and numerical results $K_{ov}a_{GL}V_{liq}$ at T=283K and P=5bar. For the 600x200μm² channel, the liquid flow rate varies from 3ml/min to 7ml/min and experimental results are drawn from Tourvieille et al. [2013].For the 1200x400μm² channel, the liquid flow rate varies from 5ml/min to 13ml/min and experimental data are drawn from Tourvieille [2014]. Error bars represent ±20%

Figure 4.6 compares experimental and numerical $K_{ov}a_{GL}V_{liq}$, as well as the evolution with liquid flow rate for the two plates with different channel geometries. The quantity $K_{ov}a_{GL}V_{liq}$ is equivalent to H_2 consumption flux normalised by the concentration difference between $C^*_{H_2}$ and the surface concentration $\overline{C_{S,H_2}}$. The computed $K_{ov}a_{GL}V_{liq}$ are very close to the experimental values except at the minimum liquid flow rate where a more significant deviation is present, this might be explained by a higher variability in the experiment. As one can see, the other numerical values are within 10% around the experimental ones, this allows us to conclude that CFD was able to capture and predict the effect of channel dimension on this coupled situation involving hydrodynamics, mass transfer and heterogeneous reaction. One interesting fact, both numerical and experimental mass transfer coefficients reach higher values with bigger channels which is counter-intuitive in micro-structuration. Indeed, micro-structuration is needed to obtain a curved and thinned liquid interface in comparison to unstructured conventional falling

films. However, because of the presence of the free interface, too much structuration can be detrimental in this case, leading to thicker films with the smaller channels at the same mean flow velocity or flow rate. This holds true as long as the three-phase contact lines remain stable and at the edges of the channels.

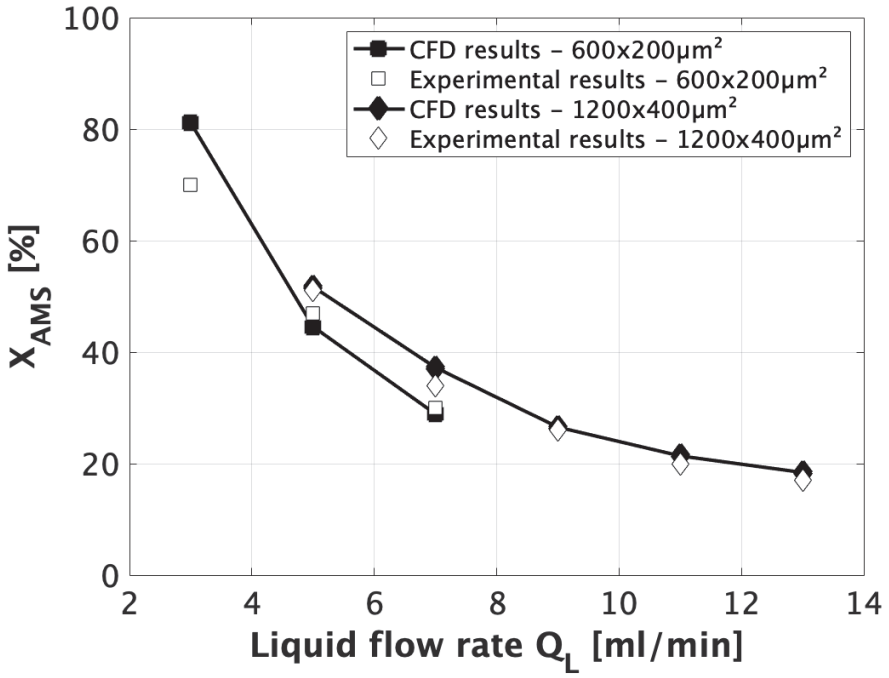

Figure 4.7 α-methylstyrene conversion comparison at P=5bar and T=283K, the initial α-methylstyrene is 1 mol/m^3. For the 600x200μm² channel, the liquid flow rate varies from 3ml/min to 7ml/min and experimental results are drawn from Tourvieille et al. [2013]. For the 1200x400μm² channel, the liquid flow rate varies from 5ml/min to 13ml/min and experimental data are drawn from Tourvieille [2014].

Figure 4.7 shows a comparison between experimental and predicted values for α-methylstyrene conversion at P=5bar. As one can see, numerical predictions are in good agreement with experimental values thus validating the developed CFD model, the liquid flow rate effect on conversion is also well represented.

The resistances-in-series model has been tested on this case study as well. The results are summarised in table 4.5. They show on average 32% deviation between the computed overall mass transfer coefficients, $K_{ov}a_{GL}$, and the resistances-in-series model, $K_R a_{GL}$. These results show that the resistances-in-series model is not adapted to describe the overall mass transfer coefficient, the liquid film thicknesses obtained in FFMRs are low, leading to the absence of a bulk concentration within the liquid film.

Table 4.5 comparison of GLS mass transfer coefficients $K_{ov}.a_{GL}$ to the ones obtained by the resistances-in-series model $K_R a_{GL}$ in isothermal conditions (T=283K), for pressure conditions from 1bar to 5bar, and liquid flow rate conditions from 3ml/min to 7ml/min.

Pressure [bar]	$C^*_{H_2}[mol/m^3]$	Liquid flow rate Q_L [ml/min]	$K_{ov}a_{GL}$ $[s^{-1}]$	$K_R a_{GL}$ $[s^{-1}]$	Relative error [%]
1	3.1	3	1.78	1.19	33%
		5	1.23	0.86	31%
		7	0.98	0.77	21%
3	9.4	3	1.77	1.19	33%
		5	1.22	0.85	30%
		7	0.97	0.74	24%
5	16.4	3	1.75	1.19	32%
		5	1.21	0.85	29%
		7	0.96	0.74	24%

Similarly to the semi-infinite planar case, the applicability of the film model was tested. An interesting difference lies in the definition of the correct characteristic length because of the encountered variable thickness in the cross section of it. Thus, different liquid film thicknesses were used to define the film model mass transfer coefficient, namely the liquid thickness at the centre of the channel δ_c, the arithmetic mean thickness δ_A, the geometric liquid thickness δ_{geo} defined as the ratio of the liquid volume to the wetted surface, and finally the harmonic mean thickness δ_H.

The film model underestimates the mass transfer coefficient using δ_c, δ_A and δ_{geo}, and strongly overestimates it using δ_H; the lowest mean relative deviation reported in table 4.6 for $K_{ov,FM}$ corresponds to the arithmetic mean liquid film thickness δ_A, the mean relative deviation is above 30% for the remaining liquid film thickness definitions. These differences are caused by the liquid film morphology, where the film thickness is very low near the three-phase contact line and reaches a maximum at the centre of the channel, causing important local differences in H_2 consumption at these locations. Nonetheless, to re-conciliate the sophisticated CFD simulations with the simple film model, a correction factor A can be introduced to the film model to predict well the mass transfer:

Table 4.6 Film model optimisation data in a 600x200μm² channel for liquid flow rates between 3ml/min and 7ml/min, pressure conditions between 1bar and 5bar, at fixed operating temperature (T=283K)

		δ_c	δ_A	δ_{geo}	δ_H
Film model: $K_{ov,FM} = D_{m,H_2}/\delta$	Mean relative deviation [%]	32.99%	10.64%	30.24%	113.71%
Modified film model:	Correction factor A [-]	1.479	1.112	1.405	0.469
$K^*_{ov,FM} = A \cdot D_{m,H_2}/\delta$	Mean relative deviation [%]	1.85%	1.48%	3.72%	6.66%

$$K^*_{ov,FM} = A\frac{D_{m,H_2}}{\delta} \tag{4.1}$$

The results are presented also in table 4.6 and the best fit was obtained using δ_A. However, δ_{geo} is considered to be the most interesting thickness value, for its easier acquisition both experimentally and numerically.

4.3 3D simulation of a reactive falling film on a string of spherical catalyst particles

4.3.1 Numerical domain and meshing

The previously studied cases consisted of falling films over a regular plane or micro-channel. In order to highlight the effect of the solid catalyst shape and to go towards more complex geometries encountered in fixed beds, simulations of reactive two-phase flow over stacked 1mm diameter spheres were carried out. The purpose of this case study is to investigate the effect of liquid film thickness distribution within the domain on GLS mass transfer involving a heterogeneous catalytic reaction, and to check the validity of resistances-in-series and film models on a such complex configuration. Contrary to the two previous cases, here the chosen geometry is likely to induce convection in other directions than the main flow direction and its impact on overall external transport from the gas phase to the solid catalyst surface will be investigated.

The three dimensional numerical domain consists of 1mm diameter spheres stacked inside a cylinder. In order to ensure developed flow conditions, 12 spheres are required in the

investigated flow rate conditions. Mesh generation is performed within SnappyHexMesh, which provides switches to control the three main meshing steps: (i) castellation, (ii) snapping and (iii) layer addition. In a majority of CFD simulations, castellation and snapping are sufficient to provide a good numerical mesh. However, when near-wall boundary layers require high resolution, wall-fitting mesh layers need to be inserted. For these reasons, two meshes with and without layers are employed in order to determine the suitable one.

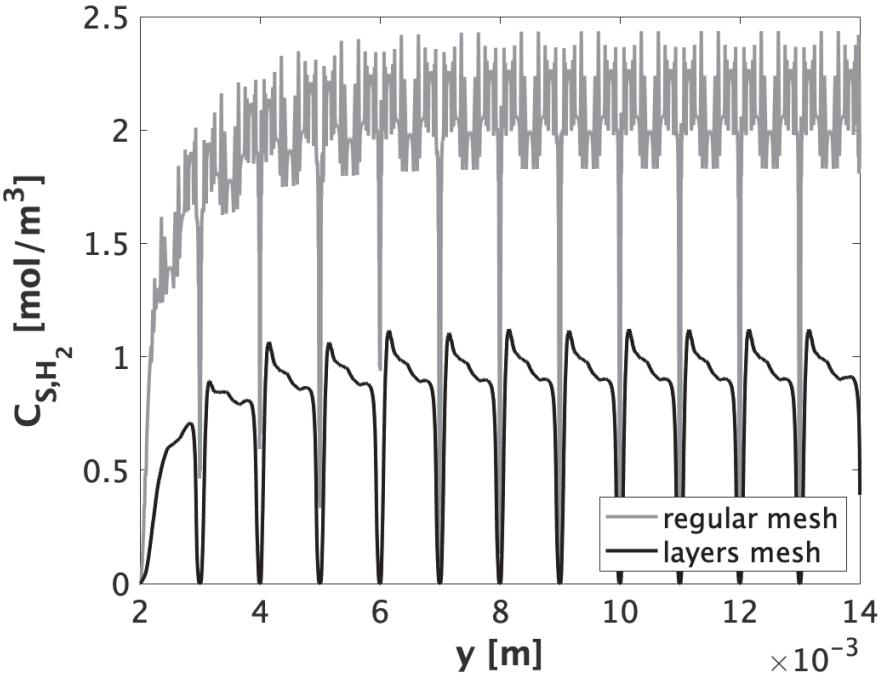

Figure 4.8 Local hydrogen surface concentrations in z=0 at $Re_G = 25$ and $Re_L = 30$ for a regular mesh and wall-fitting layers mesh. The two-phase flow is solved in isothermal and isobaric conditions (T=283K and P=1bar)

Preliminary simulations are conducted for $Re_L = 30$ and $Re_G = 25$, coupling hydrodynamics with mass transfer and heterogeneous catalytic reaction. Figure 4.8 reports concentration profiles at the spheres' surface for both meshes. It is important to note that absence of layers results in noisy surface concentration profiles (figure 4.8), and reach nonphysical negative concentration values. This is mainly due to the presence of poor cells near the spheres surface, resulting from the snapping step of SnappyHexMesh, as shown in figure 4.9-a. In contrast, wall-fitting mesh layers provide physical and smoother surface concentration profiles (figure 4.8), since layer coverage achieved 99% of the spheres' surface.

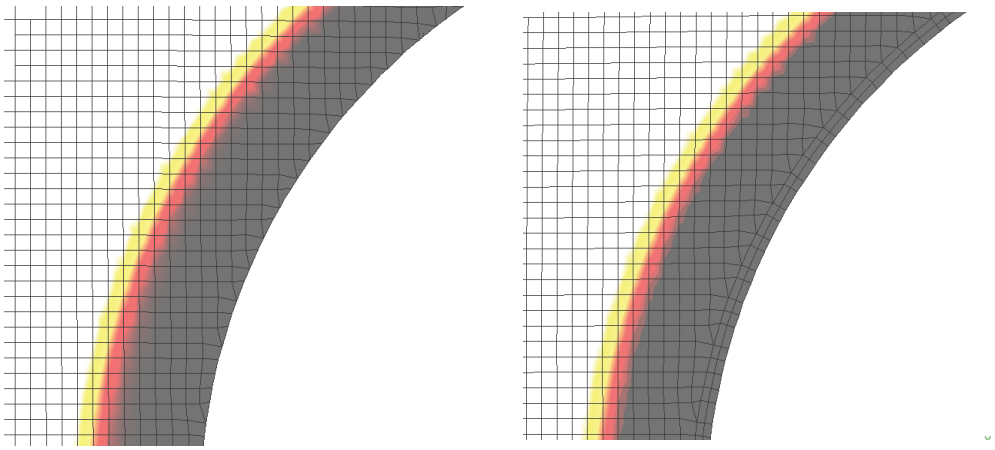

(a) (b)

Figure 4.9 Near-wall topology in the (a) mesh without layers and (b) mesh with layer. The liquid film is indicated by the dark colour

It should be noted that this issue was not encountered previously, since near-wall cells were fitting the catalyst's surface. Following this investigation, the mesh employed hereinafter contains two spheres-fitting layers.

4.3.2 Numerical set-up and boundary conditions

Hydrodynamic and mass transfer predictions are achieved considering boundary conditions shown in figure 4.10. To simulate gas-liquid downward co-current flow, gas an liquid are injected separately at the top of the domain. Liquid inlet velocity is specified at the point-source injection, while gas inlet velocity is specified at the remaining inlet surface. A no-slip boundary condition and static contact angle value describe the near-spheres flow. Finally, a regular pressure outlet condition is specified at the domain's exit.

Regarding mass transfer, hydrogen concentration is specified at the liquid and gas inlets respectively to 0 and $C^*_{H_2}$. Within the gas phase, solute concentration is homogeneous and fixed to $C^*_{H_2}$. The reactive flux is applied at the spheres' surface to include the catalytic reaction. Finally, zero concentration flux is specified at the remaining boundaries.

4.3.3 Hydrodynamic predictions

For the first hydrodynamic investigation, the gas and liquid inlet Reynolds numbers are 25 and 30 respectively, and the flow takes place in isothermal (T=283K) and isobaric conditions.

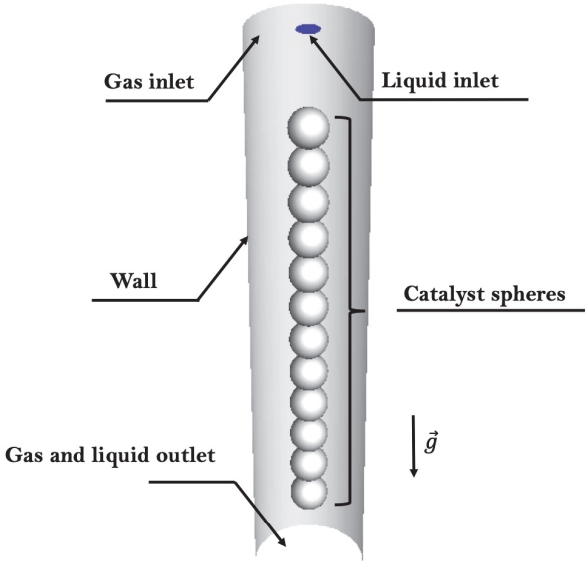

Figure 4.10 Boundary conditions employed to predict hydrodynamic and mass transfer performances

The liquid forms a continuous film over the catalyst particle string at steady state as shown in figure 4.11-a, the thickness varies throughout the domain. As one can see from figure 4.12-a, the liquid film is thinner at the equatorial plane of each particle and accumulates at the contact region between spheres. Similarly, as shown in figure 4.11-b and figure 4.12-b, the interface velocity reaches its maximum value where the liquid film is thin and vice-versa, due to mass conservation inside the computational domain. The total number of spheres was chosen in order to ensure the fully developed regime is reached.

4.3.4 Mass transfer analysis

The convection diffusion equation of concentration (equation (2.34)) was solved at different pressure conditions, that is to say at different thermodynamic equilibrium concentrations $C^*_{H_2}$. In order to investigate the effect of particle shape on mass transfer, purely diffusive conditions are also considered. The pure diffusion is an artificial calculation since the convective term is artificially considered equal to zero in the concentration transport equation, but the liquid film thickness profile remains the same as for convection-diffusion conditions.
As one can see from figure 4.13, when convection is neglected in transport analysis, the diffusion boundary layer is equivalent to the whole liquid film thickness (figure 4.13-a). Whereas when

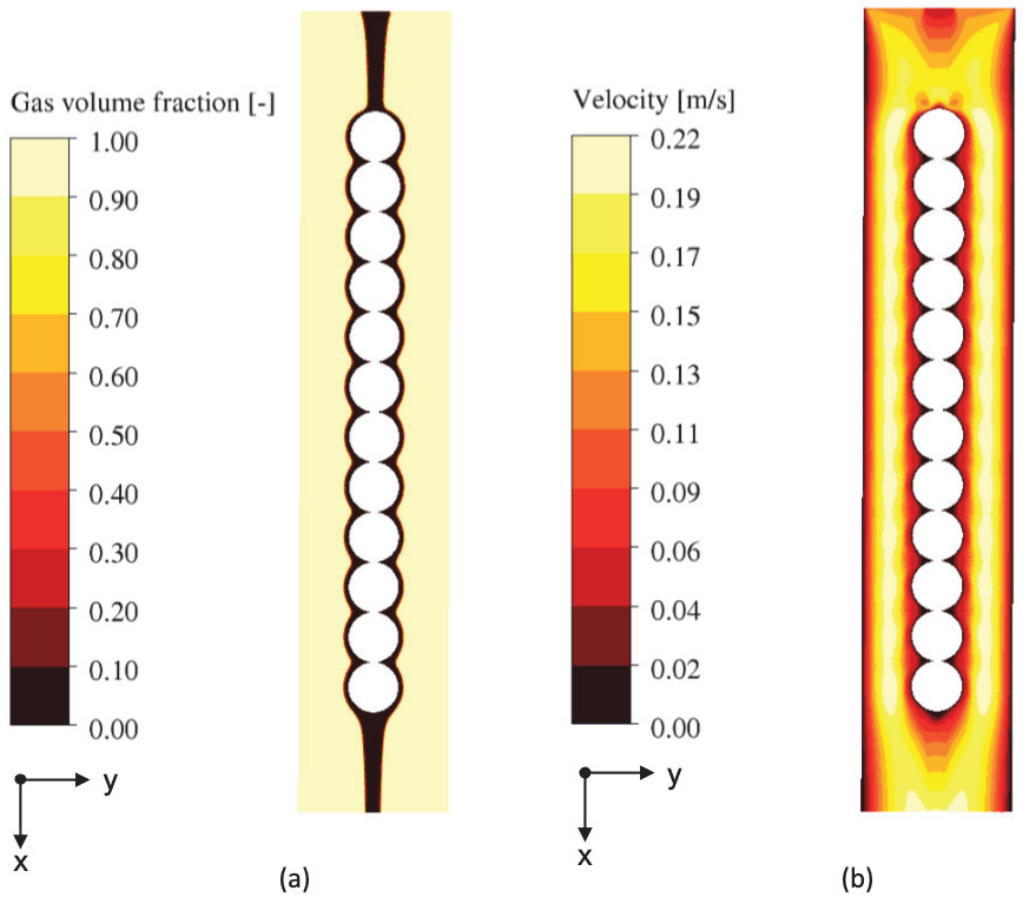

Figure 4.11 (a) Liquid volume fraction distribution in z=0 plane cut for $Re_G = 25$ and $Re_L = 30$ (b) velocity magnitude profile in z=0 plane cut for $Re_G = 25$ and $Re_L = 30$. The two-phase flow is solved in isothermal and isobaric conditions (T=283K and P=1bar)

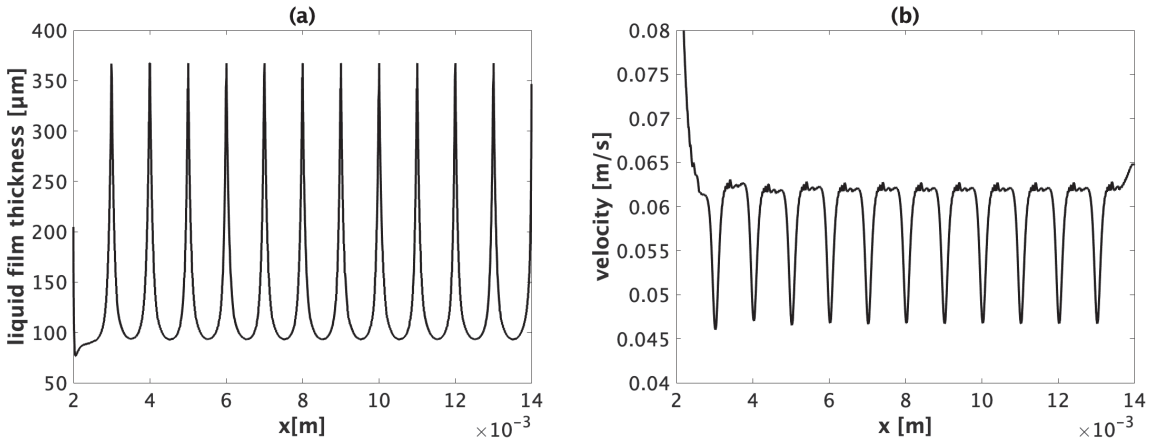

Figure 4.12 (a) Liquid film thickness variation and (b) gas-liquid interface velocity variation throughout the domain at $Re_G = 25$ and $Re_L = 30$ in isothermal and isobaric conditions (T=283K and P=1bar)

the convection effects are taken into account, the diffusion boundary layer is closer to the particles (figure 4.13-b), the liquid film is loaded with hydrogen since the concentration is maximum in a large proportion of the liquid film, the concentration then decreases near the surface of the spheres where it is consumed by the heterogeneous catalytic reaction.

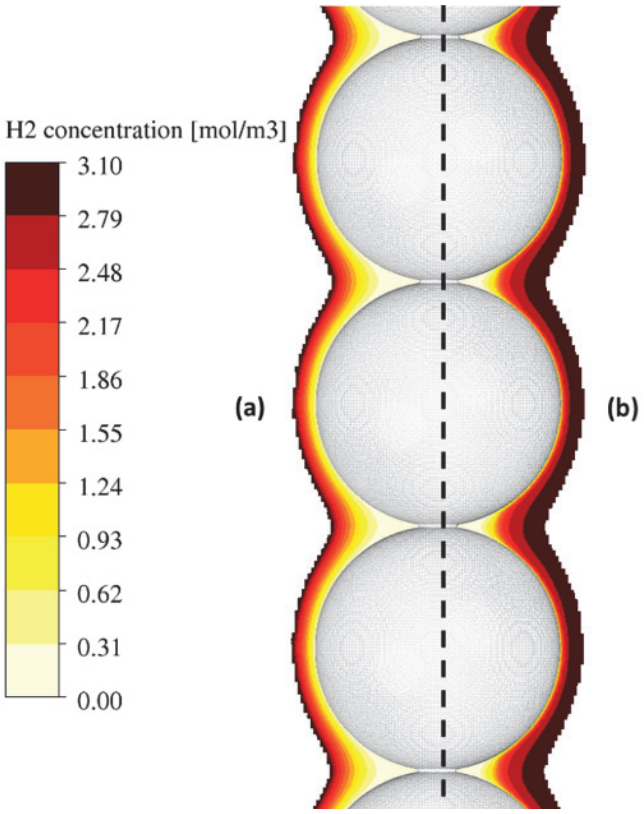

Figure 4.13 Hydrogen concentration profiles at P=1bar, T=283K, $Re_G = 25$ and $Re_L = 30$ for (a) pure diffusion (b) convection-diffusion

In order to bring out the effect of convection, figure 4.14-a compares the concentration profiles in the liquid film at the great circle of a particle. As one can notice, the concentration profile is linear when convection is neglected. In contrast, the convection boosts the solute transfer since the concentration is nearly constant far from the spheres, and the diffusion is predominant near the spheres as the concentration profile becomes linear.

Figure 4.14-b shows a comparison between the hydrogen consumption flux with and without convection. The flux is significantly increased by convection in comparison to pure diffusion, it is on average 6 times higher. This result is substantially different from the two previous study cases for the radial velocity profile contributes to radial transport enhancement in this case. In addition, one can also notice that the flux profile shape is smooth for pure diffusion and reaches peaks at the great circle of particles. In contrast, when convection is considered, the flux profile

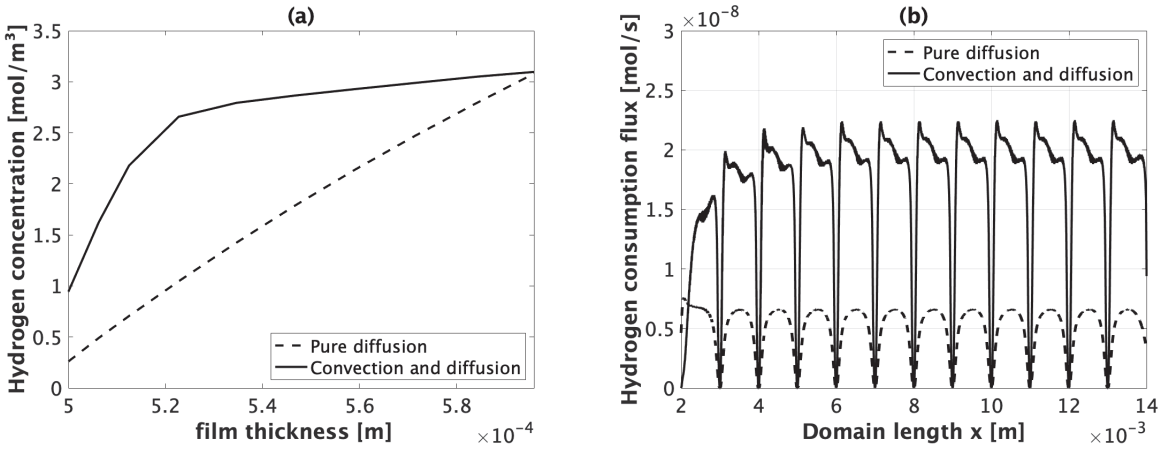

Figure 4.14 (a) Concentration profile comparison at the equatorial plane of the 10^{th} sphere between pure diffusion conditions and convective-diffusive conditions at P=1bar, T=283K, $Re_G = 25$ and $Re_L = 30$ and (b) axial evolution of hydrogen consumption flux for pure diffusion and convection-diffusion regimes at P=1bar, T=283K, $Re_G = 25$ and $Re_L = 30$

shape is asymmetric and reaches a peak at the top of each particle, following the shape of the radial velocity as shown in figure 4.15.

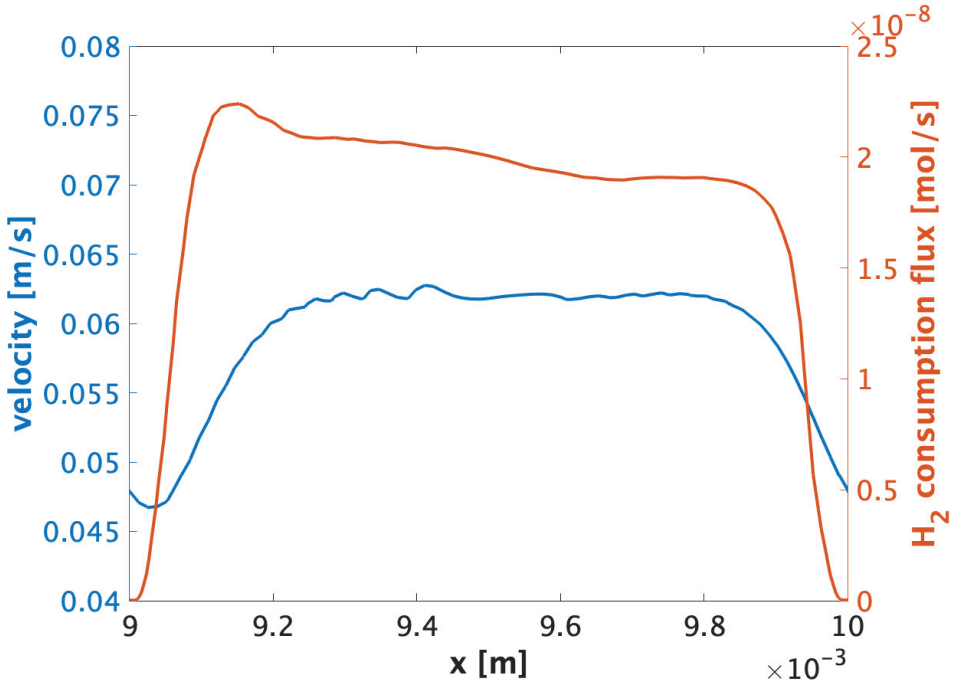

Figure 4.15 Axial evolution of gas-liquid interface velocity magnitude and hydrogen consumption flux variation throughout one pellet in convection-diffusion regime at P=1bar, T=283K, $Re_G = 25$ and $Re_L = 30$

The same evolution is noticed for the distribution of the solute surface concentration on the spheres surface. Figure 4.16 shows the difference in surface concentration of the solute with and without convection on the 10^{th} sphere. For pure diffusion, the surface concentration is symmetric, whereas the radial velocity boosts the concentration at the first hemisphere of the particles when convective transport is considered.

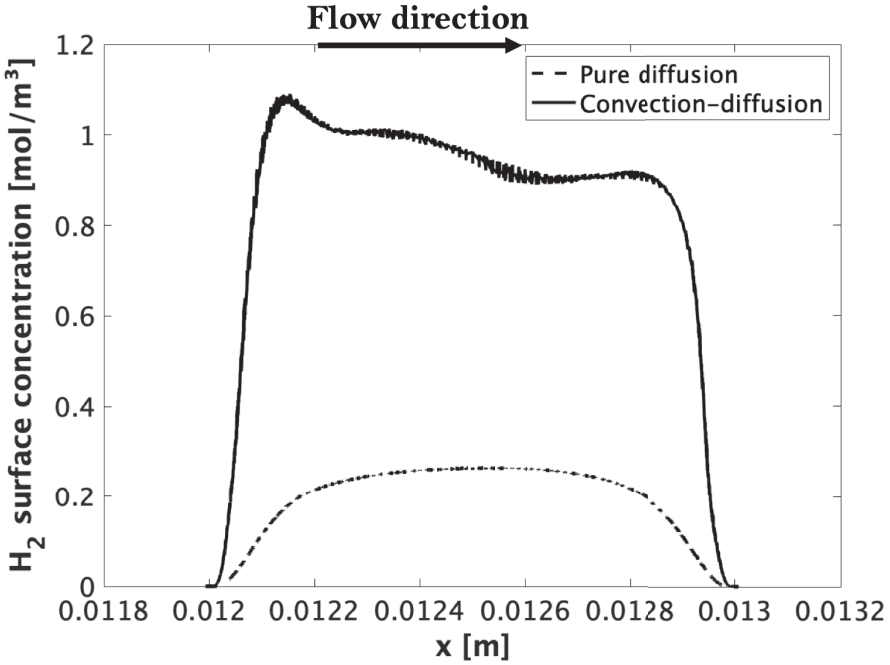

Figure 4.16 Hydrogen surface concentration comparison at the 10^{th} sphere for P=1bar, T=283K, $Re_G = 25$ and $Re_L = 30$ for pure diffusion and convection-diffusion conditions

The local overall external mass transfer K_{ov} obtained for convection-diffusion is represented in figure 4.17. K_{ov} is calculated at each mesh cell of the gas-liquid interface, and defined as the ratio of the local hydrogen consumption flux and the local concentration difference $(C^*_{H_2} - \overline{C_{S,H_2}})$ .K_{ov} follows the same trend as the surface hydrogen consumption flux and surface concentration, figure 4.17 reports only the data at P=1bar because the K_{ov} profiles are exactly the same for P=3bar and P=5bar. After going through the flow stabilisation zone at the inlet, for the 2-4 first spheres, the mass transfer coefficient profile becomes similar from one sphere to another and is maximised at the first hemisphere of each particle, with the liquid acceleration, then decreases at the second hemisphere with the liquid deceleration.

The average external overall mass transfer coefficients are obtained by integrating the local overall external mass transfer coefficient presented in figure 4.17 throughout one sphere in the fully developed mass transfer regime, that is to say on the 10^{th} sphere for instance. As done

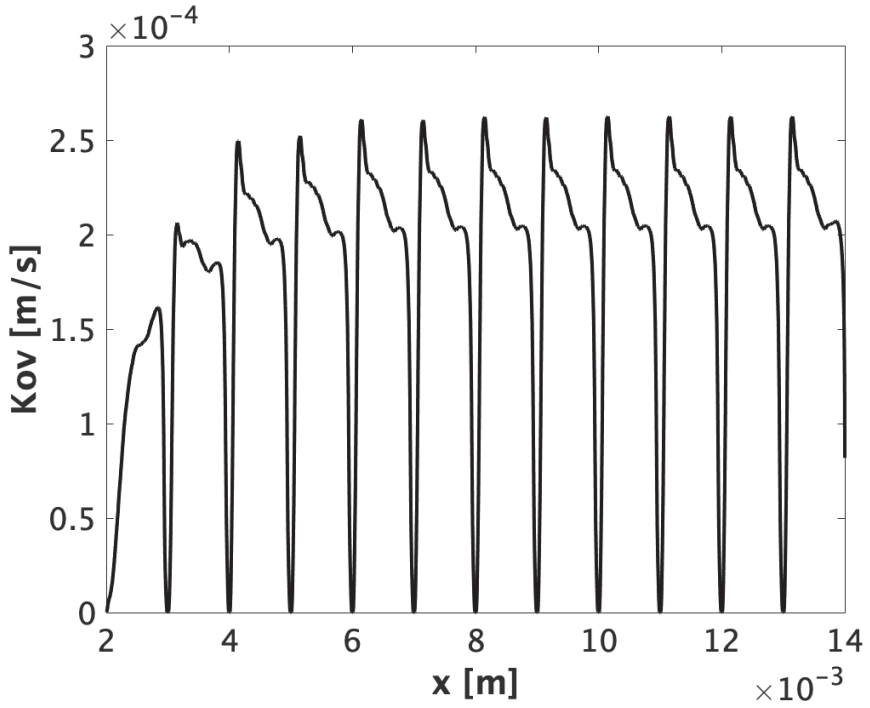

Figure 4.17 Overall mass transfer coefficient axial variation throughout the domain in convection-diffusion regime for P=1bar, T=283K, $Re_G = 25$ and $Re_L = 30$

previously, the apparent diffusion layer thickness is obtained from the average K_{ov} using the film model. The apparent diffusion layer thicknesses reported in table 4.7. The results show that the radial convection enhances mass transfer. The apparent diffusion layer thickness is low when convection is accounted for, this means that diffusion takes place in a small liquid film thickness near the surface, which was explicitly noticed in figure 4.14-a.

Table 4.7 comparison of GLS mass transfer coefficients $K_{ov}.a_{GL}$ to the ones obtained by the resistances-in-series model $K_R a_{GL}$ in isothermal conditions (T=283K), for pressure conditions from 1bar to 5bar, at $Re_G = 25$ and $Re_L = 30$.

Pressure [bar]	$C^*_{H_2}$ [mol/m^3]	$K_{ov}a_{GL}$ $[s^{-1}]$	$K_R a_{GL}$ $[s^{-1}]$	Relative error [%]
1	3.1	2.60	1.90	36%
3	9.4	2.60	1.89	37%
5	16.4	2.60	1.89	37%

As shown in table 4.7, The mass transfer coefficients determined by resistances-in-series model are on average 37% higher than the obtained overall mass transfer coefficient, once

again because the gas-liquid and liquid-solid mass transfer layers overlap, since there is no bulk concentration in the liquid film.

Concerning the film model, neither the geometric thickness nor the average thickness gives good results, as the apparent diffusion layer thickness δ_{app} is very small compared to the liquid hydrodynamic thickness. Further investigation of the convection effect on mass transfer has been made, considering several liquid Reynolds number conditions to investigate the liquid velocity and viscosity effects, the diffusion coefficient remains fixed at $4.88.10^{-9}$m²/s. As one can see from figure 4.18-a, the geometric thickness increases with Reynolds number as well as viscosity.

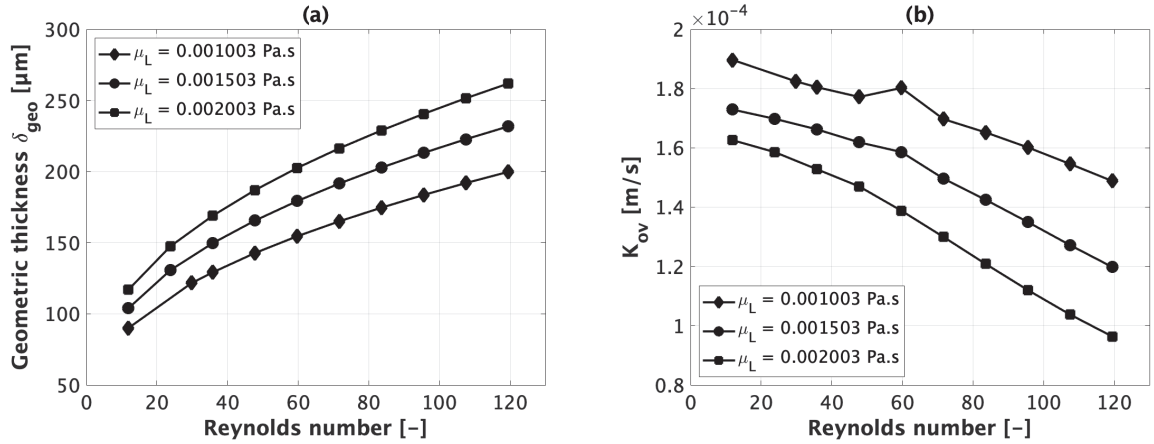

Figure 4.18 (a) Geometric liquid film thickness variation with Reynolds number and liquid viscosity and (b) overall mass transfer coefficient variation with Reynolds number and liquid viscosity in convection-diffusion regime for H_2/mehylcyclohexane and α-methylstyrene mixture two-phase flow, for different inlet liquid Reynolds number conditions ($10 < Re_L < 120$) and fixed inlet gas Reynolds number $Re_G = 25$, at P=1bar and T=283K.

The overall mass transfer coefficient is represented in figure 4.18-b since the liquid film thickness increases with the Reynolds number, the mean mass transfer layer becomes thicker and the mass transfer coefficient decreases. However, convection enhances mass transfer since the convective mass transfer coefficient remains higher than the purely diffusive mass transfer coefficient.

In order to gather all these data in a single correlation, a gas-liquid-solid Sherwood number Sh_{GLS} corresponding to the overall external mass transfer has been estimated. Figure 4.19 shows that this Sherwood number increases with the Reynolds number, and seems to reach an asymptotic value of 6 in the investigated conditions since the flow regime is laminar. When the convection is neglected, the mass transfer coefficient was equal to D/δ_{geo}, leading to a

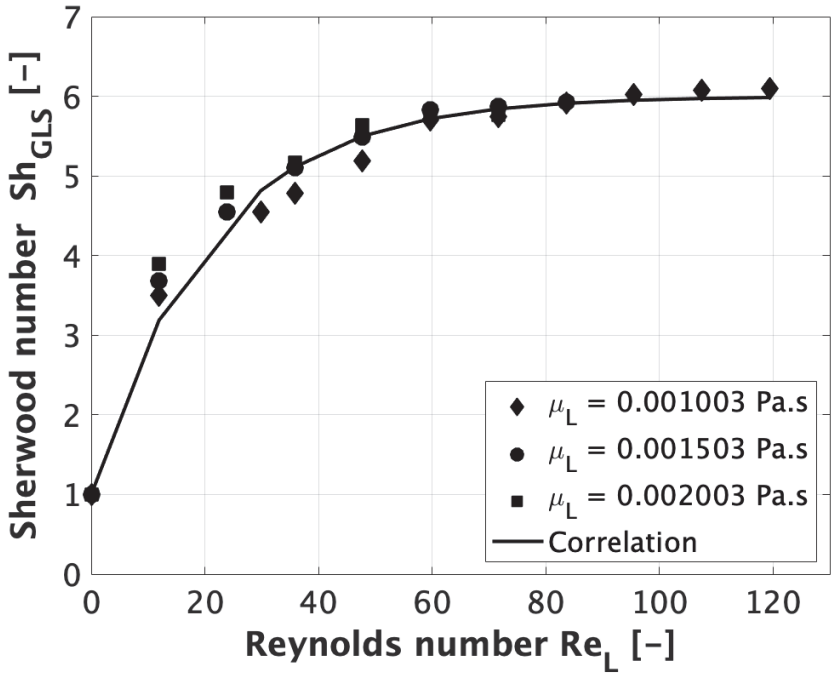

Figure 4.19 Gas-liquid-solid Sherwood number Sh_{GLS} variation with Reynolds number and liquid viscosity for inlet liquid Reynolds numbers between 0 and 120, inlet gas Reynolds number of $Re_G = 25$, at P=1bar and T=283K.

Sherwood number equal to 1. Thus, a tentative correlation has been derived for this overall Sherwood number, taking the following form:

$$Sh_{GLS} = Sh_{asymptotic} - (Sh_{asymptotic} - Sh_{diff}).exp(-A.Re_L) \tag{4.2}$$

Where Sh_{diff} is the Sherwood number for pure diffusion and $Sh_{asymptotic}$ is the asymptotic value of the Sherwood number equal to 6 in this case. The constant A was fitted on the obtained numerical data, and the tentative correlation is given by:

$$Sh_{GLS} = 6 - 5.exp(-0.048.Re_L) \tag{4.3}$$

As one can see from figure 4.19, Sherwood numbers estimated by the correlation presented in equation (4.3) and by CFD are close, the maximum relative error is 11% and the average relative error is 4.74%.

In summary, This case illustrates the effect of a more complex geometry corresponding to pellet string reactor on hydrodynamic and mass transfer performances. It is found that the convection enhances drastically the mass transfer rate, in contrast with the two previous study

cases where diffusion was the exclusive radial transport phenomenon. However, since the string of few particles are stacked in a perfectly aligned pattern, the two-phase flow behaviour is different from the one encountered in trickle-bed reactors, where the catalyst particles are stacked randomly and are more packed, leading to more complex phase distributions inside the reactor. Nevertheless, this work shows that CFD simulation allows investigating realistic complex reactive systems such as trickle-bed reactors.

4.4 Conclusion

A numerical model has been developed in order to improve the understanding of reactive falling liquid films flow over different catalytic surfaces. This model coupled a robust hydrodynamic VOF description with a consistent gas-liquid-solid mass transfer and a surface heterogeneous catalytic reaction. Two case studies have been simulated, namely a 3D falling film micro-reactor and a 3D falling liquid film over a string of spherical particles.

First, the CFD modeling of two-phase flow in a three dimensional micro-channel reactor has been investigated. The simulation results were compared to experimental data of Tourvieille et al. [2013]. Subsequently, the predicted liquid film profiles were close to experimental results. In addition, the predicted gas-liquid interfacial areas were within ±15% in respect to experimental results. Therefore, the simulation results showed a very good agreement in both cases.

Regarding mass transfer, the overall external gas-liquid-solid mass transfer behaviour encountered under heterogeneous catalytic reaction conditions is significantly different in the two study cases. Indeed, a good agreement is obtained between experimental and simulated overall mass transfer coefficients in the 3D falling film micro-reactor (FFMR). It is found that the gas-liquid-solid mass transfer is predominantly diffusive, a correction factor “A” is proposed and introduced to the film model to account for the non-uniform liquid film thickness in the channel. For FFMR system, it is also found that the resistances-in-series model overestimates the overall mass transfer coefficient by 32% for similar aforementioned reasons as the 2D falling liquid film.

Finally, using the validated CFD model, mass transfer in trickling flow conditions over a string of 12 spherical catalyst particles with a heterogeneous catalytic reaction at the catalyst surface has been studied, using the validated CFD model. It is found that the gas-liquid-solid mass transfer regime is mainly dominated by the convection induced radially by this geometry. The convection enhances mass transfer, leading to thin mass transfer boundary layers. In

addition, it is found that the film model does not give representative results for this case, and a new Sherwood number correlation is developed to correct the model. This work shows also that the overall GLS external mass transfer coefficients estimated by the resistances-in-series model are on average overestimated by 37% again because of bulk concentration absence.

To conclude, this work shows that the mass transfer in two-phase laminar flows with reaction occurring at the solid surface are dependent on the solid geometry and behave differently regarding the overall external mass transfer. Not all the cases are equivalent to a simple falling liquid film, thus each case needs to be studied separately. In addition, this work proves that CFD can be a powerful tool, not only to predict complex flow patterns, but also to simulate physically relevant mass transfer processes coupled with heterogeneous reactions, as well as to improve the understanding of multi-physics phenomena in gas-liquid-solid fixed bed contactors. Nowadays, Thanks to the development of high performance calculations resources, this approach might be extended to fixed-bed reactors. However, the predictions would be limited to a few hundreds of particles instead of the entire reactor. Even though the simulated scales are far from the reactor scale, the presented numerical model can be applied to improve understanding of local mass transfer mechanisms.

Chapter 5

Experimental and numerical investigation of a 3D-printed milli-reactor

5.1 Introduction

This chapter investigates gas-liquid-solid mass transfer in a 3D-printed milli-reactor, the geometry consists of two reactive plates containing hemispherical particles, packed together in a staggered arrangement, in order to mimic catalytic fixed beds.

The purpose of this study is to improve understanding of gas-liquid-solid mass transfer in liquid flow throughout a bed of spherical catalyst particles, and to collect data from gas-liquid-solid mass transfer experiments in reactive conditions, in order to further validate CFD modelling on another set-up, closer to the final packed bed geometry. In the vein of gradually increasing complexity, the milli-reactor's geometry lies between the string of spherical particles and spherical loadings encountered in trickle-bed reactors. Further detailed in next sections, the adopted design complies with the following criteria: (i) turtuous flow path, (ii) small fluid domain for prompt simulations and (iii) long-enough fluid domain to reach developed flow conditions.

This chapter is divided in two main sections. First, an experimental characterisation of the milli-reactor is presented. Thus, qualitative hydrodynamic and quantitative mass transfer results are detailed. Next, the milli-reactor is simulated using the developed CFD model. Both hydrodynamic and mass transfer performances are compared to experimental results.

5.2 Experimental study

5.2.1 Reactor design

Experiments are conducted within a milli-reactor (figure 5.1) designed as an ideal geometry of trickle-bed reactors. The reactor consists of two reactive plates, containing each 52 hemispherical objects on the front and embedded cooling circuit at the back. The former are arranged in a staggered configuration, as shown in figure 5.2b, while the latter hosts cold water flow for temperature control purposes. These plates were manufactured through 3D-printing by Proto Labs and are made of stainless steel or WaterShed XC 11122. In order to separate gas and liquid inlets, bound fluid flow domain and prevent leaks, a customised silicon-sheet sealing-joint is positioned between both reactive plates. Once all the elements assembled, the reactor is sealed uniformly using a torque wrench to avoid leakage.

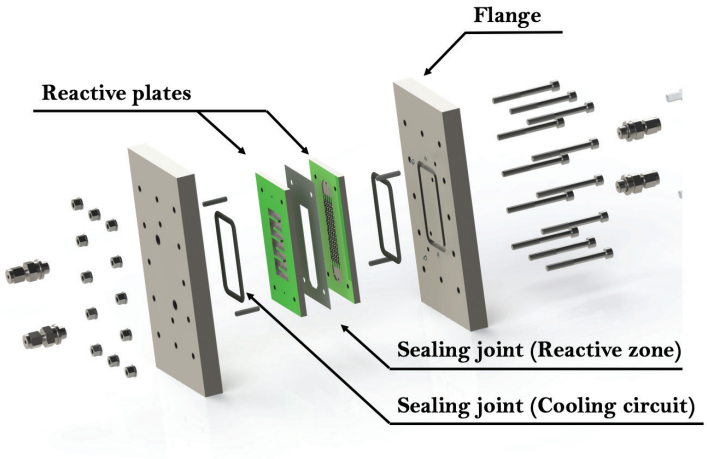

Figure 5.1 Exploded view of the reactor

Since the sealing-joint acts as separator for inlet zones, incoming gas and liquid first reach their respective chambers before being distributed through inlet channels, as shown in figure 5.2a. The same does not apply at the outlet, since gas and liquid exit simultaneously the reactor. The characteristics of the reactor are summarised in table 5.1. 3D-printing is used to manufacture all the reactive plates employed in this investigation (printed by ProtoLabs).
For two-phase flow visualisations, a full-size mock-up is 3D-printed using an ABS-like translucent material named WaterShed XC 11122. Whereas, a stainless steel 3D-printed milli-reactor is employed to conduct gas-liquid-solid mass transfer experiments.

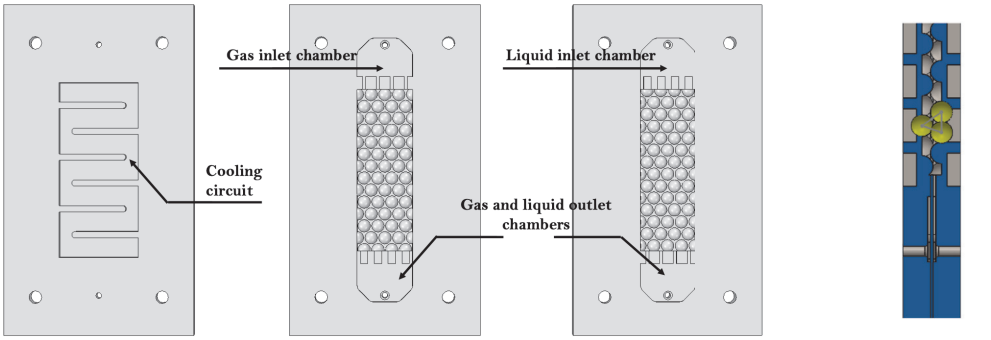

(a) (b)

Figure 5.2 (a) From left to right: cooling circuit at the back of reactive plates, gas-side reactive plate and liquid-side reactive plate. (b) Slice view of the reactive plates assembled in a staggered configuration

Table 5.1 Reactor characteristics

Specifications of the reactor design	
Reactor size (length x width x depth) [mm^3]	180 x 100 x 38
Porosity ε_B [%]	40.9
Sealing joint thickness [mm]	0.5
Characteristics of reactive plates	
Length [mm]	104
Width [mm]	60
Depth [mm]	5
Spheres' diameter [mm]	4
Pitch length [mm]	4.35
Number of hemispheres per plate	52
Inlet and outlet diameters [mm]	0.5
Chambers' specifications	
Height [mm]	0.5
Liquid inlet width [mm]	2
Gas inlet width [mm]	1
Gas and liquid inlets' height [mm]	0.5

5.2.2 Hydrodynamic visualisation study

When dealing with gas-liquid flow throughout a catalytic tortuous path, it is of high importance to assess flow regime as well as phase distribution. The objective of this cold experiment is to investigate qualitatively flow pattern and liquid flow distribution quality. Due to limited time devoted to experimental work, no residence time distribution (RTD) measurements were developed and conducted. Mass transfer reactive experiments were prioritised indeed. In the following, the mock-up employed for two-phase flow visualisation is described and image processing techniques are detailed.

Cold contactor features

Two-phase flow visualisation is conducted in a full-size WaterShed mock-up. This material (WaterShed XC 11122) is a photopolymer which provides colorless parts with good mechanical and chemical resistances. The experimental set-up is shown in figure 5.3b. First, a dual piston pump (P 4.1S/ P 2.1S, Knauer) covering a flow rate range of 0.001-10ml/min is employed to feed liquid. After reaching the inlet chamber, liquid is distributed through inlet channels, as discussed previously. The gas flow rate is controlled by a mass flow meter (EL-FLOW PRESTIGE FG-201CV, Bronkhorst). At the outlet, both phases exit simultaneously the mock-up and are directed to a waste collector.

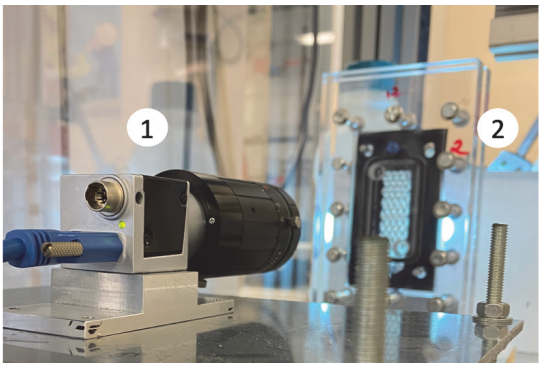

(a)

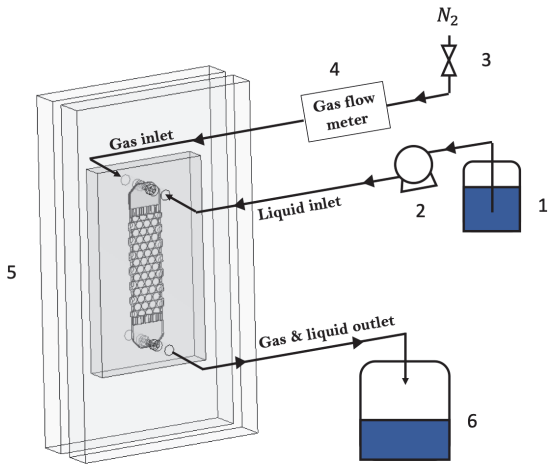

(b)

Figure 5.3 (a) Video and image acquisition set-up: (1) camera and (2) WaterShed mock-up. (b) Experimental set-up for two-phase flow visualisation: (1) liquid feed, (2) dual piston pump, (3) nitrogen feed valve, (4) gas flow meter, (5) WaterShed mock-up and (6) waste collector

Image acquisition and processing

In order to capture qualitatively two-phase flow pattern, the WaterShed mock-up was fixed to the test bench for optimum stability. Brilliant Cresyl Blue ALD (Sigma-Aldrich) was employed to dye liquid phases. As shown in table 5.2, two solvents exhibiting different surface tensions were used: (i) demineralised water and (ii) ethanol (VWR, $\geq$99.8%). Liquid feed mixture used in reactive experiments (methylcyclohexane+α-methylstyrene) could not be employed to visualise its flow because of (i) chemical compatibility issues with WaterShed and (ii) dye solubility.

Table 5.2 Physico-chemical properties of liquid solvents

Solvent	Viscosity μ_L $[mPa.s]$	Density ρ_L $[kg.m^{-3}]$	Surface tension σ_L $[mN.m^{-1}]$
Water	1	998	72.8
Ethanol	1.31	789	21.8

Image acquisition is performed using two cameras: (i) CR600x2 CamRecord high-speed monochrome camera and (ii) Basler ace U high-speed colour camera (figure 5.3a). The former is equipped with a large view objective, while the latter's objective enables a closer visualisation (Fujinon lens CF50ZA-1S) of the reactive zone.

The images acquired by CR600x2 CamRecord high-speed monochrome camera are processed in Adobe Photoshop. For each recorded video, an initial frame corresponding to the empty mock-up is selected. In order to delimit the liquid film, pixel division is used between the initial and following frames. For the sake of visualisation, the liquid film is afterwards coloured in blue.

Concerning images collected using Basler ace U high-speed colour camera, a MatLab code is used to highlight liquid flow within the WaterShed mock-up. In the RGB space, true colour images are three-dimensional matrices where blue (B), green (G) and red (R) components are separately stored. In this case, it is found that pixels describing liquid flow are stored in both the red and green matrices. Therefore, in order to isolate liquid flow, pixels for which the following criterion is satisfied are selected: $G+R \leq 0.5*B$. On the other hand, white colour is used for the remaining pixels.

Following liquid film identification, processed images are employed to estimate apparent wetting efficiency. To do so, white and coloured pixels are counted in the RGB matrix. Assuming that liquid/solid interface is defined by the coloured pixels, wetting efficiency is

defined as the ratio of coloured pixels to the total number of pixels. It is important to note that obtained results are semi-quantitative since post-processing is conducted on 2D images, while the flow takes place in a 3D complex geometry.

5.2.3 Gas-liquid-solid mass transfer experimental study

Catalyst preparation and deposition

Mass transfer is investigated in presence of the hydrogenation of α-methylstyrene to cumene. This reaction requires a solid catalyst, usually deposited on reactive surfaces by coating or impregnation. In order to prepare the catalyst suspension, water (25ml) is mixed gradually with nitric acid (65%, 3ml) to prevent exothermicity, then 23g of commercial catalyst (1% Pd/Al_2O_3, Johnson Matthey) are added gradually over a 15 minutes interval. Afterwards, the suspension is ground in a planetary mill (15 Agate 10mm grinding balls) at 500rpm during 50 minutes. Following this step, catalyst suspension is retrieved, 5ml of water are added to complete cleaning and grinding balls are sieved to minimise mass loss. Finally, catalyst suspension is then aged for three days before being used.

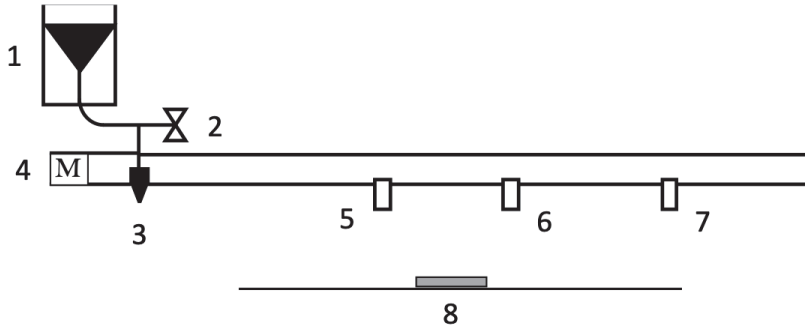

Figure 5.4 Catalyst coating set-up: (1) spray container, (2) valve, (3) nozzle, (4) motor, (5-6) sensors to start/stop spraying, (7) limit sensor and (8) the object to coat (reactive plate)

Prior to catalyst coating, an ultrasound cleaner is employed to degrease reactive plates in acetone for 30 minutes at ambient temperature conditions. Next, reactive plates are first dried (12h at 120°C) then heated under air atmosphere to 550°C (5°C/min ramp) to achieve a two hours plateau at 550°C.

For planar geometries, usual manual dip-coating techniques are sufficient to obtain a uniform layer. However, given the complex reactive plate's geometry, a spray method is used instead to ensure uniform distribution. The automated coating set-up used in the present work

is illustrated in figure 5.4. First, the reactive plates are placed at 15cm from the nozzle. Then, the catalyst suspension is loaded in the spray container while maintaining the valve closed. Since the suspension is viscous, a funnel is placed within the spray container to improve its flow. Once motion is initiated, the valve is opened and spray reservoir travels back and forth. The motor's speed and number of round trips are specified in the control panel.

For the sake of reproducibility, the same settings are used for both reactive plates. 3 round trips at maximum motor speed (5cm/s) were used to deposit a uniform catalyst layer. Subsequently, the coated plates are dried at 120°C for 3 hours, then calcined under air atmosphere (2 hours at 550°C). In order to activate the catalyst, in-situ reduction under hydrogen atmosphere is performed at 150°C for 3 hours.

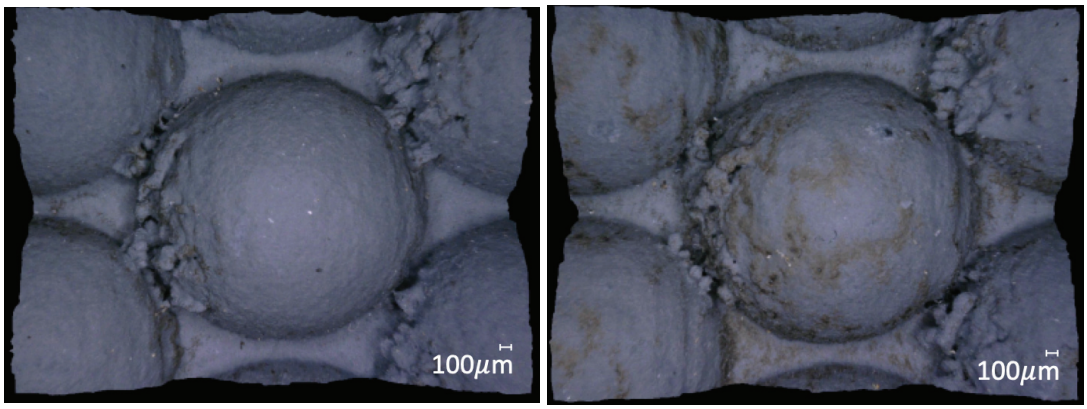

(a) (b)

Figure 5.5 Textural aspect of hemispherical plots in coated reactive plates

Catalyst distribution is observed in 3D using a digital microscope (VHX-6000, Keyence), as shown in figure 5.5. First, it is important to note that visible imperfections are observed after each hemisphere, resulting from the 3D printing resolution of reactive plates. Catalyst coating is found homogeneous over a significant fraction of the reactive plates (figure 5.5a). However, some locations exhibited lower coating thickness and heterogeneity as shown in figure 5.5b. This can be attributed to the reactive plate positioning during the spray coating step. Indeed, a slight deviation from the nozzle's path can cause uniformity issues in surface coverage and catalyst layer thickness.

The deposited catalyst mass m_{cata} is determined by a weighing method. The reactive plates are weighed before (m_1) and after (m_2) catalyst deposition, then catalyst mass is computed by substracting m_1 from m_2. Afterwards, given alumina density and catalyst's mass m_{cata}, it is possible to compute catalyst layer volume as the following:

$$\rho_{cata} = \frac{m_{cata}}{V_{cata}} \Rightarrow V_{cata} = \frac{m_{cata}}{\rho_{cata}} \tag{5.1}$$

Assuming that catalyst volume is given by $V_{cata} = A_{cata} \cdot \delta_{cata}$, an estimation of catalyst layer can be achieved as the following:

$$\delta_{cata} = \frac{m_{cata}}{\rho_{cata} \cdot A_{cata}} \tag{5.2}$$

A_{cata} is the coated surface of the reactive plate. The latter is accurately determined by a Computed Aided Design (CAD) Software using the reactive plate design. Therefore, an apparent average catalyst thickness of $40\mu m$ is achieved.

Experimental procedure

Gas-liquid-solid mass transfer experiments are carried out in a stainless-steel reactor, detailed characteristics are reported in table 5.1. The experimental set-up is presented in figure 5.6. Gas and liquid flow co-currently downward through the coated reactive plates, their respective flow rates are controlled by a mass flow meter (EL-FLOW PRESTIGE FG-201CV, Bronkhorst) and a dual piston pump (P 4.1S/ P 2.1S, Knauer). Reaction temperature within the reactor is controlled by a thermostatic bath. At the reactor's outlet, gas and liquid mixture is directed to the back-pressure regulator (Equilibar). Since high amplitude fluctuations were noticed in operating pressure, isopropanol dilution is included to comply with operating range of the back-pressure regulator. Gas, liquid and isopropanol mixture is then directed to the waste collector, except when samples are taken from the sampling valve. Mass transfer investigations are conducted in experimental conditions reported in table 5.3.

A solution of α-methylstyrene (99.9%, Acros Organics, $C^i_{AMS} = 0.2 mol/l$ or $C^i_{AMS} = 1.0 mol/l$) is prepared in methylcyclohexane (99%, Acros Organics). n-dodecane (99%, Alfa Aesar) is the internal standard used to determine product concentrations. Since hydrogenation of α-methylstyrene is sensitive to water traces, a 3Å molecular sieve is employed [Meille et al., 2002, Meille and de Bellefon, 2004]. The molecular sieve is first activated through overnight heating at 350°C before being added to the liquid mixture.

Hydrogenation of α-methylstyrene is highly exothermic. Therefore, temperature control is ensured through circulation of cooling water at the back of reactive plates. The temperature is controlled by a thermostatic bath, as shown in figure 5.6. For each gas/liquid flow rate

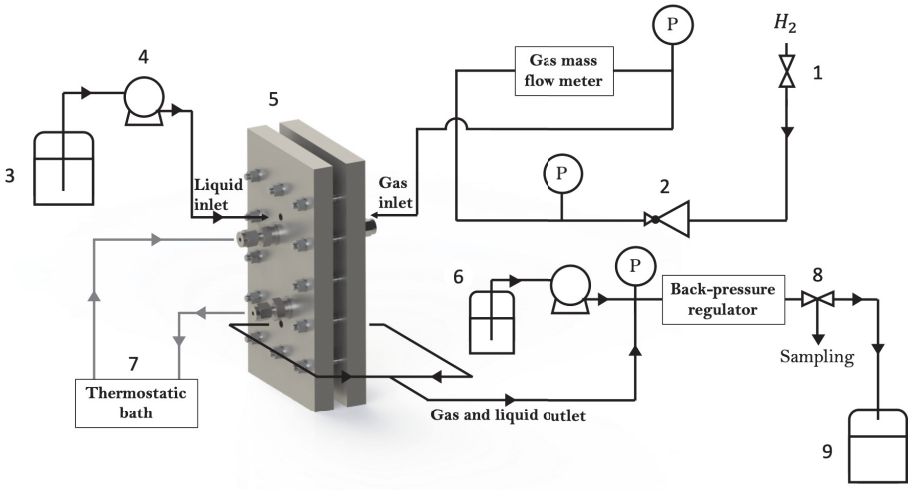

Figure 5.6 Mass transfer characterisation experimental set-up: (1) hydrogen inlet, (2) pressure regulator, (3) liquid reservoir, (4) dual piston pump, (5) stainless-steel reactor, (6) isopropanol reservoir, (7) thermostatic bath, (8) sampling valve and (9) waste collector

Table 5.3 Experimental conditions for gas-liquid-solid mass transfer characterisation

Operating conditions	
Liquid flow rate Q_L [ml/min]	0.1-10
Gas flow rate Q_G [Nml/min]	2-100
Pressure P [bar]	5
Temperature T [K]	278
Catalyst characteristics	
Total Pd/Al_2O_3 mass m_{cata} [mg]	108
Catalyst area A_{cata} [mm^2]	3117
Catalyst volume V_{cata} [cm^3]	0.127
Catalyst density ρ_{cata} [g/m^3]	692974
Estimated catalyst layer thickness δ_{cata} [μm]	40

condition, the reaction is carried on for 15 minutes until stabilisation. Afterwards, four samples are collected every 5 minutes to control conversion development.

An Agilent 6890 gas chromatography system (Agilent Technologies) equipped with an automated sampler and a Flame Ionization Detector (FID) was employed for calibration and sample analysis. The column consists of a DB-heavyWAX (10m x 0.1 mm, internal diameter 0.10 μm, Agilent Technologies). Regarding the method, optimal peak separation was obtained

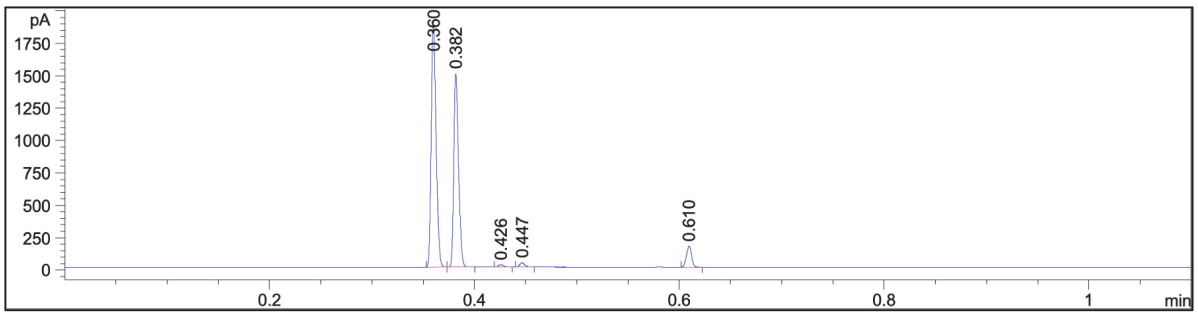

Figure 5.7 Typical gas chromatography signal of a diluted sample (C^i_{AMS}=0.2mol/l). Isopropanol at 0.36, methylcyclohexane at 0.382, α-methylstyrene at 0.426, cumene at 0.447 and n-dodecane at 0.610

using a slope of 100°C/min, with initial and final temperatures of 150°C and 200°C respectively and a flow rate of 0.4ml/min.

The aforementioned chromatography method provides peak separation in the following order: (i) isopropanol, (ii) methylcyclohexane, (iii) cumene, (iv) α-methylstyrene and (v) n-dodecane. The overall analysis duration was of 2 minutes, and the product (cumene) eluted at 0.42seconds. The developed method allows access to liquid mixture composition before and after reactive tests, making it therefore possible to establish reagent/product mass balance. Besides, eventual stripping or evaporation is possible to detect through peak area variations.

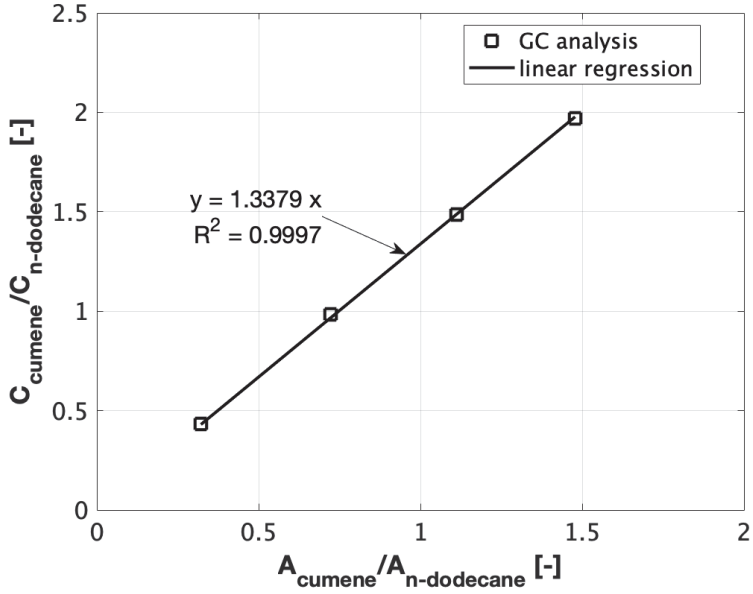

Figure 5.8 Gas chromatography calibration curve for cumene

In order to assess the method's linearity, samples containing different concentrations of cumene and α-methylstyrene were prepared and analysed. The peak areas (A_i) for each sample were plotted versus their corresponding cumene and α-methylstyrene concentrations, as shown in figure 5.8. The corresponding correlation coefficients are 1.34 and 1.33.
For each liquid feed mixture, n-dodecane concentration is specified as $C^i_{AMS}/2$. The reagent/product concentrations are then determined relative to the internal standard (n-dodecane), since its concentration remains constant at all times. Given the correlation coefficients k_i and peak area ratios, concentration of component i is computed by: $C_i = C_{n-dodecane} \cdot k_i \cdot A_i / A_{n-dodecane}$.

Theoretical background on catalytic hydrogenation of α-methylstyrene to cumene

Catalytic hydrogenation of α-methylstyrene to cumene is a very fast reaction, for which the reaction rate is likely to exhibit mass transfer limitations. In the investigated temperature and pressure conditions (T=283K and P=5bar), the reaction rate is zeroth order with respect to α-methylstyrene and 0.73 with respect to hydrogen. According to Meille et al. [2002], the reaction rate is given by the following expression:

$$a_C = k \cdot C^n_{H_2} \tag{5.3}$$

Where k is the reaction rate constant ($8.33 \cdot 10^{-3} mol^{1-n} m^{3n}/s.g_{Pd}$), n the reaction rate order and C_{H_2} hydrogen concentration.

The following assumptions are set to determine the overall gas-liquid-solid mass transfer coefficient:

— Ideal plug flow hydrodynamics
— Negligible gas-side mass transfer (gas phase consists of pure H_2)
— Hydrogen is the limiting reagent (excess of α-methylstyrene)
— Constant liquid film thickness throughout the milli-reactor
— Uniform catalyst layer over the solid surface
— Fully developed flow conditions reached promptly
— Constant molecular diffusivity
— Isobaric and isothermal conditions

Through integration of α-methylstyrene mass balance over the catalytic layer, the apparent reaction rate is given by:

$$r_{app} = \frac{Q_L C^i_{AMS} X_{AMS}}{m_{Pd}} \qquad [mol/g_{Pd}.s] \tag{5.4}$$

Where X_{AMS} is α-methylstyrene conversion, C^i_{AMS} is the initial α-methylstyrene concentration and m_{Pd} is palladium mass. The overall hydrogen comsumption rate, according to flux continuity, is obtained through mass balance under steady state operation as the following:

$$K_{ov} a_{GL} V_{liq} (C^*_{H_2} - \overline{C_{S,H_2}}) = r_{app} \cdot m_{Pd} = f \cdot \eta_s \cdot r(\overline{C_{S,H_2}}) \cdot m_{Pd} \tag{5.5}$$

Where K_{ov} is the overall gas-liquid-solid mass transfer coefficient (m/s), a_{GL} is gas-liquid interfacial area, f the wetting efficiency to account for partial wetting and $\overline{C_{S,H_2}}$ is the average hydrogen concentration on catalyst surface. To account for α-methylstyrene dilution, hydrogen concentration at thermodynamic equilibrium $C^*_{H_2}$ proposed by Herskowitz et al. [1978] is modified as the following:

$$C^*_{H_2} = 1.3 \cdot (0.0145 \cdot T(K) - 1.6985) \cdot P(bar) \tag{5.6}$$

The efficiency factor η_s is modelled assuming large Thiele modulus values as the following:

$$\eta_s = \frac{1}{\Phi_n} \tag{5.7}$$

Where Φ_n is the Thiele modulus given by the following expression for an irreversible n-th order reaction:

$$\Phi_n^2 = \delta_{cata}^2 \frac{(n+1) \cdot k \cdot C_{S,H_2}^{n-1} \cdot w_{Pd} \cdot \rho_{cata}}{2D_e} \tag{5.8}$$

The catalyst layer thickness δ_{cata} was previously estimated to $40\mu m$. D_e is the effective hydrogen diffusivity, defined as $D_{m,H_2}/4$ assuming 2 to 3 tortuosity and 0.6 internal porosity. The molecular diffusion coefficient $D_{m,H2}$ is estimated by a modified Wilke-Chang correlation to $4.88 \cdot 10^{-9} m^2/s$.

In order to determine hydrogen surface concentration, the following optimisation problem is solved using a MatLab program:

$$Hydrogen\ consumption\ flux = f \cdot \eta_s(\overline{C_{S,H_2}}) \cdot r(\overline{C_{S,H_2}}) \cdot m_{Pd} \tag{5.9}$$

Equation (5.9) is based on two assumptions: (i) internal wetting is negligible and (ii) reaction takes place only in the externally wetted solid. The only unknown in equation (5.9) is the mean surface concentration. To ensure global minimum determination, a multistart macro is

employed to test several starting points. Since the optimisation problem is non-linear and both η_s and r depend on $\overline{C_{S,H_2}}$, the solution is achieved through lsqnonlin solver.

5.3 Experimental results and discussion

5.3.1 Hydrodynamics

Influence of surface tension

The effect of surface tension was investigated through water/nitrogen and ethanol/nitrogen flows. Figure 5.9 shows liquid film distributions for both two-phase systems in the same gas and liquid flow rate conditions. As one can see, poor surface coverage is reached using water (figure 5.9-b), while ethanol on the other hand is distributed evenly within the flow domain (figure 5.9-a). However, dye intensity indicates that liquid film thickness is higher for water than ethanol, especially since liquid flow rates are equal for both cases. In addition, ethanol flow appears to circulate between the different hemispheres without (or slightly) covering them.

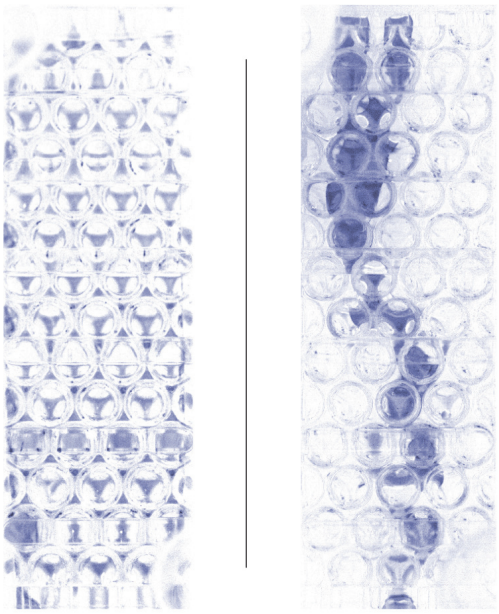

(a) **(b)**

Figure 5.9 Liquid distribution within the WaterShed mock-up in developed flow conditions at $Q_L = 10ml/min$ and $Q_G = 100Nml/min$ for (a) ethanol/nitrogen and (b) water/nitrogen. Image acquisition using CR600x2 CamRecord high-speed monochrome camera. Liquid is indicated by the blue color.

Another contributor to the observed two-phase flow behaviour is liquid/solid interaction. Using an optical tensiometer (Krüss Drop Shape Analyzer - DSA30), static contact angle values are measured for droplets of water and ethanol on WaterShed reactive plates. As shown in figure 5.10, ethanol droplet is more spread than water, with measured contact angles respectively of 28.5° and 86.3°. This means that liquid distribution spread out is enhanced by low contact angle values.

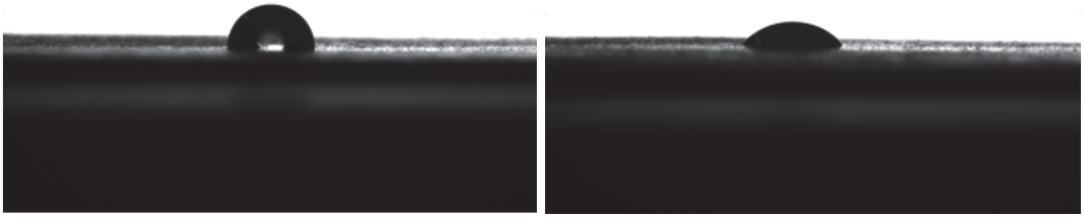

(a) (b)

Figure 5.10 Static contact angle measurements on WaterShed reactive plates for (a) demineralised water and (b) ethanol

Consequently, two-phase flow is governed by surface tension and contact angle. In reactive conditions, broad liquid distributions are preferred since catalyst utilization is maximised. Therefore, the combination of low surface tension and low contact angle is necessary to enhance milli-reactor's performance. Since liquid feed mixture in reactive experiments has similar properties to ethanol, an even distribution is expected within the milli-reactor. Indeed, ethanol and reactive liquid feed mixture surface tensions are respectively 21.8mN/m and 22mN/m, while both fluids are characterised by low contact angles ($\approx 20°$). In what follows, ethanol is used for further hydrodynamic behaviour analysis.

Flow regime and wetting efficiency

Two-phase flow behaviour within reactors equipped with solid particles has been thoroughly studied in the literature. Several researchers introduced the concept of four flow regimes: (i) trickle regime, (ii) pulse regime, (iii) spray regime and (iv) bubble regime. For more details, the reader is referred to chapter 2.

Flow regime is governed by several parameters, among which are fluid flow rates, physico-chemical properties, particle loading density and so forth. To have a sense of potential flow regimes in the milli-reactor, TBR flow map proposed by Charpentier and Favier [1975] is selected as a reference. The variables G/λ and $L\lambda\Psi/G$ are computed over the entire flow rate ranges of gas and liquid.

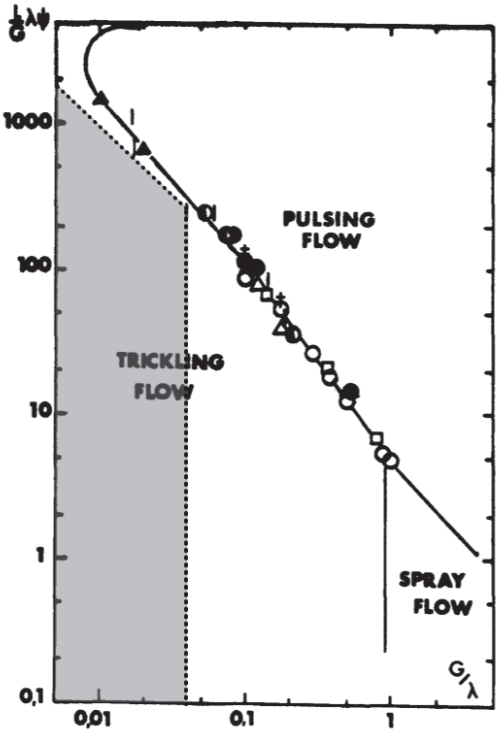

Figure 5.11 Delimitation of milli-reactor's experimental conditions for ethanol/nitrogen flow (grey area) on the trickle-bed reactor flow map proposed by Charpentier and Favier [1975]

According to Charpentier and Favier [1975], the milli-reactor is constantly operating in trickle-flow. The upper limit of the grey area in figure 5.11 is located close to the transition between trickling and pulsing flow. Therefore, to verify flow regime, particularly at the limit, two-phase flow visualisation is conducted at the corresponding fluid flow rates. Experimental observations show that ethanol/nitrogen flow is in trickle-regime regardless of gas and liquid flow rates. Besides, a common flow behaviour is noticed within the WaterShed mock-up. First, liquid covers one reactive plate in early stages, as shown in figure 5.12 at t=0.8s. Afterwards, liquid flows through the opposite reactive plate before stabilising, as shown in figure 5.12 at t=2.7s. Following this stabilisation phase, the two-phase flow is fully developed, and liquid/solid interface becomes stationary (t=8.3s - t=9.6s).

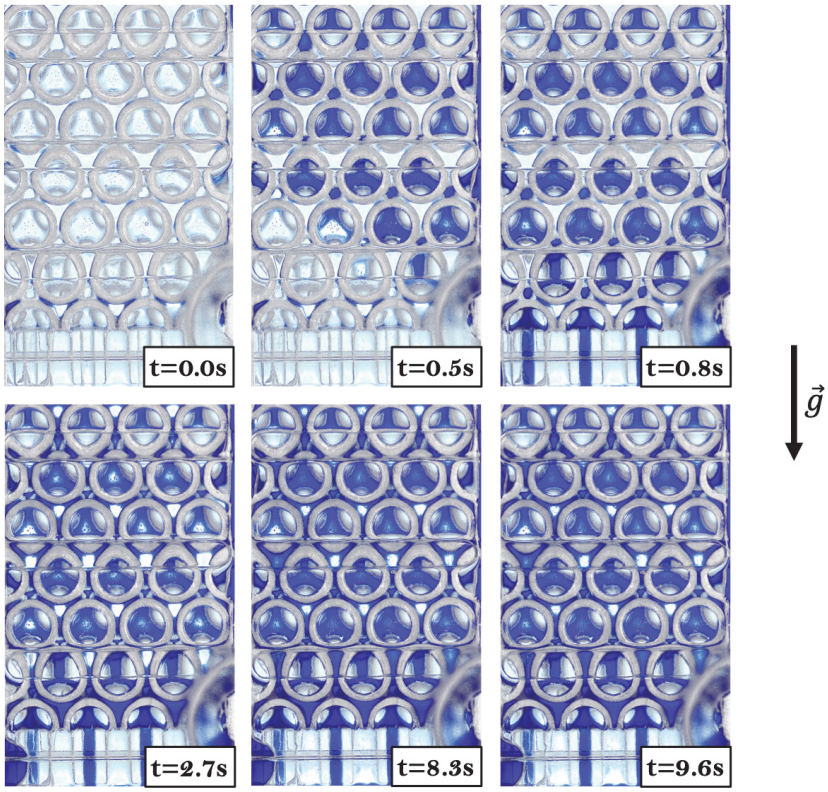

Figure 5.12 Transient ethanol/nitrogen flow visualisation at $Q_L = 7ml/min$ and $Q_G = 70Nml/min$. Image acquisition using Basler ace U high-speed colour camera

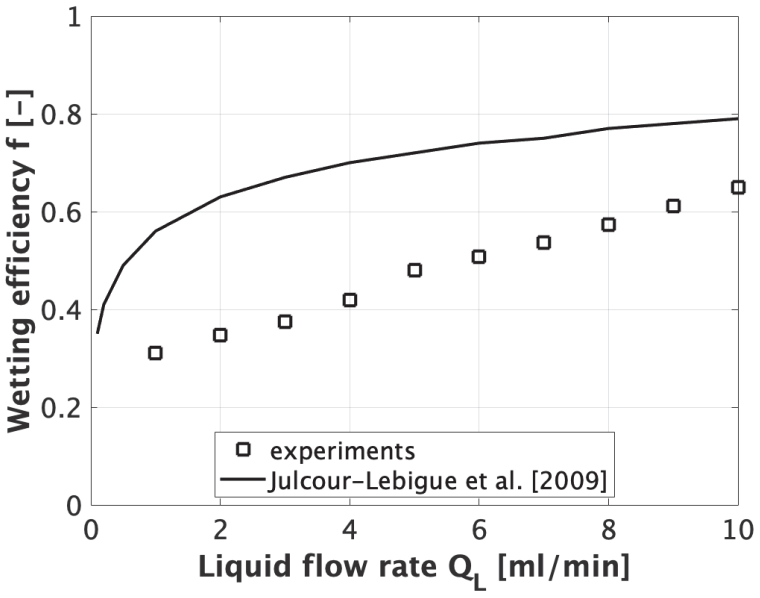

Figure 5.13 Comparison between experimental solid wetting efficiency and the correlation of Julcour-Lebigue et al. [2009] for ethanol/nitrogen flow at different flow rates. Analysis based on image acquisition by Basler ace U high-speed colour camera

Since two-phase flow visual behaviour is found similar regardless of flow rate conditions, qualitative results are presented in figure 5.12 only for $Q_G = 70Nml/min$ and $Q_L = 7ml/min$. Further image processing is conducted in order to extract an estimation of wetting efficiency, following the procedure explained in section 5.2.2. It is observed from figure 5.13 that solid wetted fraction increases with liquid flow rate. These results are an indication of wetting efficiency since the analysis is developed assuming that liquid/solid surface corresponds to the blue image pixels. Besides, comparison to the correlation of Julcour-Lebigue et al. [2009] shows that in similar liquid flow rate conditions, wetting efficiency is lower in the milli-reactor than in trickle-bed reactors. This is attributed to the contact between catalyst particles, since catalyst particles in trickle-bed reactors are in contact, leading to a better liquid distribution over solid particles. Meanwhile, in the milli-reactor, preferential liquid flow paths are observed between hemispherical plots since they are not in contact. It is worth noting that close wetting efficiencies were observed for ethanol and heptane in unpublished data associated with the previous work of Julcour-Lebigue et al. [2009], as shown in figure 5.14. Therefore, it is assumed that liquid flow in reactive conditions would be similar to observed patterns for ethanol.

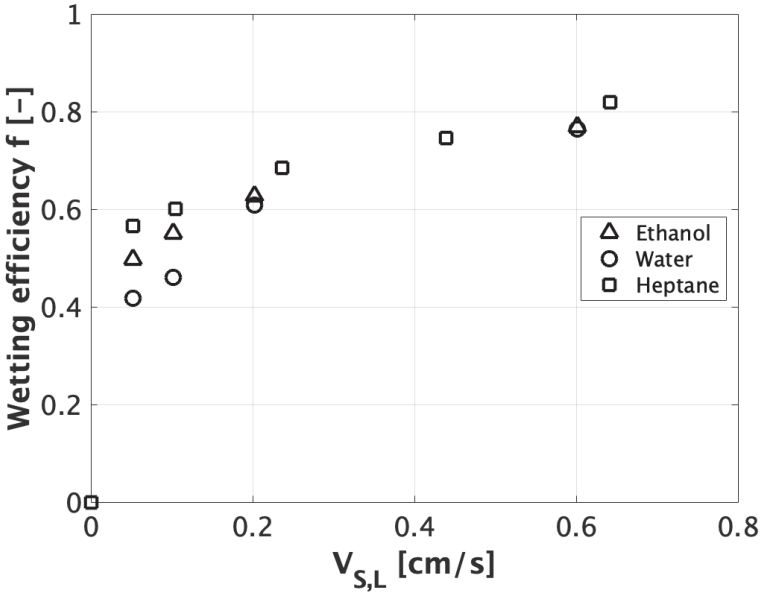

Figure 5.14 Catalyst wetting efficiencies for water, ethanol and heptane. Unpublished data associated with the work of Julcour-Lebigue et al. [2009]

5.3.2 Gas-liquid-solid mass transfer

Influence of operating temperature

α-methylstyrene hydrogenation is a very fast reaction which is usually mass transfer limited even at low temperature conditions. In order to measure overall external gas-liquid-solid mass transfer coefficients, it is important to identify which mass transfer resistances are predominant (internal or external). To do so, experiments are conducted at two temperature conditions, i.e 5°C and 10°C. As one can see from figure 5.15, results show that α-methylstyrene conversions overlap for both temperature conditions. Slight deviations are noticed at 0.1ml/min and 0.4ml/min, but they are within limits of experimental error of 10%. This result indicates the presence of a strong external mass transfer limitation.

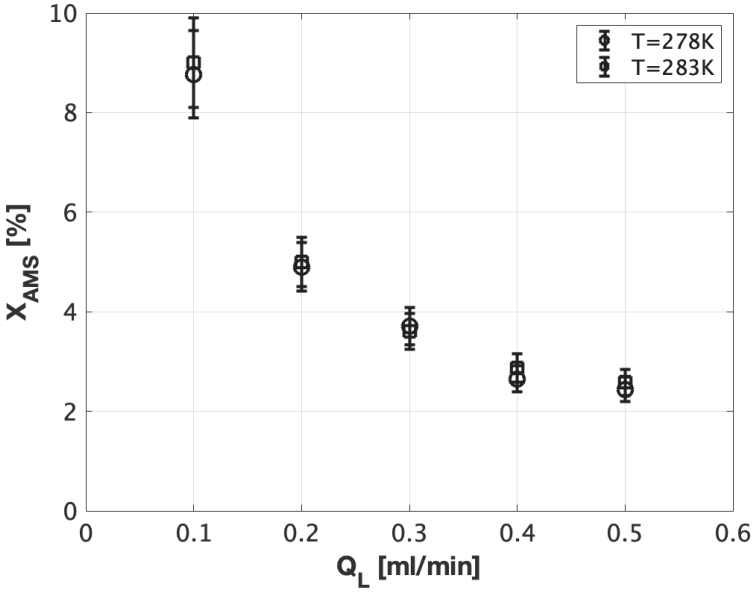

Figure 5.15 Evolution of α-methylstyrene (AMS) conversion with liquid flow rate ($0.1 < Q_L(ml/min) < 0.5$) and operating temperature. The experiments are performed for $Q_G = 10.Q_L$ and $C^i_{AMS} = 1mol/l$ at P=5bar. Error bars represent repetability ($\pm 10\%$)

The results presented in figure 5.15 were obtained with $C^i_{AMS} = 1mol/l$. It can be observed that α-methylstyrene conversion levels reached are low, even at low liquid flow rate conditions. Nevertheless, since hydrogen consumption fluxes are close for $C^i_{AMS} = 1mol/l$ and $C^i_{AMS} = 0.2mol/l$ as shown in figure 5.16, experimental results will be presented hereinafter for $C^i_{AMS} = 0.2mol/l$.

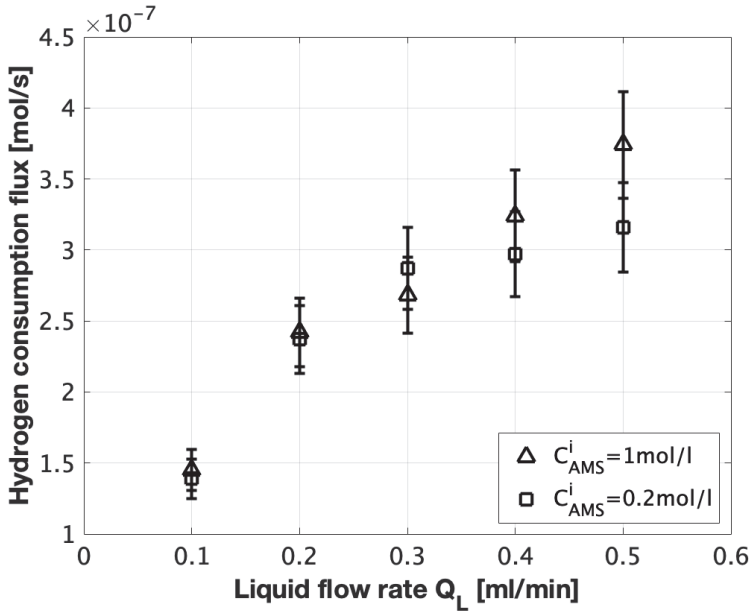

Figure 5.16 Evolution of hydrogen consumption flux with initial α-methylstyrene concentration. The experiments are performed for $0.1 < Q_L(ml/min) < 0.5$, T=278K and P=5bar. Error bars represent repetability ($\pm 10\%$)

Influence of gas flow rate

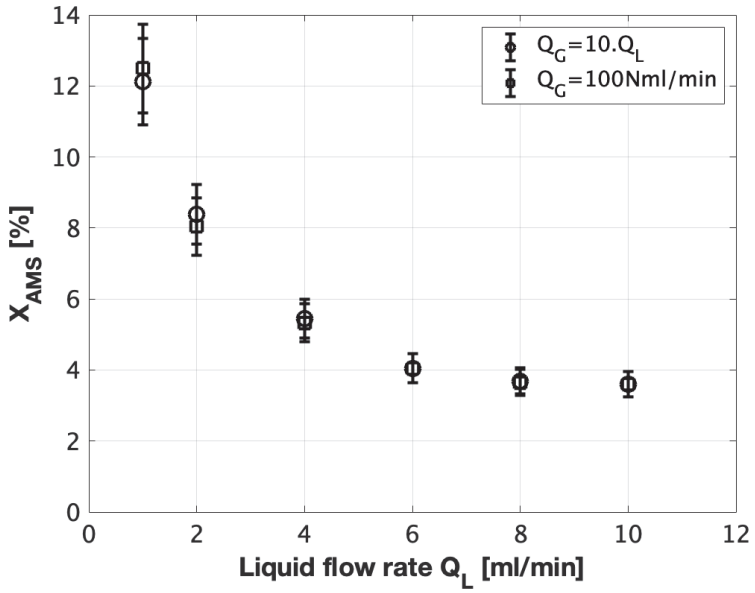

Figure 5.17 Evolution of α-methylstyrene (AMS) conversion with liquid flow rate ($1 < Q_L(ml/min) < 10$) and gas flow rate. The experiments are performed for $Q_G = 10.Q_L$ and $C^i_{AMS} = 0.2mol/l$ at P=5bar and T=278K. Error bars represent repetability ($\pm 10\%$)

In order to investigate gas flow rate impact, experiments are performed in two gas-flow rate conditions: (i) $Q_G = 10 \cdot Q_L$ and (ii) $Q_G = 100 Nml/min$ regardless of liquid flow rate. α-methylstyrene conversions deviations are found negligible with gas flow rate, as shown in figure 5.17. Besides, in the investigated gas flow rate conditions, the molar ratio of hydrogen to α-methylstyrene is at least of 1.78. Indeed, molar ratio is defined by the fraction of hydrogen and AMS inlet molar flow rates. Therefore, regardless of liquid flow rate, hydrogen supply excess is satisfied since the molar ratio is greater than 1.

5.3.3 Hydrogen consumption flux

Hydrogen consumption fluxes are calculated from experimental α-methylstyrene conversions by the following expression:

$$Hydrogen\ consumption\ flux = Q_L \cdot C^i_{AMS} \cdot X_{AMS} \cdot m_{Pd} \tag{5.10}$$

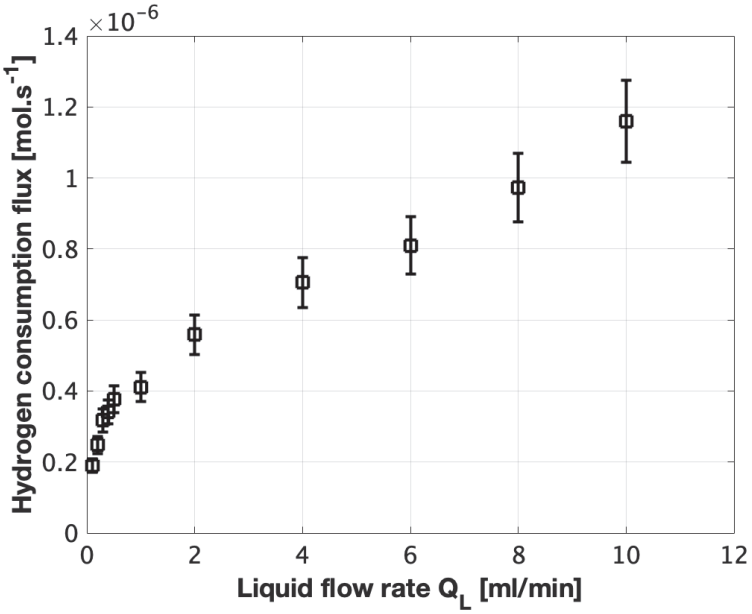

Figure 5.18 Evolution of hydrogen consumption flux with liquid flow rate ($0.1 < Q_L(ml/min) < 10$). The experiments are performed for $Q_G = 10 \cdot Q_L$, $C^i_{AMS} = 0.2 mol/l$, P=5bar and T=278K. Error bars represent repetability ($\pm 10\%$)

It is observed that hydrogen consumption flux increases with liquid flow rate. This behaviour is different from what was previously observed in the FFMR, where hydrogen consumption fluxes decreased with liquid flow rate then reached stabilisation. The main difference between

the FFMR and the milli-reactor is wetting, the former operated in total wetting conditions while the latter in partial wetting conditions. Therefore, the behaviour observed in the milli-reactor is attributed to partial wetting and enhancement of wetting efficiency with liquid flow rate. These aspects will be further detailed in the CFD section.

Further post-processing is conducted in order to determine the evolution of hydrogen surface concentrations and catalyst efficiency factor. To do so, equation (5.9) is optimised by a MatLab code. Experimental wetting efficiency estimations are used in order to account for catalyst partial wetting.

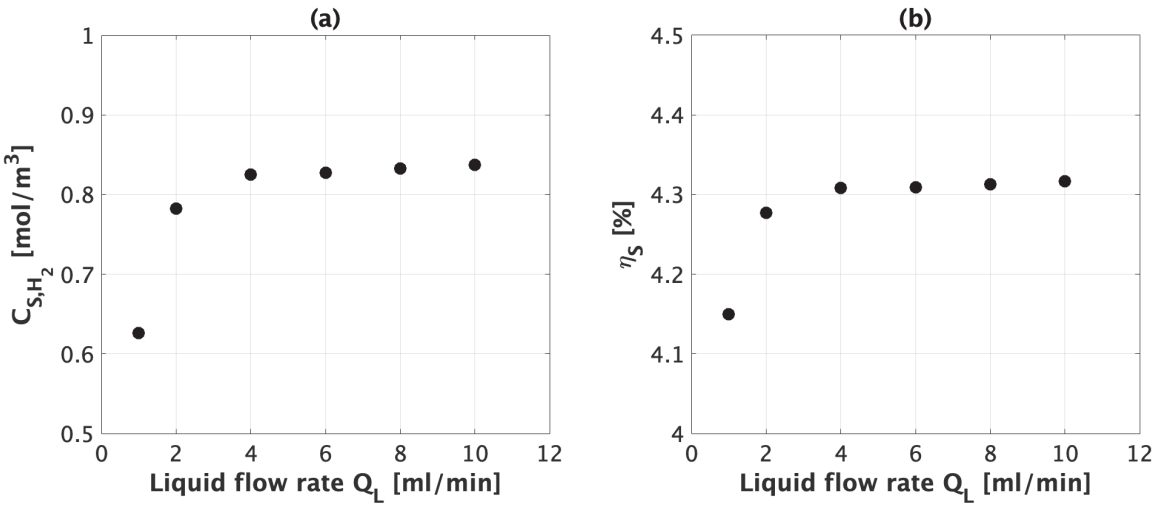

Figure 5.19 Evolution of (a) hydrogen surface concentration and (b) efficiency factor with liquid flow rate ($1 < Q_L(ml/min) < 10$). The experiments are performed for $Q_G = 10 \cdot Q_L$, $C^i_{AMS} = 0.2 mol/l$, P=5bar and T=278K

Hydrogen surface concentration exhibits a slight increase at low liquid flow rates before reaching a plateau, as shown in figure 5.19-a. This behaviour is attributed to the coupling between wetting efficiency and hydrogen consumption flux. Indeed, both parameters follow a semi-linear evolution for liquid flow rates above 2ml/min and their combined growths compensate to result in surface concentration stabilisation. Subsequently, efficiency factor is found to follow the same trend, as shown in figure 5.19-b. Moreover, efficiency factor reached a maximum value of 0.043, indicating fast surface reaction conditions and high internal diffusion limitation. Therefore, hydrogen is consumed close to the external catalytic surface.

Following determination of hydrogen surface concentration, overall gas-liquid-solid mass transfer values are accessible, as shown in figure 5.20. It can be observed that the overall mass transfer coefficient follows a similar trend as hydrogen consumption flux, since surface concentrations become nearly constant for high liquid flow rates. It should be noted that $K_{ov}a_{GL}$

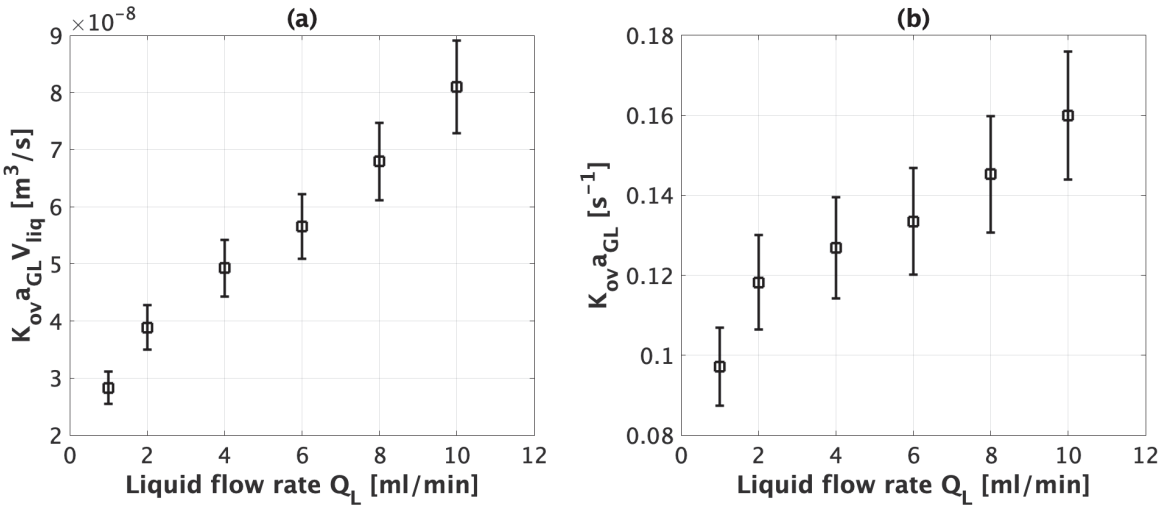

Figure 5.20 Evolution of experimental overall gas-liquid-solid mass transfer coefficient with liquid flow rate ($1 < Q_L(ml/min) < 10$). The experiments are performed for $Q_G = 10 \cdot Q_L$, $C^i_{AMS} = 0.2mol/l$, P=5bar and T=283K

values are determined assuming applicability of liquid saturation correlation of Larachi et al. [2004].

5.3.4 Catalyst layer thickness characterisation

After the end of experimental investigation, the milli-reactor is disassembled in order to measure actual catalyst layer thickness. Using the 3D digital microscope (VHX-6000, Keyence), a magnified view is performed on catalyst cracks located on different hemispherical plots, as shown in figure 5.21. The aim is to estimate a mean catalyst layer thickness coated on the reactive plates. Based on thickness measurements over 4 different hemispherical plots, catalyst thickness ranges from $33.5\mu m$ to $47.4\mu m$. Therefore, the average thickness is $38.2\mu m$, which is close to the previously reported $40\mu m$ estimation.

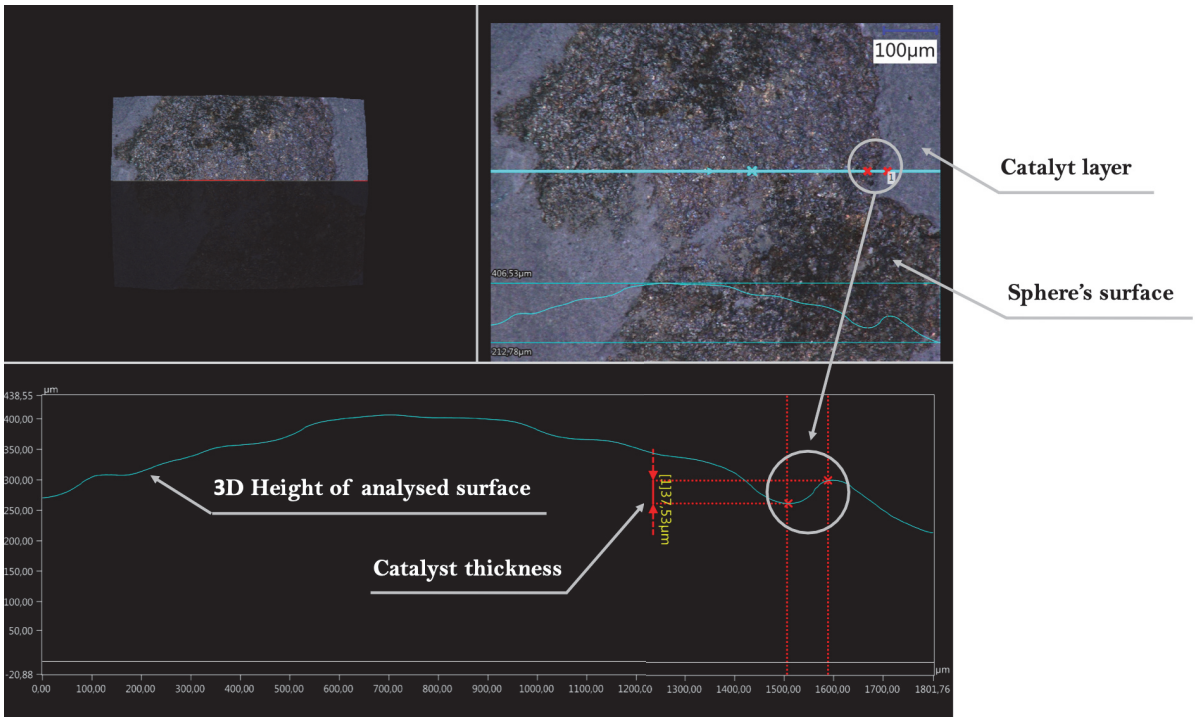

Figure 5.21 Catalyst layer thickness measurement using a 3D digital microscope (VHX-6000, Keyence). Magnification power is 100X

5.4 Computational Fluid Dynamics study

5.4.1 Numerical domain

As explained previously, the milli-reactor has been designed with a small fluid domain to facilitate numerical simulation using VOF approach. Therefore, preliminary tests were conducted in order to define the optimum numerical domain, providing high accuracy in low computation times. First, the milli-reactor's total fluid domain was meshed using SnappyHexMesh. The domain's mesh contained nearly 10Million cells, with a coarse near-wall boundary layer resolution. Consequently, developed flow conditions were reached after 10 days on 288 cores. This long simulation time does not allow for thorough mesh convergence and parametric studies on the total milli-reactor fluid domain. Besides, based on observed experimental flow patterns, one can say that an even phase distribution is obtained within the milli-reactor. In addition, the reactive plates are characterised by a symmetrical geometry. Therefore, the fluid domain is reduced to a smaller portion, as shown in figure 5.22. The aim is to increase mesh resolution, particularly near the solid catalyst layer, in order to improve mass transfer predictions accuracy.

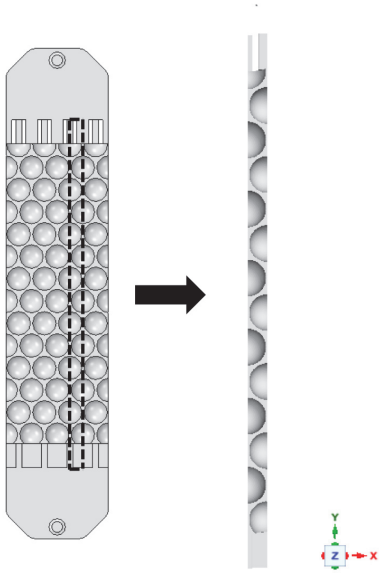

Figure 5.22 Numerical domain extraction from the reactor's fluid domain

Meshing generation is conducted within SnappyHexMesh, following recommendations discussed in the case of spherical string reactor (chapter 4). For a high mass transfer boundary layer resolution, the mesh contains two surface-fitting mesh layers, with a total surface coverage

of 98%. In addition, volume refinement is applied at a distance of 100μm from the catalyst layer.

5.4.2 Numerical set-up and boundary conditions

In order to simulate two-phase flow, gas-liquid-solid mass transfer and catalytic reaction, boundary conditions shown in figure 5.23 are considered. Since the milli-reactor operates in co-current downflow configuration, gas and liquid flow rates are specified at their respective inlets. A no-slip boundary condition is specified at the catalyst's surface to describe near-surface flow. Moreover, external wettability of the catalyst layer is described through a static contact angle condition. To account for fluid domain reduction, the lateral boundaries are set to symmetry conditions. Finally, a regular pressure outlet condition is specified at the outlet.

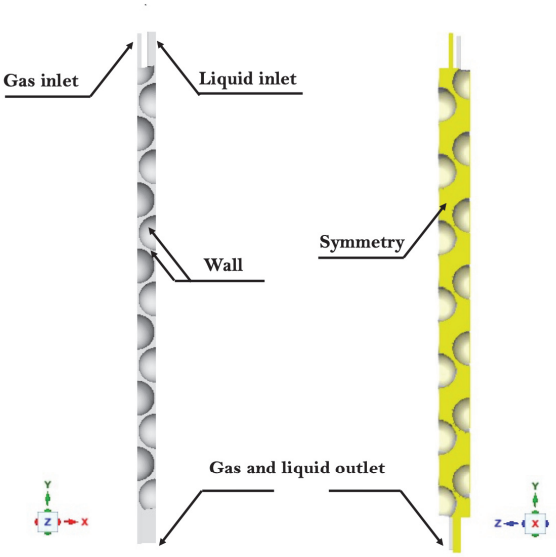

Figure 5.23 Boundary conditions used to predict the milli-reactor's performance. From left to right, front and side view of the milli-reactor

When mass transfer is analysed simultaneously to hydrodynamics, hydrogen concentration is specified at the liquid and gas inlets respectively to 0 and $C^*_{H_2}$. The reactive flux method is used to include heterogeneous catalytic reaction at the catalyst's wall. At the lateral and outlet boundaries, a null-flux condition is specified for hydrogen concentration. It is worth noting that the reactive flux method requires an adequate mesh to ensure accuracy. Therefore, the mesh contains 2 cell layers perfectly fitting the catalyst layer. Based on experimental observations, the milli-reactor is likely to operate in partial wetting conditions. Therefore, for mass transfer simulations, the reactive flux is given by :

$$Flux = -\frac{\mathbf{f} \cdot \rho_m \cdot r(C_{H_2})}{S_{cata}} \tag{5.11}$$

Where f is a wetting efficiency updated at each time iteration. The reactive flux is specified on the wetted surface only, that is to say when liquid volume fraction is greater than 0.5.

To be fully representative of the experimental mass transfer characterisation, CFD simulations are conducted for α-methylstyrene and hydrogen flow in experimental conditions, their respective properties are reported in table 5.4.

Table 5.4 Physical properties of the fluids composing the two-phase system at P=5bar and T=278K

System	Property	Liquid	Gas
α-methylstyrene solution-Hydrogen system	Density $[kg.m^{-3}]$	770	0.43
	Viscosity $[mPa.s]$	0.734	0.008
	Surface tension $[mN.m^{-1}]$	22	

The static contact angle condition is specified assuming high wettability of porous catalyst. Therefore, in order to evaluate contact angle effect on wetting, two low values are tested, namely $\theta = 1^\circ$ and $\theta = 10^\circ$. Decreasing contact angle to 1° increases wetting by and average of 1.5%, as shown in table 5.5. Therefore, in the following simulations, 10° contact angle is specified at the catalyst's surface.

Table 5.5 Evaluation of contact angle effect on wetting efficiency for the minimum and maximum liquid flow rates

	liquid flow rate [ml/min]	$\theta = 1^\circ$	$\theta = 10^\circ$	deviation [%]
Wetting efficiency [-]	4	0.437	0.431	1.34%
	10	0.579	0.570	1.58%

5.4.3 Mesh convergence study

In order to find the optimum mesh size, CFD simulations are conducted for three mesh densities: (i) 1 Million cells, (ii) 3 Million cells and (iii) 5.3 Million cells. The aim is to identify minimum mesh density providing stable results, particularly for wetting efficiency and hydrogen consumption flux. The results are reported in table 5.6.

Table 5.6 Predicted wetting efficiency and hydrogen consumption flux for three mesh densities. Results obtained for $Q_G = 40Nml/min$ and $Q_L = 4ml/min$, in isobaric and isothermal conditions (P=5bar and T=278K)

Mesh density [cell number]	1 Million	3 Million	5.3 Million
Wetting efficiency f [-]	0.472	0.481	0.487
Hydrogen consumption flux $[mol.s^{-1}]$	$7.82 \cdot 10^{-7}$	$7.06 \cdot 10^{-7}$	$6.98 \cdot 10^{-7}$

Predicted wetting efficiencies are in the same order of magnitude. This is attributed to near-wall mesh topology, which is similar for tested meshes. However, differences arise in hydrogen consumption flux values. Indeed, the highest value is predicted by the coarser mesh, which is due to a low mass transfer boundary layer resolution. The number of cells in the liquid film is low, which leads to high diffusion rates in comparison to reactive consumption. Therefore, hydrogen surface concentrations increase, and so does the hydrogen consumption flux. Nevertheless, the 5.3Million and 3Million cells meshes predict very close hydrogen consumption flux values. The absolute standard deviation is 1.13%. Therefore, the 3Million cells mesh is selected to conduct the following simulations.

5.4.4 Hydrodynamic analysis

Two-phase flow is simulated for α-methylstyrene mixture at different inlet conditions. Following the experimental procedure, the simulated configurations correspond to $Q_G = 10Q_L$. It is important to note that simulations were performed for $4 \leq Q_L[ml/min] \leq 10$, as lower liquid flow rates require high mesh resolutions to capture concentration gradients within the liquid film. Since simulations were carried out in transient conditions, the wetting efficiency was monitored at each time step to identify fully developed flow conditions, as shown in figure 5.24. The developed flow is reached earlier for higher liquid flow rates, and simulations are stopped when both wetting efficiency and hydrogen consumption flux are stable.

After reaching developed flow conditions, predicted phase distributions are visualised within the milli-reactor, as shown in figure 5.25. Even at maximum liquid flow rate ($Q_L = 10ml/min$), CFD simulations predict partial wetting of the catalytic surface. This behaviour is consistent with experimental observations, since liquid was found to flow between the hemispherical plots regardless of gas and liquid flow rates.

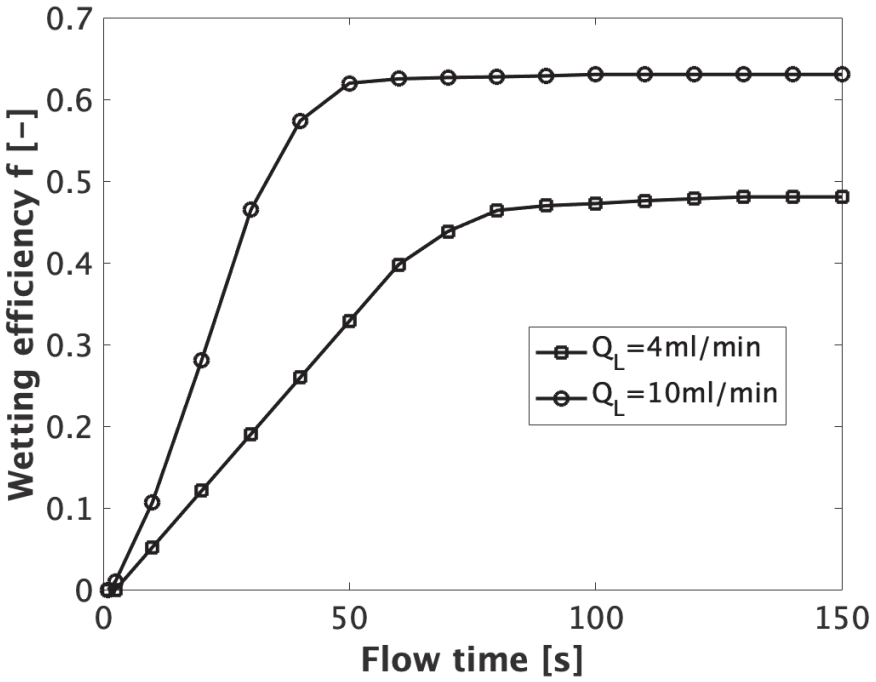

Figure 5.24 Wetting efficiency evolution with flow time for $Q_L = 4ml/min$ and $Q_L = 10ml/min$

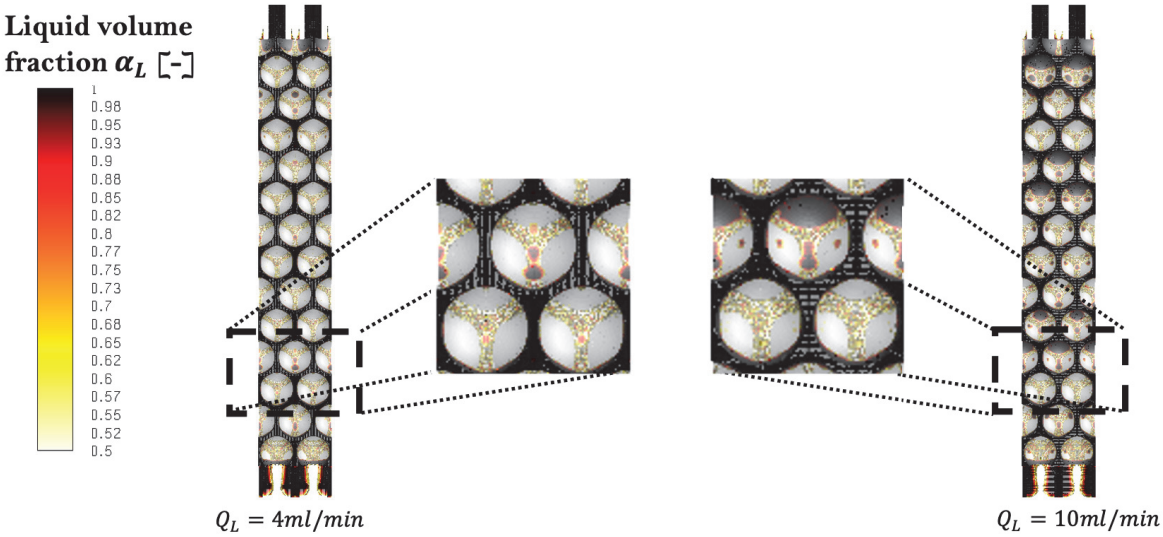

Figure 5.25 Liquid volume fraction in the milli-reactor for $Q_L = 4ml/min$ and $Q_L = 10ml/min$. Numerical domain is mirrored at symmetry planes for graphical display purposes

First, CFD-predicted wetting efficiencies are computed from predicted phase distributions. Figure 5.26-a presents a comparison between CFD predictions, experimental results and wetting efficiency estimations by the correlation of Julcour-Lebigue et al. [2009], developed for trickle bed reactors. As one can see, predicted wetting efficiencies in the milli-reactor are much lower than correlation estimations. This behaviour is explained by the geometry of the reactor. Indeed, the correlation of Julcour-Lebigue et al. [2009] was developed on trickle-bed reactors, where liquid needs to flow over a particle to reach the next one. Whereas in the milli-reactor, hemispherical plots are non-overlapping, leading to the development of preferential paths between the hemispherical plots for the liquid. Therefore, at the same liquid flow rate, wetting efficiencies are lower in the milli-reactor when compared to trickle-bed reactors. It is worth noting that numerical and experimental wetting efficiency are in a good agreement.

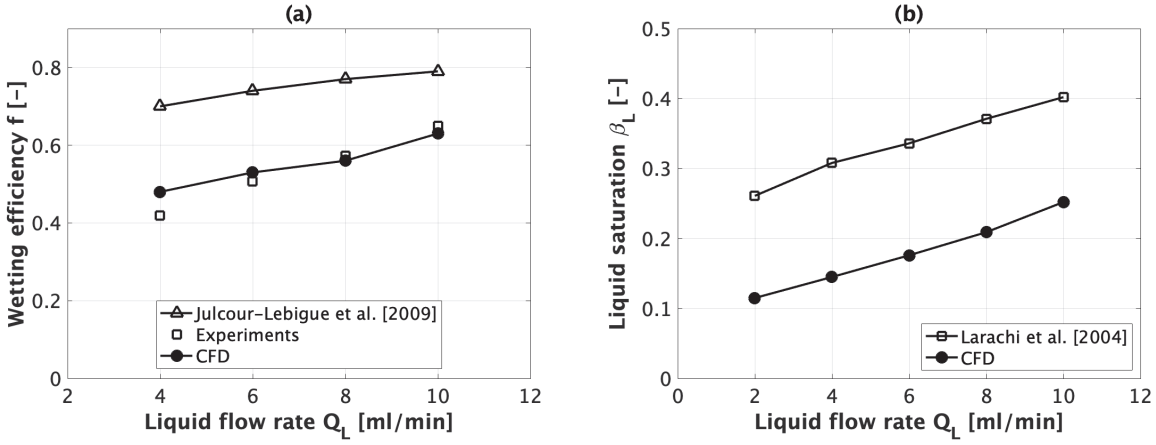

Figure 5.26 (a) Wetting efficiency comparison between predicted results and the correlation of Julcour-Lebigue et al. [2009] and (b) total liquid saturation comparison between predicted results and estimated by the correlation of Larachi et al. [2004]

Liquid saturation ($\beta_L = V_{liq}/V_{fluid}$) is computed as well, as shown in figure 5.26-b. A trickle-bed reactor simulator based on the correlation of Larachi et al. [2004] is employed for the sake of comparison. CFD results and correlation estimations follow the same trend, even though high deviations are observed between both results. These deviations are justified by the geometrical features of the milli-reactor as well. Indeed, liquid accumulation in trickle-bed reactors is higher due to more confined flow paths. Whereas, in the milli-reactor, liquid follows a smooth flow-path throughout the reactive plates, hence lowering static and total liquid holdups in comparison to classical particle beds.

Furthermore, given the coordinates of gas-liquid interfacial area and catalyst wall, it is possible to access local liquid film thickness values. First, the gas-liquid interface is located at

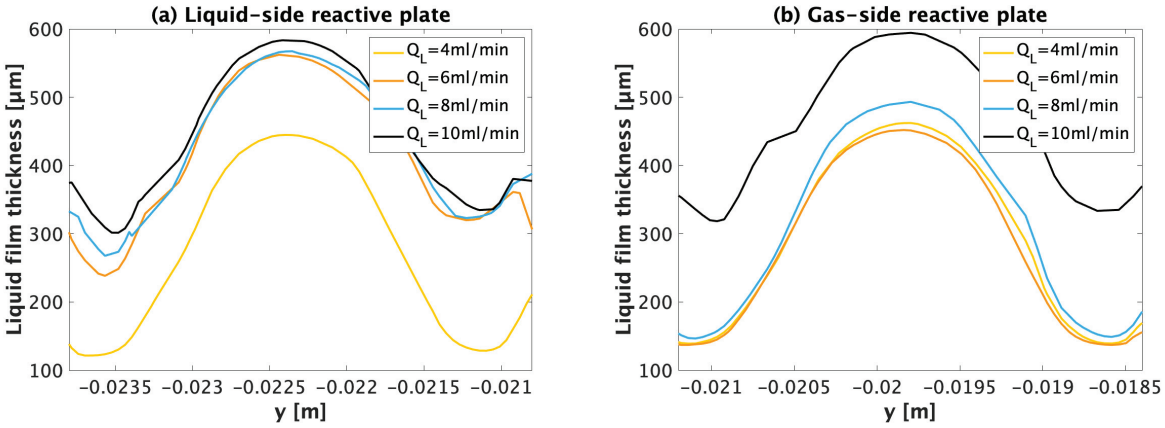

Figure 5.27 Liquid film thickness between two hemispherical plots in (a) the liquid-side reactive plate and (b) the gas-side reactive plate

α_L=0.5, then its coordinates are extracted at each mesh cell. Subsequently, liquid film thickness is defined as the minimum distance between each interface cell and the catalyst wall. Due to inlet asymmetry, this analysis is conducted separately for gas-side and liquid-side reactive plates, as shown in figure 5.27. Apart from $Q_L = 10ml/min$, it can be observed that liquid film thickness on gas-side reactive plate is lower than liquid-side. This is attributed to liquid feed asymmetry, as it supplies directly the liquid-side reactive plate, while the gas-side reactive plate is supplied as a result of capillarity effects. Nevertheless, liquid distribution from one plate to another appears to be more homogeneous for $Q_L = 10ml/min$. This is explained by higher gas-liquid shear force since gas flow rate is much higher than other cases ($Q_G = 100Nml/min$).

5.4.5 Mass transfer analysis

Coupled to hydrodynamic resolution, hydrogen concentration transport is simulated in isobaric and isothermal conditions (P=5bar and T=278K). As a reminder, the reactive flux is applied on the wetted surface only. After reaching convergence, average hydrogen consumption fluxes are computed over the wetted catalyst surface. Figures 5.28 and 5.29 illustrate a comparison between experimental and predicted hydrogen consumption fluxes and α-methylstyrene conversions. For tested conditions, results exhibit a good agreement between CFD predictions and experimental values while following a similar trend. It should be noted that low liquid flow rates conditions were not tested, since very high mesh densities are required near the catalyst wall to accurately describe concentration gradients within low thickness liquid films.

The complexity of liquid film thickness distribution within the milli-reactor leads to complex distribution of hydrogen consumption flux over the wetted surface. As shown in figure 5.30, as

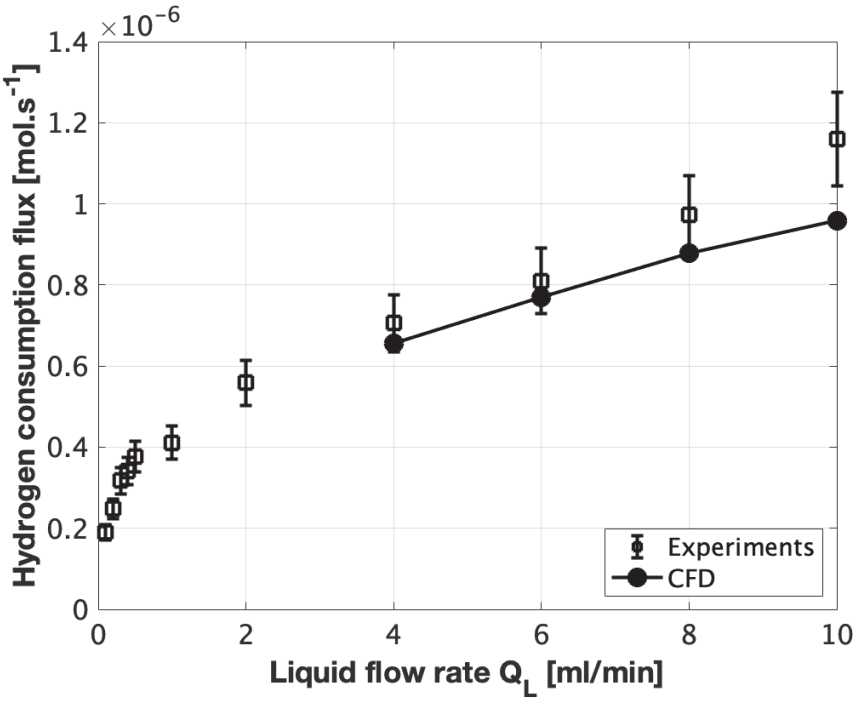

Figure 5.28 Comparison between experimental and predicted hydrogen consumption fluxes for P=5bar and T=283K. The gas flow rates are fixed to $10 \cdot Q_L$. Error bars represent repetability ($\pm 10\%$)

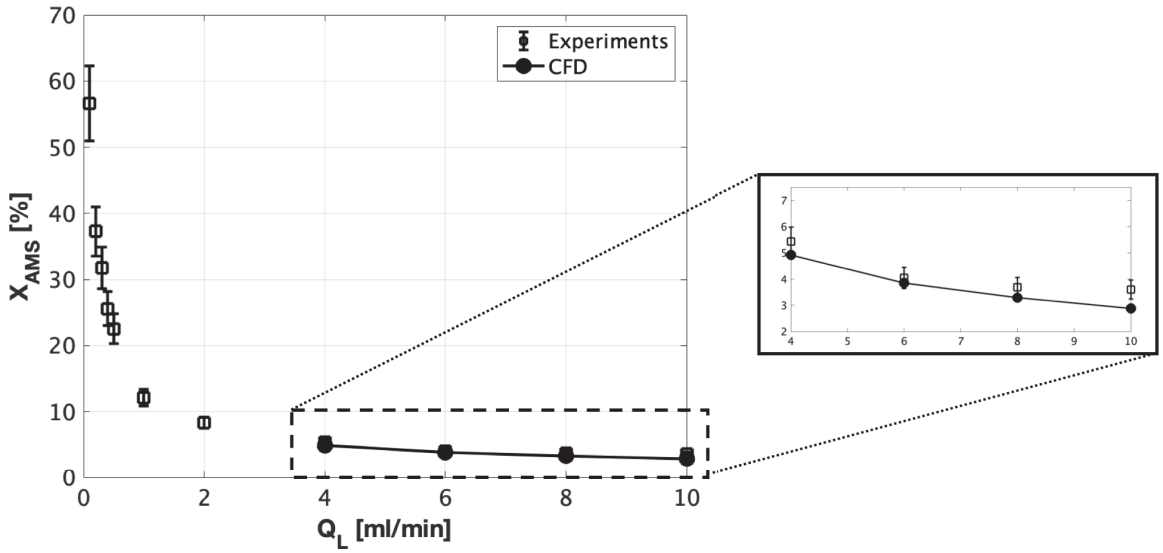

Figure 5.29 Experimental and predicted α-methylstyrene conversions at P=5bar and T=283K. The gas flow rates are fixed to $10 \cdot Q_L$. Error bars represent repetability ($\pm 10\%$)

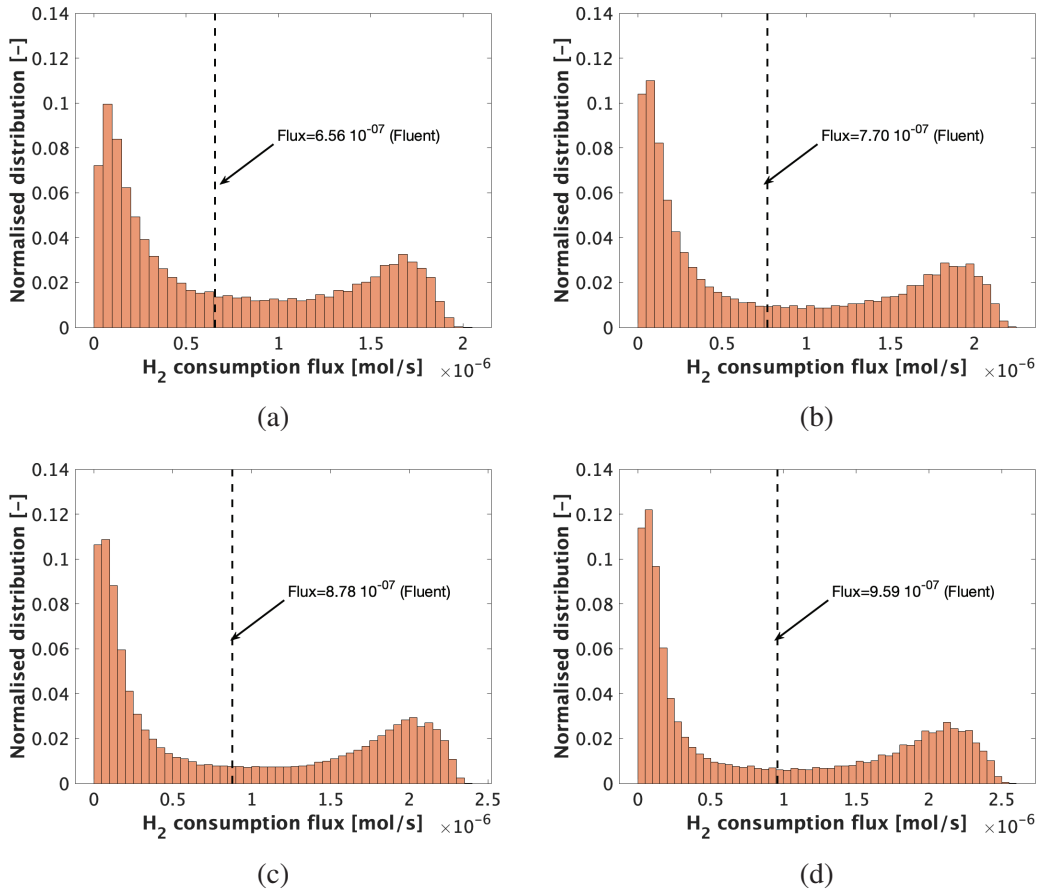

Figure 5.30 Normalised hydrogen consumption flux distributions over the wetted surface for (a) $Q_L = 4ml/min$, (b) $Q_L = 6ml/min$, (c) $Q_L = 8ml/min$ and (d) $Q_L = 10ml/min$. The mean hydrogen surface fluxes are reported on the figures.

liquid flow rate increases (from a to d) hydrogen consumption fluxes decrease and distributions become narrower at low flux values. Given predictions of hydrogen consumption fluxes and wetting efficiencies, optimisation is employed to determine the corresponding hydrogen surface concentrations C_{S,H_2} through a MatLab program (equation (5.12)).

$$Flux_{H_2} = f \cdot \eta_s \cdot k \cdot C_{S,H_2}^{0.73} \tag{5.12}$$

Following mean hydrogen consumption flux optimisation, the average hydrogen surface concentrations are accessed and compared to local surface concentration distributions provided by CFD, as reported in figure 5.31. It can be noticed that the complexity of surface concentration distribution is not observable from mean values. Similarly to hydrogen consumption flux,

surface concentration distribution become narrow with increasing liquid flow rates. This is attributed to external mass transfer limitations, which increase with liquid flow rate.

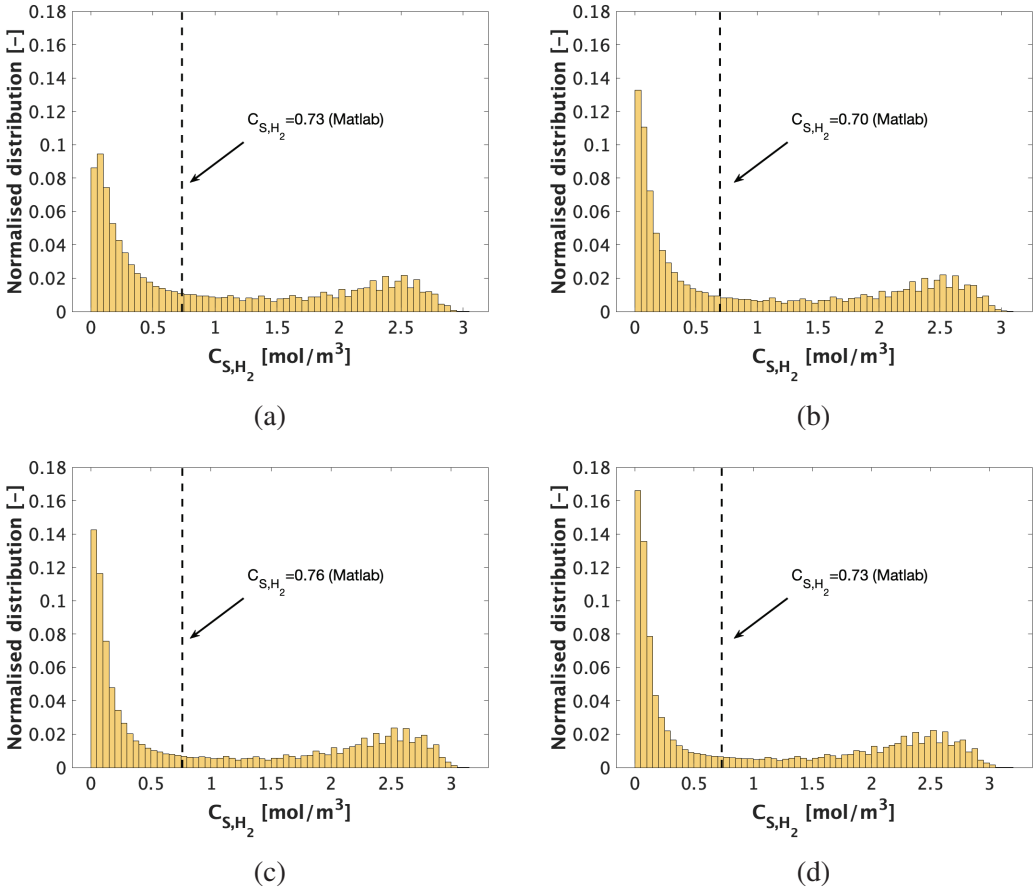

Figure 5.31 Normalised hydrogen surface concentration C_{S,H_2} distributions over the wetted surface for (a) $Q_L = 4ml/min$, (b) $Q_L = 6ml/min$, (c) $Q_L = 8ml/min$ and (d) $Q_L = 10ml/min$. The mean hydrogen surface concentrations are reported on the figures.

In order to gain insight on local hydrogen surface concentrations, figure 5.32 represents their distribution over the solid surface for $Q_L = 4ml/min$ and $Q_L = 10ml/min$. First, since hydrogen consumption flux is specified only over the wetted solid fraction, it can be observed that very low concentration values are achieved within the liquid film. Meanwhile, over the dry catalyst surface, concentrations reach $C^*_{H_2} = 15.16mol/m^3$. Besides, fully developed mass transfer regime is promptly achieved since surface concentrations are stable throughout the numerical domain. When qualitatively comparing liquid flow rate effect on concentration profile, a few cells with relatively higher concentration values are noticed for $Q_L = 4ml/min$. This is attributed to liquid film thickness decrease, therefore shortening reagent diffusion distance.

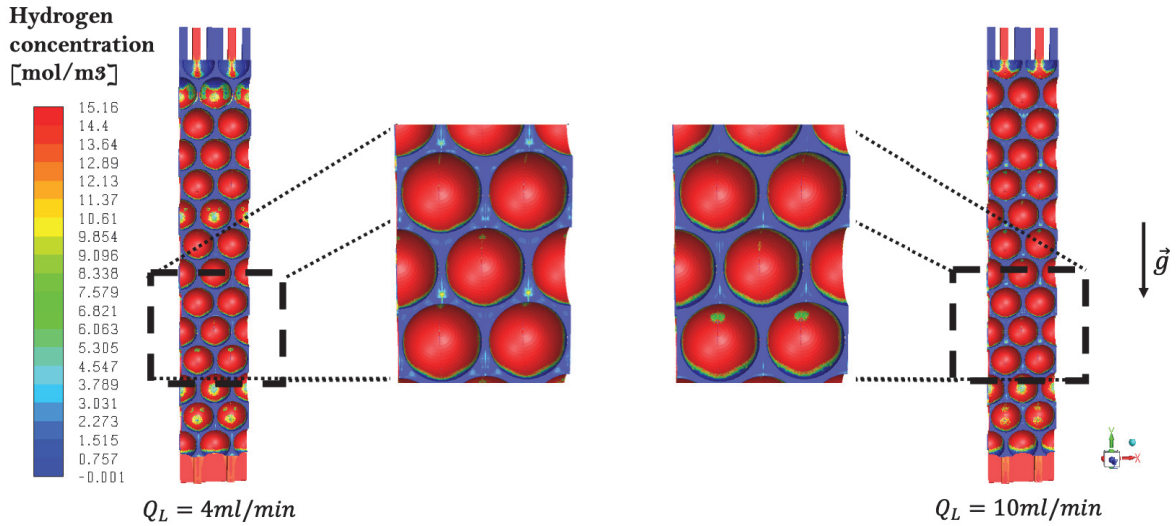

Figure 5.32 Overview of predicted hydrogen surface concentration profiles for $Q_L = 4ml/min$ (left) and $Q_L = 10ml/min$ (right). Numerical domain is mirrored at symmetry planes for graphical display purposes

In order to compute overall mass transfer coefficients, the average surface concentrations determined through optimisation are used in the following equation:

$$K_{ov}a_{GL}V_{liq} = \frac{Flux_{H_2}}{C^*_{H_2} - \overline{C_{S,H_2}}} \tag{5.13}$$

Where $Flux_{H_2}$ is the average hydrogen consumption flux and $\overline{C_{S,H_2}}$ the optimisation result of CFD-predictions reported in figure 5.31.

The experimental and predicted overall mass transfer coefficients are in good agreement, as shown in figure 5.33. Since high deviations were previously observed between predicted liquid saturations and Larachi et al. [2004] estimations, the experimental $K_{ov}a_{GL}$ are based on CFD-predicted liquid volumes. Assuming that the film model ($K_{ov} = D_{m,H_2}/\delta_c$) is applicable, mass transfer boundary layer thickness is analysed in two configurations of hydrogen concentration transport: (i) convection-diffusion and (ii) pure diffusion. The former accounts for both diffusive and convective contributions, while the latter is an artificial case where convective flux is equal to zero. The results are reported in table 5.7 for convection-diffusion and pure diffusion conditions.

When compared to pure diffusion conditions, mass transfer boundary layer thicknesses are much lower for convection-diffusion. This is attributed to convective hydrogen supply to the liquid film, which accelerates gas-liquid-solid mass transfer indeed. In pure diffusion conditions,

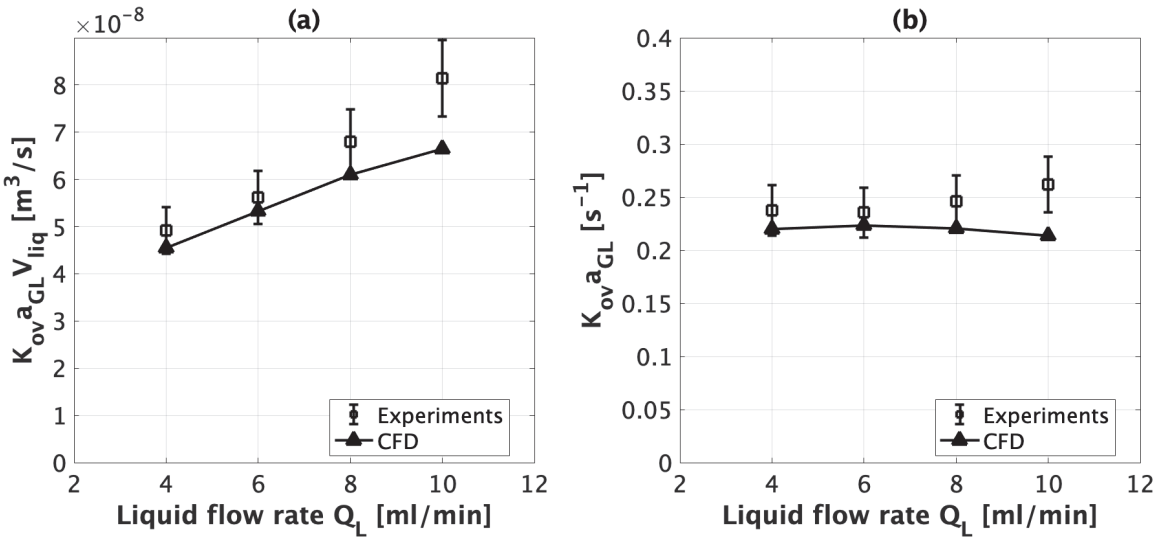

Figure 5.33 Comparison between predicted and experimental gas-liquid-solid mass transfer coefficients. Error bars represent repetability (±10%)

the obtained δ_c values are much higher and are close to actual liquid film thicknesses (δ_{geo}). These results are consistent with behaviour observed in the spherical particles' string reactor.

Table 5.7 Gas-liquid-solid mass transfer boundary layer thickness in convection-diffusion conditions

Convection-diffusion						
Q_L [ml/min]	Q_G [Nml/min]	Gas-liquid interfacial area a_{GL} $[m^2/m_R^3]$	Liquid film thickness δ_{geo} $[\mu m]$	Mass transfer coefficient K_{ov} [m/s]	Mass transfer coefficient $K_{ov}a_{GL}$ $[s^{-1}]$	$\delta_c = \frac{D_{m,H_2}}{K_{ov}}$ $[\mu m]$
4	40	699	130	$4.19 \cdot 10^{-4}$	0.036	11.66
6	60	723	143	$4.75 \cdot 10^{-4}$	0.043	10.28
8	80	744	161	$5.27 \cdot 10^{-4}$	0.049	9.26
10	100	779	172	$5.49 \cdot 10^{-4}$	0.054	8.88
Pure diffusion						
Q_L [ml/min]	Q_G [Nml/min]	Gas-liquid interfacial area a_{GL} $[m^2/m_R^3]$	Liquid film thickness δ_{geo} $[\mu m]$	Mass transfer coefficient K_{ov} [m/s]	Mass transfer coefficient $K_{ov}a_{GL}$ $[s^{-1}]$	$\delta_c = \frac{D_{m,H_2}}{K_{ov}}$ $[\mu m]$
4	40	699	130	$5.08 \cdot 10^{-5}$	0.0044	95.80
6	60	723	143	$4.63 \cdot 10^{-5}$	0.0042	110.41
8	80	744	161	$4.54 \cdot 10^{-5}$	0.0042	114.28
10	100	779	172	$3.43 \cdot 10^{-5}$	0.0033	166.71

5.5 Conclusion

This chapter investigated gas-liquid-solid mass transfer in a 3D-printed milli-reactor, designed to provide an intermediate geometry between falling liquid films over simple geometries and trickle-bed loadings.

First, experimental two-phase qualitative characterisations were conducted within a WaterShed mock-up. The milli-reactor is found to operate in trickling flow regime, regardless of gas and liquid flow rate conditions. Besides, flow image acquisition showed that partial wetting is encountered at all times, even when highly wetting and low contact angle fluids are used. Therefore, flow images were processed to extract wetting efficiency estimations.

The hydrodynamic study was then followed by reactive gas-liquid-solid mass transfer characterisation. Indeed, catalytic hydrogenation of α-methylstyrene to cumene was performed within a stainless steel milli-reactor. Pd/Al_2O_3 was coated on reactive plates using a spray method. The results show that α-methylstyrene conversions are independent of operating temperature, indicating external mass transfer limitations. Hydrogen consumption fluxes and conversions were collected for several gas/liquid flow rate conditions. Since liquid volumes could not be characterised within the milli-reactor, complementary information was retrieved from CFD simulations to determine the experimental overall mass transfer coefficient.

Following the experimental investigation, coupled two-phase flow and reactive gas-liquid-solid mass transfer was simulated using the CFD numerical model. First, predicted wetting efficiencies) are found to be close to experimental estimations, therefore validating accuracy of hydrodynamic CFD modeling. Since the milli-reactor operates in partial wetting conditions, it is assumed in the numerical model that the reaction takes place over the wetted solid surface only. As a result, experimental and predicted hydrogen consumption fluxes are found in good agreement. The same conclusion applies subsequently to α-methylstyrene conversion. Therefore, CFD modeling was validated against experimental results for both hydrodynamics and mass transfer.

Finally, the mass transfer boundary layers were analysed using the film model. In realistic concentration transport conditions, thin boundary layers are achieved when both convection and diffusion are considered. Whereas, neglecting convection results in thick mass transfer boundary layers. Therefore, convection is found to accelerate significantly mass transfer. This conclusion is consistent with the previous numerical investigations (chapters 3 and 4).

Chapter 6

CFD investigation of trickle-bed reactors with different catalyst particle shapes

6.1 Introduction

Owing to their relatively convenient conception and operability, trickle-bed reactors are considered the best gas-liquid-solid contactors technology in a wide application spectrum. Within these reactors, a gas and a liquid flow co-currently downward throughout the catalyst fixed bed, allowing both phases to react at the catalyst's surface or volume. Even though they are easy to operate, these reactors combine simultaneous intricate phenomena, namely two-phase momentum transport, mass transfer and reaction. Therefore, in an effort to improve understanding of the aforementioned phenomena, several literature studies took interest in trickle-bed reactors' characterisation.

Most often experimental, these contributions provide quantitative data on parameters of interest, such as pressure drop or mass transfer coefficients. They employ either (i) invasive or (ii) non-invasive techniques to access data. The former are suitable for low temperature and pressure conditions, while the latter allow for industrial operating conditions (high temperature and pressure). The majority of these investigations focused on hydrodynamic description, while few contributions addressed interfacial mass transfer. In order to help estimate parameters of interest, many correlations were proposed for pressure drop, liquid saturation, wetting efficiency, gas-liquid and liquid-solid mass transfers. However, as a consequence of experimental techniques and operating conditions variations, high disparities are observed in parameters' estimation through correlations. For a more detailed review and listing, the reader is referred to chapter 2.

In an effort to achieve a better comprehension of local phenomena, the present work relies on numerical investigations using Computational Fluid Dynamics. Following its validation on analytical solutions and experimental results, the numerical model is applied on trickle-bed reactors in this chapter. The purpose is to investigate the complex coupling between hydrodynamics and mass transfer, in realistic industrial operating conditions. To do so, hydrodynamic predictions are validated against reliable literature models (namely Ergun law and the correlation of Boyer et al. [2007]) in terms of pressure drop and liquid holdup. Afterwards, the solid's wetting efficiency is compared to the correlation of Julcour-Lebigue et al. [2009]. The latter correlation is then broadened to account for gas flow rate and particle shape effects on wetting efficiency. Finally, predictive gas-liquid-solid mass transfer simulations are conducted, and the results are analysed and discussed.

6.2 Numerical domain generation

Prior to CFD calculations, defining the appropriate numerical domain's geometry is of high importance. Conventionally, particle packing algorithms are used to generate fixed bed loadings with a shape of choice. Among these algorithms, the Discrete Element Method (DEM) is the most widely used technology. The vast collection of numerical packing techniques can be divided in two main categories: (i) constructive techniques and (ii) dynamic techniques. The former rely on geometrical calculations to generate the loading, while the latter rely on an initial particle packing previously generated through DEM simulations. For a more extensive listing of particle packing algorithms, the reader is referred to Recary et al. [2019].

In spite of its wide use, DEM exhibits the following limitations: (i) computationally heavy and (ii) only suitable for simple particle shapes (spheres). To overcome these issues, Boccardo et al. [2015] proposed an alternative method to DEM, using the open-source software Blender. The authors achieved realistic particle loadings using complex particle shapes, namely spheres, cylinders and trilobes. An excellent agreement was found between predicted pressure drops and Ergun law estimations. The authors pointed out the importance of choosing the right mesh resolution in order to accurately capture geometrical details.

Similarly, in this work, Blender is employed to generate the particle loadings. Considering a particle shape, the packing generation is grounded on the Bullet Physics Library (BPL) available in Blender. This advanced physics simulation library solves the Newton's second law for a number of particles N, and is able to detect collisions between solid particles as well as their final position. According to Boccardo et al. [2015], Blender is capable of handling

complex particle shapes. Therefore, three particle shapes are considered in this work, namely spheres, trilobes and quadrilobes, as shown in figure 6.1. The trilobe and quadrilobes shapes were selected carefully to ensure close equivalent diameter values.

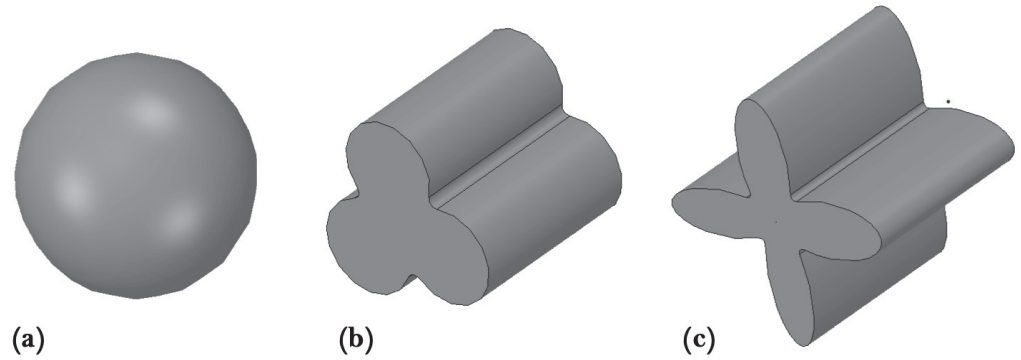

Figure 6.1 Particle shapes' geometry: (a) spheres with $d_p = 2mm$, (b) trilobes with $d_e = 1.8mm$ and (c) quadrilobes with $d_e = 1.95mm$

Particle loadings were afterwards generated in Blender, as shown in figure 6.2. Spherical particles are loaded in a mono-dispersed configuration, meaning that all the spheres have equal diameters. In contrast, poly-dispersion is included in trilobes and quadrilobes loadings, with a mean particle length of 4.77mm and standard deviation of 1.77mm. The packings were generated within cylindrical containers of equal diameter (3.5cm) and height (3cm), as shown in figure 6.2. Spheres and trilobes loadings have similar void fractions, while the quadrilobes loading is characterised by a higher void fraction, as can be seen from table 6.1. Since loadings were generated following the exact same procedure, high quadrilobe bed porosity is attributed to the particle's geometrical features. In contrast with spheres and trilobes, quadrilobes exhibit larger concavities.

Table 6.1 Characteristics of particles and packings

Particle shape	Particle's equivalent diameter d_e [mm]	Polydispersity		Bed porosity ε_B
		Mean particle length [mm]	Standard deviation [mm]	
Sphere	2.00	—		0.372
Trilobe	1.80	4.77	1.77	0.377
Quadrilobe	1.95	4.77	1.77	0.628

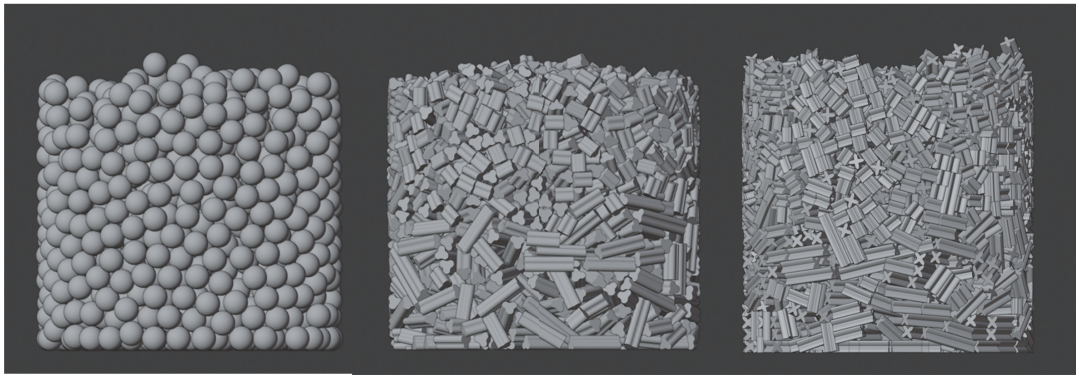

Figure 6.2 Cylindrical packings (Diameter=3.5cm and Height=3cm) of (a) spheres, (b) trilobes and (c) quadrilobes

Given that VOF approach requires high computational resources, the numerical domain needs to be further reduced. Therefore, cuboid Representative Elementary Volumes (REV) are extracted from the cylindrical containers. In order to obtain a surface-fitted mesh, the REVs are meshed using SnappyHexMesh following the recommendations of Boccardo et al. [2015], as shown in figure 6.3.

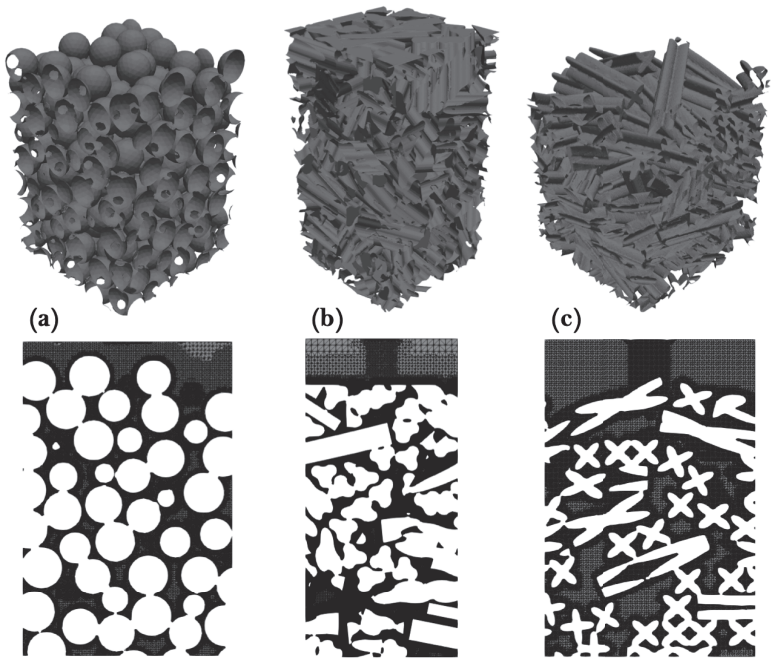

Figure 6.3 The three numerical domains and slices of their respective meshes (a) spheres (1.0x1.0x1.5 cm^3, d_e=2.00mm, ε_B=37.2%) (b) trilobes (1.0x1.0x2.1 cm^3, d_e=1.80mm, ε_B=37.7%) and (c) quadrilobes (1.0x1.0x1.5 cm^3, d_e=1.95mm, ε_B=62.8%)

6.3 Numerical set-up and boundary conditions

In order to simulate hydrodynamic and mass transfer performance within the aforementioned loadings, boundary conditions shown in figure 6.4 are considered. Regarding the multiphase flow, the gas and liquid enter the domain from the top, where their corresponding inlet velocities are specified. To describe the flow near the solid particles, a no-slip boundary condition is applied at the catalyst's surface. In addition, since porous catalyst particles are commonly considered in full internal wetting conditions, very low static contact angle values are specified at the particles' surface. Since the numerical domains were extracted from larger cylindrical loadings, the lateral boundaries are set to symmetry-type conditions. Finally, at the bottom, gas and liquid exit the domain at operating pressure, meaning that the gauge pressure is equal to zero at the outlet.

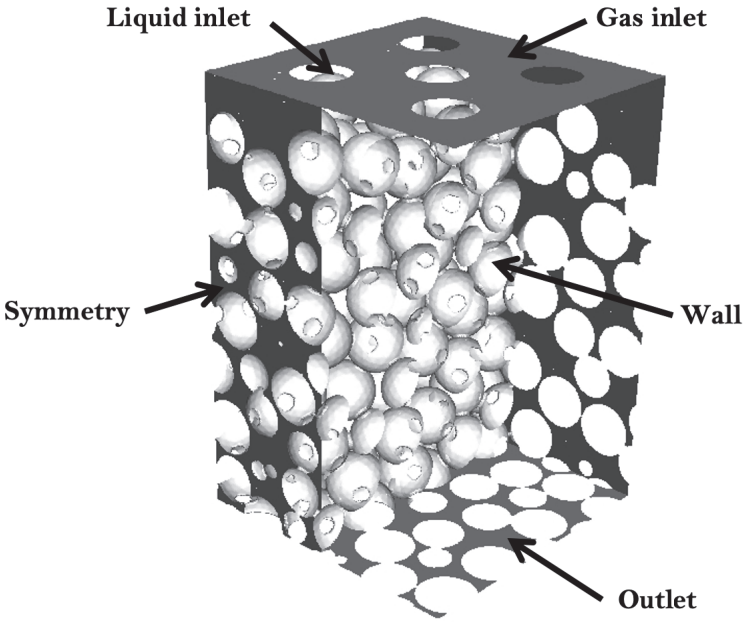

Figure 6.4 Numerical domain and boundary conditions for the two-phase flow predictions. Representative Elementary Volume of 1.0x1.0x1.5 cm^3 extracted from the spherical particles loading

When mass transfer is analysed simultaneously to hydrodynamics, hydrogen concentration is specified at the liquid and gas inlets respectively to 0 and $C^*_{H_2}$. As explained in the previous chapters, the heterogeneous catalytic reaction is implemented as a flux condition at the catalyst's wall. At the lateral and outlet boundaries, a null-flux condition is specified for hydrogen concentration. It is important to stress that the reactive flux method requires an adequate mesh

to ensure accuracy. Therefore, the mesh contains 2 cell layers perfectly fitting the solid catalyst. This will be further detailed in the mass transfer results discussion.

Table 6.2 Physical properties of the fluids composing the two-phase systems

System	Property	Liquid	Gas
Heptane-Nitrogen system	Density $[kg.m^{-3}]$	683.8	1.249
	Viscosity $[cP]$	0.39	0.017
	Surface tension $[mN.m^{-1}]$	20	
Hydrotreatment system (hydrocarbon-hydrogen)	Density $[kg.m^{-3}]$	750	15
	Viscosity $[cP]$	0.11	0.013
	Surface tension $[mN.m^{-1}]$	3.44	
Isohexadecane-Nitrogen system	Density $[kg.m^{-3}]$	784.4	1.249
	Viscosity $[cP]$	3.75	0.017
	Surface tension $[mN.m^{-1}]$	24.2	

Three different fluid systems were considered in this study: (i) heptane-nitrogen at standard conditions, (ii) a gas-liquid mixture with properties commonly encountered in the middle distillate hydrocracking processes and (iii) isohexadecane-nitrogen at standard conditions. The properties of the aforementioned systems are presented in table 6.2.

It is important to point out that the minimum contact angle value was specified for the heptane-nitrogen system. One of the objectives of this chapter is to develop a new wetting correlation based on the work of Julcour-Lebigue et al. [2009]. The authors considered that heptane is highly wetting since the catalyst quickly absorbs the liquid at the pores. Therefore, to reproduce this experimental observation, a static contact angle of 1° is chosen to conduct the simulations.

6.4 Mesh convergence study

As explained previously, the VOF approach requires a good quality mesh to provide accurate predictions. Therefore, a mesh independence study was performed on a representative volume of spheres in order to find the optimum mesh size. Four mesh densities are tested: (i) 1.7 Million, (ii) 3.4 Million, (iii) 4.3 Million and (iv) 11.2 Million cells. In order to capture the geometrical details, particularly at the solid-solid contact points, these meshes share in common

a refinement near the catalyst's wall. The mesh independence study is conducted for constant $V_{S,L}$ and $V_{S,G}$ conditions of: $V_{S,L} = 0.5cm/s$ and $V_{S,G} = 5cm/s$.

Table 6.3 Mesh resolutions and corresponding wetting efficiency values for $V_{S,L} = 0.5cm/s$ and $V_{S,G} = 5cm/s$

Mesh resolution	Coarse mesh	Medium mesh	Fine mesh	Very fine mesh	Correlation of Julcour-Lebigue et al. [2009]
Number of cells [Millions]	1.7	3.4	4.3	11.2	
Wetting efficiency f [-]	0.66	0.71	0.73	0.74	0.89

Table 6.3 summarises considered mesh resolutions and their corresponding wetting efficiency predictions. Following the increase of mesh resolution, the predicted wetting efficiency values increase until reaching a plateau. In addition, almost tripling mesh density (from 4.3M to 11.2M) increases wetting efficiency by merely 1.37%. Figure 6.5 shows the level of refinement in the coarse and very fine meshes.

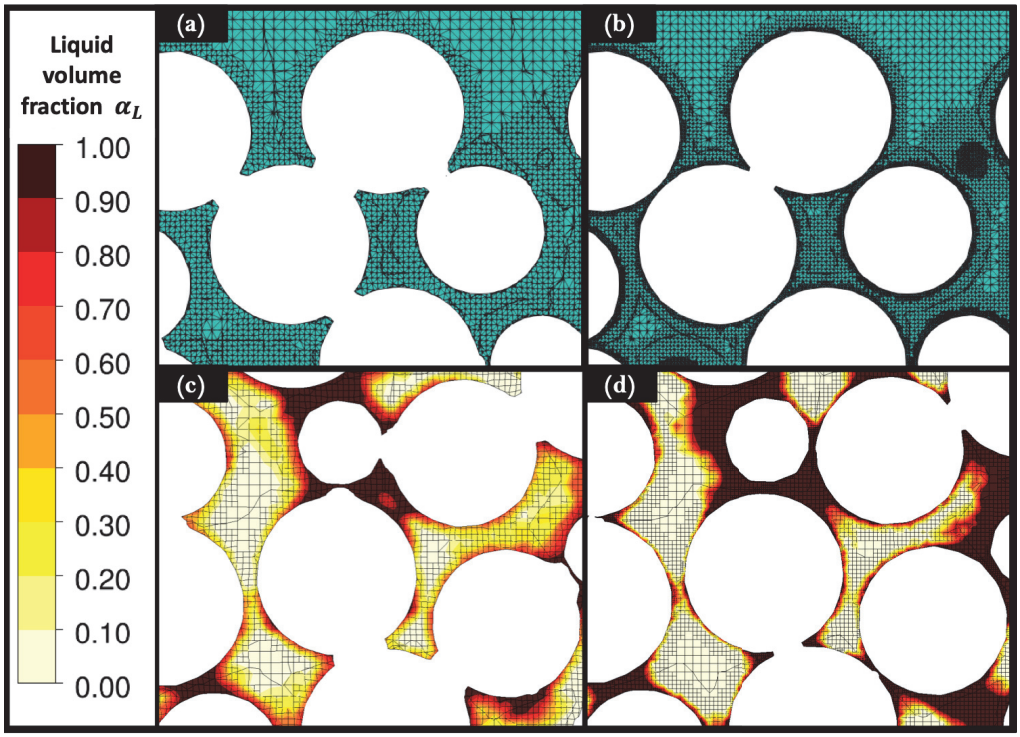

Figure 6.5 Minimum and maximum mesh densities : (a) 1.7Million, (b) 11.2Million cell meshes and Liquid fraction contour plot for (c) 1.7Million (d) 11.2Million cell meshes

Figure 6.5 illustrates contour plots of liquid volume fraction within the numerical domain for minimum and maximum mesh resolutions. The plots show clearly that the gas-liquid and liquid-solid interfaces are more distinguished for higher mesh resolutions. This means that numerical diffusion decreases with mesh resolution.
Numerical diffusion is evaluated from the predicted interface thicknesses, corresponding to $0 < \alpha_L < 1$. The more cells covered with intermediate volume fraction values there are, the more significant numerical diffusion is. For instance, the coarser mesh (1.7 Million) exhibits considerable numerical diffusion, leading to a non-realistic representation of the gas-liquid interface. In fact, as the grid gets sharper, numerical thicknesses decrease, resulting in sharp fluid-fluid and fluid-solid interfaces.
In addition, mesh sharpness ensures a good definition of the boundary layer near the particles. As a result, the real particle loading geometry is better fitted, particularly at the contact points between particles. Theoretically, the contact between two particles is a point, yet this point becomes a bridge during the meshing process, unless mesh resolution is heavily refined at these locations. It is therefore important to guarantee a correct resolution at the contact points with cells as small as possible.

To sum up, the 4.3 Million cell mesh gives similar results to those obtained with the 11.2 Million cell mesh, as shown in table 6.3. In addition, both meshes allow for a sharp description of the gas-liquid interface. However, when compared to the 4.3 Million cell mesh, the 11.2 Million cell mesh takes 6 to 7 times more time to reach convergence. Therefore, the 4.3 Million cell mesh is employed in the hereinafter simulations since it provides a trade off between result's precision and reasonable calculation times.

6.5 Inlet effect on gas-liquid flow distribution and stabilisation

Liquid inlet effect on hydrodynamics is studied in order to identify the flow establishment zone within calculation domains. Indeed, since the liquid feed consists of 5 point sources, liquid distribution might require a certain bed depth to stabilise. Also called "calming bed depth", this stabilisation distance is achieved when liquid reaches a steady distribution. In order to check the distance required for flow stabilisation, wetting efficiency is monitored in different regions of the numerical domains for HDT flow in several $V_{S,L}$ and $V_{S,G}$ conditions .

The numerical domain is divided into four sub-domains: (i) from 0 to 25% of the length L, (ii) from 25%L to 50%L, (iii) from 50%L to 75%L and (iv) from 75%L to 100%L, given that inlet is located at z=0 and outlet at z=L. Then, the wetted solid surface is calculated within each sub-domain. This study was for all particle shapes at different operating conditions. However, results are presented only for spherical particles since equivalent behaviours are found for all particle shapes.

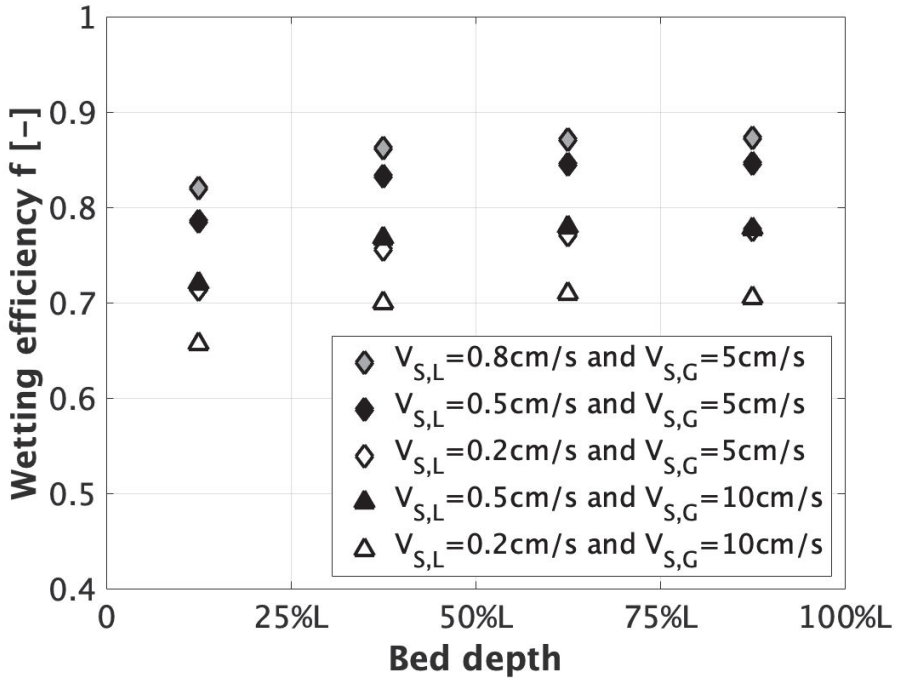

Figure 6.6 Wetting efficiency evolution within spherical particles' packing for HDT flow in different gas and liquid superficial velocities

Figure 6.6 presents wetting efficiency evolution obtained at different bed depths for spherical particles' loading. In the investigated $V_{S,L}$ and $V_{S,G}$ conditions, it can be observed that wetting efficiency reaches a plateau for bed depths beyond 6 cm (50%L), indicating that the developed flow is reached at 6 cm from the reactor's inlet. Indeed, wetting efficiency increases on average by 6% between (i) and (ii) sub-domains, then by 1.49% from (ii) to (iii) sub-domain, and finally by 0.03% from (iii) to (iv) sub-domains. Moreover, wetting efficiency follows a similar evolution regardless of gas and liquid superficial velocities. Due to complex phase interactions occurring near the inlet, and in order to achieve accurate and consistent results analysis, post-processing is conducted within the developed flow domain only.

6.6 Hydrodynamic predictions

6.6.1 Pressure drop predictions

A preliminary study was performed in order to validate pressure drop across the reactors. First, liquid downward flow was simulated in single-phase conditions for various Reynolds numbers at steady-state. These simulations were performed for loadings of spheres, trilobes and quadrilobes. Regarding boundary conditions, liquid superficial velocities ranging from 0.02mm/s to 30.75mm/s are investigated. The latter superficial velocities correspond to $0.05 < Re_L^* < 100$, where Re_L^* is a modified Reynolds number defined as follows:

$$Re_L^* = \frac{V_{S,L} d_e^* \rho_L}{\mu_L (1 - \varepsilon_B)} \tag{6.1}$$

d_e^* is the particles' equivalent diameter. Since Ergun law was originally developed for spherical particles, a sphericity factor is required to apply Ergun law on non-spherical particles [Trahan et al., 2014]. Indeed, the sphericity factor ψ is a measurement of how close a particle's shape is to a sphere. According to Brown [1950], the sphericity factor is expressed as follows:

$$\psi = \frac{\pi^{\frac{1}{3}} (6V_p)^{\frac{2}{3}}}{S_p} \tag{6.2}$$

Where V_p and S_p are respectively the particle's volume and surface area. The factor ψ is described as the ratio of (i) the surface area of a sphere with the same volume as the non-spherical particle to (ii) the surface area of the non-spherical particle. The modified equivalent diameter d_e^* is then defined as the following:

$$d_e^* = \psi d_e = \psi \frac{6V_p}{S_p} \tag{6.3}$$

Pressure drop estimations in porous media are achieved through Ergun law. A comparison between CFD results and Ergun law estimations is presented in figure 6.7. The parity plot highlights the accuracy of CFD in predicting single-phase pressure drop, since 95% of results are within ±20% and the majority is close to the identity line.

After checking the ability of CFD to handle pressure drop in single-phase flow conditions, the two-phase flow behaviour through three different loadings was predicted using the Volume-Of-Fluid approach. Table 6.4 summarises the investigated gas and liquid superficial velocities, as well as particle shapes. Thus, for each particle shape, 9 different ($V_{S,L}$,$V_{S,G}$) couples were simulated.

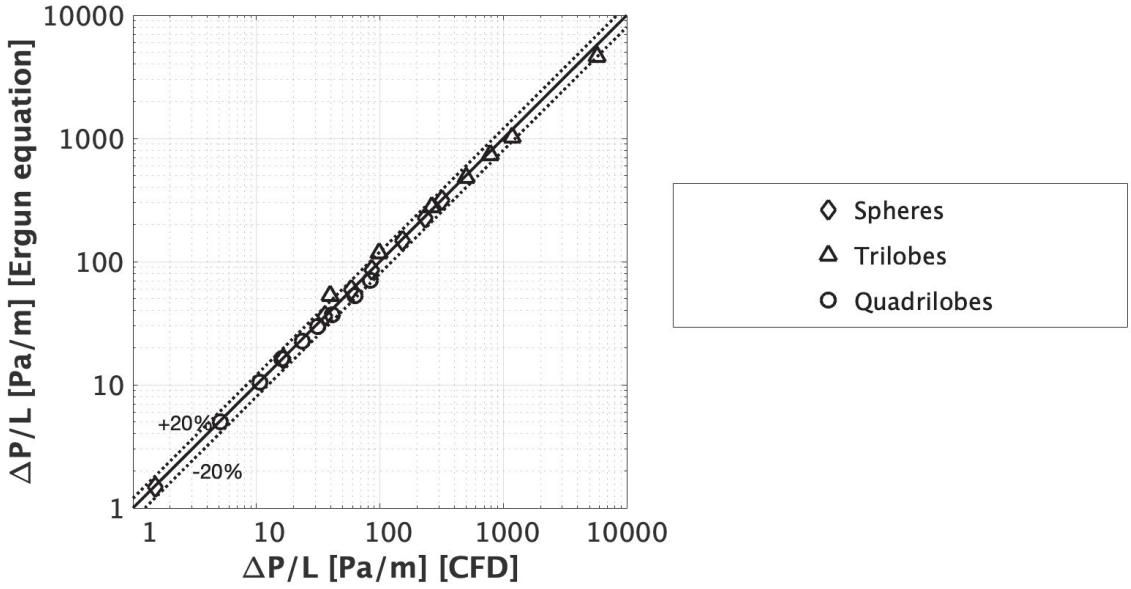

Figure 6.7 Parity diagram of single-phase pressure drop comparison between Ergun law and CFD. Sphericity factors are respectively $\psi = 1$, $\psi = 0.81$ and $\psi = 0.42$ for spheres, trilobes and quadrilobes. 20% error envelope

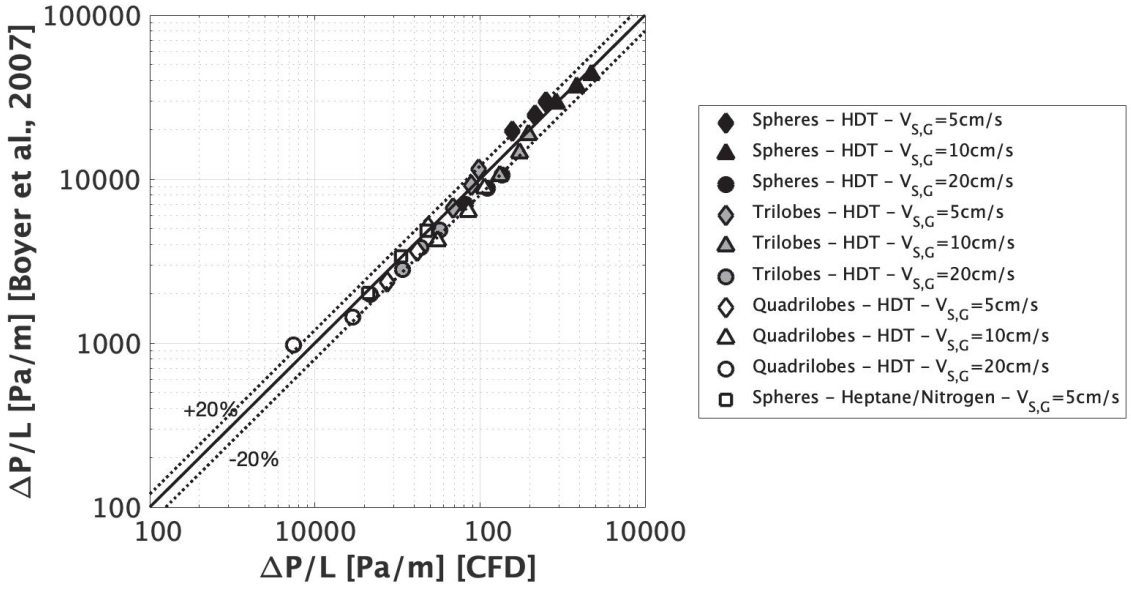

Figure 6.8 Parity diagram of two-phase pressure drop. Comparison between Boyer et al. [2007] and CFD for $V_{S,L} = 0.2, 0.5, 0.8 cm/s$ and $V_{S,G} = 5, 10, 20 cm/s$. Sphericity factors are respectively $\psi = 1$, $\psi = 0.81$ and $\psi = 0.42$ for spheres, trilobes and quadrilobes. 20% error envelope

Table 6.4 Loading properties and gas/liquid superficial velocities tested to validate the model

Particle shape	Modified equivalent diameter d_e^* [mm]	Bed void fraction ε_B [-]	$V_{S,L}[cm/s]$	$V_{S,G}[cm/s]$
Sphere	2.00	0.372	0.2	5.0
Trilobe	1.44	0.377	0.5	10.0
Quadrilobe	0.85	0.628	0.8	20.0

Boyer et al. [2007] investigated pressure drop and liquid retention in two-phase flow in the trickling regime and proposed predictive models for these two physical parameters.The authors validated these models over several experimental conditions and for different catalyst shapes. A two-phase pressure drop parity plot between CFD results and the model of Boyer et al. [2007] is presented in figure 6.8. The results show a very good agreement between CFD simulation and the model. Indeed, 80% of the plotted points lie within the ±20% deviation envelope, with an average relative error of 12.78%. It is interesting to note that the pressure drop obtained with quadrilobes is low in comparison to spheres and trilobes as shown in figure 6.8. This is mainly due to the high void fraction of the quadrilobe particles' loading. In addition, it is observed that the most significant deviation between correlation and simulation results is obtained at the highest $V_{S,G}$ values. The deviation could be attributed to a transition from laminar to turbulent flow, which is not accounted for in the CFD simulations.

6.6.2 Liquid saturation

Concurrently with two-phase pressure drop, liquid saturation is computed from the predicted liquid volume flowing through the particle loadings in established flow region. Figure 6.9 shows typical multiphase flow inside the investigated representative volumes, after reaching developed flow conditions. In the results presented hereinafter, liquid saturation is calculated by the ratio of predicted liquid volume to bed void volume.

For both investigated fluid systems, i.e hydrotreatment and heptane-nitrogen systems, predicted liquid saturation values are compared to the values given by the correlation of Boyer et al. [2007], as shown in figure 6.10. Even though CFD results slightly over-estimate liquid saturation compared to Boyer et al. [2007] model's predicted values, simulation results show a satisfactory agreement with an average relative deviation of 34%. Besides, it is interesting to

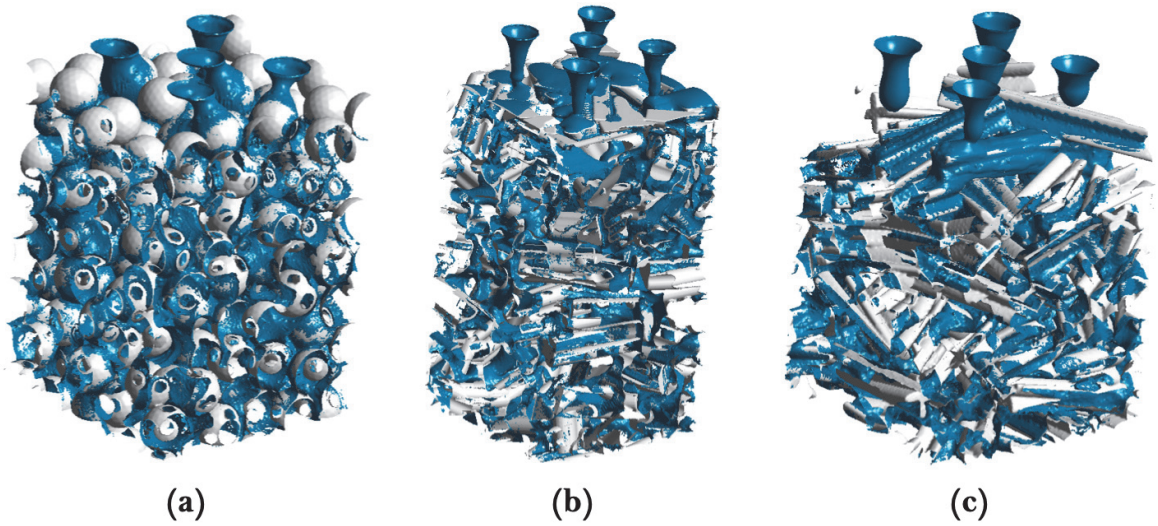

Figure 6.9 HDT flow through the different numerical domains: (a) spheres, (b) trilobes and (c) quadrilobes at $V_{S,L} = 0.5cm/s$ and $V_{S,G} = 10cm/s$. The liquid is represented by the dark colour

note that the highest deviations are obtained for quadrilobe-shaped particles. These deviations could be attributed to the fact that the model of Boyer et al. [2007] has not been validated on quadrilobe shapes. Moreover, it would be important to confront these CFD predictions to experimental data, not yet available.

From these results, it is observed that the higher the gas superficial velocity is, the lower the liquid saturation becomes. Such effect is a result of increased shear force at the gas-liquid interface, subsequently decreasing liquid film thickness through the particle loading. Furthermore, quadrilobe shaped particles have particularly deep concavities leading to liquid accumulation (cf. figure 6.9). Therefore, higher liquid saturation values are obtained for quadrilobes. Besides, in comparison to spheres and trilobes, the void fraction was previously reported to be higher for the quadrilobe loading, promoting lower interstitial gas velocities within the particle bed, and thus higher liquid saturations.

6.6.3 Liquid film thickness and flow regime

It is well known that liquid film thickness has significant effect on mass transfer, and thus it is of high importance in trickle-bed reactors. Since CFD allows access to local flow parameters, the CFD predicted average liquid film thicknesses are compared to the ones predicted by Nusselt's falling film theory estimations [Nusselt, 1916] assuming total catalyst wetting, as shown in figure 6.11. Initially developed for liquid flow over infinite vertical planes, Nusselt's

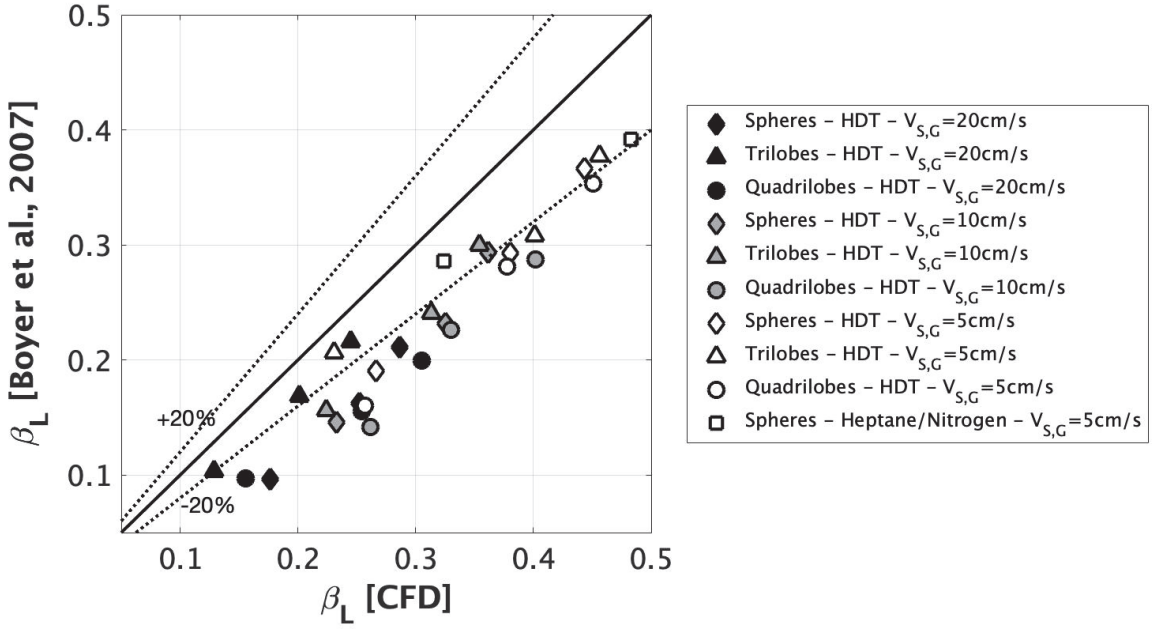

Figure 6.10 Parity diagram of liquid saturation. Comparison between Boyer et al. [2007] and CFD for $V_{S,L} = 0.2, 0.5, 0.8 cm/s$ and $V_{S,G} = 5, 10, 20 cm/s$. 20% error envelope

theory is assumed to be a reasonable reference candidate to describe liquid flow over complex surfaces, such as particle loadings. Commonly, in steady-state conditions, the average liquid film thickness is defined as the ratio of liquid volume to the wetted catalyst surface. To avoid inlet effects, liquid film thickness is computed within the developed flow domain.

Results plotted in figure 6.11 highlight the effect of gas and liquid superficial velocities on liquid film thickness. Indeed, the results show that increasing liquid superficial velocities lead to thicker liquid films, while the increase of gas flow rate results in the opposite effect. These conclusions are consistent with previous observations on liquid saturation. As the gas velocity increases, the gas-liquid shear interactions are enhanced, resulting in liquid entrainment and liquid film thickness reduction. Besides, for identical superficial velocities, liquid film thicknesses are on average higher for quadrilobes than the rest of the shapes. As was discussed previously, quadrilobe's geometrical characteristics (concavities) as well as lower interstitial gas velocities (high bed porosity) tend to promote an increase in film thickness.

Furthermore, results show that Nusselt's model [Nusselt, 1916] provides good predictions of $V_{S,L}$ effect on liquid film thickness. Thus, the model can be used to obtain an order of magnitude of the mean liquid film thickness, since mean relative deviations of 14.7 %, 18.1% and 20.6% are achieved respectively for spheres, trilobes and quadrilobes. Nevertheless, the

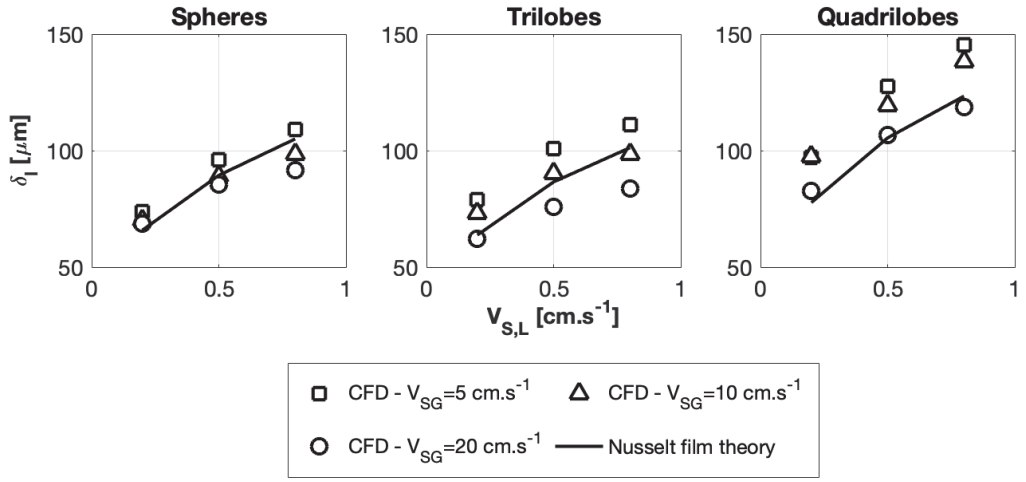

Figure 6.11 Comparison of Nusselt [1916] liquid film thickness to CFD results for spheres, trilobes and quadrilobes at $V_{S,L} = 0.2, 0.5, 0.8 cm/s$ and $V_{S,G} = 5, 10, 20 cm/s$

effect of $V_{S,G}$ is not captured by the model of [Nusselt, 1916], and more significant deviations may be expected for different contact angle values or resulting wetting efficiencies.

Besides accessing averaged parameters, CFD allows for a more local analysis of liquid film thickness distributions. To do so, the gas-liquid interface is first detected at $\alpha_L = 0.5$, then liquid film thickness is computed at each cell of the latter iso-surface. Using a Fluent built-in macro, the distance from catalyst's surface is computed at each mesh cell of the gas-liquid interface.

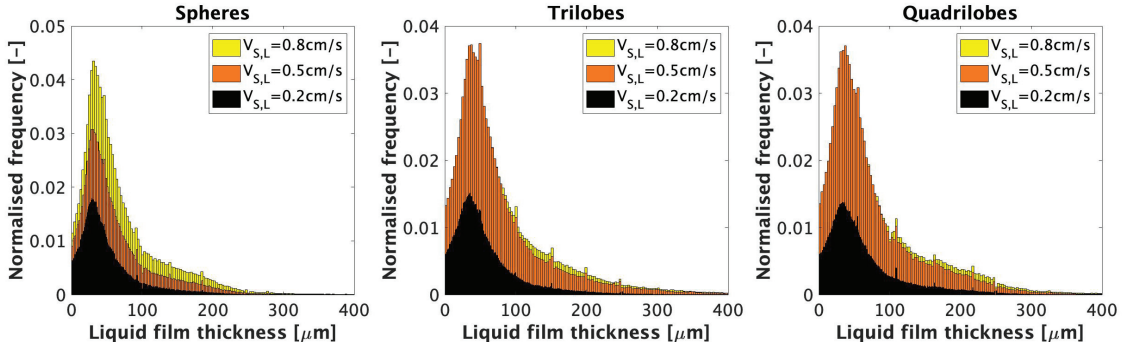

Figure 6.12 Effect of liquid superficial velocity on normalised local liquid film thickness distributions within the developed flow domain for spheres, trilobes and quadrilobes. Figures correspond to iso-gas superficial velocity of $V_{S,G} = 10 cm/s$

Figure 6.12 illustrates $V_{S,L}$ effect on local thickness distributions at constant gas superficial velocity ($V_{S,G}$=10cm/s). For spherical particles, increasing liquid superficial velocities leads to

a gradual distribution expansion since higher liquid film thicknesses are achieved. However, a different effect is observed for trilobes and quadrilobes. At $V_{S,L}$ values greater than 0.5cm/s, liquid film thickness distributions appear not to be affected by liquid superficial velocity. Even though figure 6.11 shows an increase in average film thickness with $V_{S,L}$ for trilobes and quadrilobes, local distributions show that film thicknesses remain similar. This can be attributed to variations in wetted catalyst area and liquid volume throughout the loadings, leading to a $V_{S,L}$ effect on averaged liquid film thicknesses.

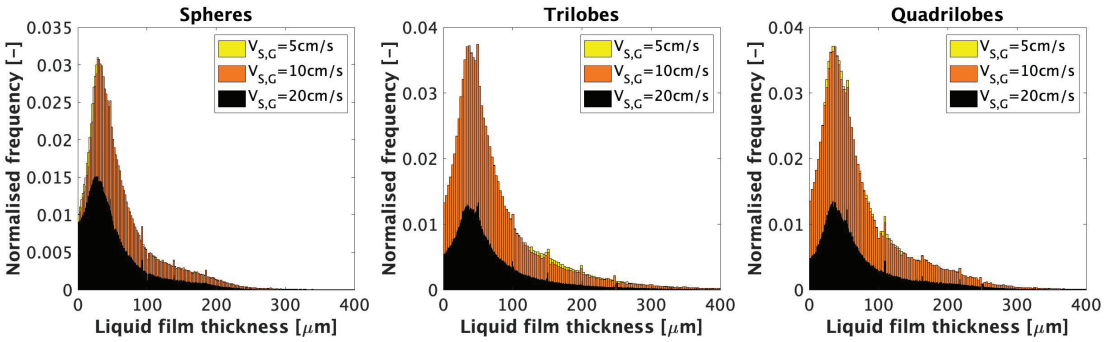

Figure 6.13 Effect of gas superficial velocity on normalised local liquid film thickness distributions within the developed flow domain for spheres, trilobes and quadrilobes. Figures correspond to iso-liquid superficial velocity of $V_{S,L} = 0.5cm/s$

Regarding $V_{S,G}$ effect at iso-liquid superficial velocity ($V_{S,L}$=0.5cm/s), local liquid film thickness distributions exhibit a decline with increasing $V_{S,G}$ values. This is attributed to higher shear forces at the gas-liquid interface. Moreover, similar $V_{S,G}$ effects are observed at $V_{S,G} = 5cm/s$ and $V_{S,G} = 10cm/s$, while a drastic liquid film thickness decrease is noticed at maximum $V_{S,G}$ regardless of particle shape.

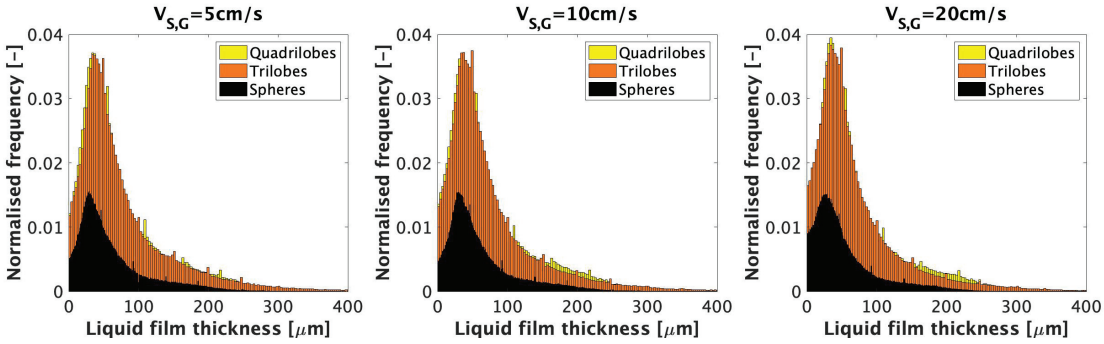

Figure 6.14 Particle shape effect on normalised local liquid film thickness distributions within the developed flow domain for $V_{S,G} = 5cm/s$, $V_{S,G} = 10cm/s$ and $V_{S,G} = 20cm/s$. Figures correspond to iso-liquid superficial velocity of $V_{S,L} = 0.5cm/s$

Finally, particle shape effect on local film thickness distributions is investigated in constant liquid and gas superficial velocities, as shown respectively in figures 6.14 and 6.15. First, at constant $V_{S,L}$ conditions, trilobes and quadrilobes manifest similar film thickness distributions, at different $V_{S,G}$ conditions. While spherical particles show the lowest liquid film thickness values, more spread distributions are achieved with trilobes and quadrilobes. This is attributed to particle cavities, which increase significantly liquid saturation and thus liquid film thickness. At constant gas superficial velocity (figure 6.15), particle shape effect is more amplified at minimum liquid superficial velocity. Different behaviours are observed since liquid film thickness decreases gradually from quadrilobes to trilobes until reaching a minimum value for spheres. At moderate and high $V_{S,G}$, similar distributions are achieved for quadrilobes and trilobes, owing to their concavities and high liquid saturations.

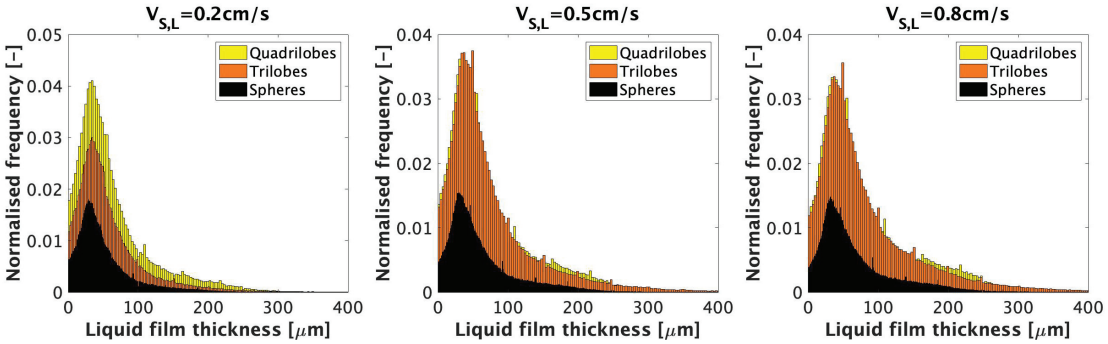

Figure 6.15 Particle shape effect on normalised local liquid film thickness distributions within the developed flow domain for $V_{S,L} = 0.2cm/s$, $V_{S,L} = 0.5cm/s$ and $V_{S,L} = 0.8cm/s$. Figures correspond to iso-liquid superficial velocity of $V_{S,G} = 10cm/s$

The effect that $V_{S,L}$ and $V_{S,G}$ have on liquid film thickness can also be carried over to flow regime. The evaluation of flow regime is achieved through analysis of the ratio between gas-liquid and liquid-solid interfacial areas. Usually, gas-liquid interface is identified by the $\alpha_L = 0.5$ iso-surface, whereas liquid-solid interface corresponds to solid wall where $\alpha_L \geq 0.5$. Following this analysis, two flow regimes can be identified: (i) film flow or (ii) rivulet flow. The former corresponds to ratios greater or equal to unity, since film flow is characterised by an even distribution of liquid over solid. Whereas, rivulet flow corresponds to ratios lower that unity, since it is characterised by liquid pockets advent. The ratios between interface and wetted areas are shown in figure 6.16.

For low and moderate $V_{S,G}$, it is clear that increasing liquid velocity decreases a_{GL}/a_{LS} due to improved wetted area. Increasing gas velocity allows for more liquid to be dragged along, resulting in reduction of wetted area and liquid pockets. Therefore, a film flow takes place in

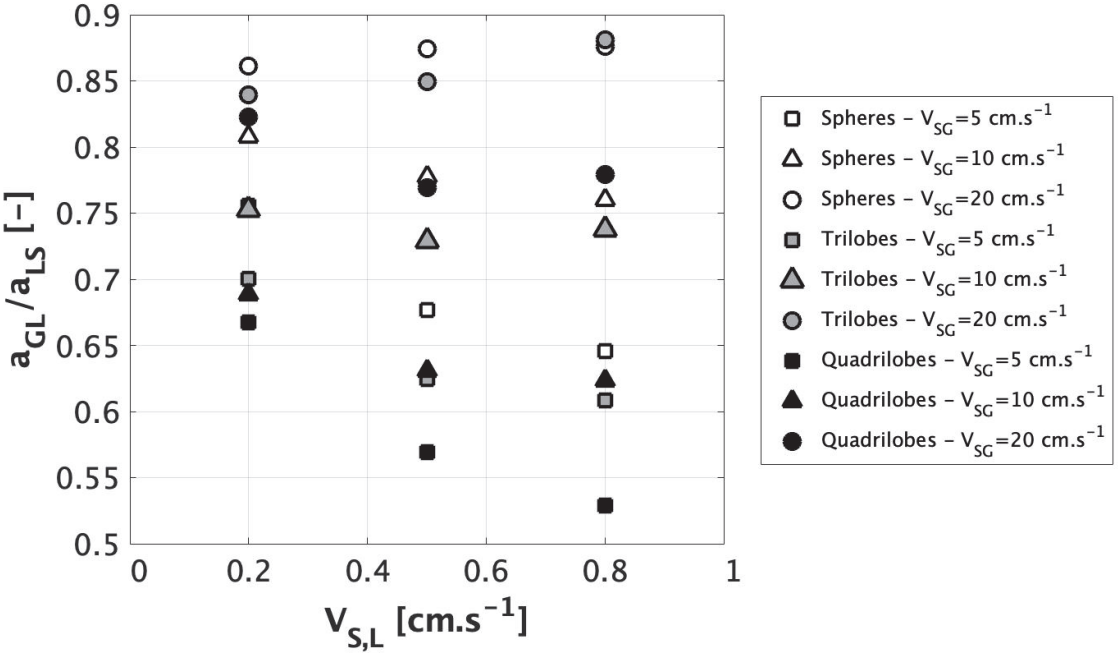

Figure 6.16 Ratio of gas-liquid interfacial area to wetted solid surface at different $V_{S,L}$ and $V_{S,G}$ conditions for HDT flow throughout spheres, trilobes and quadrilobes

the bed, as shown in figure 6.16 for $V_{S,G} = 20cm.s^{-1}$. On the other hand, since more liquid volume is available within the loadings, more liquid pockets are formed for higher superficial liquid velocities. Consequently, for low $V_{S,G}$, liquid flows under rivulet form as observed in figure 6.16.

6.7 Wetting efficiency analysis

6.7.1 Wetting efficiency predictions

Wetting efficiency is the criterion used to depict fully developed flow in simulations. This parameter is defined as the ratio of predicted wetted solid area to total solid area. For the sake of consistency, wetting efficiencies are computed in the developed flow domain, beyond the calming depth. The results are compared to the correlation of Julcour-Lebigue et al. [2009], given by the following equation:

$$f = 1 - exp\left[-1.986 \cdot Fr_L^{0.139} \cdot Mo_L^{0.019} \cdot \varepsilon_B^{-1.55}\right] \tag{6.4}$$

Where Fr_L and Mo_L are respectively the liquid Froude and Morton dimensionless numbers, which accurately describe both liquid velocity and physical properties effects. This correlation was developed for $V_{S,G} = 0$, $0.015 \leq V_{S,L}(cm/s) \leq 0.8$, $0.367 \leq \varepsilon_B \leq 0.410$ and three different particle shapes, namely spheres, trilobes and cylinders.

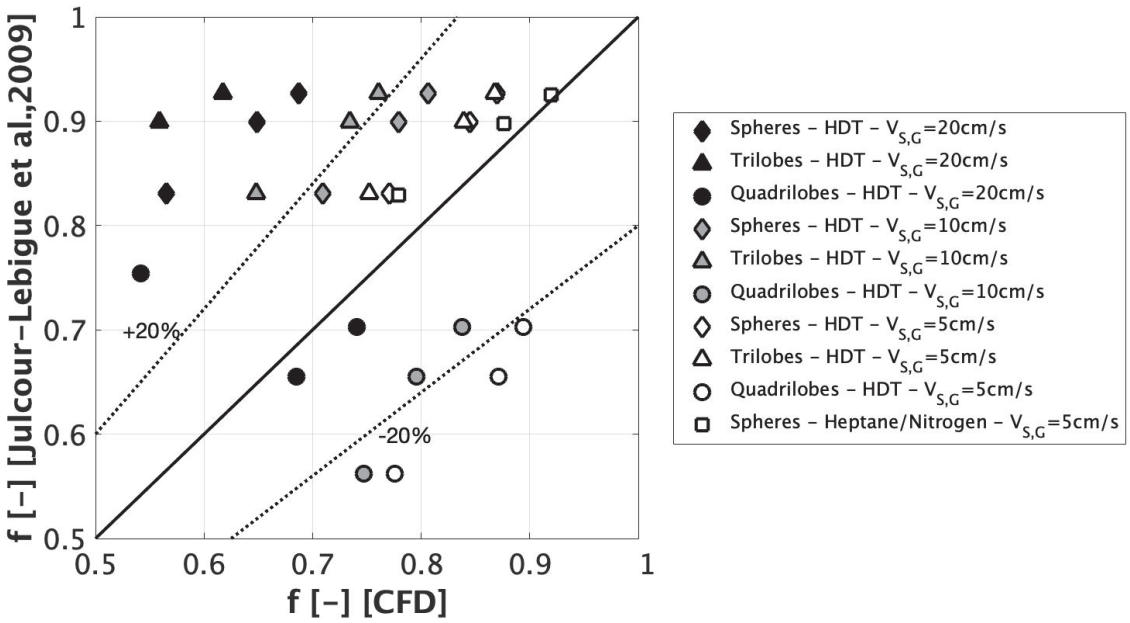

Figure 6.17 Wetting efficiency parity diagram. Comparison between Julcour-Lebigue et al. [2009] and CFD for $V_{S,L} = 0.2, 0.5, 0.8 cm/s$ and $V_{S,G} = 5, 10, 20 cm/s$. 20% error envelope

Figure 6.17 shows a comparison between wetting efficiencies obtained by CFD and the correlation of Julcour-Lebigue et al. [2009]. Several observations arise from the analysis of this parity plot. For spheres and trilobes, predicted wetting efficiency values are in a good agreement with the correlation of Julcour-Lebigue et al. [2009] at low gas superficial velocities. However, a significant deviation is observed for quadrilobe particles as the offset between CFD and correlation values is much higher than 20%. Although Julcour-Lebigue et al. [2009] developed a wetting efficiency correlation for different particle shapes, their investigation did not include quadrilobe shaped particles. In addition, the authors performed experiments in the absence of gas flow, thus equation (6.4) does not account for gas superficial velocity $V_{S,G}$ effect. For these reasons, high deviations between CFD and correlation are reported in figure 6.17.

It is interesting to note that CFD predictions show a negative impact of gas velocity $V_{S,G}$ on wetting efficiency. This is attributed to liquid disruption resulting in low liquid adherence to the solid surface. Wetting efficiency decrease with gas superficial velocities has also been observed in other CFD simulations, more recently on the work of Deng et al. [2020]. The authors argued

that these decreases are mainly due to higher gas-liquid interactions. Similarly, Herskowitz and Mosseri [1983] observed a global negative impact of $V_{S,G}$ on the global rate of a catalytic reaction. One proposed explanation was the increase of dry catalyst area with gas velocity, thus reducing the apparent effectiveness of the catalyst. This has been confirmed by Burghardt et al. [1990], who employed a mathematical description of the dynamic tracer method in order to review literature results. The authors reached the same observations.
In this context, a new correlation is developed on the basis of CFD simulations and former experimental data of [Julcour-Lebigue et al., 2009] to include the effect of catalyst shape and gas superficial velocity.

6.7.2 Development of a new wetting efficiency correlation

In their work, Julcour-Lebigue et al. [2009] correlated wetting efficiency to n=3 parameters, namely bed porosity ε_B, liquid Morton number Mo_L and Froude number Fr_L. In this section, an improvement of aforementioned correlation is proposed in order to include gas velocity and particle shape effects. In addition to predictions of hydrotreatment system and heptane-nitrogen, isohexadecane-nitrogen system was investigated by CFD in the conditions presented in table 6.2. In an effort to broaden physico-chemical properties, isohexadecane-nitrogen system was selected for its high liquid viscosity and surface tension.

Analysis of simulation results unveiled important physical scales to account for in the new correlation: (i) gas superficial velocity $V_{S,G}$, (ii) gas-phase properties (ρ_G,μ_G) and (iii) particle characteristics (d_p,a_s). Therefore, the proposed general formulation is given by:

$$f = 1 - exp\left[-A \cdot Fr_L^{0.139} \cdot Mo_L^{0.0195} \cdot \varepsilon_B^{-1.55} \cdot S^{C_0} \cdot \left(1 - C_1 \prod_{i=2}^{n} N_i^{C_i}\right)\right] \tag{6.5}$$

where $C_0, C_i, \ldots, C_n$ are fitted constants, N_i are different gas-phase dimensionless groups, A is a multiplication factor and S is a shape factor.
Gas-phase dimensionless groups N_i are chosen from the following dimensionless numbers: Re_G, Fr_G, Ga_G. Mathematical optimisation is conducted to determine the best group combination and fit the new correlation. The Sum of Squared Errors (SSE) between correlation and CFD/experimental values is minimised using a Generalised Reduced Gradient (GRG) algorithm. Table 6.5 summarises the obtained standard deviations with different group combinations. The minimum standard deviation was reached in Case 2 and Cases 4-7. Therefore, for the sake of simplicity, the gas Froude number is selected to include gas phase properties effect on wetting

efficiency. It is important to point out that for liquid flow at $V_{S,G} = 0$, Fr_G is equal to zero and the model resumes to the correlation of Julcour-Lebigue et al. [2009] (equation (6.4)).

Table 6.5 Standard deviations obtained with different dimensionless numbers' group combinations

Case number	C_1	Exponents C_i for i>1			Standard deviation σ [%]
		Re_G	Fr_G	Ga_G	
1	-0.092	0.283	0	0	7.40%
2	-0.437	0	0.367	0	4.98%
3	0.074	0	0	0.141	8.72%
4	-0.459	-0.006	0.362	0	4.98%
5	-0.451	0	0.359	-0.003	4.98%
6	-0.451	0.718	0	-0.362	4.98%
7	-0.451	0.118	0.300	0.062	4.98%

In order to expand the correlation of Julcour-Lebigue et al. [2009] to different particle shapes and sizes, a shape factor S is introduced in the wetting efficiency correlation (equation (6.5)). First, the shape factor $a_s d_p/\varepsilon_B^2$ used by Mills and Dudukovic [1981] was tested, but a good wetting efficiency estimation could not be reached. Nevertheless, a good fit was achieved using the shape factor proposed by Ellman et al. [1990]:

$$S = \frac{a_s d_h}{1-\varepsilon_B} \tag{6.6}$$

This factor accounts for particle's shape and size through the hydraulic diameter d_h. Whereas, bed characteristics are included through specific area of the bed a_s and its porosity ε_B. Considering the aforementioned shape factor, the wetting efficiency correlation is expressed as the following:

$$f = 1 - exp\left[-0.649 \cdot Fr_L^{0.139} \cdot Mo_L^{0.0195} \cdot \varepsilon_B^{-1.55} \left(\frac{d_h a_s}{1-\varepsilon_B}\right)^{1.147} \cdot (1 - 0.436 \cdot Fr_G^{0.371})\right] \tag{6.7}$$

Ellman et al. [1990] observed that the shape factor proposed in equation (6.6) could be further simplified since:

$$\frac{a_s d_h}{1-\varepsilon_B} \propto const \cdot \frac{\varepsilon_B^3}{(1-\varepsilon_B)^2} \tag{6.8}$$

Due to the proportionality observed in equation (6.8), the correlation expression given by equation (6.7) can be further simplified. Another correlation expression, accounting for both bed void fraction and particle shape, is presented in the following equation:

$$f = 1 - exp\left[-4.065 \cdot Fr_L^{0.139} \cdot Mo_L^{0.0195} \cdot \varepsilon_B^{-1.55} \left(\frac{\varepsilon_B^3}{(1-\varepsilon_B)^2}\right)^{0.376} \cdot (1 - 0.434 \cdot Fr_G^{0.376})\right] \tag{6.9}$$

The standard deviations for each correlation with different particle shape factors are shown in table 6.6. It can be seen that very good agreement is achieved by either expression, since standard deviation is under 10%.

Table 6.6 Standard deviation obtained by the model of Julcour-Lebigue et al. [2009] and the new developed correlation for two shape expressions

	Julcour-Lebigue et al. [2009]	Shape factor for the new correlation	
		$\frac{d_h a_s}{1-\varepsilon_B}$	$\frac{\varepsilon_B^3}{(1-\varepsilon_B)^2}$
Standard deviation	13.18%	6.04%	6.04%

The same standard deviation value is reached using equation (6.7) and equation (6.9), owing to the proportionality observed between shape factors used in both correlation expressions. Wetting efficiency is estimated using equation (6.7), and compared to experimental and CFD results for over 110 data points. Figure 6.18 presents a parity diagram of correlation estimations against CFD and experimental results.

It is possible to observe from figure 6.18 that all multiphase CFD results and almost all experimental results ($V_{S,G} = 0$) are well fitted with the new developed correlation, even for more irregular particle shapes. It should be noted that experiments and CFD simulations are carried out assuming a very low contact angle between liquid and solid. For this reason, important deviations are observed for liquids which are not “highly wetting” -such as water and ethanol-. A corrective term was developed by Julcour-Lebigue et al. [2009] which reasonably accounts for the contact angle effect through a critical liquid phase Froude number.

Without any doubt, table 6.6 and figure 6.18 confirm the good agreement between simulated and experimental values, highlighting the relevance of adding gas velocity and particle shape

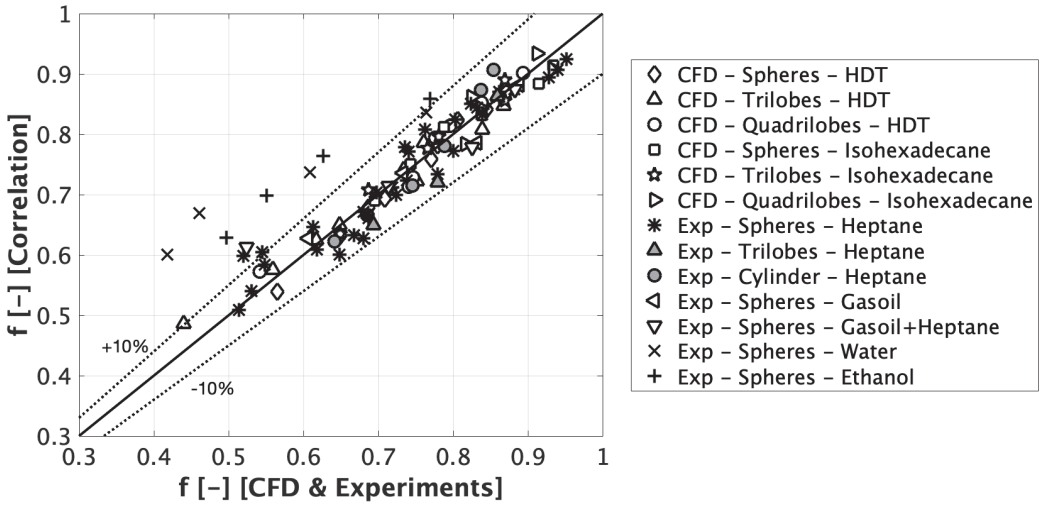

Figure 6.18 Wetting efficiency parity diagram. Comparison between the correlation derived in this work (equation (6.7)), CFD results and former experimental results of Julcour-Lebigue et al. [2009]. Dotted lines represent a $\pm 10\%$ error envelope

effects to the wetting efficiency correlation. Validity ranges of the wetting correlation are summarised in table 6.7, excluding water and ethanol studies.

6.7.3 Radial distributions

The effect of radial liquid distribution in TBRs is an important factor since it affects not only the reactor's performance, but also the effective wetting of catalyst particles. Experimentally, the radial liquid distribution is measured by collecting liquid flowing through different annular sections at the bottom of the reactor. In this section, wetting efficiency, liquid saturation and liquid film thickness were calculated within 50 different volume elements distributed radially at the bottom of the numerical domain. The objective is to provide insight on hydrodynamic parameters uniformity. Subsequently, radial distributions were analysed for $V_{S,L} = 0.5 cm/s$ and $V_{S,G} = 5 cm/s$ considering the three different particle shapes, as shown in figure 6.19.

It can be observed that particle shape influences liquid distribution within loadings. Indeed, when compared to spheres and trilobes, quadrilobe-shaped particles provide wider distributions, indicating heterogeneities in spatial liquid saturations, liquid film thicknesses and wetting efficiencies. Meanwhile, more uniform distributions are provided by spheres and trilobes since narrower distributions are achieved. This is attributed to bed porosity differences between particles. Spheres and trilobes are characterised by low bed porosities, resulting in high interstitial velocities, high interfacial shear force and thus better liquid distributions.

Table 6.7 Range of physical properties of gases and liquids used, geometric properties of packings used and operating conditions

Physical properties of gases and liquids used	
Liquid density, ρ_L [kg.m^{-3}]	$680 \leq \rho_L \leq 830$
Gas density, ρ_G [kg.m^{-3}]	$1.249 \leq \rho_G \leq 15$
Liquid viscosity, μ_L [Pa.s]	$0.11 \cdot 10^{-3} \leq \mu_L \leq 3.75 \cdot 10^{-3}$
Gas viscosity, μ_G [Pa.s]	$1.3 \cdot 10^{-5} \leq \mu_G \leq 1.7 \cdot 10^{-5}$
Surface tension, σ_L [mN.m^{-1}]	$3.44 \leq \sigma_L \leq 28.1$
Geometric properties of packings used	
Equivalent diameter, d_p [mm]	$1.44 \leq d_p \leq 7$
Bed porosity, ε_B [-]	$0.367 \leq \varepsilon_B \leq 0.611$
Particle shape	Spheres, trilobes and quadrilobes
Packing's specific surface area, $a_p[m^2/m^3]$	$516 \leq a_p \leq 2604$
Operating conditions	
Liquid mass flow rate, L $[kg.m^{-2}.s^{-1}]$	$1.34 \leq L \leq 60.1$
Gas mass flow rate, G $[kg.m^{-2}.s^{-1}]$	$0 \leq G \leq 3$

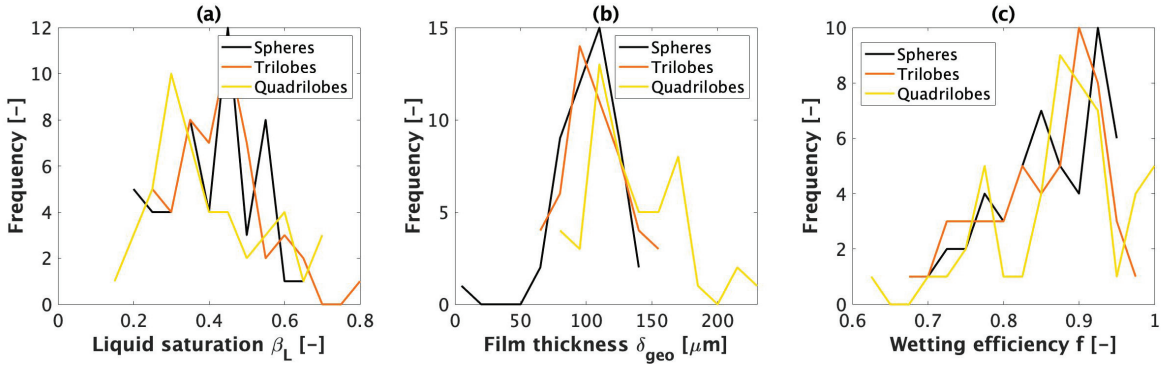

Figure 6.19 Effect of particle shape (spheres, trilobes and quadrilobes) on radial distributions for (a) liquid saturation, (b) liquid film thickness and (c) wetting efficiency. Predictions obtained for hydrotreatment system, at $V_{S,L} = 0.5cm/s$ and $V_{S,G} = 5cm/s$

As discussed in previous sections, higher wetting efficiency values are reached for quadrilobe-shaped particle. However, particle's geometrical features (concavities) promote high liquid saturations and liquid film thicknesses. Indeed, capillarity effects lead to liquid accumulation

in quadrilobe concavities. Therefore, higher mean liquid saturation and liquid film thickness values are achieved, as shown in figure 6.19.

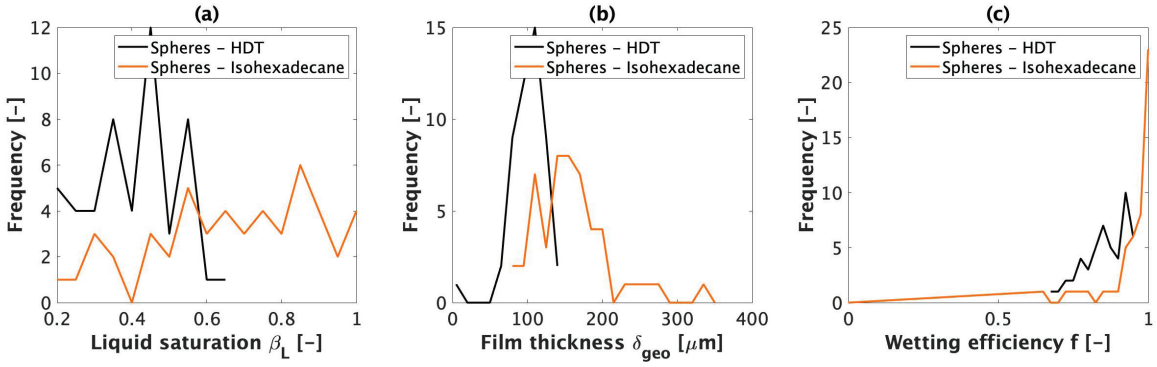

Figure 6.20 Effect of liquid viscosity on radial distributions in spherical particles loading for (a) liquid saturation, (b) liquid film thickness and (c) wetting efficiency. Predictions obtained for HDT and isohexadecane/nitrogen systems, at $V_{S,L} = 0.5cm/s$ and $V_{S,G} = 5cm/s$

HDT and isotecane systems are compared in terms of radial distributions within spherical particle's loading, as shown in figure 6.20. First, average liquid saturation and film thickness indicate the presence of liquid pockets in high viscosity liquids (Isohexadecane). Concurrently, a better liquid distribution is achieved for high gas-phase density values (Nitrogen). These conclusions are more apparent on distribution characteristics, as summarised in table 6.8.

Table 6.8 Characteristics of hydrodynamic parameters' distributions (mean values μ and variance σ^2) for different two-phase systems and particle shapes

		HDT system		Isohexadecane-Nitrogen system	
Particle shape	Parameter	μ	σ^2	μ	σ^2
Spheres	Liquid film thickness δ_{geo} [μm]	91.9	23.0	151.8	49.3
	Wetting efficiency [–]	0.84	0.07	0.87	0.10
	Liquid saturation [-]	0.38	0.12	0.64	0.22
Trilobes	Liquid film thickness δ_{geo} [μm]	97.5	22.7	152.7	29.8
	Wetting efficiency [–]	0.84	0.07	0.87	0.10
	Liquid saturation [-]	0.41	0.12	0.71	0.18
Quadrilobes	Liquid film thickness δ_{geo} [μm]	126.6	36.1	218.0	63.4
	Wetting efficiency [–]	0.87	0.08	0.94	0.08
	Liquid saturation [-]	0.41	0.17	0.71	0.25

6.8 Gas-liquid-solid mass transfer

Considering hydrogenation of α-methylstyrene, gas-liquid-solid mass transfer is simulated within the three trickle-bed loadings. Boundary conditions presented in section 6.3 are applied in a similar manner to the considered loadings. Based on hydrodynamic observations, the reactors operate in partial wetting conditions. Therefore, it is important to note that the reactive flux is applied on the wetted surfaces. First, mass transfer has been compared in non-reactive and reactive conditions, as shown in figures 6.21 and 6.22. Through comparison of non-reactive simulations for different liquid superficial velocities, it is possible to observe the evolution of calming depth. Concentration profile requires longer calming depths as liquid superficial velocity increases. Therefore, to overcome inlet effects, the post-processing will be conducted in the second half of the domain, where all transport quantities reach developed conditions.

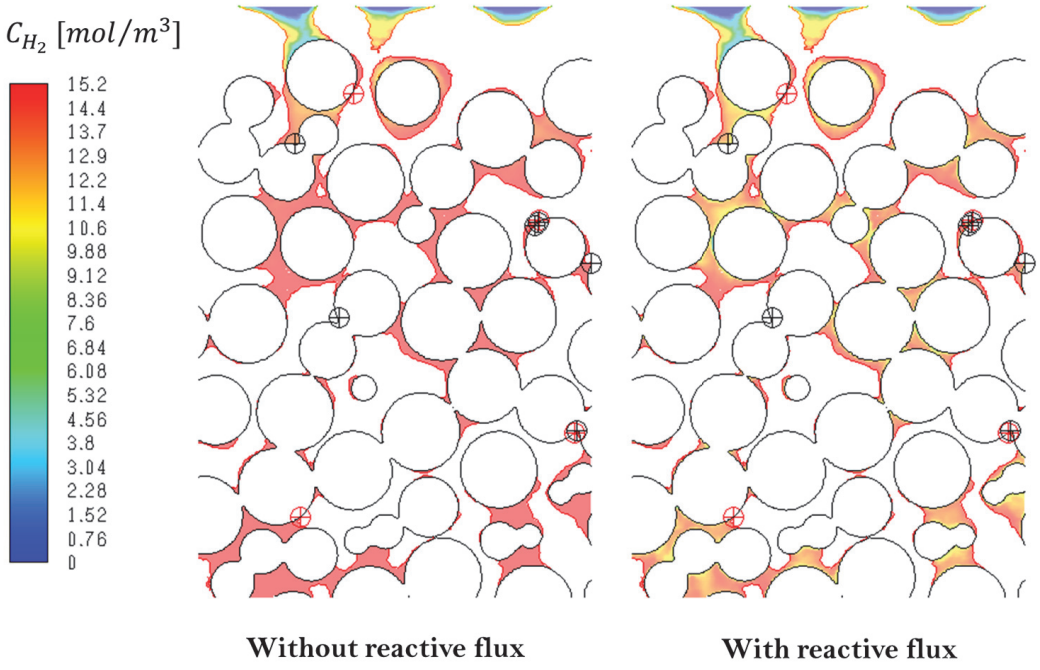

Figure 6.21 Converged hydrogen concentration profiles within spherical particles loading at $V_{S,L} = 0.2cm/s$ and $V_{S,G} = 5cm/s$

At the same gas and liquid superficial velocities, an apparent difference is observed between concentration profiles in reactive and non-reactive conditions. When a reactive flux is applied at the wetted catalyst surface, a hydrogen consumption is noticed near the catalyst wall. However, qualitatively, the observed mass transfer boundary layers are thin since concentration gradient

is located a few cells further from the catalyst wall. This is confirmed quantitatively in what follows. Simulations were performed on trilobe and quadrilobe loadings as well, as shown in figure 6.23. The aim is to determine whether catalyst extrudates provide better mass transfer performance.

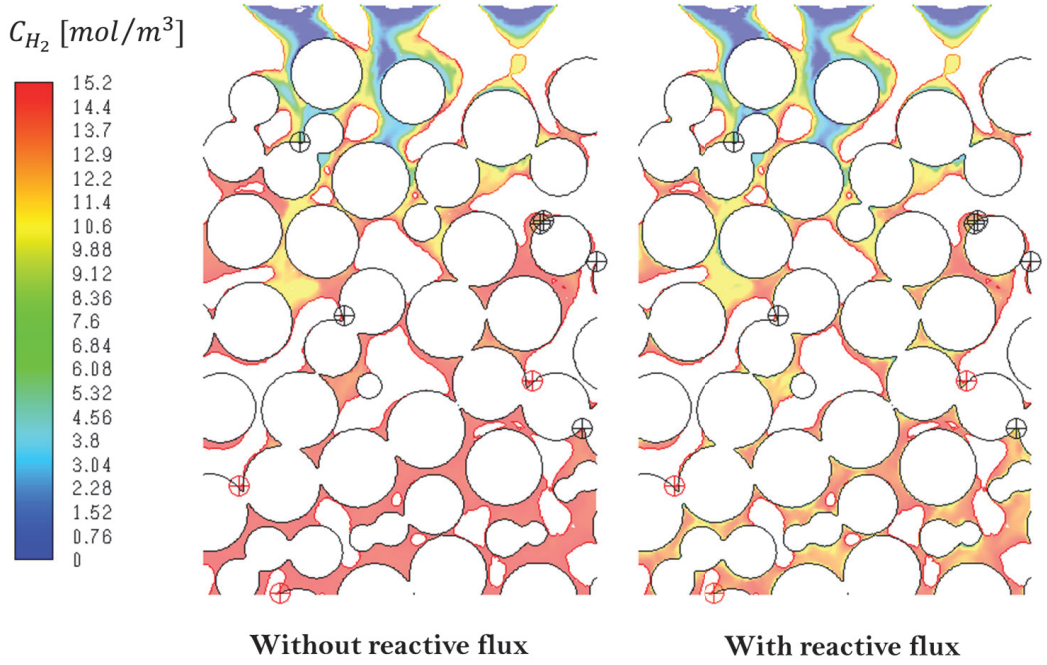

Figure 6.22 Converged hydrogen concentration profiles within spherical particles loading at $V_{S,L} = 0.8cm/s$ and $V_{S,G} = 5cm/s$

After reaching stabilisation, wetting efficiency, hydrogen consumption flux and mean hydrogen concentration are post-processed within fully developed flow domains. Gas-liquid-solid mass transfer coefficients are computed for each shape at constant $V_{S,G}$ and different $V_{S,L}$ conditions, as shown in figure 6.24. The highest overall mass transfer coefficients are achieved for quadrilobes. This is attributed to their high surface to volume ratio in comparison to spheres and trilobes. In addition, due to its geometrical features, this particular shape allows for higher liquid saturations and wetting efficiencies, therefore enhancing the reactive flux. Besides, a similar trend is observed with liquid superficial velocity evolution, regardless of particle shape. This is mainly due to improved solid wetting with increasing liquid flow rates.

Subsequently, based on the film model, the mass transfer boundary layers are computed and reported in table 6.9. First, it is observed that hydrodynamic liquid film thicknesses (δ_{geo}) are much higher than mass transfer boundary layer thicknesses. In addition, increasing particle's

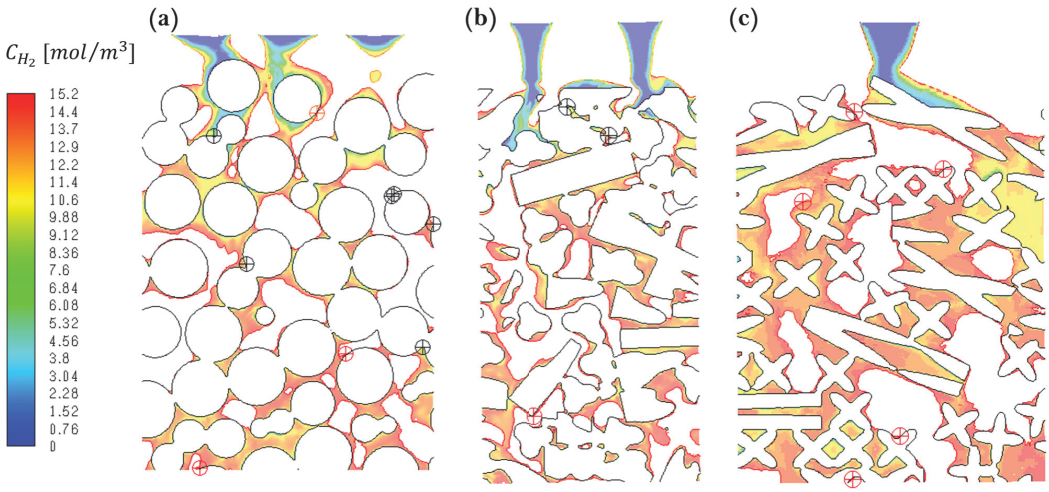

Figure 6.23 Converged hydrogen concentration profiles at $V_{S,L} = 0.5cm/s$ and $V_{S,G} = 5cm/s$ within (a) spheres, (b) trilobes and (c) quadrilobes loadings

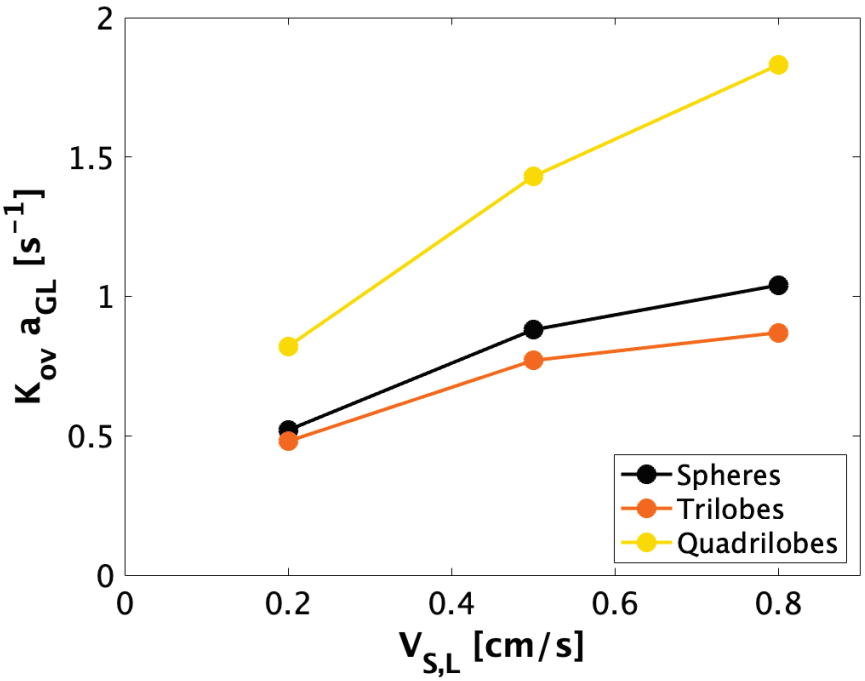

Figure 6.24 Gas-liquid-solid mass transfer coefficient evolution with liquid superficial velocity and particle shape. Simulations are conducted at $V_{S,G} = 5cm/s$

surface-to-volume ratio decreases significantly mass transfer boundary layer thickness, for which the lowest value is achieved using quadrilobes. This is consistent with behaviour observed in tortuous flow paths, within the spherical particles string reactor and the 3D-printed milli-reactor. This is attributed to the effect of convective concentration transport, supplying the liquid film with high hydrogen quantities.

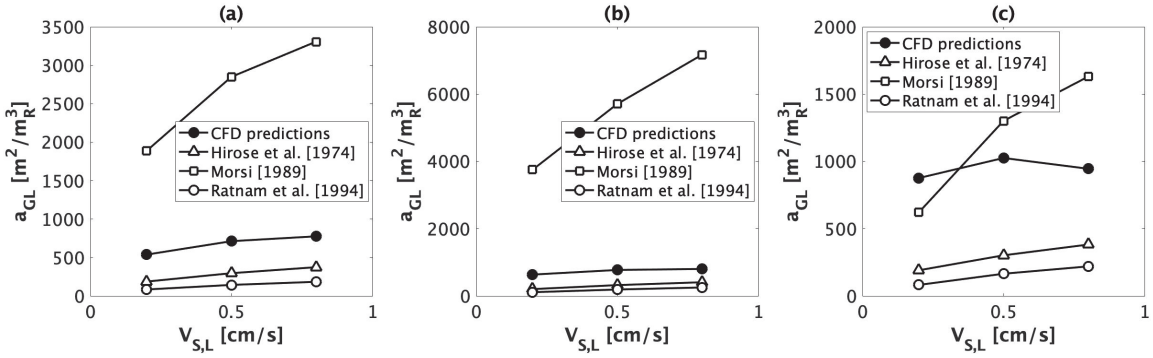

Figure 6.25 Comparison between predicted gas-liquid interfacial area and correlations of Hirose et al. [1974], Morsi [1989] and Ratnam et al. [1994] for (a) spheres, (b) trilobes and (c) quadrilobes. Simulations are conducted at $V_{S,G} = 5cm/s$

Furthermore, gas-liquid interfacial area values are compared to correlations of Hirose et al. [1974], Morsi [1989] and Ratnam et al. [1994], as shown in figure 6.25. First of all, predicted interfacial areas follow the same trend anticipated by all correlations, that is to say increasing values with liquid superficial velocities. Besides, regardless of particle shape, correlations of Hirose et al. [1974] and Ratnam et al. [1994] underestimate interfacial area values. For spheres and trilobes, the correlation of Morsi [1989] highly overestimates gas-liquid interfacial area, while the same does not apply on quadrilobes. This is attributed to a combined effect of bed porosity, pressure drop and liquid saturation. Indeed, spheres and trilobes have similar porosities, and thus close pressure drops. Meanwhile, quadrilobes loading is characterised by a higher porosity, lower pressure drop and high liquid saturation values. Since correlation of Morsi [1989] is very much dependent on the latter parameters, different deviations are achieved between particle shapes. Overall, even though high deviations are observed, CFD predictions are bounded between correlation estimations.

Table 6.9 Gas-liquid-solid mass transfer boundary layer thickness for the considered particle shapes (spheres, trilobes and quadrilobes) at different gas and liquid superficial velocities

Particle shape	$V_{S,L}$ [cm/s]	$V_{S,G}$ [cm/s]	Gas-liquid interfacial area a_{GL} $[m^2/m_R^3]$	Liquid-solid interfacial area a_{LS} $[m^2/m_R^3]$	Liquid holdup $\varepsilon_{l,t}$ [%]	Liquid film thickness δ_{geo} $[\mu m]$	Mass transfer coefficient K_{ov} [m/s]	Mass transfer coefficient $K_{ov}a_{ov}[s^{-1}]$	$\delta_c = \frac{D_{m,H_2}}{K_{ov}}$ $[\mu m]$
Spheres	0.2	5	537.92	928.12	9%	100.4	$1.73 \cdot 10^{-4}$	0.52	5.00
	0.5	5	712.2	1252.90	14%	115.5	$3.06 \cdot 10^{-4}$	0.88	3.95
	0.8	5	775.18	1362.09	17%	122.72	$3.66 \cdot 10^{-4}$	1.04	3.62
Trilobes	0.2	5	634.83	1105.69	11%	96.5	$7.54 \cdot 10^{-4}$	0.48	6.47
	0.5	5	772.54	1391.59	16%	115.38	$9.90 \cdot 10^{-4}$	0.77	4.93
	0.8	5	803.19	1476.04	18%	124.09	$1.08 \cdot 10^{-3}$	0.87	4.52
Quadrilobes	0.2	5	876.35	1457.52	17%	121.06	$1.14 \cdot 10^{-3}$	0.82	4.27
	0.5	5	1025.26	1921.46	28%	144.54	$1.40 \cdot 10^{-3}$	1.43	3.49
	0.8	5	945.21	1951.77	32%	151.30	$1.52 \cdot 10^{-3}$	1.83	3.20

6.9 Conclusion

In this chapter, Computational Fluid Dynamics were employed to investigate the influence of catalyst shape, fluids' properties and gas/liquid flow operating conditions on pressure drop, liquid saturation, liquid flow behaviour, wetting efficiency and gas-liquid-solid mass transfer in trickle-bed reactors.

A numerical model grounded on the Volume-Of-Fluid approach was used. The multiphase CFD results were compared to validated and well-established correlations from literature for pressure drop, liquid saturation, liquid film thickness and wetting efficiency. A good agreement was achieved between CFD results and existing correlations (Boyer et al. [2007]) and Julcour-Lebigue et al. [2009]). Therefore, these results validated the numerical model and showed that CFD can be a powerful tool to predict complex flow patterns in trickle-bed reactors. In addition, CFD allows access to local phenomena and spatial distributions of transport parameters within the loadings, such as liquid film thicknesses.

The CFD model is then employed to investigate effects of (i) gas and liquid velocity, (ii) gas and liquid properties and (iii) catalyst shape on flow behaviour and wetting efficiency. It is found that increasing gas velocity leads to the decrease of wetting efficiency, with stronger effects noticed at higher pressures due to the increase of gas density. This was already observed in previous studies (such as the study conducted by Al-Dahhan and Dudukovic [1995]). Moreover, particle geometry effect on hydrodynamic parameters was found greater for irregular shapes (quadrilobes). Overall results analysis revealed the significant influence of gas superficial velocity and particle shape on hydrodynamic parameters, particularly wetting efficiency. Therefore, an expansion of the wetting efficiency correlation of Julcour-Lebigue et al. [2009] is proposed. In order to account for gas velocity and particle shape effects, two additional dimensionless numbers are added into the initial correlation. The gas velocity effect is included through gas Froude number Fr_G, while particle shape effect is accounted for through two shape factor expressions, depending on available characteristics.

The new correlation, developed in this chapter, can predict wetting efficiency with good accuracy (less than 10% deviation) for CFD experiments and already published experimental results of Julcour-Lebigue et al. [2009]. The correlation is valid for a wide range of physico-chemical conditions, at high and low pressures, involving highly wetting liquid-solid systems as hydrocarbon and alumina. Further investigations may be required to extend the models to much less wetting two-phase systems.

Regarding mass transfer, gas-liquid-solid mass transfer was analysed considering α-methylstyrene hydrogenation to cumene. First, concentration profiles are compared in non-reactive and reactive conditions. Qualitatively, the reactive flux is found to consume hydrogen near the catalyst surface, which is later confirmed quantitatively through mass transfer boundary layer thickness values. Besides, it is found that particles with high surface-to-volume ratio provide better mass transfer performance. This is mainly attributed to their geometrical features, allowing for higher wetting and liquid saturations. In the same vein, liquid superficial velocity is found to have a positive effect of overall mass transfer, for the same reasons aforementioned.

Chapter 7

Results summary and discussion

7.1 Introduction

This chapter presents an overall discussion on obtained results for different reactor configurations. First, the numerical model employed to perform simulations is recalled. Then, study cases are described to highlight the increasing complexity. Afterwards, hydrodynamic and mass transfer analysis is conducted to point out performance similarities and differences between study cases.

7.2 Numerical model

CFD simulations are conducted using ANSYS Fluent, which is a commercial CFD code. The numerical model couples two-phase flow predictions to gas-liquid-solid mass transfer, as well as heterogeneous catalytic reaction. First, the two-phase flow is solved using Volume-Of-Fluid approach, which provides access to local interfacial information. This method is suitable to describe immiscible phases flows, and offers an explicit description and tracking of the involved interfacial areas. This is achieved through numerical resolution of a volume fraction transport equation.
Similarly, to predict mass transfer performance, a concentration transport equation is solved for the limiting reagent. The heterogeneous catalytic reaction is accounted for through the reactive flux method, which consists of specifying a flux boundary condition at the catalyst surface to describe the catalytic reaction. Although the reactive contribution is reduced to a surface flux, diffusion within catalyst layer is achieved through a surface efficiency factor.

Cocurrently with the aforementioned equations, continuity and momentum transport equations are solved to provide local velocity and pressure profiles.

7.3 Study cases

In the present work, considered study cases fall within an increasing complexity strategy, as explained previously. An exhaustive listing of these cases is presented in figure 7.1. First, a bi-dimensional vertical falling liquid film is simulated, and the numerical model was validated against analytical solutions of Nusselt [1916], Higbie [1935] and Danckwerts [1970], respectively for hydrodynamics, physical gas absorption and chemical gas absorption. Afterwards, in analogy to the investigation conducted by Tourvieille et al. [2013] on a Falling Film Micro-structured Reactor (FFMR), gas-liquid-solid reactive mass transfer is predicted using the developed numerical model. Following the latter validation, more complex geometries with tortuous flow paths are considered. Therefore, two-phase flow is simulated within a spherical string reactor, 3D-printed milli-reactor and catalyst particles' loading.

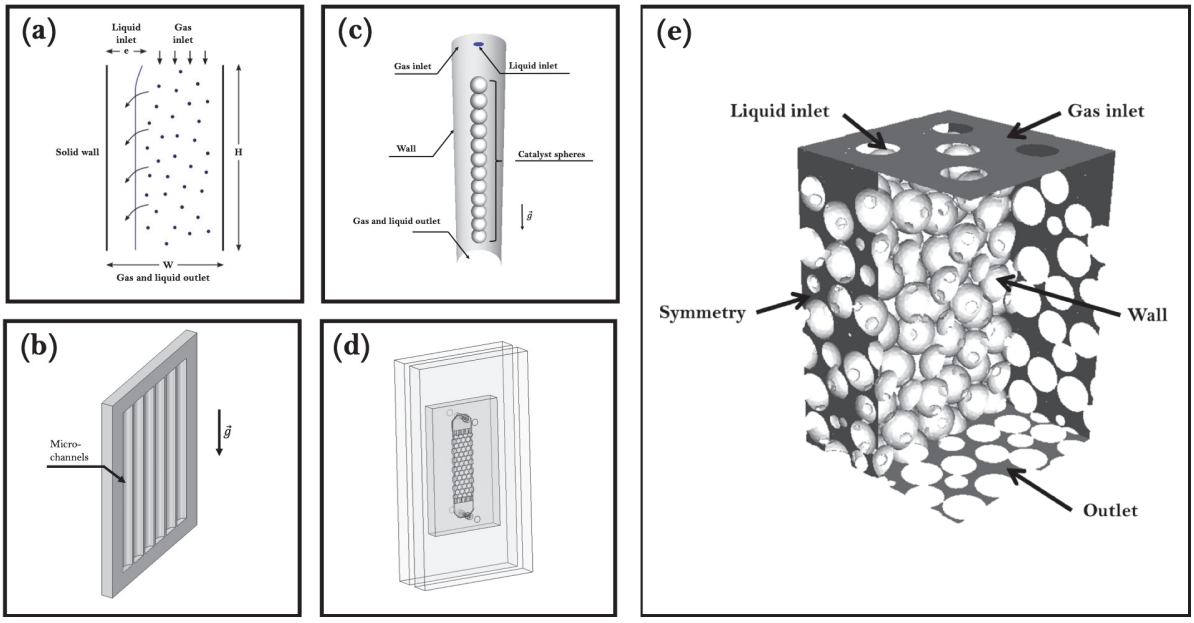

Figure 7.1 Investigated study cases listing from least to most complex configurations: (a) bi-dimensional vertical falling liquid film, (b) Falling Film Micro-structured Reactor (FFMR) [Tourvieille et al., 2013], (c) Spherical particles' string reactor, (d) 3D-printed milli-reactor and (e) trickle-bed reactor loadings (with spheres, trilobes or quadrilobes)

Behaviour complexity is induced through catalyst geometry. Indeed, both the vertical falling film and FFMR are characterised by uniformly shaped catalyst walls. Meanwhile, the

string reactor contains an ideal spherical loading. The latter presents geometrical features which would significantly impact the performance by inducing periodic hydrodynamic changes. The same principle applies on the milli-reactor and trickle-bed reactors.

The present work covered reactor performance in several configurations, summarised in table 7.1.

Table 7.1 Summary of covered configurations in the present work

Case	(a)	(b)	(c)	(d)	(e)
Catalyst features	Vertical plane	Vertical semi-elliptic channel	Stacked spherical particles	3D-printed hemi-spherical plots	Particle loading (spheres, trilobes, quadrilobes)
Catalyst wetting	Total	Total	Total	Partial	Partial
Flow path	Non-tortuous	Non-tortuous	Tortuous	Tortuous	Tortuous
Validation	+	+	-	+	+
Validated parameters	U_I	a_{GL}	-	wetting efficiency	wetting efficiency
	film thickness	film thickness profile	-	H_2 flux	single-phase ΔP
	k_{GL}	H_2 flux	-	α-methylstyrene conversion	Two-phase ΔP
	E = f(Ha)	α-methylstyrene conversion	-		equivalent diameter
Wetting efficiency f [-]	1	1	1	0.31 to 0.65	0.44 to 0.89
δ_{geo} $[\mu m]$	85	76 to 92	90 to 200	130 to 172	61 to 145
K_{ov} $[s^{-1}]$	0.69	2.54 to 4.31	0.09 to 0.19	0.2 to 0.23	0.48 to 1.83
$\delta_{transfer}/\delta_{geo}$	~ 1	0.65 to 0.73	0.17 to 0.29	0.05 to 0.09	0.015 to 0.067
Mass transfer regime	Diffusive	Diffusive	Significant convective supply		

7.4 Hydrodynamic analysis

Overall analysis of hydrodynamic behaviour in the study cases highlights some differences in liquid flow patterns, as shown in figure 7.2. First of all, a velocity profile establishment over the reactor's length is observed in the bi-dimensional and micro-structured falling films (cases a and b), which is not the case for the remaining cases. Indeed, flow path tortuosity promotes several liquid acceleration and deceleration stages while flowing throughout the domains (cases c to e). These velocity profile variations highly impact other parameters such as liquid film thickness or mass transfer.

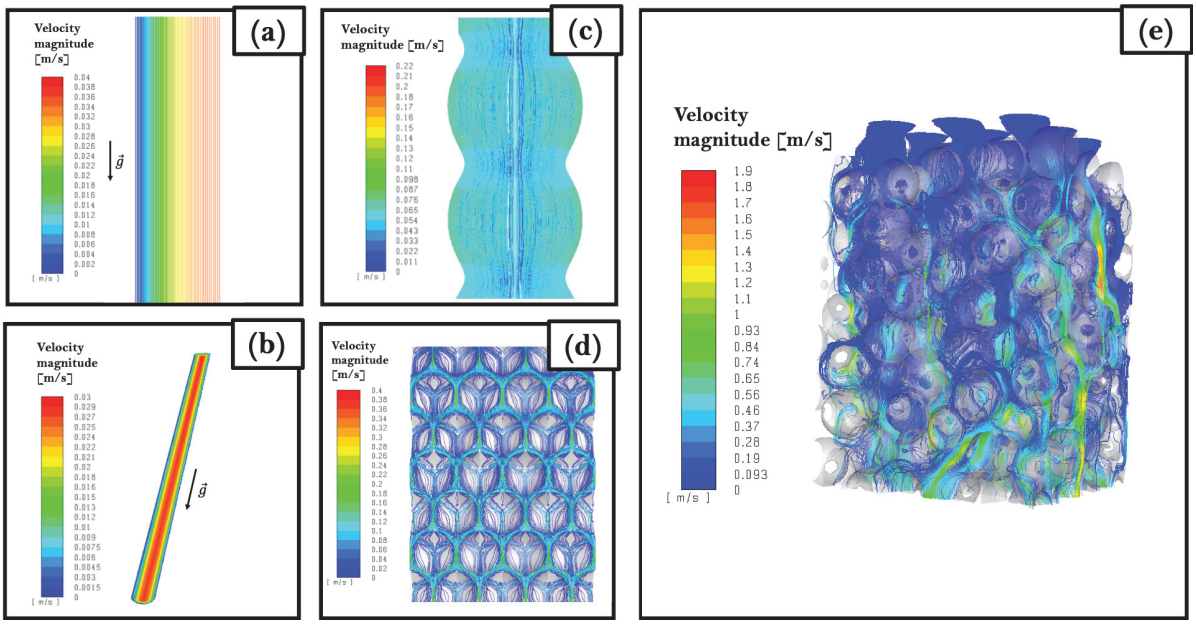

Figure 7.2 3D liquid phase pathlines coloured by velocity magnitude in the different investigated study cases : (a) bi-dimensional vertical falling liquid film, (b) Falling Film Micro-structured Reactor (FFMR) [Tourvieille et al., 2013], (c) Spherical particles' string reactor, (d) 3D-printed milli-reactor and (e) trickle-bed reactor spherical loading

In the bi-dimensional falling liquid film, liquid film thickness remains constant throughout the numerical domain. Similarly, even though a radial liquid film thickness distribution is observed in the micro-channels (case b), the longitudinal liquid film thickness profile does not change throughout the numerical domain. Regarding the spherical particles' string reactor, liquid film thickness reaches a minimum value at the equatorial plane of each particle, while the maximum value corresponds to the contact points between particles. In addition, a periodic pattern is observed since liquid film profile is similar around each spherical particle. The same is observed in the milli-reactor (case d) where an acceleration/deceleration pattern leads to

periodic liquid film thickness profiles around hemispheres. Nevertheless, a more randomised behaviour is encountered in particle loadings owing to the random nature of packing generation.

The considered study cases have different geometrical features, leading to different solid wetting configurations. The present work studied reactor performance in both total (cases a, b and c) and partial wetting conditions (cases d and e). Based on CFD validation of the 3D-printed milli-reactor, predicted wetting efficiency values were considered reliable since a close agreement was achieved. Besides, simulating trickle-bed hydrodynamic performance (case e) shed the light on the influence of gas superficial velocity and particle shape on wetting efficiency. Subsequently, correlation proposed by Julcour-Lebigue et al. [2009] was expanded to account for the aforementioned effects.

7.5 Mass transfer analysis

Mass transfer simulation results differed from one case to another. For non-tortuous flow paths (cases a and b), mass transfer was found to be predominantly diffusive. This is attributed to steady velocity and liquid film thickness profiles throughout the numerical domains. However, a significant increase in mass transfer performance was achieved with the string reactor (case c). Indeed, it was observed that solute transfer to the liquid film was highly boosted. A high proportion of the liquid film contained reagent at its maximum concentration ($C^*_{H_2}$), therefore establishing a concentration gradient near catalyst surface. Subsequently, low theoretical mass boundary layer thicknesses (δ_c) are achieved, reflecting mass transfer acceleration.

A similar mass transfer performance was achieved for the milli-reactor (case d) and trickle-bed loadings (case e). When comparing thicknesses of mass transfer (δ_c) and hydrodynamic (δ_{geo}) boundary layers, it is observed that mass transfer is significantly accelerated as well. This mass transfer performance is attributed to flow path tortuosity and convective reagent supply. Gas-liquid-solid mass transfer is then governed by gas-liquid interfacial velocity, and highly boosted with local velocity variability.

Chapter 8

General conclusions and perspectives

Gas-liquid-solid mass transfer in the presence of a heterogeneous catalytic reaction is an important aspect of several industrial processes. For this reason, a collection of experimental research works investigated mass transfer processes in laboratory and industrial operating conditions. However, due to the complexity of mass transfer characterisation, gas-liquid-solid mass transfer is usually investigated separately: (i) gas-liquid mass transfer through absorption experiments and (ii) liquid-solid mass transfer through solid dissolution experiments. Subsequently, several research works proposed correlations for both gas-liquid and liquid-solid mass transfer coefficients. Nevertheless, these correlations show high disparities and are unreliable mainly due to the difference between laboratory (low temperature and pressure, smooth particles, straightforward analysis) and industrial (high temperature and pressure, porous particles, reactor modeling) methods. Furthermore, to the best of our knowledge, insight was yet to be provided about particle shape effect on mass transfer.

In this context, the present work focused on the complex coupling between multiphase hydrodynamics, gas-liquid-solid mass transfer and heterogeneous catalysis. More precisely, our task was to highlight particle shape effect on mass transfer for a better understanding. To do so, Computational Fluid Dynamics (CFD) investigations were conducted in different reactors, following a strategy of increasing complexity of solid geometries.

In an effort to shed some light on local information, the CFD model predicts multiphase flow using the "Volume-Of-Fluid" approach. This numerical approach is capable of tracking gas-liquid and liquid-solid interfaces, giving therefore access to accurate descriptions of interfacial areas and local film thickness variations. Concurrently, a convection-diffusion transport equation is solved for solute concentrations. The heterogeneous catalytic reaction is implemented through the reactive flux method, describing solute consumption as a surface

flux boundary condition. The developed numerical model was applied on several case studies, namely: (i) bi-dimensional vertical falling liquid film, (ii) falling film micro-structured reactor (FFMR), (iii) spherical particles string reactor, (iv) 3D-printed milli-reactor and (v) trickle-bed loadings equipped with spheres, trilobes and quadrilobes.

Before conducting predictive simulations, the numerical model must be validated to evaluate its accuracy. Accordingly, the bi-dimensional falling film over a vertical plane was simulated in several mass transfer configurations. First, the predicted interface velocity and liquid film thickness were in excellent agreement with analytical solution of Nusselt [1916]. In physical and chemical absorption conditions, gas-liquid mass transfer coefficients were found in a good agreement with analytical solutions of Higbie [1935] and Danckwerts [1970] respectively. Similarly, including α-methylstyrene hydrogenation to cumene, gas-liquid-solid mass transfer was found in a good agreement with a developed analytical solution (cf. chapter 3). Subsequently, it was concluded that high accuracy is achieved using the selected set of physical models and numerical algorithms.

Afterwards, the numerical model was applied to a 3D falling film micro-structured reactor (FFMR), employed by Tourvieille et al. [2013] to characterise experimentally gas-liquid-solid mass transfer. The specific feature of this reactor lies in its internal geometry. Indeed, gas and liquid flow takes place within semi-elliptic micro-structured channels, leading to a meniscus shaped liquid film flow. First, hydrodynamic predictions were compared to experimental visualisations through confocal microscopy. Meniscus shape and location of gas-liquid interface was well represented by the numerical model, for different liquid flow rate conditions. In addition, hydrogen consumption fluxes and α-methylstyrene conversions were in agreement with experimental data. In view of these results, we concluded that the model guarantees accuracy even in complex film thickness settings.

Following the previous validations, a string reactor of 12 spherical particles was simulated using the developed numerical model. The aim was to analyse mass transfer in tortuous flow paths. In developed flow conditions, the reactor operated in total surface wetting conditions since a continuous liquid film was formed over the catalyst particles. Subsequently, interface velocity and liquid film thickness are changing periodically throughout the tortuous flow path. The minimum liquid film thickness and maximum interface velocity were encountered at the equatorial plane of each particle, while the opposite configuration was found between spherical particles. This flow behaviour enhanced gas-liquid-solid mass transfer, since convection promotes fluid's radial mixing and renewal in all areas surrounding the particles.

Further mass transfer evaluations were conducted, particularly to assess the following models: (i) resistances-in-series and (ii) film model. In the considered study cases, liquid film thicknesses do not allow for the presence of a bulk within liquid phase. Therefore, the resistances-in-series model was found to overestimate the overall mass transfer coefficient by 27%, 32% and 37% respectively in the case of bi-dimensional falling film, FFMR and spherical particles string reactor. Regarding the film model, since mass transfer regime was predominantly diffusive, the film model was applicable to the bi-dimensional falling liquid film, and was slightly modified to account for liquid film thickness distribution in the FFMR. Nevertheless, it was found that when the effect of convection is significant, the film model was no longer applicable. Therefore, a gas-liquid-solid Sherwood number correlation was proposed for the spherical particles string reactor.

Before proceeding to trickle-bed predictions, an additional assessment was conducted on a catalytic milli-reactor. In the vein of increasing complexity, the adopted milli-reactor design was small-enough for prompt simulations, and representative of a small portion of a spherical loading. The milli-reactor was characterised both experimentally and numerically. First, two-phase flow was found to be in trickling regime, regardless of gas and liquid flow rate conditions. This pattern was highlighted experimentally through high speed imaging, and numerically through hydrodynamic simulations. Furthermore, the milli-reactor operated in partial wetting conditions even at maximum liquid flow rate. Based on these observations, the reactive flux expression was modified to include catalyst external wetting efficiency. Both predictions and experimental hydrogen consumption fluxes and α-methylstyrene conversions were in good agreement. Analysis of gas-liquid-solid mass transfer unveiled an enhancement with convection, in line with spherical particles string reactor observations.

Finally, predictive simulations were conducted on three trickle-bed loadings equipped with: (i) spheres, (ii) trilobes and (iii) quadrilobes. First, a thorough hydrodynamic investigation was carried out to highlight the influence of catalyst geometry, flow rates and physico-chemical properties on the performance of trickle-bed reactors. A good agreement was achieved between CFD results and correlation considered as references at IFPEN the calculations of pressure drop, liquid saturation, wetting efficiency and liquid film thickness. CFD predictions unveiled a significant influence of gas superficial velocity and particle shape, in particular on wetting efficiency. Therefore, the correlation of Julcour-Lebigue et al. [2009] is expanded to account for the aforementioned effects. The new correlation predicts wetting efficiency values with a 10% accuracy. Regarding gas-liquid-solid reactive mass transfer, behaviour in trickle-bed reactors was found in consistency with previous study cases. The tortuous flow path was found

to enhance mass transfer through high convective solute supply. In addition, when compared to spheres and trilobes, quadrilobe-shaped particles provided the highest mass transfer coefficients. This was attributed to high wetting efficiency and liquid saturation levels.

Although most objectives of this thesis are achieved, more is yet to be done to supplement and reinforce the results. In the short term, further post-processing on trickle-bed reactors can be conducted for an advanced analysis of hydrodynamics and mass transfer. First, comparison of gas-liquid interfacial area values with literature correlations unveiled high discrepancies. Since the CFD model was found to provide high accuracy predictions, the predicted a_{GL} and a_{LS} values can be correlated to gas/liquid superficial velocities, bed characteristics, two-phase system properties and particle shape. In the same vein, through the definition of a critical velocity u_c, the static and dynamic components of liquid saturation can be analysed. Indeed, velocities lower than u_c point out static liquid saturation, while velocities higher than u_c indicate dynamic liquid saturation. As a result, it would be possible to assess liquid saturation literature correlations, and to propose new correlations to parameters of interest. Furthermore, the apparent diffusion layer thickness could be more profoundly analysed. The latter was found to be linked to both the physical liquid film thickness and hydrodynamic characteristics such as fluid velocity and flow tortuosity. Further post-processing may help to describe and model diffusion boundary layer thickness. Moreover, the numerical model developed in the present work proved to be efficient in particle shape characterisation. It can be therefore easily employed to assess TBR performance with other innovative catalyst shapes.

So far, the numerical model was used to simulate reactive mass transfer for a simple reaction involving one limiting reagent (hydrogen). Nevertheless, CFD modelling can be adjusted to solve concentrations of all involved species, since ANSYS Fluent enables concurrent resolution of 50 additional scalar transport equations. For example, considering α-methylstyrene hydrogenation, the different species would be hydrogen, α-methylstyrene and methylcyclohexane. As a result, the numerical model would become more representative of actual mass transfer phenomena, particularly at the gas-liquid-solid contact lines. In the same vein, composition changes in the liquid phase due to mass transfer can be included in the model. Furthermore, the reaction rate expression can be modified to adapt CFD modelling to other TBR applications, such as biomass conversion.

In the present work, the numerical model was used in isothermal conditions. However, trickle-bed reactors are known for their poor heat transfer performances, particularly in the presence of an exothermic catalytic reaction. Therefore, the CFD model can be coupled to

an energy balance to account for temperature changes. As a result, the model would include possible apparition of hot spots, or help prevent thermal runaway of the reactor.

It is worth noting that the model's flexibility allows to investigate other innovative catalytic reactors. Even though a significant share of industrial catalytic processes relies on fixed-bed reactors, new unconventional contactors are designed to amplify advantageous and limit inconvenient performances. In this context, alternatives to regular catalyst pellets are emerging, such as solid foams, monoliths or highly ordered porous media. Therefore, it would be of interest to conduct multiphase flow and mass transfer predictions in such original reactors using the developed CFD method in order to assess their performances and assist their design.

Regarding experimental work, the 3D-printed milli-reactor unveiled interesting information on gas-liquid-solid mass transfer in partial wetting conditions. Broadening gas and liquid flow rate ranges would result in a wider hydrodynamic and mass transfer investigation. Perhaps, the milli-reactor's performance can be assessed in total wetting conditions or other two-phase flow regimes. In addition, instead of hemispheres, extrudate plots (trilobes, quadrilobes, etc.) can be 3D-printed on reactive plates, therefore allowing for mass transfer characterisation using different particle shapes.

Bibliography

Al-Dahhan, M. and Dudukovic, M. (1991). Pressure drop and liquid holdup in high pressure trickle-bed reactors. *Chemical Engineering Science*, (49):5681–5698.

Al-Dahhan, M. and Dudukovic, M. (1994). Pressure drop and liquid holdup in high pressure trickle-bed reactors. *Chemical Engineering Science*, (49):5681–5698.

Al-Dahhan, M. and Dudukovic, M. (1995). Catalyst wetting efficiency in trickle-bed reactors at high pressure. *Chemical Engineering Science*, (15):2377–2389.

Al-Dahhan, M., Khadilkar, M., Wu, Y., and Dudukovic, M. (1998). Prediction of pressure drop and liquid holdup in high-pressure trickle-bed reactors. *Industrial Engineering Chemistry Research*, (37):793–798.

Al-Naimi, S., Al-Sudani, F., and Halabia, E. (2011). Hydrodynamics and flow regime transition study of trickle bed reactor at elevated temperature and pressure. *Chemical Engineering Research and Design*, (89):930–939.

Ambekar, A., Mattey, P., and Buwa, V. (2021). Pore-resolved two-phase flow in a pseudo-3d porous medium: Measurements and volume-of-fluid simulations. *Chemical Engineering Science*, (230):1–15.

Atta, A., Roy, S., and Nigam, K. (2007a). Investigation of liquid maldistribution in trickle-bed reactors using porous media concept in cfd. *Chemical Engineering Sience*, (62):7033–7044.

Atta, A., Roy, S., and Nigam, K. (2007b). Prediction of pressure drop and liquid holdup in trickle bed reactor using relative permeability concept in cfd. *Chemical Engineering Sience*, (62):5870–5879.

Atta, A., Roy, S., and Nigam, K. (2010). A two-phase eulerian approach using relative permeability concept for modeling of hydrodynamics in trickle-bed reactors at elevated pressure. *Chemical Engineering Research and Design*, (88):369–378.

Attou, A. and Boyer, C. (1999). Revue des aspects hydrodynamiques des réacteurs catalytiques gaz-liquide-solide à lit fixe arrosé. *Oil Gas Science and Technology - Rev IFP*, (1):29–66.

Attou, A., Boyer, C., and Ferschneider, G. (1999). Modelling of the hydrodynamics of the cocurrent gas-liquid trickle flow through a trickle-bed reactor. *Chemical Engineering Science*, (54):785–802.

Attou, A. and Ferschneider, G. (2000). A two-fluid hydrodynamic model for the transition between trickle and pulse flow in a cocurrent gas-liquid packed-bed reactor. *Chemical Engineering Science*, (55):491–511.

Augier, F., Fourati, M., and Haroun, Y. (2017). Characterization and modelling of a maldistributed trickle bed reactor. *The Canadian Journal of Chemical Engineering*, (95):222–230.

Augier, F., Koudil, A., Royon-Lebeaud, A., Muszynski, L., and Yanouri, Q. (2010). Numerical approach to predict wetting and catalyst efficiencies inside trickle bed reactors. *Chemical Engineering Science*, (65):255–260.

Baker, O. (1954). Simultaneous flow of oil and gas. *Oil and Gas Journal*, (53):185–195.

Baldi, G. and Specchia, V. (1976). Distribution and radial spread of liquid in packed towers with two-phase cocurrent flow: Effect of packing shape and size. *Quaderni dell'Ingegnere Chimico Italiano*, (12):107–111.

Baussaron, L. (2007). *Étude du Mouillage Partiel et du Transfert de Matière Liquide-Solide en Réacteur à Lit Fixe Arrosé*. Phd thesis, Institut National Polytechnique de Toulouse.

Baussaron, L., Julcour-Lebigue, C., Wilhelm, A., Boyer, C., and Delmas, H. (2007a). Partial wetting in trickle bed reactors: Measurement techniques and global wetting efficiency. *Industrial and Engineering Chemistry Research*, (46):8397—-8405.

Baussaron, L., Julcour-Lebigue, C., Wilhelm, A., Boyer, C., and Delmas, H. (2007b). Wetting topology in trickle bed reactors. *AIChE Journal*, (53):1850–1860.

Bazer-Bachi, F., Augier, F., and Santos, B. (2011). 1d and 2d simulations of partially wetted catalyst particles: A focus on heat transfer limitations. *Chemical Engineering Science*, (66):1953–1961.

Beni, A. and Khosravi-Nikou, M. (2015). Modeling hydrodynamics of trickle-bed reactors at high and low pressure using cfd method. *Petroleum Science and Technology*, (33):1770–1779.

Benkrid, K., Rode, S., and Midoux, N. (1997). Prediction of pressure drop and liquid saturation in trickle-bed reactors operated in high interaction regimes. *Chemical Engineering Science*, (52):4021–4032.

Boccardo, G., Augier, F., Haroun, Y., Ferré, D., and Marchisio, D. (2015). Validation of a novel open-source work-flow for the simulation of packed-bed reactors. *Chemical Engineering Journal*, (279):809–820.

Bondi, A. (1971). Handling kinetics from trickle-phase reactors. *Chemical Technology 1*, pages 185—-188.

Bothe, D. and Fleckenstein, S. (2013). A volume-of-fluid-based method for mass transfer processes at fluid particles. *Chemical Engineering Science*, (101):283–302.

Bourlioux, A. (1995). A coupled level-set volume-of-fluid algorithm for tracking material interfaces. *International symposium on Computational Fluid Dynamics*, (4):15–22.

Boyer, C., Koudil, A., Chen, P., and Dudukovic, M. (2005). Study of liquid spreading from a point source in a trickle-bed via gamma-ray tomography and cfd simulation. *Chemical Engineering Science*, (60):6279–2688.

Boyer, C., Volpi, C., and Ferschneider, G. (2007). Hydrodynamics of trickle bed reactors at high pressure: Two-phase flow model for pressure drop and liquid holdup, formulation and experimental validation. *Chemical Engineering Science*, (62):7026–7032.

Brackbill, J., Khote, D., and Zemach, C. (1992). A continuum method for modelling surface tension. *Journal of Computational Physics*, (100):335–354.

Brown, G. (1950). *Unit Operations*. New York; Chapman & Hall: London.

Burghardt, A., Bartelmus, G., Jaroszynski, M., and Kolodziej, A. (1995). Hydrodynamics and mass transfer in a three-phase fixed-bed reactor with cocurrent gas-liquid downflow. *Chemical Engineering Journal*, (58):83–99.

Burghardt, A., Bartelmus, G., and Szlemp, A. (2004). Hydrodynamics of pulsing flow in three-phase fixed-bed reactor operating at an elevated pressure. *Industrial Engineering and Chemistry Research*, (43):4511–4521.

Burghardt, A., Kolodziej, A., and Jaroszynski, M. (1990). Experimental studies of liquid-solid wetting efficiency in trickle-bed cocurrent gas-liquid downflow. *Chemical Engineering and Processing: Process Intensification*, (28):35–49.

Charpentier, J. (1976). Recent progress in two-phase gas-liquid mass transfer in packed beds. *Chemical Engineering Journal*, (11):161–181.

Charpentier, J. and Favier, M. (1975). Some liquid holdup experimental data in trickle-bed reactors for foaming and nonfoaming hydrocarbons. *AIChE Journal*, (21):1213–1218.

Charpentier, J., Prost, C., and Le Goff, P. (1969). Chute de pression pour des Écoulements à co-courant dans les colonnes à garnissage arrosés: Comparaison avec le garnissage noyé. *Chemical Engineering Science*, (24):1777–1794.

Chou, T., Worley, F., and Luss, D. (1979). Local particle-liquid mass transfer fluctuations in mixed-phase cocurrent downflow through a fixed bed in the pulsing regime. *Industrial and Engineering Chemistry Fundamentals*, (18):279–283.

Coenen, J., Tchouparova, E., and Jing, X. (2004). Measurement parameters and resolution aspects of micro x-ray tomography for advanced core analysis. *International Symposium of the Society of Core Analysts held in Abu Dhabi, UAE*.

Colombo, A., Baldi, G., and Sicardi, S. (1976). Solid-liquid contacting effectiveness in trickle bed reactors. *Chemical Engineering Science*, (31):1101–1108.

Danckwerts, P. (1970). *Gas-Liquid Reactions*. McGraw-Hill Book Co., New-York.

Deising, D., Marschall, H., and Bother, D. (2016). A unified single-field model framework for volume-of-fluid simulations of interfacial species transfer applied to bubbly flows. *Chemical Engineering Science*, (139):173–195.

Deng, H., Guo, B., Dong, H., Liu, C., and Geng, Z. (2020). Computational investigation of liquid holdup and wetting efficiency inside trickle bed reactors with different catalyst particle shapes. *Applied Sciences*, (10):1–18.

Dong, H. and Blunt, M. (2009). Pore-network extraction from micro-computerized-tomography imaged. *Physical Review*, (80):1–11.

El-Hisnawi, A., Dudukovic, M., and Mills, P. (1982). Trickle-bed reactors: Dynamic tracer tests, reaction studies, and modeling reactor performance. *ACS Symposium Series*, (196):421—-440.

Ellman, M., Midoux, N., Wild, G., Laurent, A., and Charpentier, J. (1990). A new, improved liquid hold-up correlation for trickle-bed reactors. *Chemical Engineering Science*, (45):1677–1684.

Ergun, S. (1952). Fluid flow through packed columns. *Chemical Engineering Progress*, (48):89–94.

Fourati, M., Roig, V., and Raynal, L. (2013). Liquid dispersion in packed columns: Experiments and numerical modeling. *Chemical Engineering Science*, (100):266–278.

Froment, G. and Bischoff, K. (1979). *Chemical Reactor Analysis and Design*. Wiley, New York.

Fujita, F. and Sacuma, S. (1954). *Chemical Engineering of Japan*, (18):64.

Fukano, T. and Ousaka, A. (1985). Relationship between pulsations of void fraction and static pressure in vertical upward air-water 2-phase flow. *Journal of the Atomic Energy Society of Japan*, (27):1147–1155.

Fukushima, S. and Kusaka, K. (1977). Interfacial area and boundary of hydrodynamic flow region in packed-column with cocurrent downward flow. *Journal of Chemical Engineering of Japan*, (10):461–467.

Germain, A., L'Homme, G., and Lefebgre, A. (1979). *The Trickle Flow and Bubble Flow Reactors in Chemical Processing*. Chemical Engineering of Gas-Liquid-Solid Catalyst Reactions, L'Homme, G.A., Ed. CEBEDOC, Liege, Belgium.

Giakoumakis, D., Kostoglou, M., and Karabelas, A. (2005). Induced pulsing in trickle-beds – characteristics and attenuation of pulses. *Chemical Engineering Science*, (60):5183–5197.

Gianetto, A., Baldi, G., Specchia, V., and Sicardi, S. (1978). Hydrodynamics and solid-liquid contacting effectiveness in trickle-bed reactors. *AIChE Journal*, (24):1087–1104.

Gianetto, A. and Silveston, P. (1986). *Multiphase Chemical Reactors: Theory, Design, Scale-Up*. Hemisphere Publishing Corp., New York.

Gianetto, A. and Specchia, V. (1992). Trickle-bed reactors: State of the art and perspectives. *Chemical Engineering Science*, (47):3197–3213.

Gianetto, A., Specchia, V., and Baldi, G. (1973). Absorption in packed towers with concurrent downward high-velocity flows—ii: Mass transfer. *AIChE Journal*, (19):916–922.

Gladden, L., Lim, M., Mantle, M., Sederman, A., and Stitt, E. (2003). Mri visualisation of two-phase flow in structured supports and trickle-bed reactors. *Catalysis Today*, (79-80):203–210.

Gladden, L. and Sederman, A. (2002). Magnetic resonance imaging of single and two-phase flow in fixed-bed reactors. *Applied Magnetic Resonance*, (22):201—-212.

Gonzalez-Mendizabal, D., Aquilera, M., and Pironti, F. (1998). Solid-liquid mass transfer and wetting factors in trickle bed reactors: Effect of the type of solid phase and the presence of chemical reaction. *Chemical Engineering Communications*, (169):37—-55.

Goto, S., Levec, J., and Smith, J. (1975). Mass transfer in packed beds with two-phase flow. *Industrial Engineering Chemistry Process Design and Development*, (14):473–478.

Goto, S. and Mabuchi, K. (1984). Oxidation of ethanol in gas-liquid upflow and downflow reactors. *The Canadian Journal of Chemical Engineering*, (62):865–869.

Goto, S. and Smith, J. (1975). Trickle-bed reactor performance. *AIChE Journal*, (21):706–713.

Grimley, S. (1945). *Transactions of the Institution of Chemical Engineers*, (23):233.

Grosser, K., Carbonell, R., and Sundaresan, S. (1988). One set of pulsing in two-phase flow cocurrent downflow through a packed bed. *AIChE Journal*, (34):1850–1860.

Gunjal, P., Kashid, M., Ranade, V., and Chaudhari, R. (2005). Hydrodynamics of trickle-bed reactors. experiments and cfd modeling. *Industrial Engineering Chemistry Research*, (44):6278–6294.

Gunjal, P., Ranade, V., and Chaudhari, R. (2003). Experimental and computational study of liquid drop over flat and spherical surfaces. *Catalysis Today*, (79-80):267–273.

Hannaoui, R., Horgue, P., Larachi, F., Haroun, Y., Augier, F., Quintard, M., and Prat, M. (2015). Pore-network modeling of trickle bed reactors: Pressure drop analysis. *Chemical Engineering Journal*, (262):334–343.

Haroun, Y., Legendre, D., and Raynal, L. (2010). Volume of fluid method for interfacial reactive mass transfer: Application to stable liquid film. *Chemical Engineering Science*, (65):2896–2909.

Hartman, M. and Coughlin, R. (1971). Oxidation of so_2 in trickle-bed packed with carbon. *Chemical Engineering Science*, (27):867–880.

Hasseni, W., Laurent, A., Midoux, N., and Charpentier, J. (1987). Hydrodynamics of a trickle bed reactor operating under pressure (0-10 mpa): Flow regimes and pressure drop. *CHISA '87 Session 17: Gas-Liquid Packed Bed, Prague*.

Haure, P., Hudgins, R., and Silveston, P. (1990). Steady-state models for so_2 oxidation in trickle-bed reactors. *Chemical Engineering Journal*, (43):121–125.

Herskowitz, M. (1981). Wetting efficiency in trickle-bed reactors: its effect on the reactor performance. *Chemical Engineering Journal*, (22):167—-175.

Herskowitz, M., Carbonell, R., and Smith, J. (1979). Effectiveness factors and mass transfer in trickle-bed reactors. *AIChE Journal*, (25):272—-283.

Herskowitz, M., Morita, S., and Smith, J. (1978). Solubility of hydrogen in α-methylstyrene. *Journal of Chemical Engineering Data*, (23):227–228.

Herskowitz, M. and Mosseri, S. (1983). Global rates of reaction in trickle-bed reactors: Effects of gas and liquid flow rates. *Industrial Engineering Chemistry Fundamentals*, (22):4–6.

Higbie, R. (1935). The rate of absorption of a pure gas into a still liquid during short periods of exposure. *Transactions of the American Institute of Chemical Engineering*, (60):365–389.

Highfill, W. and Al-Dahhan, M. (2001). Liquid-solid mass transfer coefficient in high pressure trickle bed reactors. *Chemical Engineering Research and Design*, (79):631–640.

Hikita, H. and Kataoka, T. (1956). *Chemical Engineering of Japan*, (20):528.

Hirose, T., Mori, Y., and Sato, Y. (1976). Liquid-to-particle mass transfer in fixed bed reactor with cocurrent gas-liquid downflow. *Journal of Chemical Engineering of Japan*, (9):220–225.

Hirose, T., Toda, M., and Sato, Y. (1974). Liquid phase mass transfer in packed bed reactor with cocurrent gas-liquid downflow. *Journal of Chemical Engineering of Japan*, (7):187—192.

Hirt, C. and Nichols, B. (1981). Volume of fluid method for the dynamics of free boundaries. *Journal of Computational Physics*, (39):201–225.

Hochman, J. and Effron, E. (1969). Two-phase cocurrent downflow in packed beds. *Industrial Engineering Chemistry Fundamentals*, (8):63–71.

Hofmann, H. (1977). Hydrodynamics, transport phenomena, and mathematical models in trickle bed reactors. *International Chemical Engineering*, (17):19–28.

Hofmann, H. (1978). Multiphase catalytic packed reactors. *Cat. Rev. Sci.*, (17):71–117.

Holub, R., Dudukovic, M., and Ramachandran, P. (1992). A phenomenological model for pressure drop, liquid holdup, and flow regime transition in gas-liquid trickle flow. *Chemical Engineering Science*, (47):2343–2348.

Horgue, P., Augier, F., Duru, P., Prat, M., and Quintard, M. (2013). Experimental and numerical study of two-phase flows in arrays of cylinders. *Chemical Engineering Science*, (102):335–345.

Iliuta, I., Ortiz-Arroyo, A., Larachi, F., Grandjean, B., and Wild, G. (1999). Hyndrodynamics and mass transfer in trickle-bed reactors: an overview. *Chemical Engineering Science*, (54):5329–5337.

Ishigaki, S. and Goto, S. (1999). Vapor-phase kinetics and its contribution to global three-phase reaction rate in hydrogenation of 1-methylnaphatalene. *Catalysis Today*, (48):31—-40.

Jabbari, M., Bulatova, R., Hattel, J., and Bahl, C. (2014). An evaluation of interface capturing methods in a vof based model for multiphase flow of a non-newtonian ceramic in tape casting. *Applied Mathematical Modelling*, (38):3222–3232.

Jiang, Y., Khadilkar, M., Al-Dahhan, M., and Dudukovic, M. (2002a). Cfd of multiphase flow in packed-bed reactors: I. k-fluid modeling issues. *AIChE Journal*, (48):701–715.

Jiang, Y., Khadilkar, M., Al-Dahhan, M., and Dudukovic, M. (2002b). Cfd of multiphase flow in packed-bed reactors: Ii. results and applications. *AIChE Journal*, (48):716–730.

Julcour-Lebigue, C., Augier, F., Maffre, H., Wilhelm, A., and Delmas, H. (2009). Measurements and modeling of wetting efficiency in trickle-bed reactors: Liquid viscosity and bed packing effects. *Industrial and Engineering Chemistry Research*, (48):6811–6819.

Kawase, Y. and Ulbrecht, J. (1981). Newtonian fluid sphere with rigid or mobile interface in a shear thinning liquid drag and mass transfer. *Chemical Engineering Communications*, (8):213–228.

Kiared, K. and Zoulalian, A. (1992). Study and modeling of catalytic sulfur dioxide oxidation in verlifix three-phase reactor. *Chemical Engineering Science*, (47):3705–3712.

Kundu, A., Nigam, K., and Verma, R. (2003). Catalyst wetting characteristics in trickle-bed reactors. *AIChE Journal*, (49):2253–22630.

Lafaurie, B., Nardone, C., Scardovelli, R., Zaleski, S., and Zanetti, G. (1994). Modelling merging and fragmentation in multiphase flow with surfer. *Journal of Computational Physics*, (113):134–147.

Lakota, A. and Levec, J. (1990). Solid-liquid mass transfer in packed beds with cocurrent downward two-phase flow. *AIChE Journal*, (36):1444–1448.

Lappalainen, K., Manninen, M., and Alopaeus, V. (2009a). Cfd modeling of radial spreading of flow in trickle-bed reactors due to mechanical and capillary dispersion. *Chemical Engineering Science*, (64):207–218.

Lappalainen, K., Manninen, M., Alopaeus, V., Aittamaa, J., and Dodds, J. (2009b). An analytical model for capillary pressure-saturation relation for gas-liquid system in a packed-bed of spherical particles. *Transport in Porous Media*, (77):17–40.

Lara-Marquez, A., Larachi, F., Wild, G., and Laurent, A. (1992). Mass transfer characteristics of fixed beds with cocurrent upflow and downflow. a special reference to the effect of pressure. *Chemical Engineering Science*, (47):3485—-3492.

Lara-Marquez, A., Menguy, T., and Wild, G. (1993). Détermination des paramètres de transfert de matière dans un réacteur à lit fixe à co-courant ascendant de gaz et de liquide. *Récents Progrès en Génie des Procédés*, (16).

Larachi, F., Belfares, L., Iliuta, I., and Grandjean, B. (2002). Heat and mass transfer in cocurrent gas/liquid packed beds. analysis, recommendations and new correlations. *Industrial Engineering Chemisty Research*, (42):222–242.

Larachi, F., Belfares, L., Iliuta, I., and Grandjean, B. (2003). Heat and mass transfer in cocurrent gas-liquid packed beds. analysis, recommendations and new correlations. *Industrial and Engineering Chemistry Research*, (42):222—242.

Larachi, F., Belfares, L., Iliuta, I., and Grandjean, B. (2004). Liquid hold-up correlations for trickle beds without gas flow. *Chemical Engineering and Processing*, (43):85–90.

Larachi, F., Cassanello, M., and Laurent, A. (1998). Gas-liquid interfacial mass transfer in trickle-bed reactors at elevated pressures. *Industrial Engineering Chemistry Research*, (37):718–733.

Larachi, F., Hannaoui, R., Horgue, P., Augier, F., Haroun, Y., Youssef, S., Rosenberg, E., Prat, M., and Quintard, M. (2014). X-ray micro-tomography and pore network modeling of single-phase fixed-bed reactors. *Chemical Engineering Journal*, (240):290–306.

Larachi, F., Laurent, A., , Wild, G., and Midoux, N. (1991a). Liquid saturation data in trickle-beds operated under elevated pressure. *AIChE Journal*, (37):1109–1112.

Larachi, F., Laurent, A., , Wild, G., and Midoux, N. (1991b). Some experimental liquid saturation results in fixed-bed reactors operated under elevated pressure in cocurrent upflow and downflow of the gas and the liquid. *Industrial Engineering Chemistry Research*, (30):2404–2410.

Larachi, F., Laurent, A., Midoux, N., and Wild, G. (1991c). Experimental study of a trickle-bed reactor operating at high pressure: Two-phase pressure drop and liquid saturation. *Chemical Engineering Science*, (46):1233–1246.

Larachi, F., Wild, G., Laurent, A., and Midoux, N. (1994). Influence of gas density on the hydrodynamics of cocurrent gas-liquid upflow fixed bed reactors. *Industrial Engineering Chemistry Research*, (33):519–525.

Larkins, R., White, R., and Jeffrey, D. (1961). Two-phase concurrent flow in packed beds. *AIChE Journal*, (7):231–239.

Latifi, M., Laurent, A., and Storck, A. (1988). Liquid-solid mass transfer in a packed bed with downward cocurrent gas-liquid flow: an organic liquid phase with high schmidt number. *Chemical Engineering Journal*, (34):47–56.

Latifi, M., Naderifar, A., and Midoux, N. (1997). Experimental investigation of the liquid/solid mass transfer at the wall of a trickle-bed reactor – influence of schmidt number. *Chemical Engineering Science*, (52):4005–4011.

Levec, J. and Smith, J. (1976). Oxidation of acetic acid solutions in a trickle-bed reactor. *AIChE Journal*, (22):159–168.

Llano, J., Rosal, R., Sastre, H., and Diez, F. (1997). Determination of wetting efficiency in trickle-bed reactors by a reaction method. *Industrial and Engineering Chemistry Research*, (36):2616—-2625.

Lockhart, R. and Martinelli, R. (1949). Proposed correlation of data for isothermal two-phase, two-component flow in piped. *Chemical Engineering Progress*, (45):39–48.

Lopes, R. and Quinta-Ferreira, R. (2007). Trickle-bed cfd studies in the catalytic wet oxidation of phenolic acids. *Chemical Engineering Science*, (62):7045–7052.

Lopes, R. and Quinta-Ferreira, R. (2009a). Numerical simulation of trickle-bed reactor hydrodynamics with rans-based models using a volume of fluid technique. *Industrial and Engineering Chemistry Research*, (48):1740–1748.

Lopes, R. and Quinta-Ferreira, R. (2009b). Volume-of-fluid based model for multiphase flow in high-pressure trickle-bed reactor: Optimization of numerical parameters. *AIChE Journal*, (55):2920–2933.

Lopes, R. and Quinta-Ferreira, R. (2010a). Assessment of cfd-vof method for trickle-bed reactor modeling in the catalytic wet oxidation of phenolic wastewaters. *Industrial and Engineering Chemistry Research*, (49):2638–2648.

Lopes, R. and Quinta-Ferreira, R. (2010b). Hydrodynamic simulation of pulsing-flow regime in high-pressure trickle-bed reactors. *Industrial and Engineering Chemistry Research*, (49):1105–1112.

Lopes, R., Silva, A., and Quinta-Ferreira, R. (2007). Kinetic modeling and trickle-bed cfd studies in the catalytic wet oxidation of vanillic acid. *Industrial and Engineering Chemistry Research*, (46):8380–8387.

M., H. and Smith, J. (1983). Trickle-bed reactors: a review. *AIChE Journal*, (29):1–18.

Mantle, M., Sederman, A., and Gladden, L. (2001). Single and two-phase flow in fixed bed reactors: Mri flow visualisation and lattice-boltzmann simulations. *Chemical Engineering Science*, (56):523—-529.

Marschall, H., Hinterberger, K., Schüler, C., Habla, F., and Hinrichsen, O. (2012). Numerical simulation of species transfer across fluid interfaces in free-surface flows using openfoam. *Chemical Engineering Science*, (78):111–127.

Mata, A. and Smith, J. (1981). Oxidation of sulfur oxide in trickle-bed reactor. *Chemical Engineering Journal*, (22):229–235.

Mayo, F., Hunter, T., and Nash, A. (1935). *Journal of the Society of Chemical Industry*, (54):376.

Meille, V. and de Bellefon, C. (2004). Effect of water on α-methylstyrene hydrogenation on pd/al_2o_3. *The Canadian Journal of Chemical Engineering*, (82):190–193.

Meille, V., de Bellefon, C., and Schweich, D. (2002). Kinetics of α-methylstyrene hydrogenation on pd/al_2o_3. *Industrial Engineering Chemistry Research*, (41):1711–1715.

Meyers, R. (1996). *Handbook of Petroleum Refining Processes, 2nd ed.* McGraw-Hill, New York.

Midoux, N., Favier, M., and Charpentier, J. (1976). Flow pattern, pressure loss and liquid holdup data in gas-liquid downflow packed beds with foaming and nonfoaming hydrocarbons. *Journal of Chemical Engineering of Japan*, (9):350–356.

Midoux, N., Morsi, B., Purwasasmita, M., Laurent, A., and Charpentier, J. (1984). Interfacial area and liquid side mass transfer coefficient in trickle bed reactors operating with organic liquids. *Chemical Engineering Science*, (39):781—-794.

Mills, P. and Dudukovic, M. (1981). Evaluation of liquid-solid contacting in trickle-bed reactors by tracer methods. *AIChE Journal*, (27):893—-904.

Mirjalili, S., Jain, S., and Dodd, M. (2017). Interface-capturing methods for two-phase flows: An overview and recent developments. *Center for Turbulence Research - Annual Research Briefs*, pages 117–135.

Montagna, A., Shah, Y., and Paraskos, J. (1977). Communications - effect of catalyst particle size on performance of a trickle bed-reactor. *Industrial Engineering Chemistry Process Design and Development*, (16):152—-155.

Morsi, B. (1979). Contribution à l'étude de l'hydrodynamique et du transfert de matière dans un réacteur gas-liquide catalytique à lit fixe fonctionnant à cocourant vers le bas. *PhD thesis, INPL, France*.

Morsi, B., Midoux, N., Laurent, A., and Charpentier, J. (1982). Hydrodynamics and interfacial areas in downward cocurrent gas-liquid flow through fixed beds. influence of the nature of the liquid. *International Chemical Engineering*, (22):142–151.

Morsi, B. I. (1989). Mass transfer coefficients in a trickle-bed reactor with high and low viscosity organic solutions. *Chemical Engineering Journal*, (41):41–48.

Morsi, B. I., Laurent, A., Midoux, N., and Charpentier, J. (1980). Interfacial area in trickle-bed reactors: Comparison between ionic and organic liquids and between raschig rings and small diameter particles. *Chemical Engineering Science*, (35):1467–1470.

Muzaferija, S., Peric, M., Sames, P., and Schelin, T. (1998). A two-fluid navier- stokes solver to simulate water entry. *Proceeding of the 22nd Symposium on Naval Hydrodynamics*.

Naderifar, A. (1995). *Étude Experimentale Locale et Globale du Transfert de Matière Liquid/Solide à la Paroi d'un Réacteur à Lit Fixe*. Phd thesis, Institut National Polytechnique de Lorraine.

Nemec, D. and Levec, J. (2005). Flow through packed bed reactors: 2. two-phase cocurrent downflow. *Chemical Engineering Science*, (60):6958–6970.

Ng, K. and Chu, C. (1987). Trickle-bed reactors. *Chemical Engineering Progress*, (83):55–63.

Nigam, K., Iliuta, I., and Larachi, F. (2002). Liquid back-mixing and mass transfer effects in trickle-bed reactors filled with porous catalyst particles. *Chemical Engineering and Processing: Process Intensification*, (41):365–371.

Nishizawa, A., Kitano, T., Ikenaga, N., Miyake, T., and Suzuki, T. (2014). Use of trickle bed reactor for fischer-tropsch reaction over co-mn/oxidized diamond catalyst. *Journal of the Japan Petroleum Institute*, (57):109–117.

Nusselt, W. (1916). Die oberflachenkondensation des wasserdampfes. *Z. Vereines Deutsch. Ing.*, (60):541–546,569–575.

Onda, K., Takeuchi, H., and Kayama, Y. (1967). Effect of packing materials on wetted surface area. *K. Kagaku Kogaku*, (31):126—-134.

Osher, S. and Sethian, J. (1988). Fronts propagating with curvature-dependent speed: Algorithms based on hamilton-jacobi formulations. *Journal of Computational Physics*, (79):12–49.

Pironti, F., Mizrahi, D., Acosta, A., and Gonzalez-Mendizabal, D. (1999). Liquid- solid wetting factor in trickle bed reactors: its determination by a physical method. *Chemical Engineering Science*, (54):3793–3800.

Puranik, S. and Vogelpohl, V. (1974). Effective interfacial area irrigated packed columns. *Chemical Engineering Science*, (29):501—-507.

Purwasasmita, M. (1985). Contribution à l'étude des réacteurs gaz-liquide à lit fixe fonctionnant à cocourant vers le bas à fortes vitesses du gaz et du liquide. *PhD thesis, INPL, France*.

Ranade, V., Chaudhari, R., and Gunjal, P. (2011). *Chapter 2 - Hydrodynamics and Flow Regimes*. Trickle Bed Reactors: Reactor Engineering Applications. Elsevier, Amsterdam ; Boston.

Rao, V., Ananth, M., and Varma, Y. (1983). Hydrodynamics of two-phase cocurrent downflow through packed beds. *AIChE Journal*, (29):467–483.

Rao, V. and Drinkenburg, A. (1985). Solid-liquid mass transfer in packed beds with cocurrent gas-liquid downflow. *AIChE Journal*, (31):1059–1068.

Ratman, G., Ananth, M., and Varma, Y. (1993). A model for pressure drop in gas-liquid cocurrent downflow through packed beds. *Chemical Engineering Journal*, (51):19–28.

Ratnam, V. and Varma, Y. (1991). Effective interfacial area in gas-liquid cocurrent downflow through packed beds. *Bioprocess Engineering*, (7):29–34.

Ratnam, V., Venkata Narasaiah, D., and Varma, Y. (1994). A correlation for interfacial area in co-current gas-liquid downflow through packed beds. *Bioprocess Engineering*, (10):53–59.

Recary, C., Pérez, I., Roselló, R., Muniz, M., Hernández, E., Giraldo, R., and Oñate, E. (2019). Advances in particle packing algorithms for generating the medium in the discrete element method. *Computational Methods in Applied Mechanics and Engineering*, (345):336–362.

Ring, Z. and Missen, R. (1991). Trickle-bed reactors: Tracer study of liquid holdup and wetting efficiency at high temperature and pressure. *The Canadian Journal of Chemical Engineering*, (69):1016—-1020.

Rode, S. and Charpentier, J. (2011). Réacteurs à lit fixe catalytique à ecoulement gas-liquide. *Technique de l'Ingénieur*.

Rode, S., Midoux, N., Latifi, M., and Storck, A. (1994). Multiple hydrodynamic states in trickle beds operating in high-interaction regims: Liquid saturation and flow regime transitions. *Chemical Engineering Science*, (49):2535–2540.

Ruecker, C. and Agkerman, A. (1987). Determination of wetting efficiency for a trickle-bed reactor at high temperatures and pressures. *Industrial and Engineering Chemistry Research*, (26):164–166.

Saez, A. and Carbonell, R. (1985). Hydrodynamic parameters for gas-liquid cocurrent flow in packed beds. *AIChE Journal*, (31):52–62.

Sai, P. and Varma, Y. (1987). Pressure drop in gas-liquid downflow through packed beds. *AIChE Journal*, (33):2027–2036.

Saroha, A. and Nigam, K. (1996). Trickle bed reactors. *Reviews in Chemical Engineering*, (12):207–347.

Sato, Y., Hirose, T., Takahashi, F., and Toda, M. (1973). Pressure loss and liquid holdup in packed bed reactor with cocurrent gas-liquid downflow. *Journal of Chemical Engineering of Japan*, (6):147–152.

Satterfield, C. (1975). Trickle bed reactors. *AIChE Journal*, (21):209–228.

Satterfield, C. and Ozel, F. (1973). Direct solid-catalyzed reaction of a vapor in an apparently completely wetted trickle bed reactor. *AIChE Journal*, (19):1259—-1261.

Satterfield, C., Van Eek, M., and Bliss, G. (1978). Liquid-solid mass transfer in packed beds with downward concurrent gas-liquid flow. *AIChE Journal*, (24):709–717.

Schwartz, J., Weger, E., and Dudukovic, M. (1976). A new tracer method for determination of liquid-solid contacting efficiency in trickle bed reactors. *AIChE Journal*, (22):894–904.

Sederman, A., Alexander, P., and Gladden, L. (2001). Structure of packed beds probed by magnetic resonance imaging. *Powder Technology*, (117):255—-269.

Sederman, A. and Gladden, L. (2001). Magnetic resonance imaging as a quantitative prove of gas-liquid distribution and wetting efficiency in trickle-bed reactors. *Chemical Engineering Science*, (56):2615—-2628.

Sedriks, W. and Kenney, C. (1973). Partial wetting in trickle bed reactors - the reduction of crotonaldehyde over a palladium catalyst. *Chemical Engineering Science*, (28):559—-568.

Seguin, D., Montillet, A., Brunjail, D., and Comiti, J. (1996). Liquid-solid mass transfer in packed beds of variously shaped particles at low reynolds numbers: Experiments and model. *Chemical Engineering Technology*, (63):1–9.

Shah, Y. (1979). *Gas-Liquid-Solid Reactor Design*. McGraw-Hill, New York.

Shende, B. and Sharma, M. (1974). Mass transfer in packed columns: co-current operation. *Chemical Engineering Science*, (29):1763–1772.

Shulman, H., Ullrich, C., Proulx, A., and Zimmerman, J. (1955). Wetted and effective-interfacial areas, gas - and liquid-phase mass transfer rates. *AIChE Journal*, (1):253—-258.

Sicardi, S., Baldi, G., Giannetto, A., and Specchia, V. (1980). Catalyst areas wetted by flowing and semi stagnant liquid in trickle bed reactors. *Chemical Engineering Science*, (35):67–73.

Sie, S. (1991). Les conséquences de l'extrapolation appliquée aux procédés à l'Écoulement ruisselant réalisés en laboratoire et dans les réacteurs des unités-pilotes. *Oil Gas Science and Technology - Rev IFP*, (46):501–515.

Sie, S. (1996). Advantages, possibilities, and limitations of small-scale testing of catalysts for fixed-bed processes. *Deactivation and Testing of Hydrocarbon-Processing Catalysts. American Chemical Society*, pages 6–41.

Sie, S. and Krishna, R. (1998). Process development and scale up: Iii scale-up and scale-down of trickle-bed processes. *Review in Chemical Engineering*, (14):203–248.

Solomenko, Z., Haroun, Y., Fourati, M., Larachi, F., Boyer, C., and Augier, F. (2015). Liquid spreading in trickle-bed reactors: Experiments and numerical simulations using eulerian-eulerian two-fluid approach. *Chemical Engineering Science*, (126):698–710.

Sosa, J. (1981). Ermittlung wichtiger fluid-dynamischcr grössen bei rieselreaktoren mit den systemen wasser-luft und cyclohexen-kohlen-dioxid. *PhD thesis, Erlangen, Germany*.

Specchia, V. and Baldi, G. (1977). Pressure drop and liquid holdup for two-phase concurrent flow in packed beds. *Chemical Engineering Science*, (32):515–523.

Specchia, V., Baldi, G., and Gianetto, A. (1978). Solid-liquid mass transfer in concurrent two-phase flow through packed beds. *Industrial and Engineering Chemistry Process Design and Development*, (17):362—-367.

Szady, M. and Sundaresan, S. (1991). Effect of boundaries on trickle bed hydrodynamics. *AIChE Journal*, (37):1237–1241.

Tosun, G. (1984). A study of cocurrent downflow of nonfoaming gas-liquid systems in a packed bed. 2. pressure drop: Seach for a correlation. *Industrial Engineering Chemistry Process Design and Development*, (23):35–39.

Tourvieille, J. (2014). *Innovating Microstructured Gas-Liquid-Solid Reactors: a Contribution to the Understanding of Hydrodynamics and Mass Transfers*. Phd thesis, Université Claude Bernard Lyon 1.

Tourvieille, J., Bornette, F., Philippe, R., Vandenberghe, Q., and de Bellefon, C. (2013). Mass transfer characterisation of a microstructured falling film at pilot scale. *Chemical Engineering Journal*, (227):182–190.

Trahan, J., Graziani, A., Goswami, D., Stefanakos, E., Jotshi, C., and Goel, N. (2014). Evaluation of pressure drop and particle sphericity for an air-rock bed thermal energy storage system. *Energy Procedia*, (57):633–642.

Tukac, V. and Hanika, J. (1992). Influence of catalyst particles orientation on the pressure drop and the liquid dispersion in the trickle bed reactor. *Chemical Engineering Science*, (47):2227–2232.

Turek, F. and Lange, R. (1981). Mass transfer in trickle-bed reactors at low reynolds number. *Chemical Engineering Science*, (36):569–579.

Turpin, J. and Huntington, R. (1967). Prediction of pressure drop for two-phase two component concurrent flow in packed beds. *AIChE Journal*, (13):1196–1202.

Ubbink, O. (1997). *Numerical Prediction of Two Fluid Systems with Sharp Interfaces*. Phd thesis, Imperial College of Science, Technology and Medicine, London, England.

Ufford, R. and Perona, J. (1973). Liquid phase mass transfer with concurrent flow through packed towers. *AIChE Journal*, (19):1223–1226.

Vachaparambil, K. and Einarsrud, K. (2019). Comparison of surface tension models for the volume of fluid method. *Processes*, (7):1–24.

van Houwelingen, A., Sandrock, C., and Nicol, W. (2006). Particle wetting distribution in trickle-bed reactors. *AIChE Journal*, (52):3532–3542.

van Klinken, J. and van Dongen, R. (1980). Catalyst dilution for improved performance of laboratory trickle-flow reactors. *Chemical Engineering Science*, (35):59—-66.

Wammes, W., Mechielsen, S., and Westerterp, K. (1991a). The influence of pressure on the liquid hold-up in a cocurrent gas-liquid trickle-bed reactor operating at low gas velocities. *Chemical Engineering Science*, (46):409–417.

Wammes, W., Middelkamp, J., Huisman, W., deBaas, C., and Westerterp, K. (1991b). Hydrodynamics in a cocurrent gas-liquid trickle bed at elevated pressures. *AIChE Journal*, (37):1849–1862.

Wang, Y., Chen, J., and Larachi, F. (2013). Modelling and simulation of trickle-bed reactors using computational fluid dynamics: A state-of-the-art review. *The Canadian Journal of Chemical Engineering*, (91):136–180.

Wild, G., Larachi, F., and Charpentier, J. (1992). *Heat and Mass Transfer in Gas-Liquid-Solid Fixed Bed Reactors*. M. Quintard M. Todorovic. Heat and Mass Transfer in Porous Media, Amsterdam, The Netherlands.

Wilhite, B., Blackwell, B., Kacmar, J., Varma, A., and McCready, M. (2005). Origins of pulsing regime in cocurrent packed-bed flows. *Industrial and Engineering Chemistry Research*, (44):6056–6066.

Yeong, K., Gavriilidis, A., Zapf, R., Kost, H., Hessel, V., and Boyde, A. (2006). Characterisation of liquid film in a microstructured falling film reactor using laser scanning confocal microscopy. *Experimental Thermal and Fluid Science*, (30):463–472.

Zaki, M., Nirdosh, I., Sedahmed, G., and Baird, M. (2004). Liquid-solid mass transfer in fixed beds. *Chemical Engineering Technology*, (27):414–416.